Pore structure characterisation: The challenge to understand heterogeneous catalysts and fuel cells

Hitchcock, Iain

Award date:
2011

Awarding institution:
University of Bath

Pore structure characterisation: The challenge to understand heterogeneous catalysts and fuel cells

Iain Hitchcock

A thesis submitted for the degree of Doctor of Philosophy

University of Bath

Department of Chemical Engineering

May 2011

Perhaps you will forgive me if I turn from my own feelings to the words of another splendid bugger: W.H. Auden. This is actually what I want to say:

Stop all the clocks, cut off the telephone,
Prevent the dog from barking with a juicy bone,
Silence the pianos and with muffled drum
Bring out the coffin, let the mourners come.

Let aeroplanes circle moaning overhead
Scribbling on the sky the message He is Dead.
Put crepe bows round the white necks of the public doves,
Let the traffic policeman wear black cotton gloves.

He was my North, my South, my East and West,
My working week and my Sunday rest,
My noon, my midnight, my talk, my song;
I thought that love would last forever: I was wrong.

The stars are not wanted now; put out every one,
Pack up the moon and dismantle the sun,
Pour away the ocean and sweep up the woods;
For nothing now can ever come to any good.

I love you so much

Preface

All the work in this thesis is believed to be original except where explicit reference to other people and authors is given.

The catalyst supports (alumina and silica) studied in this thesis were supplied by Johnson Matthey. The SBA-15 sample studied in Chapter 7 was synthesised by Prof. Alexei Lapkin and the Pt-ZSM-5 zeolite catalyst studied in Chapter 11 was supplied by Dr Li Min Chua. A reference to their work is given in the named Chapters.

The MRI work in Chapter 4 was carried out by Dr Sandy Chudek. I prepared all the samples and inserted them into the NMR tube but Dr Sandy Chudek inserted the samples into the MRI machine and set-up the experimental parameters. I was however present during this procedure and analysed the experimental data.

The experiments to obtain the results in Table 10.2 of Chapter 10 were carried out by Dr John Lowe. I was not present during the experiments, but I analysed the data. I carried out all the other experiments in Chapter 10.

The tortuosity values calculated in Chapter 10 required the free diffusion coefficient of water at different temperatures below 0°C to be known. Dr Emily Perkins found how the diffusion coefficient of water varied as a function of temperature using data found in the literature (Perkins 2009). This correction curve has been used in this thesis.

Acknowledgements

I must first acknowledge the three people who have been with me from the start of my education; Mum, Dad and David. All three of you have helped me and supported all the decisions I have made. Sorry if at times during my studies I was not the most pleasant son or brother to be around, but it's because what I was doing was pretty hard!

Next I should thank Sean my supervisor. Sean, you have been the best supervisor I could have hoped for! You have turned me into a much better scientist over these four years and during a tough period of my life you sorted everything out for me; thank you! Sean, I will always see you as my boss, but also as a good friend.

Big thanks should go to Johnson Matthey. As well as EPSRC, Johnson Matthey financially supported my project, but they did more than this! Liz Holt my industrial supervisor and Edward Abram were both a great help during my project when I was at JM or Bath. Without visits to JM, half of this thesis would not exist! So I am extremely grateful to Steve Bailey, Rob Fletcher and Sandra Riley for allowing me full use of their analytical equipment. Not only that, if I needed any help when I was on site Steve, Rob, Sandra and other members of Steve's team went out of their way to help me! I would also like to thank David Davis. Dave allowed me to stay at his house when I visited JM and he also took time out to proof read my thesis; I really appreciated this!!

I should also thank John Lowe the NMR spectroscopist in Bath. Sean's new students will probably never meet John, which is a shame. John helped on all matters and is a great person to work with. Following Sean's new job at Nottingham John took over as my co-supervisor; if I needed him to do anything for me he wouldn't hesitate. While I am discussing new supervisors I want to mention Davide Mattia too. Davide also became my supervisor following Sean leaving Bath and he again helped me whenever I needed it. Any problem he immediately sorted them out for me.

I wish to thank Sandy Chudek for allowing me to use his MRI machine. Sandy was retiring at the start of my Ph.D, but before he retired he made sure I could run my samples on his machine (free of charge!) to complete my experiments. Not only did he allow me to use the machine, but once the sample was in place he set up all the experiments for me and generally gave me a lot of his time.

Thank you to anyone in Bath (Chemistry and Chemical Engineering) who has helped out over these 4 years, especially Sarah Jones and Merv Newnes. Sarah was the first person I met in Bath and helped a lot over these past few years. Merv has been priceless too; he provided fun discussions when he came to our office and sorted out all my IT problems (ie converting my thesis into a pdf!!)

Finally, thanks should go to members of the Sean Rigby group in Bath; especially Emily (for helping me out on all NMR matters), Li Min (for helping me out on all gas sorption matters), Navin (for putting up with me and helping out on everything) and Eleni (for just being herself and being from the country of all the Greek letters and words used in this thesis).

Summary

The work in this thesis is focussed on improving the accuracy, precision and range of descriptors that can be obtained from the gas sorption and cryoporometry characterisation techniques.

The conversion of gas adsorption isotherms into pore size distributions generally relies upon the assumption of independent pores. Hence, co-operative effects between pores, which might result in a significantly skewed pore size distribution, are neglected. In this work, co-operative adsorption effects (advanced adsorption) in water adsorption on a mesoporous silica material have been studied using MRI experiments. Evidence for advanced adsorption has been seen directly using transverse relaxation time weighted MR images. The spatial distribution of filled pores has been found to be highly non-random. Moreover, pixels containing the largest pores present in the material have been observed to fill in conjunction with pixels containing much smaller pores.

The theories of adsorption-desorption hysteresis of mesoporous solids have been rigorously tested using the integrated gas-mercury-gas experiment. The experiment has been used to deconvolve the capillary condensation and evaporation processes within a specific subset of pores contained within mesoporous materials. The size of these pores has been obtained independently of gas sorption using mercury porosimetry. This has enabled the meniscus geometry for the capillary condensation process to be determined in these pores. In addition, the Kelvin-Cohan equations and DFT theories of capillary condensation and evaporation have been directly tested. This has been done by comparing the relationship between the adsorption and desorption relative pressures for the pores which entrap mercury. It was found that the Kelvin-Cohan equations and DFT do not correctly predict the width of adsorption-desorption hysteresis in independent pores.

Gas sorption scanning loop experiments on a mesoporous material have been studied. It was observed that hysteresis in scanning loop experiments can be virtually purged which indicates a reversible adsorption and desorption mechanism. Additionally, scanning curve experiments have been studied as part of the integrated gas-mercury-gas experiment. The data for pores which entrapped mercury were deconvolved from that for all other pores and the scanning curves for these pores were determined. It was found that the scanning curves for the pores which entrapped mercury crossed between the boundary curves, which is anticipated for independent pores.

The theories of freeze-thaw hysteresis in cryoporometry of mesoporous solids have been rigorously tested using analogous scanning loop and curve experiments together with concurrently obtained (PFG) NMR diffusometry and relaxometry data. PFG NMR and relaxometry have revealed that the spatial disposition of frozen and molten phases, at a particular point in a loop, depends upon the prior thermal history. The data has also shown that there is an advanced melting process similar to advanced adsorption, and that it must be accounted for in order to adequately interpret cryoporometry data.

An experimental method has been developed that determines the amount of platinum incorporated inside the micropores of a ZSM-5 zeolite support. The method studies a chemisorption experiment before and after a nonane pre-adsorption experiment. The nonane becomes entrapped only in the micropores so the amount of platinum in these pores has been determined.

One of the main findings throughout the work has been that co-operative effects between pores (advanced adsorption and advanced melting) are neglected in conventional gas adsorption and cryoporometry measurements. Hence, pore size distributions derived are highly inaccurate. The work in this thesis illustrates the importance of understanding the underlying physics of these techniques before they are applied to characterise porous materials.

List of publications

Below is a list of publications to date based on the work contained within this thesis:

1. Hitchcock, I., Chudek, J. A., Holt, E. M., Lowe, J. P. and Rigby, S. P., *Langmuir*, **26**, 2010, 18061.

2. Hitchcock, I., Holt, E. M., Lowe, J. P. and Rigby, S. P., *Chemical Engineering Science*, **66**, 2011, 582.

3. Hitchcock, I., Chudek, J. A., Holt, E. M., Lowe, J. P. and Rigby, S. P., *American Institute of Physics Conference Proceedings*, in press.

List of presentations

Hitchcock, I., Chudek, J. A., Holt, E. M., Lowe, J. P. and Rigby, S. P, 2010. 'MRI and PGSE NMR studies of long-range pore-pore interactions effects in gas adsorption'. 10th Bologna Conference on Magnetic Resonance in Porous Media.

Contents

List of Figures

List of Tables

Nomenclature

A list of abbreviations and symbols used in this thesis are given below. Where possible, the symbols used are consistent with the predominant use in the literature.

Acronym	Definition
ASAP	Surface area and porosimetry
BPLED	Bipolar longitudinal eddy current delay
CPG	Controlled pore glass
DFT	Density functional theory
DSC	Differential scanning calorimeter
FID	Free induction decay
GCMC	Grand canonical Monte Carlo
MRI	Magnetic resonance imaging
NMR	Nuclear magnetic resonance
OMCTS	Octamethylcyclotetrasiloxane
PFG	Pulsed field gradient
RMS	Root mean square
STE	Stimulated echo
TEM	Transmission electron microscopy
TMS	Trimethylsilyl
STP	Standard temperature and pressure (273.15 K and 101300 Pa)

Greek letters	Definition	Units
γ	Surface tension (Chapters 2, 5, 6)	Nm^{-1}
γ	Magnetogyric ratio	$radT^{-1}s^{-1}$
Δ	Diffusion time	s
δ	Length of gradient pulse	s
ε	Potential energy (Chapter 2)	$Jmol^{-1}$
ε	Voidage	
θ	Contact angle	Degrees
$\varkappa$	Integral mean surface curvature of pore	m^{-1}
λ	Surface layer thickness	m
ϱ_s	Density of solid	kgm^{-3}
σ	Molecular cross sectional area	nm^2
σ_m	Atomic metal cross sectional area	m^2
σ_m	Thickness of a monolayer	m
σ_{sl}	Surface tension at solid liquid interface	Nm^{-1}
τ	Time for correction between bi-polar gradient pulses	s
τ_p	Tortuosity	
υ	Frequency of the Larmor precession	s^{-1}
υ	NMR resonance frequency	s^{-1}
$\upsilon(r)$	NMR resonance frequency located at position r	s^{-1}
υ_a	Volume fraction of dispersed phase	
$\Delta\varphi$	Phase shift	Radians
$\varphi_i(z)$	Potential energy of a molecule i as a function of its distance from a surface z	$Jmol^{-1}$
χ^2	Chi squared statistic	

Symbol	Definition	Units
A	Region of area (Chapter 4)	
A	Metal surface area per gram of catalyst	m^2g^{-1}
B_0	Static magnetic field	T
C	BET constant	
D	Diffusion coefficient	m^2s^{-1}
d	Fractal dimension of the surface	
$D(T)$	Diffusion coefficient as a function of T	m^2s^{-1}
D_a	Diffusion coefficient of phase, a	m^2s^{-1}
D_b	Diffusion coefficient of phase, b	m^2s^{-1}
D_{eff}	Effective diffusivity	m^2s^{-1}
D_{PFG}	Diffusion coefficient from PFG experiment	m^2s^{-1}
D_w	Effective diffusion coefficient of a composite medium	m^2s^{-1}
G	Magnetic field gradient vector	Tm^{-1}
g	Strength of pulsed field gradient	Tm^{-1}
ΔG	Gibbs free energy	$Jmol^{-1}$
h	Planck's constant	$6.626x10^{-34}Js$
ΔH	Molar enthalpy of adsorption	$Jmol^{-1}$
$\Delta H_{desorption}$	Molar enthalpy of desorption	$Jmol^{-1}$
ΔH_f	Enthalpy of fusion	$Jmol^{-1}$
$\Delta H_{vaporisation}$	Molar enthalpy of vaporisation	$Jmol^{-1}$
I_0	Reference NMR signal intensity	
I_{NMR}	NMR signal intensity	
K	Number of 4x4 squares	
K_{GT}	Gibbs-Thomson constant	nmK
m	Mass	g
M	Net magnetisation vector	JT^{-1}
M_x, M_y, M_z	Components of the magnetisation in the x, y, z directions	JT^{-1}
n	Amount of substance	mol
N	Number of filled pixels	
n^a	Amount of gas adsorbed	mol
N_A	Avogadro's number	$6.0223x10^{23}$ mol^{-1}
n_m	Monolayer capacity	m^3
P	Equilibrium pressure	Pa
$P(d)$	dV/dx normalised to 1	
P/P_0	Relative pressure	
P_0	Saturation pressure	Pa
$P_{adsorption}/P_0$	Adsorption relative pressure	
$P_{desorption}/P_0$	Desorption relative pressure	
P_{Hg}	Applied pressure to intrude mercury into a sample	MPa
R	Ideal gas constant	8.315 $Jmol^{-1}K^{-1}$
r_k	Radius of curvature of meniscus	m
r_p	Pore radius	m
$\langle r(t)^2 \rangle$	Mean square displacement	
S	BET surface area per gram	m^2g^{-1}
s	Stoichiometry factor	
ΔS	Entropy	$Jmol^{-1}K^{-1}$
S/V	Surface to volume ratio	m^{-1}
s^2	Sample variance	
T	Temperature	K or °C
t	Thickness of the multimolecular layer (gas sorption)	m
t	Time	s
t	Thickness of non-frozen layer (cryoporometry)	m
T_1	Longitudinal relaxation time constant	s
T_2	Transverse relaxation time constant	s
T_{2av}	Average transverse relaxation time constant	s
T_{2B}	Transverse relaxation time constant for the	s

	bulk	
T_{2s}	Transverse relaxation time constant for the surface layer	s
t_c	Critical thickness of multimolecular layer	m
T_c	Critical temperature	K or °C
t_d	Time delay between pulses	s
ΔT_f	Freezing point depression	K or °C
T_h	Hysteresis critical temperature	K or °C
T_m	Bulk melting point	K or °C
ΔT_m	Melting point depression	K or °C
$T_m(x)$	Bulk melting point of crystal sized x	K or °C
V	Volume	m^3
V_a	Volume of adsorbed gas	cm^3(STP)
V_m	Molar volume	m^3mol^{-1}
V_p	Volume of liquid adsorbate per gram	cm^3g^{-1}
$W(T)$	Energy of solidification of water as a function of temperature	Jg^{-1}
x	Pore size	m
x_i	Number of filled pixels in square i (Chapter 4)	
$\bar{x}$	Sample mean	
Y	Heat recorded in a DSC experiment	Js^{-1}

Chapter 1

Introduction

1.1 Characterising heterogeneous catalysts

Heterogeneous catalysis is an exciting and potentially lucrative technology. More than 90 % of the chemical manufacturing processes involve catalysts at one stage or another (Lu and Zhao 2004); oil, chemical, food and pharmaceutical industries all utilise catalysis to make their processes more cost efficient and environmentally friendly. There are, however, many challenges in catalysis, with the industries necessitating stringent performance criteria, such as high catalyst activity and selectivity, to maximise their revenue; if met, these can give a catalyst a higher sale price.

Heterogeneous catalysts are typically supported on microporous or mesoporous solids, such as alumina or silica. A reason for this is because these materials have a high surface area making them ideal for catalyst supports. For a chemical reaction to occur, the reactants and products must be transported between the outer surface of the porous solid and the catalytic surfaces inside. It is this diffusion process that can affect both the apparent activity of the catalyst and its deactivation behaviour. If intra-particle diffusion of the reactants is slow and the chemical reaction is relatively fast, it may lead to incomplete utilisation of the catalyst as the reactants do not reach the interior of the support material. Therefore, the pore structure of the catalyst is characterised to understand its performance in a chemical reaction(s). Hence, characterisation is a major step that aids the development of new-advanced-efficient catalysts. In particular, an accurate knowledge of the pore size distribution is essential as this aids the understanding of different reaction rates. This can be found by standard characterisation techniques such as gas sorption and mercury porosimetry (Gregg and Sing 1982; Rouquerol *et al.* 1999; Lowell *et al.* 2004).

Existing characterisation techniques, however, are yet to be fully understood and fail, perhaps, to account the system accurately. For example, despite many years of work, the debate concerning whether to use the adsorption or desorption branch of a gas isotherm hysteresis loop, for calculating pore size distributions, and which theory, or model, to use to analyse the isotherm data is still not settled. Current recommendations, of the International Union of Pure and Applied Chemistry (IUPAC) (Rouquerol *et al.* 1994), suggest the use of the adsorption branch. A further addition to the argument, however, is

the theory, known as the advanced adsorption effect. The theory suggests adsorption pore size distributions overestimate smaller pores, and derived pore sizes can have a potential error of 100 %. It is, therefore, vital to determine whether the effect occurs as the interpretation of the adsorption data will be influenced and, consequently, final conclusions about pore size cannot be drawn without prior knowledge of the effect.

The complexity that can arise from gas sorption work, such as the advanced adsorption effect, has led, in recent years, to the study of other characterisation methods, such as NMR (Nuclear magnetic resonance) and/or DSC (Differential scanning calorimetry) cryoporometry. The current state of development of the cryoporometry characterisation method is substantially less than that of gas sorption and mercury porosimetry. It is presently unclear what set of pore space descriptors can be obtained from the method. However, cryoporometry offers a range of advantages over gas sorption and mercury porosimetry that are currently not being exploited. It requires little time for sample preparation, compared to porosimetry or gas sorption, and this could potentially facilitate high-throughput pore characterisation. The method also uses relatively innocuous chemicals, such as water or cyclohexane, compared with mercury, which is used in porosimetry.

The lack of understanding of the gas sorption technique and the newer cryoporometry technique to describe pore structures has encouraged the majority of work carried out in this research. The study will examine a range of catalyst supports and it will focus on improving the fundamental understanding of the underlying physics of the gas sorption and cryoporometry characterisation techniques.

1.2 The thesis structure

This thesis is divided into 12 Chapters, which will focus on the issues raised above. The thesis will be divided into approximately two halves. The start of the thesis will focus on the gas sorption characterisation technique and the second half will investigate new characterisation techniques. A summary of each Chapter is now given.

Chapter 1: Introduction

Chapter 2: Chapter 2 introduces the reader to the gas sorption experiment and it explains the range of void space descriptors that can be obtained from the technique. Attention is given to isotherms for mesoporous materials and it demonstrates how a pore

size distribution is calculated. A review of the literature shows that there is current uncertainty over how a pore size distribution should be calculated using gas sorption isotherm data. A reason for this uncertainty is because of a theory, mentioned above, known as advanced adsorption. Advanced adsorption is explained in detail in Chapter 2.

Chapter 3: Chapter 3 provides the reader with some background theory to NMR.

Chapter 4: Chapter 4 uses NMR imaging to assess the validity of the advanced adsorption mechanism. MRI (Magnetic resonance imaging) is used to study the adsorption process in a porous silica pellet. The experiment spatially resolves a gas adsorption isotherm and directly shows that advanced adsorption occurs.

Chapter 5: Chapter 5 develops a test, using an integrated gas-mercury-gas experiment, to determine the gas adsorption mechanism in pores which entrap mercury. The sizes of the pores which entrap mercury are determined by analysing the gas adsorption and mercury porosimetry data. The calculated pore sizes from the two techniques are compared and a discussion is made about the adsorption mechanism.

Chapter 6: Chapter 6 uses the integrated gas-mercury-gas experiment to study the adsorption and desorption processes in pores which entrap mercury. The experimental data is compared to adsorption and desorption models that were introduced in Chapter 2.

Chapter 7: Chapter 7 introduces 'gas sorption scanning curve and loop experiments'. These experiments are used in the literature to further understand the theories of gas sorption hysteresis. Chapter 7 studies these experiments before and after a mercury porosimetry experiment (the integrated gas-mercury-gas experiment) to determine the scanning curves for the pores which entrap mercury.

Chapters 8-10: Chapters 8-10 present the cryoporometry work studied in this thesis. Chapter 8 introduces the cryoporometry technique and provides the reader with background theory of the technique.

Chapter 9: Chapter 9 directly compares the NMR and DSC cryoporometry techniques.

Chapter 10: Chapter 10 uses freezing and melting scanning curve and loop experiments alongside PFG (Pulsed Field Gradient) NMR to investigate the freezing and melting

mechanisms in cryoporometry. The Chapter demonstrates that there is an analogous mechanism to advanced adsorption, which is termed advanced melting.

Chapter 11: Chapter 11 develops an experiment to determine the location of platinum in two Pt-ZSM-5 zeolite catalysts. The platinum can either be located in the micropores or the mesopores and its location determines the activity/selectivity of the catalyst. The experiment which is developed combines a carbon monoxide chemisorption experiment with a nonane pre-adsorption experiment. After locating the platinum in the two catalysts, the Chapter compares the results to catalyst performance data from a previous study.

Chapter 12: Chapter 12 will conclude the experimental work and will propose future work.

Chapter 2

Gas sorption and the impact hysteresis has on pore size distributions

2.1 Introduction

Gas sorption, a non-spatially resolved characterisation technique, is a widely used method to investigate porous materials. It can give a composite average pore size, pore size distribution, surface area and porosity measurement. In addition, gas sorption theory is continually being developed, to improve the accuracy of these measurements. The introduction of MCM-41, for example, that has a structure which exhibits a hexagonal arrangement of purportedly uniform cylindrical pores, has aided the development of the gas sorption theory. This is because it can act as a model adsorbent and this is discussed in detail below and throughout this thesis. Chapter 2 aims to initially give some background theory of the gas sorption process and will move onto how it has developed. It will include the different pore models that have been used to explain the origin of hysteresis and it will assess the validity of the Kelvin Equation when it is used to calculate a pore size.

Prior to further discussions in this Chapter, some of the main terms associated with porous solids have been defined by the International Union of Pure and Applied Chemistry (IUPAC) and are presented in Table 2.1. These terms will be referred to in this Chapter and also following Chapters.

Term	Definition
Porous Solid	Solid with cavities or channels which are deeper than wide
Open Pore	Cavity of channel with access to the surface
Interconnected Pore	Pore which communicates with other pores
Closed Pore	Cavity not connected to the surface
Void	Space between particles
Micropore	Pore of internal width less than 2 nm
Mesopore	Pore of internal width between 2-50 nm
Macropore	Pore of internal width greater than 50 nm
Pore Size	Pore width - minimum dimension
Pore Volume	Volume of pores determined by stated method
Porosity	Ratio of pore volume to the apparent volume of the material
Surface Area	Extent of total surface area as determined by given method under stated conditions
Specific Surface Area	Surface area per unit mass of powder, area determined under stated conditions
External Surface Area	Area of surface outside pores
Internal Surface Area	Area of pore wall
Tortuosity	The path available for diffusion through a porous bed in relation to the shortest distance across the bed

Table 2.1: Terms and definitions of porous materials by the IUPAC (Sing *et al.* 1985). The table has been adapted from Rouquerol *et al.* (1999)

2.2 The different types of adsorption: chemical or physical

When a solid is exposed to a gas at a given pressure, the gas is adsorbed onto the surface until equilibrium is reached. The gas is typically referred to as the adsorbate, and the solid the adsorbent. The adsorption process may be split into two categories, chemical, or physical adsorption, depending on the strength of the interaction between the adsorbent and the adsorbate. Chemical adsorption (chemisorption) (Gregg and Sing 1967) is an irreversible process which is characterised by heats of adsorption that are similar to chemical bond energies. For the purposes of the current work further details of chemical adsorption are omitted until Chapter 11.

Physical adsorption (physisorption) is the attractive interaction between a solid surface and a gas that arises from van der Waal's forces (Rouquerol *et al.* 1999). Unlike chemisorption the process is accompanied only by low heats of adsorption, where no formal chemical bonds are made. Typical heats of adsorption values for physisorption are between ~5-50 KJ mol^{-1} (Rouquerol *et al.* 1999).

2.3 The process of physical adsorption

When a gas is physisorbed to a solid surface it becomes more ordered and loses a state of translational freedom (Gregg and Sing 1982). This means the entropy change for the process is negative. The adsorbents change in entropy is strictly positive, but a reasonable assumption is that it remains unchanged (Rouquerol *et al.* 1999). The overall entropy change for the system is, therefore, negative. For the adsorption process to take place the change in Gibb's free energy must be negative, and from Equation 2.1 the process of adsorption has to be exothermic.

$$\Delta H = \Delta G + T\Delta S \qquad 2.1$$

where ΔH is the change in heats of adsorption, ΔG the change in Gibbs free energy, T the temperature and ΔS the change in the entropy.

As stated above, physisorption is because of van der Waal's forces. These forces occur when there is a rapid fluctuation in the electron density of an atom which gives rise to an instantaneous dipole, which then induces an electrical moment in a neighbouring atom. The total potential energy between two interacting atoms, $\varepsilon(r_{ij})$, can be represented by:

$$\varepsilon\left(r_{ij}\right) = \frac{B}{r_{ij}^{12}} - \frac{C}{r_{ij}^{6}} \qquad 2.2$$

where B and C are arbitrary constants that are related to the polarisability of the isolated atoms and r_{ij} the distance between atoms i and j. Equation 2.2 is commonly referred to as the Lennard-Jones potential (Atkins and de Paula 2002). If atoms are a large distance apart, the interaction between the two atoms is very small. As the atoms approach one another they can induce their electrical moments (discussed above) and they attract one another. At very short distances the electron clouds of each atom interact and the two atoms then repel one another.

A similar approach can be used to describe the adsorption of a gas on a solid (Gregg and Sing 1982). The potential energy of a single atom (or molecule), i, as a function of its distance from a solid surface, z, can be expressed as:

$$\varphi_i(z) = B_{ij}\sum_j\left(r_{ij}^{-12}\right) - C_{ij}\sum_j\left(r_{ij}^{-6}\right) \qquad 2.3$$

where r_{ij} is the distance between an atom (or molecule), *i*, in the gas phase with an atom *j* in the solid.

2.4 The adsorption isotherms

The quantity of gas adsorbed, n^a, by the mass of a solid, *m*, is a function of the equilibrium pressure, *P*, the temperature, *T*, and the nature of the gas-solid interaction, which can be expressed as (Rouquerol *et al.* 1999):

$$\frac{n^a}{m} = f(P, T, system) \qquad 2.4$$

If the temperature and gas-solid system is kept constant this may be simplified to:

$$\frac{n^a}{m} = f(P)_{T,system} \qquad 2.5$$

For a system which is below the critical temperature of the adsorbate it can be written:

$$\frac{n^a}{m} = f(P/P_0)_{T,system} \qquad 2.6$$

where P_0 is the saturation pressure of the adsorbate. Both Equations 2.5 and 2.6 represent the amount of gas adsorbed on a solid as a function of pressure or relative pressure respectively.

As the molecules are adsorbed onto the solid surface they begin to interact with neighbouring molecules. This effect is enhanced as the fractional coverage of the solid surface increases. On the surface becoming more densely populated, a monolayer of adsorbed gas will form on the surface. The monolayer acts as an extension to the solid surface and will attract additional gas molecules, again by van der Waal's interactions. This process of the gas molecules continually adsorbing is known as multilayer adsorption.

2.4.1 The formal classification of isotherms

The International Union of Pure and Applied Chemistry (IUPAC) have defined a set of six standard isotherms (Sing *et al.* 1985). Figure 2.1 illustrates the six isotherm categories.

Type I isotherms are characteristic of microporous materials. At low relative pressures the amount adsorbed increases rapidly, and this corresponds to the micropores filling with adsorbed gas. At relative pressure 1 the isotherm has plateaued, which means all the pores are filled with adsorbed gas.

Type II isotherms are typical of non-porous or macroporous materials. Initially the adsorbate forms a monolayer of adsorbed gas on the adsorbent. As the pressure is increased it leads to multilayer build up of the adsorbate.

Type III isotherms represent the situation where the interaction between the adsorbent and adsorbate is weak. As more gas adsorbs on the surface the interaction strength to additional gas molecules is enhanced.

Type IV isotherms are typical for porous materials with pore diameters in the range of ~2-50 nm. Initially, it follows the type II isotherm corresponding to a monolayer forming and further multilayer build up of the adsorbate molecules. At increased relative pressures, a sharp increase in amount of gas uptake is seen. This corresponds to the filling of the mesopores by the process of capillary condensation, which is discussed in detail below. The top of the isotherm forms a plateau that represents complete pore filling. In addition, when the pressure is lowered there is hysteresis between the adsorption and desorption process. An explanation of the hysteresis region is also discussed below.

Type V isotherms are similar to type III isotherms in that weak interactions exist between the adsorbent and the adsorbate. Materials exhibiting type V isotherms also have pore diameters in the range ~2-50 nm. Therefore the characteristic sharp gas uptake with increasing P/P_0 is observed. As with type IV isotherms, a part of the type V isotherm is not reversible.

Type VI isotherms, commonly referred to as stepped isotherms, are associated with layer by layer adsorption on highly uniform surfaces. Krypton on pure graphite at 77 K has shown this shape isotherm (Thomy *et al.* 1972).

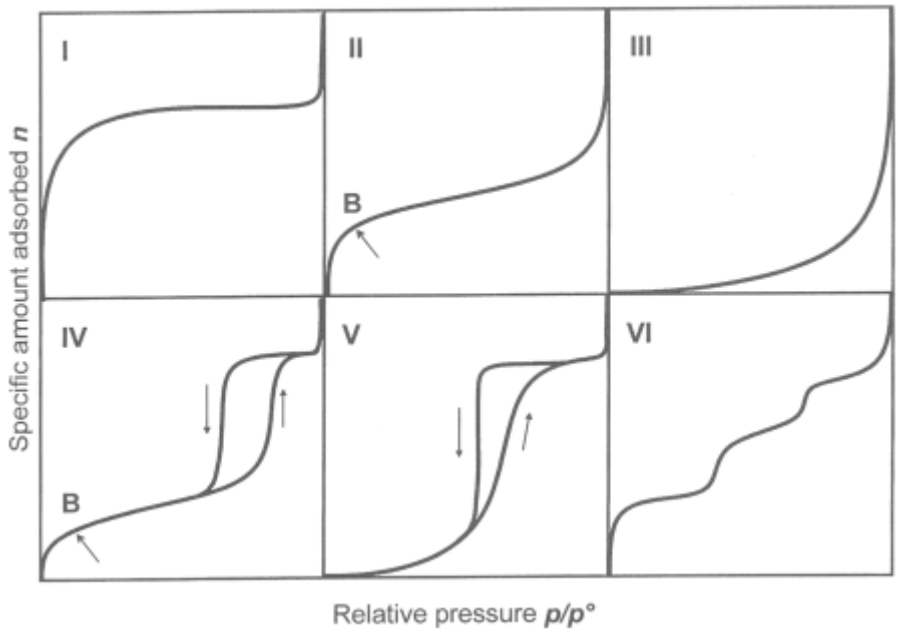

Figure 2.1: The IUPAC classification of isotherms (Sing *et al.* 1985)

2.5 Surface area measurements

A surface area measurement is commonly quoted for heterogeneous catalysts, and is used as an indirect measurement to gauge likely catalyst activity. The work of this thesis will not study surface areas in depth, but for completeness surface area measurements will be quoted for all samples detailed.

A method to characterise the surface area of a material has been described by Brunauer, Emmett and Teller (1938) and is commonly termed the BET method. The BET equation (equation 2.7), in its most general form, is given by:

$$\frac{P/P_0}{n(1-P/P_0)} = \frac{1}{n_m C} + \frac{C-1}{n_m C}\frac{P}{P_0} \qquad 2.7$$

where n is the amount adsorbed, n_m is the monolayer capacity and C is an empirical constant related to the heat of adsorption of the gas onto the solid by the expression:

$$C \approx \exp\left[\frac{\left(\Delta H_{desorption} - \Delta H_{vaporisation}\right)}{RT}\right] \qquad 2.8$$

where R is the ideal gas constant, $\Delta H_{\text{desorption}}$ is the enthalpy of desorption of the adsorbate from the adsorbent and $\Delta H_{\text{vaporisation}}$ is the enthalpy of vaporisation of the adsorbate. The

BET surface area can be calculated in the following way. A plot of $(P/P_0)/[n(1-P/P_0)]$ against P/P_0 , which is referred to as a BET plot, allows the monolayer capacity, n_m, and the empirical constant C to be determined. From the monolayer capacity the BET surface area, S, can then be calculated from the following expression:

$$S = n_m N_A \sigma \qquad 2.9$$

where N_A is the Avogadro constant and σ is the average area occupied by each adsorbed molecule in the completed monolayer. The BET equation may be applied to non-porous and mesoporous materials with pore diameters typically greater than 4 nm. For pore sizes smaller, which include microporous materials, the BET equation becomes inaccurate. This is because the potential well of these pores causes pore filling at low relative pressures and the surface area is greatly overestimated.

2.6 Type IV isotherms and capillary condensation

The materials studied in this thesis are mainly mesoporous and have Type IV isotherms. For this thesis, the region of the isotherms of most interest is the capillary condensation and evaporation region. Therefore, a detailed discussion of this region will be given so the reader has some background knowledge before the experimental Chapters.

The capillary condensation and evaporation regions are associated with gas condensing in the pores to become a liquid like state or the liquid in the pores evaporating respectively. The pressure at which these processes happen can be related to a pore size by the Kelvin equation, which is given by:

$$\ln\left(\frac{P}{P_0}\right) = -\frac{2\gamma V_m \cos\theta}{RT(r_p)} \qquad 2.10$$

where P is the equilibrium vapour pressure, P_0 is the saturation vapour pressure, r_p the pore radius, T the temperature, γ the surface tension of the liquid, V_m the molar volume of the adsorbate and θ the contact angle with which the adsorbate meets the adsorbent. The Kelvin equation predicts that for increasing pore sizes, the pressure necessary for condensation increases.

To give the reader a visual picture of the pore condensation process a schematic representation is shown in Figure 2.2. Figure 2.2 (a) shows a cylindrical pore closed at one end. At the closed end of the pore the adsorbate (shading) adsorbs and forms a hemispherical meniscus. When the pressure is increased the pore will fill suddenly as the adsorbate condenses in the pore (see Figure 2.2 (b)). The pore radius can then be calculated, using the Kelvin equation (equation 2.10), from the pressure at which capillary condensation occurs.

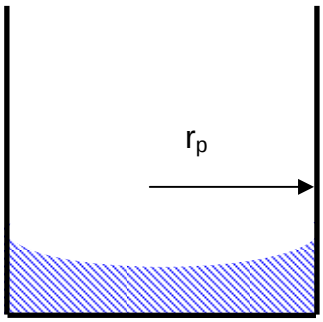

Figure 2.2 (a): Schematic of the pore filling process. The shading shows the adsorbed phase

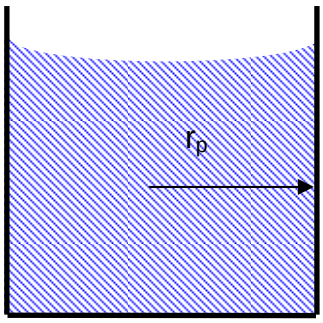

Figure 2.2 (b): Schematic of the pore filling process where the gas has condensed in the pore

However, this schematic is too simplified as initially there is a multilayer build up of gas before capillary condensation. A more accurate schematic is presented in Figure 2.3 and the pressure at which capillary condensation occurs is related not to the pore radius, r_p, but to radius, r_k, instead.

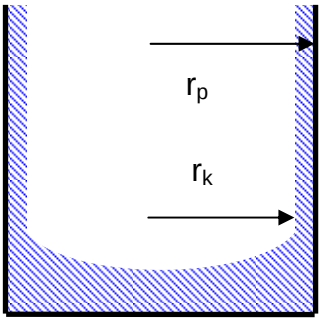

Figure 2.3: Schematic of the pore filling process following an adsorbed layer of gas. The shading shows the adsorbed phase

To account for the multilayer adsorption thickness, t_c,a modification to the Kelvin equation can be made and is given by:

$$\ln(\frac{P}{P_0}) = -\frac{2\gamma V_m \cos\theta}{RT(r_p - t_c)} \qquad 2.11$$

The contact angle in equations 2.10 and 2.11 depends on the adsorbate-adsorbent interaction and can vary between 0 and 180°. If the adsorbate fully wets the surface the contact angle is assumed to be 0°, which means the cosθ term becomes 1. In the experimental Chapters it will be assumed that the adsorbate completely wets the adsorbents surface and so the contact angle used will be 0°.

2.7 The multilayer thickness

The contribution from the multilayer thickness is important when calculating pore sizes and must be accounted for correctly. For example, Rouquerol *et al.* (1999) report that the multilayer thickness would contribute 18 % of the pore diameter for a cylindrical pore that fills at relative pressure 0.8. This indicates the importance of being able to calculate the multilayer thickness accurately before calculating a pore size using the Kelvin equation, for example.

The method employed to estimate the thickness of the adsorbed layer, *t*, is to measure the adsorption isotherm on a non-porous reference material that is comparable to the porous solid being studied. The thickness layer can be found from the expression (Rouquerol *et al.* 1999):

$$t = \sigma_m \frac{n}{n_m} \qquad 2.13$$

where n is the amount adsorbed, n_m the amount adsorbed for a monolayer and σ_m the thickness of a monolayer. In Chapter 5, pore sizes will be calculated using nitrogen as the adsorbate. The thickness of a monolayer of adsorbed nitrogen at 77 K will be assumed to be 3.54 Å (Lippens *et al.* 1964).

Nitrogen at 77 K is a commonly used adsorbate to characterise porous materials. Due to this universal thickness layer equations have been found by Halsey (equation 2.14), Harkins-Jura (equation 2.15) and de Boer (equation 2.16), which describe the adsorption of nitrogen on a non-porous adsorbent at 77 K. The latter two equations (equations 2.15 and 2.16) are for when the adsorbent contains oxygen within its structure such as silica and alumina.

$$t = 3.54\left[\frac{5}{\ln(\frac{P_0}{P})}\right]^{\frac{1}{3}} \qquad 2.14$$

$$t = \left[\frac{13.99}{\log_{10}(\frac{P_0}{P}) + 0.034}\right]^{\frac{1}{2}} \qquad 2.15$$

$$t = \left[\frac{13.99}{0.034 - \log_{10}(\frac{P}{P_0})}\right]^{\frac{1}{2}} \qquad 2.16$$

The validity of all the thickness equations is however questionable. The thickness layer equations, as stated above, are based on adsorption on non-porous materials. The thickness layer will not be the same in a porous material with narrow pores (e.g. mesopores). This is because the potential well of the pore is a parameter that governs the multilayer thickness (Rouquerol *et al.* 1999). Evans and Marconi 1985 have suggested, by a theoretical approach, that the multilayer thickness for curved pores is greater than for the

corresponding non-porous flat surface. Moreover, all three equations assume that the surface of the adsorbent is homogeneous and the adsorbate is distributed evenly across the surface, which is unlikely for a real catalyst system. Many catalysts are based on silica or alumina supports with an active metal deposited on the surface and, therefore, their surfaces cannot be described as homogenous.

A refinement of the multilayer thickness equations was developed by Broeckhoff and de Boer (1968), which related the thickness of the adsorbed layer to the pore curvature, as well as the relative pressure. Despite perhaps a more sophisticated approach to multilayer adsorption the Broeckhoff and de Boer approach has not received widespread acceptance.

2.8 Calculating a pore size distribution

The Kelvin equation is regularly used in industry to calculate a pore size distribution. A pore size distribution is defined as the change in volume, V, with respect to the pore size, x, as a function of pore size ($\frac{dV}{dx}$ as a function of x). The common algorithm applied to calculate a pore size distribution is the Barret, Joyner and Helenda (1951) method. The algorithm assumes that the adsorption experiment can be represented as a set of thermodynamically independent pores of simple cylindrical shape. The term thermodynamically independent pores means that each pore does not interact with a neighbouring pore. The assumption that the pores are cylindrical and thermodynamically independent is discussed below and in later Chapters.

2.9 Hysteresis

The capillary condensation and evaporation region of Type IV isotherms is associated with hysteresis, which is from the Greek language meaning 'coming later'. Hysteresis is defined formally as "the lag in a variable property of a system with respect to the effect producing it as this effect varies" (Merriam-Webster dictionary). A formal classification of hysteresis loops found for Type IV isotherms has been presented by the IUPAC (Sing *et al.* 1985) and is shown in Figure 2.4. H1 loops are associated with materials that have a narrow distribution of well defined cylindrical pores. Materials such as MCM-41 and SBA-15 give such loops. H2 hysteresis is common for disordered materials, such as silica gels, that are believed to have a broad distribution of both pore size and shape. H3 and H4 hysteresis loops will not be looked at in this thesis, but for completeness have been included. Both

are typical of materials that have slit shape pores, and H4 loops have a larger amount of micropores.

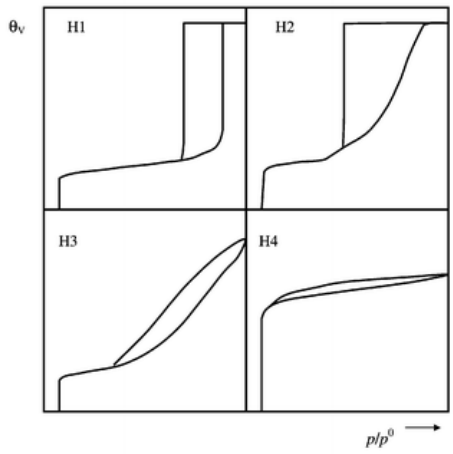

Figure 2.4: The IUPAC formal classifications of hysteresis loops (Sing *et al.* 1985)

2.9.1 The adsorption or desorption isotherms

The sections above have discussed that the pressure at which capillary condensation and evaporation occur can be related to a pore size, but also that capillary condensation and evaporation happen at different pressures. Therefore, both branches would give a different pore size measurement.

When deriving a pore size from, for example the Kelvin equation, it is assumed that the system is at equilibrium. So an understanding of which branch of the hysteresis loop is at equilibrium is necessary. Discussions to explain the origins of hysteresis have been made over the past ~100 years to understand whether it is the capillary condensation or evaporation processes that are at equilibrium and, thus, allowing a true pore size to be found. The following section will discuss the origins of hysteresis from works in the literature dating back to the start of the last century.

An explanation of gas sorption hysteresis was first proposed by Zsigmondy (1911, cited by Rouquerol *et al.* 1999) who suggested that it arose due to the different contact angles for the condensation and evaporation processes. Zsigmondy believed that for desorption, the adsorbate completely wetted the surface so the contact angle was assumed to be zero. For adsorption, however, because of surface impurities he claimed the adsorbate could not initially wet the surface and so the contact angle was non-zero. As the pressure of the gas was increased the adsorbed gas would progressively displace the impurities meaning the adsorbate wetted the surface and condensation would occur once the impurities had been

displaced. The explanation is very similar to the delayed adsorption theory (Foster 1932), which is discussed in detail below. The theory proposed by Zsigmondy suggested that hysteresis was not a result of either the adsorbate or the adsorbent, but an external factor. He concluded that the desorption process would be at equilibrium as it was this process that represented complete wetting of the surface. The explanation, however, was found to be unlikely as once the impurities had been removed hysteresis should then become absent. This is never the case for real systems.

A later theory discussed by McBain (1935) is the concept of pore blocking, which is explained as follows. McBain used an idea of a bell jar shaped pore model (Figure 2.5), which is now commonly termed an ink bottle pore model, to explain his theory. It was suggested that the gas would initially condense at the closed end of the large pore (a dead end pore), at pressure P1 via a hemispherical meniscus. The narrow neck would fill automatically as the pressure to fill the neck would have been exceeded. On lowering the pressure the large pore body cannot empty as it is blocked by the narrower outer neck. Therefore, the condensate becomes metastable until the pressure P2 is reached. At pressure P2 the outer neck empties, which allows the pore body to empty too. Therefore, hysteresis would be the result of structural effects. Brunauer (1945) concluded that if pore blocking exists during desorption then some filled pores cannot be in equilibrium with their vapour phase and the equilibrium process must be the adsorption process.

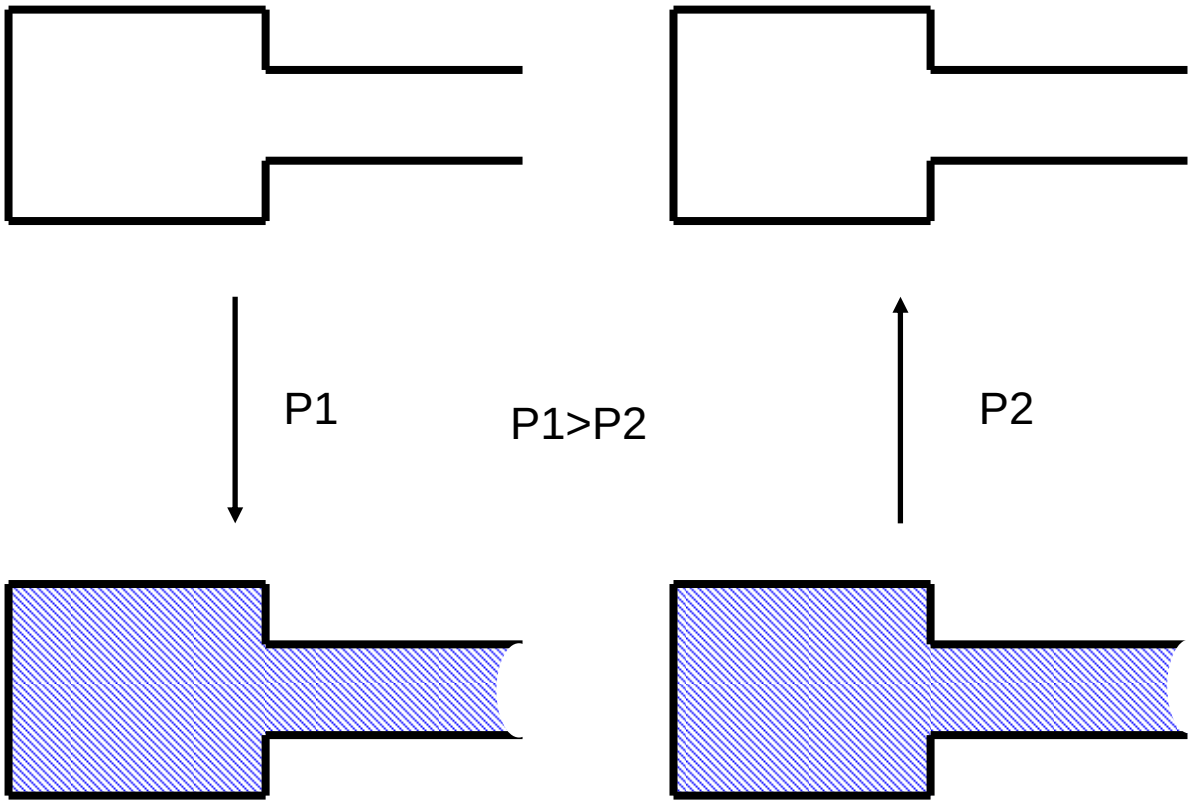

Figure 2.5: McBain's bell jar pore model. The condensed gas is shown as shading. The text explains the schematic

More general descriptions of hysteresis have been explained through the mechanism of meniscus formation for both the adsorption and desorption processes (Foster 1932; Cohan 1938; de Boer 1958; Everett 1979 and Findenegg *et al.* 1994). Foster suggested that pores do not necessarily have dead ends where condensation can initiate from, such as the bell jar pore McBain discussed. The pores instead could be through pores where the pore is open at both ends. For such a pore, the condensation process is 'delayed' as there is no flat surface for a hemispherical meniscus to form. Instead, the adsorbate forms a multilayer on the pore wall, which becomes thicker and thicker as the pressure is increased. There becomes a point where the multilayer, at a position in the pore, bridges the pore gap. At this point a hemispherical shape meniscus forms and it can propagate through the pore. This process continues for pores of increasing size as the pressure is raised. Desorption, however, is not delayed as there is a hemispherical meniscus already formed at the end of the pore. Due to this, Foster (1932) concluded that the desorption process was at equilibrium. This mechanism was furthered by Cohan (1938) who quantified it and predicted the pressure at which adsorption would occur in an open-end cylindrical pore by equation 2.17. Cohan, however, described the adsorption meniscus as cylindrical in shape, and here on in it will be termed a cylindrical meniscus. A cylindrical meniscus is when the gas adsorbs on the surface of an open cylindrical pore. At the point of capillary

condensation, the gas propagates from the surface of the pore to the pore centre. Although the geometry of the meniscus is perhaps better described as a 'sleeve', within the gas sorption community the term cylindrical meniscus is commonly used.

$$\ln(\frac{P}{P_0}) = -\frac{\gamma V_m \cos\theta}{RT(r_p - t_c)} \qquad 2.17$$

Cohan (1938) also explained that the desorption process would occur by a hemispherical type meniscus, as predicted by the Kelvin equation. Due to the different meniscus geometries, the adsorption and desorption processes occur at different relative pressures, which causes hysteresis. This explanation of hysteresis, where the adsorption and desorption processes have a different meniscus geometry, is referred to as single pore hysteresis. If this mechanism is real, the Kelvin (equation 2.11) and Cohan (equation 2.17) equations can calculate a pore size from either the adsorption or desorption branch of the hysteresis loop. From the Kelvin-Cohan equations it can be predicted that the relative pressure of desorption, in an open cylindrical pore, is equal to the relative pressure of adsorption squared. This can be expressed by:

$$\left(\frac{P_{Desorption}}{P_0}\right) = \left(\frac{P_{Adsorption}}{P_0}\right)^2 \qquad 2.18$$

In equation 2.18 it is assumed that the thickness of the adsorbed layer is small compared to the pore size. This test can be used to determine whether pores are independent and will be used in Chapter 6.

Later work, by Saam and Cole (1975), has explained hysteresis in terms of the metastability of the multilayer thickness. As previously stated, before capillary condensation occurs the surface is initially wetted by the adsorbate and a multilayer of adsorbate builds up. The adsorbed multilayer is stabilised by the interactions with the pore wall as well as liquid-liquid interactions. The multilayer build up continues providing that these interactions are sufficient to stabilise it. At the point where the interactions from the solid surface become weak the stability is governed then by the liquid-vapour curvature. At this critical thickness of the multilayer, pore condensation then occurs. For pore evaporation the pressure needs to be lowered further than that for capillary condensation. This means the multilayer thickness is now less and the difference between the multilayer thicknesses, at the points of condensation and evaporation, was deemed the metastability thickness

range. Findenegg *et al.* (1993) gave experimental support to the Saam-Cole theory by studying the adsorption of isopentane in Controlled Pore Glasses (CPGs). The point where condensation started experimentally was the point where Saam and Cole predicted the multilayer to become unstable.

2.9.2 Computational simulations of Type IV isotherms and hysteresis

The thermodynamic concepts discussed so far to explain hysteresis are termed the 'classical approach' to hysteresis. These concepts are based on macroscopic theories, which are being applied to the microscopic (pore) level. For example it is assumed in the Kelvin equation that pore condensation (or evaporation) is a gas to liquid (or liquid to gas) phase transition between a homogeneous bulk liquid and a homogeneous bulk gas. This assumption may not be correct on the pore level. In addition, bulk surface tension and bulk molar volume values are also used in the Kelvin equation to calculate a pore size. Despite these assumptions, the Kelvin equation is commonly used for relating relative pressures to a pore size in industry. For this to be done correctly a *priori* knowledge of the equilibrium transition must be known, and the above discussions have shown already that there is uncertainty over whether it is the adsorption or desorption branch. Further discussion below will show that this argument is still ongoing (Neimark and Ravikovitch 2001; Esparza *et al.* 2004; Grosman and Ortega 2008) and without knowing the equilibrium transition, the Kelvin equation should not be applied. Furthermore, many authors have drawn attention to the validity of the Kelvin equation for determining a pore size. In small pores where surface forces become important Neimark and Ravikovitch (2001) have shown an appreciable error from the Kelvin equation, with deviations in pore sizes as large as 20 nm. Coasne *et al.* (2001) have supported this experimentally by studying gas sorption on a porous silicon layer and comparing the pore size distribution measurement with a transmission electron micrograph (TEM) of the silicon layer. They found that the Kelvin equation could misquote the pore size between a factor of 2-3.

An alternate method to the macroscopic approach was therefore sought (Evans and Marconi 1986), with the gap bridged by Density Functional Theory (DFT). DFT has been used as it provides a microscopic model of the gas sorption process taking into account gas-gas, gas-liquid, gas-solid and liquid-solid interactions as well as the pore geometry. The sum of the named interactions is known as the grand free energy potential. The DFT method can be used to minimise these interactions in a pore system with the bulk phase, which can simulate a gas sorption experiment. The DFT method leads to a more realistic

density profile of the adsorbed gas as a function of pressure and temperature when compared to the macroscopic methods.

Evans and Marconi (1986) used DFT and found the sorption process to mimic the simple models that have been discussed above. There was an initial adsorption on the pore wall, and for pores large enough, capillary condensation occurred. In contrast to the macroscopic approach of the Kelvin equation, the DFT method suggested the fluid confined in a pore could be both an inhomogeneous adsorbed gas phase and an adsorbed liquid phase. Additionally, the capillary condensation process was found to be the transition from the inhomogeneous gas phase to the liquid (Evans 1990). Using DFT, Ball and Evans (1989) have theoretically calculated sorption isotherms for a set of independent cylindrical pores and an interconnected network of pores. They found that the interconnected network model reproduced previous experimental findings (Nutall 1974, cited by Ball and Evans 1989) where sorption of xenon on Vycor had been studied. The similarity between the experimental and simulated work suggested that it was unrealistic to interpret gas sorption isotherms for Vycor as a set of thermodynamically independent cylindrical pores.

With the development of highly regular templated mesoporous silicas such as MCM-41 (Beck *et al.* 1992) and SBA-15 (Zhao *et al.* 1998) a direct test of DFT has been allowed. Neimark and Ravikovitch (2001) have compared DFT calculations, assuming cylindrical shaped pores, to experimental gas sorption isotherms of MCM-41. They found that DFT can correctly predict pore sizes from 4.8 nm diameters upwards. They also compared the macroscopic methods for determining pore sizes and found the Broeckhoff and de Boer method correctly predicts pores sizes that are above ~ 7 nm. It was suggested that the Kelvin equation, however, can only correctly predict pores that are greater than 20 nm in diameter. For both MCM-41 (Ravikovitch *et al.* 1995) and SBA-15 (Ravikovitch and Neimark 2001) it was also discussed that the point where the grand free energy potential of the liquid phase and gas phase are equal corresponds to the experimental desorption branch. The authors therefore concluded that the desorption branch for a thermodynamically independent cylindrical pore is at equilibrium, which is what Foster (1932) suggested.

The more recent computational methods have also questioned the classical idea of pore blocking (McBain 1935). As discussed above, this occurs when outer necks control desorption by preventing larger pore bodies emptying. Sarkisov and Monson (2001) have

shown that desorption in an ink bottle type pore does not have to be controlled by the outer neck. This desorption mechanism is termed cavitation and is when spontaneous nucleation and growth of gas bubbles occurs in a pore, which can then empty by diffusion through a neighbouring pore. Sarkisov and Monson (2001) demonstrated this using an ink bottle type pore model, where the walls were made up of hexagonally packed spheres to replicate a real porous surface. They then simulated a gas sorption experiment using Grand Canonical Monte Carlo (GCMC). They found that the pore system went through a number of different stages, which are detailed as follows. First there was an initial layering of the gas molecules on the surface, corresponding to a multilayer adsorption process, followed by filling of the small outer necks and then the large pore body. When the pressure was lowered, evaporation from the large pore body took place, while the small necks remained filled with condensate. On lowering the pressure further, desorption from the small outer necks then occurred. The reason why desorption from the pore body can happen first is because density fluctuations in the condensate increase as the pressure is lowered so there becomes regions of high and low density. If a region becomes of low enough density, a bubble can nucleate, which causes cavitation of the large pore body. Libby and Monson (2004) furthered this work by varying the pore body to neck ratio. They found that when the ratio was small, desorption was controlled by the outer neck and occurred in one step, which is the pore blocking mechanism. When the ratio was increased, desorption from the pore body by cavitation happened before the outer neck emptied. They therefore concluded that cavitation was a function of the outer neck size. Experimentally cavitation induced desorption is expected to occur when mesopores are blocked by micropores (Vishnyakov and Neimark 2003). More recently, Woo, Porcheron and Monson (Woo *et al.* 2004) have shown that cavitation is also a function of the solid fluid interaction strength. When the interaction strength is increased there is a tendency for desorption to be driven by cavitation.

The cavitation mechanism has also been predicted by other research groups. Vishnyakov and Neimark (2003) used Monte Carlo simulations to study the capillary desorption in an ink bottle pore model. The pore model consisted of a spherical cavity that was connected to the bulk phase by two cylindrical necks of smaller size. They found that when the cylindrical necks were large, desorption from the neck and cavity occurred at the same pressure. The pressure corresponded to the equilibrium vapour pressure for a receding meniscus in the pore neck, which suggested pore blocking was the desorption mechanism. When the neck size was reduced a two staged desorption process then occurred. The first stage involved the adsorbate in the cavity emptying by diffusing through the pore neck

(cavitation). When the pressure was lowered further the adsorbate in the outer narrow necks then emptied.

A need to distinguish experimentally between pore blocking and cavitation is therefore required. Thommes *et al.* (2006) and Thommes (2010) proposed a test where gas sorption isotherms are measured using different adsorbates, at different temperatures. This is then followed by a comparison of the desorption branch pore size distributions. If the desorption mechanism is pore blocking it means the desorption pressure is controlled by the outer necks. Therefore, the pore size distribution determined from the desorption branch should be independent of both the adsorbate and temperature. The opposite would be true if cavitation was the desorption mechanism. It is important to determine the desorption mechanism as information about the neck size can be found only if the mechanism is pore blocking (Thommes 2010). The neck size cannot be characterised by gas sorption experiments if the desorption mechanism is indeed cavitation.

This section has shown that the simulated gas sorption models are useful to test gas sorption theories, but the pore models used are not necessarily appropriate for real catalysts. Catalysts are made up of complex interconnected pore networks and not a series of independent pores with simple ink bottle pore geometries. Attempts, therefore, to replicate amorphous porous materials, such as controlled pore glasses (CPGs), have been made (Gelb and Gubbins 1998; Gelb and Gubbins 1999). The next sub-section will explain to the reader how these materials can be replicated computationally and how they can be useful as model materials to study gas sorption.

2.9.3 Statistically reconstructed pore structures

CPGs are interconnected amorphous mesoporous materials and are synthesized as described by Haller (1965). A molten mixture of Na_2O, B_2O and SiO_2 when cooled will phase separate into silica rich (silica) and silica poor (borosilicate) liquid regions. When the system is cooled further the two regions solidify and the borosilicate region is etched out with an acid. This leaves behind a high porosity silica rich region. Gelb and Gubbins (1998) have used a quench molecular dynamic simulation to reproduce the experimental synthesis of CPGs. A mixture of two sphere molecules, where the attractive interaction between unlike pairs of spheres is weakened relative to the attractive interaction between spheres of the same kind, is relaxed to a local minimum energy (quenched). As the interactions between the spheres are different a phase separation is induced and one of the

phases is then removed, which is analogous to the experimental synthesis. The remaining phase is then equilibrated leaving a system that mimics the structure of a CPG. To tune the surface area, porosity, and pore size of the simulated material the starting mole fraction and the quench period can be varied. The method proposed by Gelb and Gubbins means the simulated structures are precisely characterised at the molecular level, as the pore size and shape will be known, so they can be used as model materials to simulate gas sorption experiments. Gas sorption experiments have thus been simulated using GCMC (Gelb and Gubbins 1998) and a pore size distribution was calculated using the BJH pore size distribution algorithm (Gelb and Gubbins 1999). The authors found that the BJH algorithm underestimated the real pore size. In addition, later work (Figueroa-Gerstenmaier *et al.* 2003) calculated the pore size distribution, but using DFT. It was found that using single-pore geometry, a cylindrical or slit shape pore was not enough to reproduce the adsorption behavior in the complex porous system. The works concluded that analysing the simulated gas sorption data using the concept of thermodynamically independent pores was not appropriate for CPGs. In addition, works by Rosinberg and co-workers (Rosinberg *et al.* 2003; Detcheverrey *et al.* 2003; Detcheverrey *et al.* 2004), have suggested that for disordered porous materials there exists a complex free energy landscape in which the system is trapped and cannot reach equilibrium on the experimental time scale. Therefore, neither the adsorption or desorption branches are at equilibrium and they should not be used for calculating pores sizes.

Another possible method to generate disordered porous network is to construct one from two-dimensional images such as transmission electron micrographs (TEM). To do this it is necessary that the TEM image shows good contrast between the solid material and void volume to distinguish what is pore and what is the solid material. To make an exact reconstruction of a porous material an infinite amount of ultra thin two dimensional images would be required, but this would be time consuming. A more simple approach has been used by Levitz (1999, cited by Van Damme 2000) where a random two dimensional TEM image for Vycor glass was used to reconstruct the three dimensional structure using oxygen and silicon atoms. Once the structure had been generated any silicon atom without a tetrahedral geometry was removed and the oxygen atoms were saturated with hydrogen atoms to charge balance the structure. Later work (Pellenq *et al.* 2001) has carried out the exact procedure but for a CPG instead and a gas sorption isotherm was simulated using GCMC. Pellenq *et al.* (2001) noted that when a gas sorption experiment was simulated using xenon gas it only partially wetted the surface. They found that pockets of xenon condensate occurred at points of high curvature and the remaining pore structure was

either partially wetted with the adsorbed gas or had no adsorbed gas. The authors concluded that monolayer based adsorption methods, such as BET surface area measurements, could not be used. This was because homogeneous adsorption across the surface did not happen.

2.9.4 Summary of computational simulations of Type IV isotherms and hysteresis

The above section has shown that there are two different approaches to simulating gas sorption work in the literature. The works of Neimark and Ravikovitch simulate gas sorption experiments using simple cylindrical pore models, like those used in the classical approach. They have then used experimental gas sorption studies on templated mesoporous silicas to validate their methods. From their work, they have concluded that MCM-41 and SBA-15 can be analysed as a composite of independent cylindrical pores and that the desorption branch is at equilibrium. Their pore models, though, are very simplistic as they are assumed to be perfectly smooth cylinders, while studies have shown that these materials (MCM-41) do not have smooth surfaces (Sonwane *et al.* 1999). In addition, Coasne *et al.* (2006) have incorporated surface roughness into their pore models and simulated gas sorption experiments using GCMC. Two model pore structures were made by carving out cylindrical shape pores in an atomistic silica block. To replicate a more realistic surface they removed silicon atoms that did not have a tetrahedral coordination and protonated lose oxygen atoms. This was the same procedure as Levitz (1999, cited by Van Damme 2000), which was discussed above. One pore model had a smooth surface while the other pore model had a degree of surface roughness introduced at length scales below 10 Å. They then simulated argon sorption isotherms at 87 K, using GCMC, and found different results for each pore model. When the surface was rough the adsorption mechanism was found to be a continuous filling mechanism. First the gas condensed into small pores, which were created by the surface roughness, and the adsorbed gas acted as a nucleation seed for more gas to adsorb onto. When the pore model was smooth the adsorption process was then a discontinuous jump from the gas phase to a liquid phase, which is capillary condensation. This study showed that the surface roughness is an important parameter as it can determine the gas sorption mechanism and should therefore be considered in any pore model. The pore models studied by Ravikovitch, Neimark and co-workers have a smooth homogeneous surface, which means the density of the adsorbed fluid varies only perpendicular to the pore wall. This situation contrasts that of MCM-41, SBA-15 and real catalysts where the surface is rough meaning the adsorbed fluid density would potentially be more complex compared to a smooth cylindrical pore. The solid-fluid

interactions used in the models are also a contentious issue. For example Ravikovitch *et al.* (1995) determine the interaction parameters from non-porous silica and apply them to MCM-41 and SBA-15. They have not accounted for the different surface chemistries between the non-porous silica and MCM-41/SBA-15. As discussed above (Woo *et al.* 2004), the surface chemistry can have an affect on the gas sorption mechanism. Moreover, to verify their theoretical models experimental studies on MCM-41 and SBA-15 were used. This is because it is thought they consist of a two-dimensional array of cylindrical shaped non interacting pores. Esparza *et al.* (2004) and Grosman and Ortega (2008) have shown that this is not necessarily the case for these materials, which is discussed in more detail in Chapter 7. Further, real catalysts are not made up of independent cylindrical type pores, and therefore these (MCM-41 and SBA-15) may not be ideal model materials to study.

Despite the work on simple pore models, doubt has been cast over whether the concept of thermodynamically independent pores is even valid for irregular solids with interconnected pores (Gelb and Gubbins 1999; Pellenq *et al.* 2001). However, the model pore structures used in these studies were very simplified. For example the reconstruction procedure used by Levitz (1999) required the assumption that the two dimensional image used statistically represents the entire pore structure. This method may be appropriate for controlled pore glasses, or Vycor glass, but for real industrial catalyst supports, that have non-uniform structures, the assumption is incorrect. This has been demonstrated by Rigby *et al.* (2006) who studied a sol gel silica material following mercury porosimetry by X-ray tomography. They found that the entrapped mercury was not uniformly located across the material suggesting the material was not isotropic. Moreover, catalyst supports are often either silica or alumina materials, which cannot be modeled as a series of spheres such as the method used by Levitz (1999, cited by Van Damme 2000). Silica and alumina supports are often calcined at a high temperature that sinters the particles. They are therefore better described as an assembly of sintered spheres that have a broad distribution of convex and concave local curvatures (Van Damme 2000). In addition, these reconstructed porous materials have very simplified surface chemistries where the surface is made up only of evenly distributed hydroxyl groups. Haukka *et al.* (1993) has discussed that silica is made up of isolated hydroxyl groups (single and geminal hydroxyls), hydrogen bonded hydroxyl groups and siloxane bridges.

2.9.5 Experimental tests to determine the equilibrium transition

As discussed above, the studies by Neimark and Ravikovitch (2001) have suggested for independent cylindrical pores that capillary evaporation is at equilibrium. However, experimental findings have suggested that capillary condensation is at equilibrium (Morishige and Nakamura 2004) and this is explained as follows. Their study measured a series of argon, oxygen and carbon dioxide sorption isotherms over a range of temperatures up to the bulk critical point (T_c), on SBA-15 and MCM-41 samples. They found that the hysteresis shrank when the isotherms were studied at increasing temperatures and disappeared completely at the hysteresis critical point (T_h). The hysteresis critical point was less than the bulk critical point temperature. In addition, between T_h and T_c capillary condensation and evaporation were reversible. Morishige and Nakamura 2004 plotted $T\ln(P/P_0)$ (T, P and P_0 have been defined above), at the midpoint of capillary condensation/evaporation, against the temperature the isotherm was studied. Between the hysteresis critical point temperature and the bulk critical point temperature they found a linear relationship. At temperatures below T_h the plot of $T\ln(P/P_0)$ versus T for capillary condensation followed the same linear relationship. The analogous plot for capillary evaporation deviated from the linear relationship at T_h. Due to this, they suggested for open cylindrical pores that capillary condensation occurs at equilibrium and not capillary evaporation. This experimental study appears to contradict the work of Neimark and Ravikovitch (2001).

2.10 Advanced adsorption

This Chapter so far has discussed how the theory of gas sorption has progressed to explain hysteresis. Despite the advances in understanding gas sorption theory the most recent IUPAC report on pore size calculations was produced in 1994 (Rouquerol *et al.* 1994). The report recommends that the adsorption branch of hysteresis should be used for calculating a pore size distribution because pore blocking means the desorption branch is not at equilibrium. However, cooperative effects between pores can also occur on the adsorption branch and the following section will discuss this effect in detail.

2.10.1 Advanced adsorption theory

Cooperative pore-pore interactions phenomena during adsorption have been discussed and studied to some extent. Esparza *et al.* (2004) has termed the effect advanced adsorption, which is the opposite to pore blocking, and is similar to proposals put forward originally by

de Boer (1958). The concept is as explained, using the Kelvin-Cohan equations and Figure 2.6, as follows.

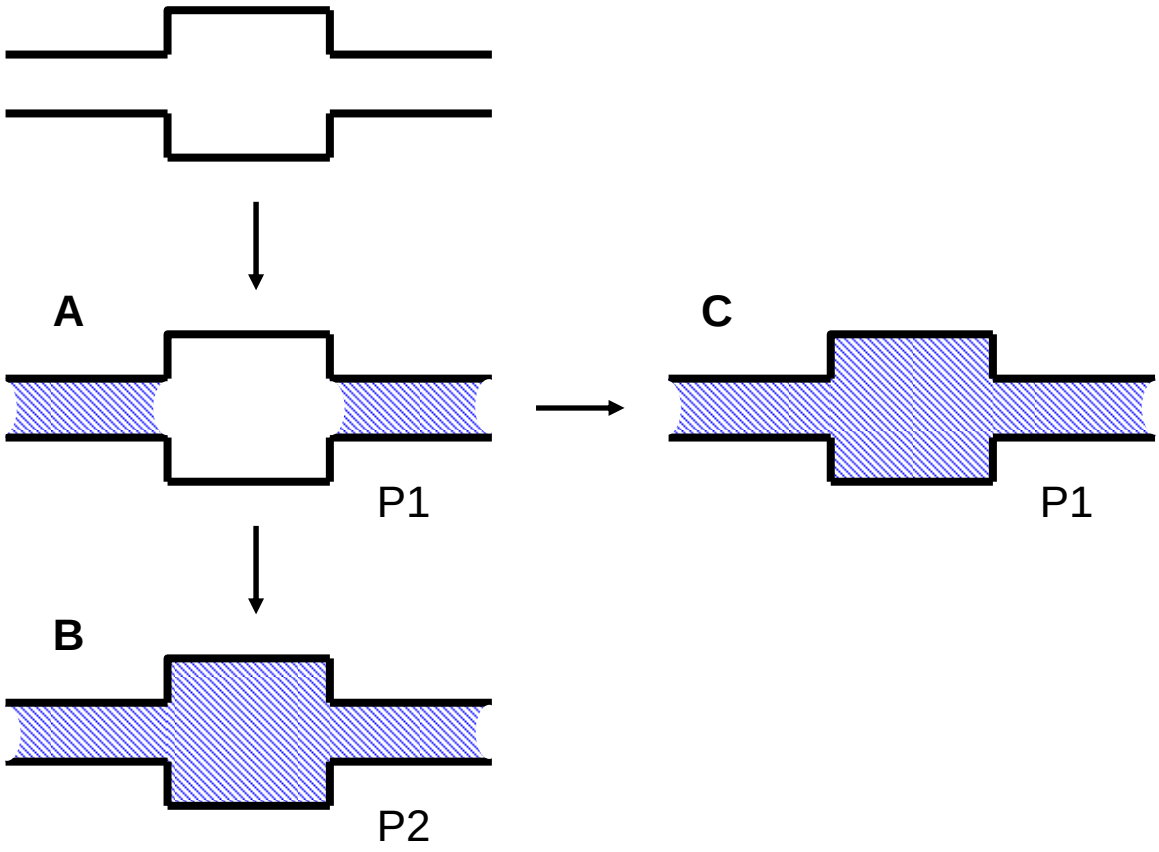

Figure 2.6: Schematic of the advanced adsorption theory, which is explained in the text. The shading refers to condensed gas in the pores and P1/P2 the pressure of the system

Figure 2.6 shows an open ink bottle type pore where the outer necks are of radius r and the pore body of radius 2r. If the pores were to fill independently, initially gas would adsorb on to the surface of the pores, and at pressure P1 the adsorbate would capillary fill the outer neck by a cylindrical type meniscus (Point A). As the pressure is increased gas would diffuse through the outer neck and the multilayer adsorption would continue in the pore body. At pressure P2 the pore body would fill by a cylindrical type meniscus (Point B). If, however, cooperative effects were to occur the whole system would be filled at P1 (Point C). This is because once the outer necks have been filled with condensate the large pore body is closed at both ends. This means the large pore body can fill by a hemispherical type meniscus. If the pore radius of the outer neck is greater than or equal to half of the pore body radius then the pressure for condensation within the pore body, for a hemispherical meniscus, is exceeded by the pressure required to condense in the neck with a cylindrical meniscus. This general picture has recently been confirmed experimentally and using GCMC simulations by Bruschi *et al.* (2010). They made porous anodised alumina

oxides with ink bottle type pore geometry. One sample (termed A for this thesis) had modulations in the pore diameter to generate a series of necks and bodies while another sample (termed B for this thesis) had a constant pore diameter equal to the pore neck diameter of sample A. The ratio between the pore necks and bodies of sample A was 2:3. The experimental gas sorption isotherm for samples A and B overlaid one another, which suggested the pore neck determined both pore filling and pore emptying processes in sample A. Therefore, the pore bodies in sample A filled at the same pressure as the pore necks, which was explained using the advanced adsorption mechanism. They then simulated the gas sorption experiment using through ink bottle type pores, similar to Figure 2.6. The simulations showed that the pore body filled at the same pressure as the neck, which was in agreement to their experimental findings. Detcheverrey *et al.* (2004) conducted DFT simulations of adsorption in disordered models for silica aerogels. They found that an initially localized condensation event can trigger further collective condensation in neighbouring cavities. These results mean that the independent pore model is completely inappropriate to calculate a pore size even for the adsorption branch of hysteresis.

The potential presence of advanced adsorption effects has significant implications for the interpretation of gas adsorption data for pore systems undergoing structural evolution. For example if an ink bottle pore geometry was being generated by progressive pore mouth blocking by coke deposition in a catalyst, then, in the presence of advanced adsorption, the pattern of adsorption would change as the neck radius declined below half that of the non-coked pore body. A complete understanding of this process is necessary to allow correct data analysis otherwise inaccurate pore size distributions would be quoted. However, in addition, the strength of the adsorbate-catalyst and adsorbate-coke interactions may be different, and some suggestion that the critical ratio of pore body-to-neck sizes for the onset of advanced adsorption is dependent on adsorbate-adsorbent interaction strength has been obtained using DFT studies (Rigby and Chigada 2009). This is similar to the reports of Woo *et al.* (2004), discussed above, who showed that pore blocking and cavitation depend on the adsorbate-adsorbent interaction.

Advanced adsorption has been used to explain the shape of hysteresis loops in various experimental studies of adsorption in regular (Kleitz *et al.* 2010**)** and amorphous (Morishige 2009) materials. However, direct observations of the effect are more limited. Casanova *et al.* (2007; 2008) have made experimental studies of advanced adsorption of hexane in model funnel, and ink bottle, shaped pores within anodized alumina using optical

interferometry. These workers observed that, in a funnel-shaped model pore system, sorption in the externally directly-accessible, larger pore section occurred without hysteresis, which would suggest that the pore filled and emptied by a hemispherical meniscus. They also observed that initial capillary condensation within the neck of the funnel lowered the relative pressure for condensation in the larger pore body (presumably by generating a dead end, and a hemispherical meniscus). The larger pore did not, however, fill at the same pressure as the pore neck, as envisaged above using classical Cohan (1938) theory, presumably because the ratio of pore body to neck size was ~4, rather than being less than 2. However, the size ratio was ~2 for the model ink bottle pores but advanced adsorption with single step filling of both pore segments was not observed, though there was a small second step in the adsorption isotherm for the pore necks at a pressure closer to that of the pore bodies than the first step. This difference from classical theory may be because the critical ratio varies with adsorbate-adsorbent interaction strength, as suggested by previous DFT studies (Rigby and Chigada 2009).

2.11 Conclusions

This Chapter has introduced the reader first to the background theory of gas sorption and then a discussion of the origin of hysteresis. This thesis will not focus heavily on determining surface area measurements or microporous pore size distributions and so was not covered in the Chapter.

The reader has been drawn to the argument about whether the adsorption or desorption branch is at equilibrium, which is important when calculating a pore size from gas sorption data. The theory of advanced adsorption has not had much experimental or theoretical attention compared to the extensive studies of pore blocking. As industry typically uses the most recent IUPAC recommendations, which assumes advanced adsorption does not occur, to determine a pore size it is important to determine whether advanced adsorption does indeed occur. The effect of advanced adsorption should be considered when evaluating porous materials. Chapter 4 will provide experimental evidence that advanced adsorption does indeed occur. Following Chapter 4, an experimental method will be developed that determines the adsorption mechanism.

Chapter 3

An introduction to NMR

3.1 Introduction

The first nuclear magnetic resonance (NMR) signal was discovered by Bloch *et al.* (1946) and Purcell *et al.* (1946). Since its discovery the NMR technique has been used in all areas of science. The technique is probably most widely recognised for medical applications (magnetic resonance imaging). More recently NMR has been used to study porous materials and examples are given in Chapters 4 and 8. This thesis will also use the NMR technique to characterise porous materials. Therefore, Chapter 3 will now provide the reader with the basic principles of NMR and the reader should refer back to this Chapter if necessary. The work in this thesis will study only hydrogen nuclei so this theoretical Chapter will only consider these nuclei.

3.2 Background to NMR

NMR is a physical phenomenon based upon the quantum magnetic properties of an atoms nucleus. Nuclei with odd atomic or mass numbers, such as hydrogen nuclei, are said to have 'spin'. Spin is a property, like mass, and nuclei have been described as behaving like "charged spinning tops" (Jones 1969). The spin is characterised by a nuclear spin quantum number, I, which can be either whole or half integer numbers. Hydrogen nuclei have a spin quantum number, I, of ½ and the spin can have $2I+1$ orientations.

Though quantum mechanics is needed to explain NMR theory in detail, some visual understanding of the technique can be gained as follows. If a hydrogen nucleus is placed into an external magnetic field, B_0, the spin can be viewed as being aligned in the same direction as the magnetic field or it can be in the opposite direction to the magnetic field. If the nuclear spin is aligned with the magnetic field, it has a +½ spin (Hore 1995). If it is in the opposite direction it has a -½ spin. When the nuclear spins are in the direction of the applied magnetic field they are in a lower energy state compared to when they are in the opposite direction. The difference in the energy levels, ΔE, can be expressed by:

$$\Delta E = \frac{\gamma \hbar B_o}{2\pi} \qquad 3.1$$

where h is Planck's constant and γ is magnetogyric ratio constant of the nucleus.

When the nuclei are in an external magnetic field they can adsorb a photon (Bloch *et al.* 1946; Purcell *et al.* 1946). By absorbing a photon, the nuclei with spin +½ are excited to the higher energy level. When the nuclei move between the energy levels they are said to resonate, which is the basic principle of NMR. The frequency of radiation, υ, associated with the transition can be expressed by:

$$\nu = \frac{\gamma B_o}{2\pi} \qquad 3.2$$

However, due to the spin of the nuclei, another visual interpretation of NMR spectroscopy is to consider hydrogen nuclei as charged spinning tops (Jones 1969). Rather than aligning themselves with or against the magnetic field, hydrogen nuclei will precesses, at some arbitrary angle, about the direction of the magnetic field, in the same way that a spinning top precesses about a gravitational field. The frequency, υ, at which they precess depends on the nucleus and the external magnetic field. The frequency can be expressed by:

$$\nu = \frac{\gamma B_o}{2\pi} \qquad 3.3$$

This frequency is said to be the Larmor precession frequency and is the same as the frequency described above when considering the frequency required to excite nuclei between energy levels.

3.2.1 The NMR experiment

The basic NMR experiment will now be described with the aid of Figure 3.1. When hydrogen nuclei are placed inside a magnetic field, their nuclear spin energy levels, as discussed above, are not degenerate. When the system is at equilibrium there will be a greater number of nuclei in the lower energy state. If the direction of B_0 is defined to be in the z-direction, it is said that there is a net magnetisation vector, M, in this direction. This is shown on the left side of Figure 3.1 by the thick red arrow in the z-direction. The net magnetisation vector can be tilted into the y-direction by applying a radio frequency (r.f.) pulse along the x-axis. This is equivalent to exciting any nuclei with a spin of +½ to the higher energy state. The tilt of the net magnetisation away from the z-axis depends on the

strength of the applied r.f. pulse and the length of the pulse (Hore 1995). Assuming the magnetisation is tilted by 90°, this means there is no longer a net magnetisation in the z-direction. This is equivalent to saying that the number of nuclei with spin +½ is equal to the number of nuclei with spin -½. The net magnetisation is instead in the x-y plane and it will precess around B_0 at the Larmor frequency. As the net magnetisation precesses, it passes through a detector coil producing an electrical signal. The signal is recorded and for reasons discussed below the signal decays. The plot of the decaying signal intensity versus time is known as the Free Induction Decay (FID). The intensity, I_{NMR}, of the signal is proportional to the magnetisation, M, (Hore 1995).

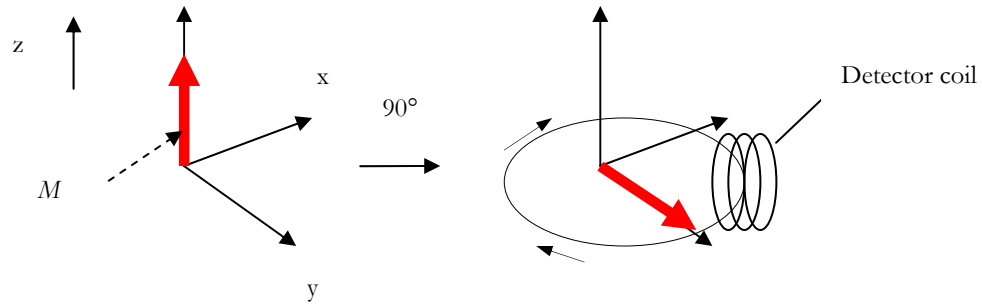

Figure 3.1: Schematic of a simple NMR experiment. The red arrows show the net magnetisation vector, M, and the text explains the schematic

3.2.2 Relaxation of the NMR signal

After the r.f. pulse, the system is now at a higher energy state. However, it will want to return to the lower energy state and this process is known as relaxation. The two relaxation processes that will be studied in this thesis are longitudinal relaxation and transverse relaxation. Longitudinal relaxation is when the net magnetisation returns to the z-direction over time and it occurs with an exponential time constant T_1. Transverse relaxation occurs when the component of the magnetisation in the x-y plane shrinks over time and this relaxation process occurs with a time constant T_2. Experiments to determine T_1 and T_2 will be presented below.

3.2.3 Enhanced relaxation in porous materials

The nuclei studied by the NMR technique in this thesis are confined within a liquid, which is imbibed in a porous material. When imbibed in a porous material the relaxation rate of the NMR signal is increased. This is due to the interactions of the molecules in a thin layer of liquid, at the pore wall, and the pore wall (see Figure 3.2). In addition, the molecules in

this layer can exchange with the molecules in the remaining bulk region of the pore. For the porous systems studied in this work, during the course of an NMR experiment the root mean square displacement of the water molecules greatly exceeds the size of the pore. Therefore, the water molecules in the thin layer of liquid will exchange many times with the remaining bulk region of the pore. The observed relaxation constant will be an average of the relaxation constant of the liquid in the thin layer and that of the liquid in the remaining bulk region of the pore, which is expressed by (Brownstein and Tarr 1977):

$$\frac{1}{T_{2av}} = \left(1 - \frac{\lambda S}{V}\right)\frac{1}{T_{2B}} + \frac{\lambda S}{V}\frac{1}{T_{2S}} \qquad 3.4$$

where λ is the thickness of the liquid layer, the subscript B refers to the bulk liquid in the pore, the subscript S refers to the thin layer at the surface of the pore, the subscript B (bulk) refers to the remaining imbibed material and S/V is the surface to volume ratio of the pore. If $T_{2B} >> T_{2S}$ then the surface to volume ratio can be expressed by:

$$\frac{S}{V} \approx \frac{T_{2S}}{\lambda}\frac{1}{T_2} \qquad 3.5$$

For a cylindrical shaped pore the surface to volume ratio is equal to $2/r$, where r is the pore radius. This means that the measured T_2 relaxation time constant is proportional to the size of the pore itself. From equation 3.5, as the pore size increases so will the T_2 relaxation time constant.

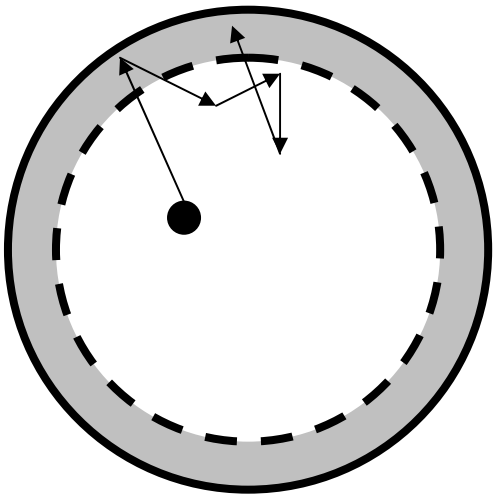

Figure 3.2: Water molecule (black circle) inside a pore (fixed black line) diffuses, which is shown by the arrows. A thin layer of water interacts with the surface of the pore wall (grey region) and the T_2 relaxation time constant is reduced

3.3 Experimental determination of the relaxation time constants T_1 and T_2

The experiments that have been used in the following Chapters to determine the T_1 and T_2 relaxation time constants will now be presented.

3.3.1 The inverse recovery experiment to measure T_1

The inversion recovery experiment is a method for determining the T_1 relaxation time constant and is explained as follows using Figure 3.3. At first a 180° pulse rotates the net magnetisation vector from the positive z-direction to the negative z-direction. During a time delay, t_d, the magnetisation relaxes towards its equilibrium state. After t_d a 90° pulse is applied and this allows the partially relaxed signal to be detected in the x-y plane. A series of experiments can be studied at different t_d values and the relationship between the magnetisation and t_d is given by:

$$M_z(t_d) = M_0[1 - 2\exp\left(\frac{-t_d}{T_1}\right)] \qquad 3.6$$

where M_0 is the magnetisation in the z-direction at time zero and $M_z(t_d)$ the magnitude of the magnetisation in the z-direction at time t_d. A plot of $\ln(M_0 - M_Z(t_d))$ versus t_d will give a linear graph with a slope of $-1/T_1$.

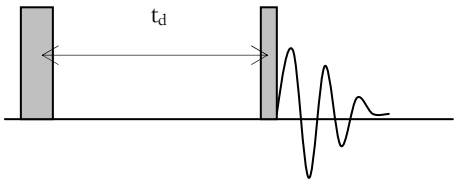

Figure 3.3: Pulse sequence for the inversion recovery experiment. The rectangles show the 90° and 180° r.f. pulses. The larger rectangle is the 180° pulse. The sine wave (with decreasing amplitude) is the free induction decay

An approximation of the T_1 time constant can be found. When the magnetisation goes through a null ($M_z(t_d) = 0$), equation 3.6 can be expressed as:

$$\exp\left(\frac{-t_d}{T_1}\right) = \frac{1}{2} \qquad 3.7$$

The T_1 time constant can then be calculated using equation 3.7 and this method to determine T_1 was used in following Chapters. All the experiments studied in this thesis used a recovery period of at least 5xT_1 relaxation time constants before the next experiment was repeated. This was to ensure that the net magnetisation vector had recovered along the z-direction.

3.3.2 The spin echo experiments to measure T_2

Relaxation in the x-y plane occurs due to the T_2 relaxation process and also because of inhomogeneities in the magnetic field. The spin echo experiment is designed to remove the effects due to inhomogeneities in the magnetic field and will now be explained using Figure 3.4. After a 90° pulse (about the x-axis) all the spins are tilted to the y-axis and will precess about the magnetic field, B_0, in the x-y plane. The spins will de-phase, by precessing at slightly different frequencies, over a period of time t_d. This is due to T_2 relaxation and inhomogeneities of the magnetic field. To remove the effects of static field inhomogeneities a 180° pulse (about the y-axis) is applied which means the spins are rotated (180°) about this axis and they will begin to re-phase. After another time t_d the spins will realign to produce an echo, known as a spin echo (Hahn 1950). The magnitude of this spin echo will vary, due to T_2, as a function of t_d and can be expressed by:

$$I_{NMR}(2t_d) = I_0 \exp\left(\frac{-2t_d}{T_2}\right) \qquad 3.8$$

By repeating the 180° pulse every $2t_d$ (Figure 3.5), the total time of the experiment increases and the signal intensity for each echo will decrease (Carr and Purcell 1954; Meiboom and Gill 1959). This is commonly referred to as the CPMG (Carr-Purcell Meiboom-Gill) pulse sequence. Plotting $\ln(I_{NMR}(2t_d))$ versus $2t_d$ will give a linear graph with a slope of $-1/T_2$.

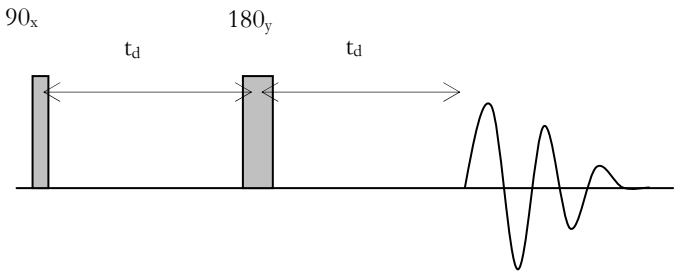

Figure 3.4: The pulse sequence for the spin echo experiment. The rectangles show the 90° (x-axis) and 180° (y-axis) pulses. See Figure 3.3 for an explanation of the symbols used

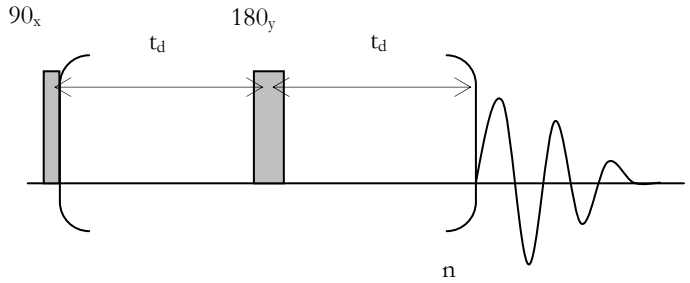

Figure 3.5: Modification to the pulse sequence in Figure 3.4. The sequence is repeated n times. This is the CPMG pulse sequence. See Figure 3.3 for an explanation of the symbols used

3.4 Pulsed field gradient NMR

The previous section has discussed NMR experiments when the magnetic field is homogenous. This means that (for a perfectly shimmed sample) all the nuclei experience the same magnetic field strength. This section will now discuss an experiment when the magnetic field gradient is not homogenous. By applying an additional magnetic field gradient, *G*, the magnetic field experienced by the nuclear spin will vary depending on its position along the direction of the applied field gradient. This means the resonance frequency will also vary linearly with the nuclear spin's position. The resonance frequency is therefore governed by not only the main magnetic field strength, but also by a product of

the position of the nuclei and the strength of the applied gradient. For the case when the field gradient is applied along the z-direction this can be expressed by:

$$\nu(z) = \frac{\gamma B_o}{2\pi} + \frac{\gamma G_z \cdot z}{2\pi} \qquad 3.9$$

where $\upsilon(z)$ is the frequency at position z along the direction of the applied gradient with strength, G.

If the gradients are pulsed on and off during the course of suitable NMR pulse programs "pulsed field gradient (PFG) NMR", the resulting experiments can be used to characterise diffusion in porous materials. Later Chapters will discuss examples where the PFG NMR experiment has been used. This Chapter will now first explain the original PFG NMR spin echo experiment and it will present the pulse sequence used in this thesis.

The PFG NMR spin echo is based on the spin echo in Figure 3.4, but two gradients of identical magnitude, g, and width, δ, are applied (Stejskal and Tanner 1965). The two gradients are separated by a time Δ. The PFG NMR spin echo pulse sequence is shown in Figure 3.6 and the gradients are shown by the sinusoidal shapes. The pulse sequence is explained as follows.

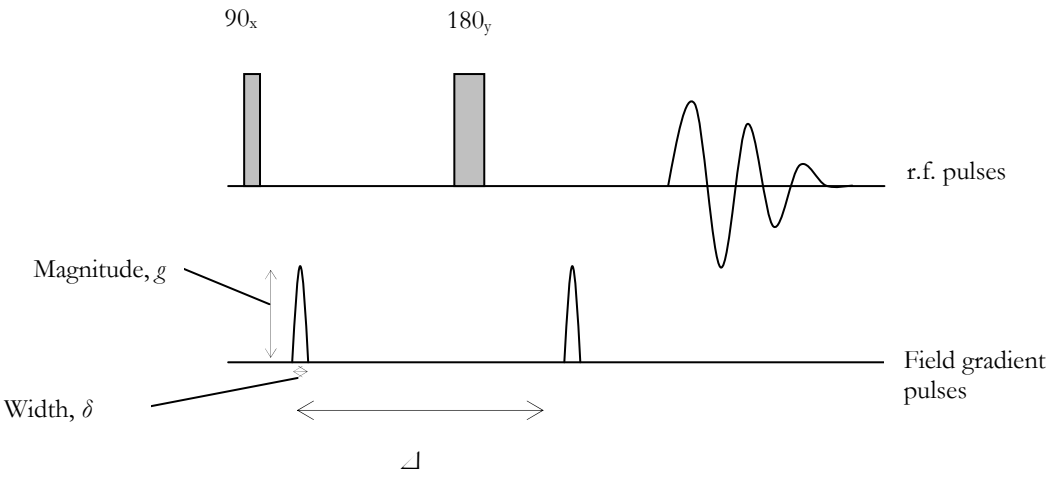

Figure 3.6: The PFG NMR spin echo pulse sequence. The r.f. pulses are shown by rectangular blocks, the magnetic field gradient pulses are shown by the sinusoidal shapes and the FID by the sine wave (with decaying amplitude)

After the 90° r.f. pulse, the net magnetisation is directed along the y-axis and it will then precesses about B_0 in the x-y plane (see above). Applying the first magnetic field gradient pulse gives the precessing frequency of each spin a phase offset. The phase offset depends on the nuclear spin position along the applied field gradient. The 180° r.f. pulse then rotates each spin frequency through "180°" in the x-y plane. A second identical magnetic field gradient is then applied. If the molecules have not diffused during time ⊿, this gradient will remove the phase offset caused by the first gradient and the signal will become refocused. If the molecules diffuse during time ⊿, the local field experienced by the nuclear spin will be different when the second field gradient pulse is applied. This means the signal will only be partially refocused. The amount of attenuation will depend on the distance the nuclei diffuse during the time ⊿. Further details of the signal attenuation are given below.

This description given ignores the transverse relaxation process. Since the net magnetisation is in the x-y plane during time ⊿, the signal will also decrease due to transverse relaxation. If diffusion is slow, the use of long ⊿ time delays can lead to very low signal. To resolve this issue, the stimulated echo sequence (STE) can be used instead. If $T_1 >> T_2$, the 180° r.f. pulse can be split into two 90° r.f. pulses which is shown in Figure 3.7. Following the 90° r.f. pulse and the first field gradient pulse, a second 90° r.f. pulse is applied. The net magnetisation is now in the z-direction so there is no transverse relaxation. Instead there is longitudinal relaxation, which is much slower. When the molecules diffuse during time ⊿, the signal loss is therefore dictated by the slower T_1 relaxation rate. Following time ⊿, the magnetisation is rotated back into the x-y plane by another 90° r.f. pulse, and the signal becomes re-focused and it is detected. Again, the amount of attenuation depends on the distance the molecules diffuse during time ⊿.

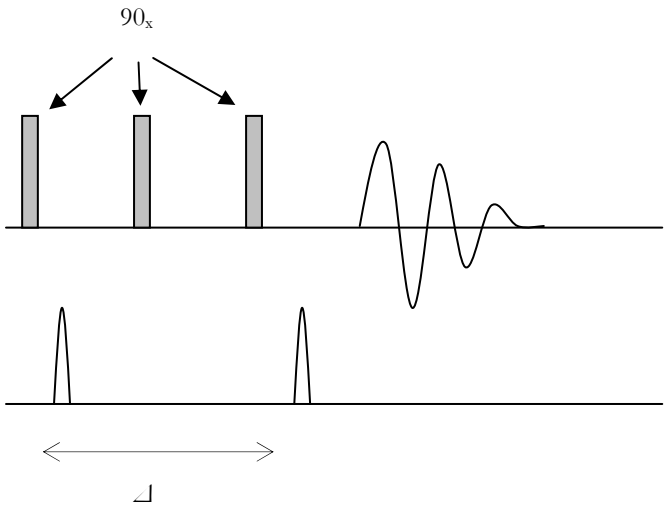

Figure 3.7: The stimulated echo pulse sequence. See Figure 3.6 for symbols used

An advanced version of the stimulated echo has been used in the following Chapters and is called a bipolar pulse longitudinal eddy current delay (BPP-LED) (Wu *et al.* 1995). The pulse sequence is shown in Figure 3.8 and is explained as follows. The stimulated pulse sequence is modified by replacing the magnetic field gradient pulse with two pulses of half the duration that are separated by a 180° r.f. pulse. After the final field gradient pulse another 90° r.f. pulse is applied to store the magnetisation in the z-direction. This allows time for eddy currents to decay. Another 90° r.f. pulse places the net magnetisation vector back into the x-y plane for detection.

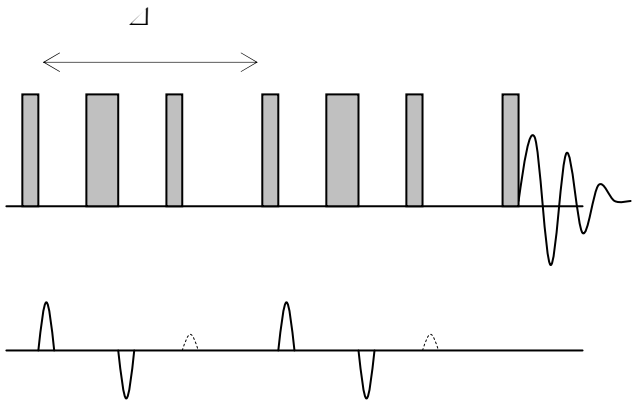

Figure 3.8: The stimulated bipolar spin echo sequence with longitudinal eddy delays. See Figure 3.6 for symbols used. Two small field gradient purging pulses (dashed lines) remove magnetisation in the x-y plane when the desired magnetisation is in the z-direction

The intensity of the observed echo depends on the diffusion time, ⊿, the length of the gradient pulse, δ, and the strength of the gradient pulse, *g*. By assuming that the nuclei do not diffuse during the gradient pulse, *δ*, the signal intensity for the PFG NMR experiments can be expressed by:

$$\frac{I_{NMR}}{I_0} = \exp\left[- D_{PFG}\gamma^2 g^2 \delta^2 \left(\Delta - \frac{\delta}{3} - \frac{\tau}{2} \right) \right] \qquad 3.10$$

where I_{NMR} is the NMR signal intensity, I_0 is the echo intensity in the absence of the gradients, D_{PFG} is the self diffusion coefficient and τ the correction time for the phasing and dephasing between bipolar gradients. A plot of $\ln(I_{NMR}/I_0)$ against $\gamma^2 g^2 \delta^2 \left(\Delta - \frac{\delta}{3} - \frac{\tau}{2} \right)$ will, under certain circumstances, give a linear slope and its gradient is the diffusion coefficient. All plots of experimental data in this thesis gave a linear slope. From Hollewand and Gladden (1995), because D_{PFG} contains a contribution from the spin density, which is proportional to the voidage, it is related to the effective diffusion coefficient, D_{eff}, by:

$$D_{eff} = \varepsilon D_{PFG} \qquad 3.11$$

where ε is the voidage. For diffusion of a liquid inside a porous material the effective diffusion coefficient is related to the bulk diffusion, the tortuosity, τ_p, and the voidage by:

$$D_{eff} = D\frac{\varepsilon}{\tau_p} \qquad 3.12$$

The tortuosity of a pore network is the measure of how far from a linear path a diffusing molecule will experience. If the tortuosity is high, it means that the molecules are not able to diffuse far in the pore network.

By combining equations 3.11 and 3.12, the tortuosity can be calculated by:

$$\tau_p = \frac{D}{D_{PFG}} \qquad 3.13$$

This means that the diffusion coefficient of a liquid imbibed in a porous material will depend on the tortuosity of the material. In the following Chapters the tortuosity will be calculated by measuring D_{PFG} (experimentally) and estimating the bulk diffusion from values given in the literature (Mills 1973; Holz *et al.* 2000 cited by Perkins 2009). As stated in the preface, this approach was used by Perkins (2009), and the calibration curve used in this thesis was found by Perkins.

In addition, the following Chapters will calculate the distance the water molecules diffuse during the experiment. The reasons for this will be explained in the Chapters themselves. To determine the distance the molecules move the Einstein equation (equation 3.14) will be used. This is expressed by:

$$\left\langle r(t)^2 \right\rangle = 6D_{PFG}\Delta \qquad 3.14$$

where $\left\langle r(t)^2 \right\rangle$ is the mean square displacement of the molecules. The distance a molecule travels can be calculated by:

$$r = \sqrt{(6D_{PFG}\Delta)} \qquad 3.15$$

3.5 The magnetic resonance imaging experiment

This Chapter so far has introduced the basic concepts of NMR to the reader and how to measure T_1/T_2 relaxation time constants and the diffusion coefficient of a liquid. In Chapter 4 magnetic resonance imaging will be used to study the spatial location of water (hydrogen nuclei) inside a porous material. Therefore, this section will now introduce some background theory to MRI.

To explain the MRI technique an example will be used where a tube of water (see Figure 3.9) will be imaged. To be able to image the tube of water, the Cartesian coordinates, x, y and z of the water molecules need to be worked out. Let's say the water molecules of interest are located in the slice between the two dashed lines in Figure 3.9.

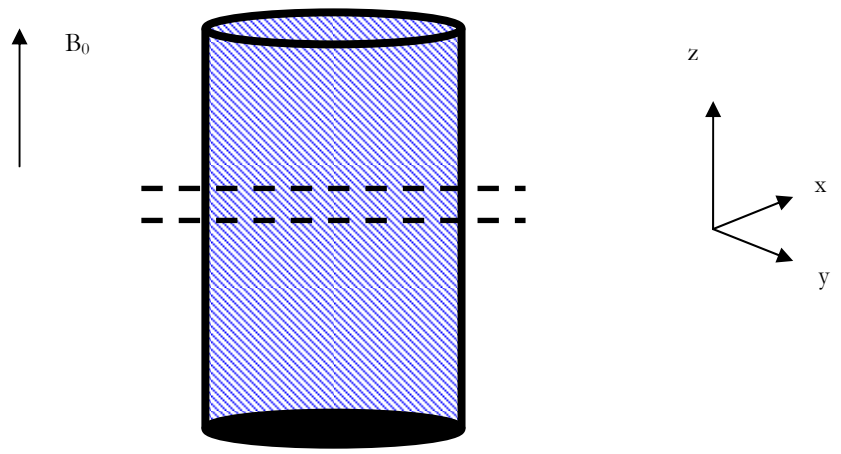

Figure 3.9: A tube of water (the water is shown by the shading). The text describes how to spatially locate the water molecules between the two dashed lines. The z-direction is the direction of the applied magnetic field, B_0

To spatially locate the water molecules in this slice the experiment can be summarised as:

1. A radio frequency pulse is applied, in the presence of a magnetic field gradient, which will selectively excite the spins within the slice.

2. A phase encoding gradient, G_y, will be applied to provide information along the y-direction within the slice.

3. A frequency encoding gradient, G_x, will be applied to provide information along the x-direction within the slice.

Figure 3.10 shows part of the multi echo imaging pulse sequence used in this thesis and the symbols used are referred to in the text below.

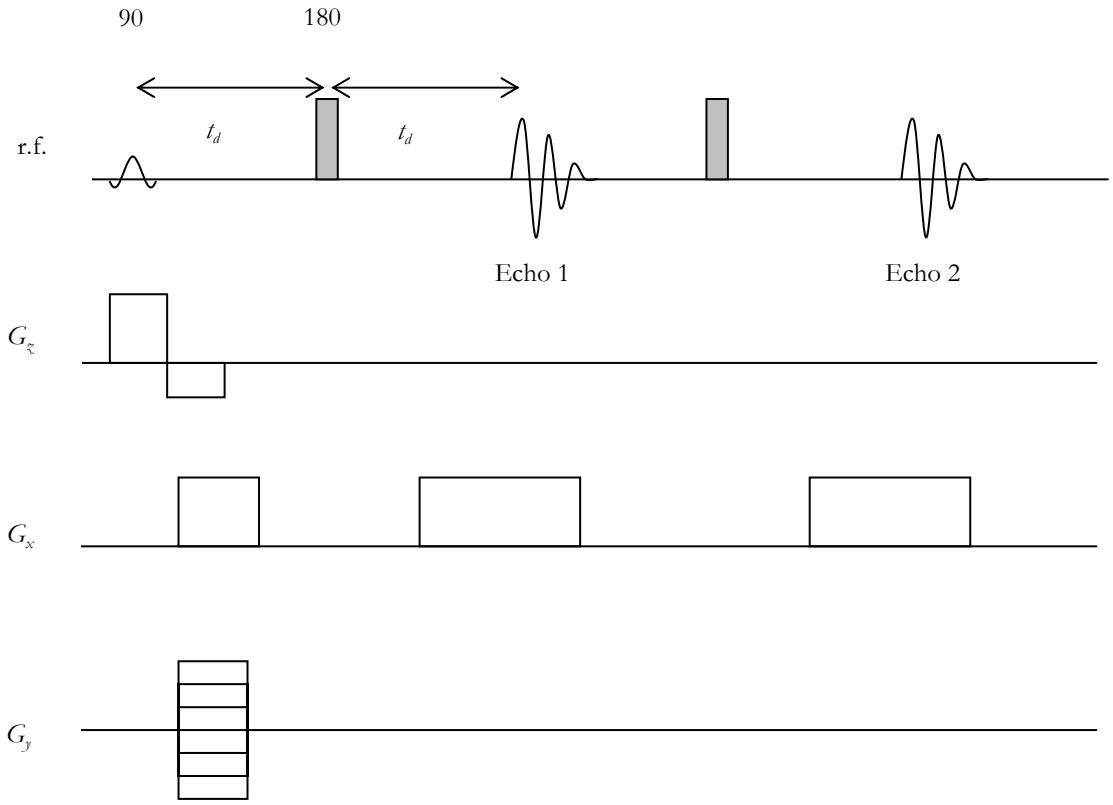

Figure 3.10: Spin (multi) echo imaging pulse sequence with a 90° slice selective pulse. The symbols used are discussed in the text

3.5.1 The selective slice

To achieve slice selection, a magnetic field gradient is applied at the same time as a r.f. pulse. If a linear magnetic field gradient is applied in the z-direction (see Figure 3.9 for the z-direction), the precession frequency of the nuclei will vary with their position along the z-direction. This was discussed above using equation 3.9. A frequency selective pulse is applied such that only nuclei with a certain range of resonance frequencies ($\Delta\upsilon$) will be excited. The thickness of the slice, Δz, is determined by the applied field gradient and the frequency bandwidth of the applied r.f. pulse, which can be expressed by:

$$\Delta z = \frac{2\pi\Delta\upsilon}{\gamma G_z} \qquad 3.16$$

Therefore, a thin slice is achieved by using an r.f. pulse with a narrow bandwidth frequency ($\Delta\upsilon$) and/or a strong gradient G_z. A selective r.f. pulse is referred to as a soft pulse and has a sinc profile (Gadian 1995).

The pulse sequence: In Figure 3.10, the slice selective pulse is shown by the sinc profile. When the pulse is applied a field gradient in the z-direction is also applied. Referring back to Figure 3.9, this excites only the nuclei in the slice and rotates the net magnetisation vector (of this slice) into the x-y plane. However, the slice-select gradient causes the spins to de-phase. This means the NMR signal will decrease in intensity relative to the signal if the spins were in phase. Therefore, a compensatory gradient is applied to re-phase the spins. This is shown in Figure 3.10 by the applied field gradient in the z-direction with the opposite sign to the slice-selective field gradient. The strength and length of this gradient is chosen so that the spins are re-phased when it is turned off. As in the case of the 1-dimensional pulse sequence discussed above, after time t_d a non-selective $180_y°$ pulse is applied. This leads to an echo at time $2t_d$ after the $90_x°$ pulse.

This section has shown how a slice can be selectively excited. In Figure 3.11, the selective slice has been rotated so it is being viewed looking along the z-axis. The following sections will now describe how the echo signal after the 180° pulse can have spatial information in the x and y directions.

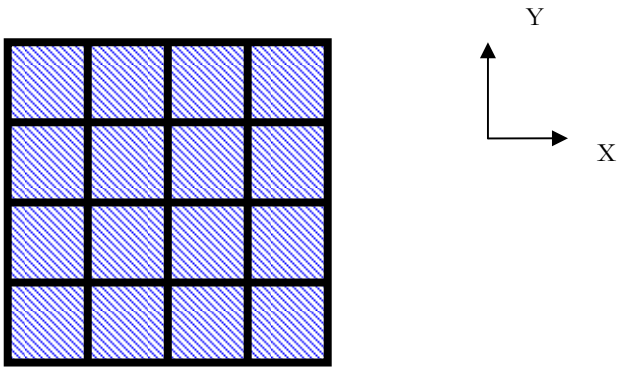

Figure 3.11: The selected slice in Figure 3.9 being viewed in the z-direction

3.5.2 Frequency encoding: the x-direction

After the 90° slice selective pulse, the magnetisation is in the transverse x-y plane. Spatial information along the x-direction can be found by applying a magnetic field gradient in this direction as the spin echo data is acquired. Analogous to equation 3.9, the Larmor frequency at position x along the direction of an applied magnetic field gradient can be expressed by:

$$\nu(x) = \frac{\gamma B_o}{2\pi} + \frac{\gamma G_x \cdot x}{2\pi} \qquad 3.17$$

This means the spins will precess at a frequency according to their position along the x-direction.

The pulse sequence: In Figure 3.10, this is shown by the magnetic field gradient (G_x) being on at the same time the echo forms and decays. This frequency encodes the echo signal with spatial information in the x-direction. However, when the data is acquired in the form of a spin echo, the magnetic field gradient (G_x) is on for a long time. This causes the spins to de-phase and, thus, the signal to decrease. To avoid this, a pulsed field gradient is applied in the x-direction before the 180° r.f. pulse, which is shown in Figure 3.10. The effect of having two pulsed magnetic field gradients either side of a 180° r.f. pulse was discussed above (see Figure 3.6). The size of the applied magnetic field gradients can be adjusted so that the gradient echo forms at the same time as the spin echo.

3.5.3 Phase encoding: the y-direction

When the magnetisation is in the x-y plane, spatial information about the y-direction is obtained using a phase encoding procedure. Instead of relying on the spin precession frequency for spatial encoding, this method depends on the spatial variation in the phase. Analogous to the frequency encoding procedure, a magnetic field gradient is applied but in the y-direction (G_y), and the Larmor frequency at position y along the direction of the gradient can be expressed by:

$$\nu(y) = \frac{\gamma B_o}{2\pi} + \frac{\gamma G_y \cdot y}{2\pi} \qquad 3.18$$

After G_y has been applied, all the spins precess at the same frequency. However, they are out of phase and the phase shift is proportional to their y-direction coordinate. The phase shift, $\measuredangle\varphi$, at position y (along the y-direction) after time t, can be expressed by (Gadian 1995):

$$\Delta\varphi = \gamma \cdot G_y \cdot y \cdot t \qquad 3.19$$

The pulse sequence: The phase encoding procedure is shown in Figure 3.10. After the 90° r.f. pulse there is a stepwise increase in the amplitude of G_y. The amplitude of this gradient is incremented to ensure enough data is acquired to resolve the y-direction. For example, a magnetic field gradient is applied with strength G in the y-direction after the 90° r.f. pulse. This causes a phase shift in the spins and this is remembered by the spins during the pulse sequence in Figure 3.10. This phase encodes the echo signal with spatial information in the y-direction. The phase encoding and frequency encoding information is then stored and system is allowed to relax back to equilibrium. A new sequence is started and another magnetic field gradient (G_y) is then applied after the 90° pulse. However, the gradient strength is now different. This means the phase shift will be different and once more the phase shift is remembered by the spins during the pulse sequence. Again this information along with the frequency encoding information is stored. This procedure is repeated a number of times to ensure enough information is gathered to generate a 2-dimensional image. The stored data is converted into a 2-dimensional image by 2-dimensional Fourier-Transform (Gadian 1995).

A multi echo pulse sequence was used in this thesis, where $180_y°$ r.f. pulses were repeated every $2t_d$. Figure 3.10 shows only two 180° r.f. pulses for simplicity. This is similar to the CPMG pulse sequence discussed above. After each 180° pulse, a gradient (G_x) is applied to frequency encode the echo signal, as described above.

3.6 Summary

Chapter 3 has given some brief background regarding NMR. It has described some NMR experiments and it has described the MRI experiment. In the following Chapters these experiments will be used and the reader should refer back to this Chapter if necessary. In addition, some of the equations introduced in this Chapter will be presented again in the following Chapters to aid the reader.

Chapter 4

NMR studies of the advanced adsorption mechanism

4.1 Introduction

Chapter 2 introduced the reader to hysteresis in Type IV isotherms. The Chapter discussed whether the adsorption or desorption branch of the hysteresis loop should be used to calculate a pore size. This is important because either branch can potentially be used to determine a pore size distribution (PSD), which is used as a method to rationalise the performance of heterogeneous catalysts. Any potential inaccuracy in this distribution would greatly undermine efforts to understand the inter-relationship between catalyst structure and performance. The theoretical data analysis methods and assumptions used for converting the adsorption isotherm into a PSD were discussed in Chapter 2. One assumption discussed was the idea that pores are thermodynamically independent, such that they do not interact with neighbouring pores. This is equivalent to treating the individual 'pores' within an irregular, interconnected porous material as if they were located within a hypothetical parallel pore bundle. Even assuming it is possible to obtain a physically meaningful definition of a 'single pore' within an interconnected porous material, this assumption neglects the possibility of interactions between neighbouring pores, such as the advanced adsorption mechanism (see Chapter 2).

NMR methods, specifically relaxometry, have been used to study pore blocking effects on the desorption isotherm of a gas sorption experiment. Porion *et al.* (1998) used NMR relaxometry to show that the relaxation time of water adsorbed in silica gels was the same, at the same fractional saturation level on the adsorption or desorption branch of the isotherm. They interpreted this finding to imply that pore blocking effects were not occurring on the desorption branch. If pore blocking effects were occurring this would give rise to a different geometrical configuration of the adsorbed phase within the pore structure at the same saturation level on the adsorption and desorption branches. Hence, it would be expected that the relaxation times should differ between the hysteresis branches if pore blocking was occurring. However, the above reasoning neglects the possibility that advanced adsorption on the adsorption branch will occur. For example in an ink bottle pore model, if the neck and body size ratio does not exceed the critical value, the pore body and pore neck should fill and empty together on both the adsorption and desorption

branches if both advanced adsorption and pore blocking effects were occurring. Hence, the results of Porion *et al.* (1998) do not necessarily imply the absence of pore blocking if advanced adsorption was occurring too. These results therefore indicate the necessity of detecting advanced adsorption effects before interpreting sorption data.

Since the advanced adsorption effect is intrinsically spatial and longer range (at least compared to pore size) in character, then this suggests they need to be studied using a technique that is capable of providing spatially resolved information on the adsorption process. Magnetic resonance imaging (MRI) can be used to obtain spatially resolved maps of spin density, relaxation time and diffusivity, which probe voidage fraction, pore size, and pore connectivity (tortuosity), respectively, of porous media over length-scales >10 μm (Hollewand and Gladden 1993). It has been used to show that amorphous mesoporous catalyst support pellets possess macroscopic heterogeneities in the spatial distribution of these parameters with correlation lengths exceeding ~100 μm (Rigby 2000). However, while MRI has been used to study adsorption processes (Beyea *et al.* 2003), it has not been used to probe more fundamental aspects. MRI has been used to study the kinetics of adsorption in packed beds (Prado *et al.* 1999) and whole pellets (Koptyug *et al.* 2000). Imaging has been used to obtain a spatially resolved isotherm, from which the spatial distribution of the BET surface area and interaction parameter have been obtained (Beyea *et al.* 2003). However, relaxation imaging pulse sequences have not been used to study adsorption, particularly in materials that possess long-range correlations in pore size visible by MRI. Farrher *et al.* (2007) have used MRI to study the spatial distribution of liquid within partially saturated silica samples. Partial saturation of the sample with condensate was achieved by halting a kinetic vapour adsorption experiment, above pure water, at a given weight. This technique may give rise to a different spatial arrangement of the adsorbed phase than would be achieved by equilibrium adsorption. Their MRI studies demonstrated a heterogeneous spatial distribution of liquid on macroscopic length-scales.

MRI can probe long-range (>10 μm) processes while pulsed field gradient (PFG) NMR can be used to study adsorption over some of the intermediate size range (~1-10 μm). Hence, PFG NMR is a useful complementary technique. Naumov *et al.* (2008) have studied the spatial arrangement of condensate, on the adsorption and desorption branches of the hysteresis loop region of the isotherm, for cyclohexane sorption in Vycor porous glass. They found that the diffusivity differed between the boundary adsorption and desorption branches of the hysteresis loop at the same degree of pore filling. This result suggested that the spatial arrangement of condensate within pores was dependent upon the

adsorption-desorption history of the sample.

In this Chapter, studies of advanced adsorption effects for water adsorption on a macroscopically heterogeneous, mesoporous silica using MRI and PFG NMR will be described. It will be shown that advanced adsorption can occur in pore bodies that are up to five times larger than their neighbouring necks, and that these effects can extend over macroscopic length scales.

4.2 Experimental

4.2.1 Studied material

The porous material studied in this work, denoted G2, is a batch of mesoporous, sol-gel silica spheres of diameter ~3 mm. The voidage fraction is 0.70±0.02, the modal pore diameter is ~30 nm, and the specific pore volume is 1 cm^3g^{-1}.

4.2.2 Water sorption experiment

Water adsorption and desorption isotherms were obtained for a sample of 5 pellets and was carried out using a Dynamic Vapour Sorption Advantage apparatus, modified with a temperature pre-heater. Samples were initially pre-soaked in pure water and heated to 100 °C to dehydrate the samples but care was taken not to dehydroxylate the silica surface. Water adsorption to relative pressure 0.90 was performed at 296 K ± 0.1 K (the quoted precision of the apparatus), in intervals of 10 % and an equilibration time of 4 hours was used for each step. Data points at higher relative pressure (>0.90) were obtained gravimetrically by suspension of similarly-sized pellet samples above large reservoirs of sodium hydroxide solutions (see below). This additional measure was required because the Dynamic Vapour Sorption Advantage apparatus was unable to study the adsorption of water at relative pressures greater than 0.90.

Wink (1946) proposed a procedure for gas sorption experiments by suspending materials over a known salt concentration. Each salt solution had a known vapour pressure, and by sealing the system the atmospheres inside could be maintained. By leaving the material suspended above the salt solution over a period of time the vapour would adsorb onto the porous material and be in equilibrium with the gas phase. A similar set up was employed in this work and is described in detail below. In this study, different sodium hydroxide solutions were used to achieve different vapour pressures. The vapour pressures of the different sodium hydroxide solutions were obtained from Perry and Green (1997).

4.2.3 The method used to suspend G2 above a sodium hydroxide solution

A sodium hydroxide solution was added to a vial and a piece of metal gauze was placed at the top. The G2 pellets were then placed on the wire gauze and the system was sealed with a lid and Parafilm; this ensured that the system was closed from the outside atmosphere. A schematic of the set up is shown in Figure 4.1.

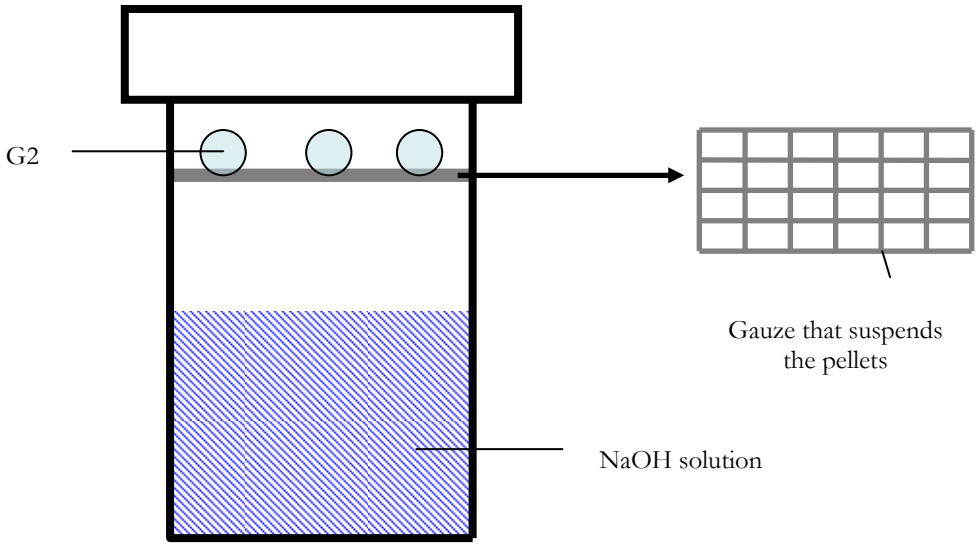

Figure 4.1: Schematic of G2 suspended above a solution of sodium hydroxide. The inset shows the wire gauze used to suspend the pellets

The set up of the system was such that when the silica adsorbed the water vapour the change in the solution concentration was minimal. To prove this statement, an example calculation will be described using a solution that generates a relative pressure of 0.965. To achieve a relative pressure of 0.965, 1.96 g of sodium hydroxide should be dissolve in 40.0 cm^3 of water (Perry and Green 1997). The set-up suspended 5 pellets (~ 500 mg) above 40.0 cm^3 of solution. From the isotherm, which is shown in the results section, at relative pressure 0.965 G2 will adsorb ~27 % of its mass. If 500 mg of sample is used this means 135 mg of water will be adsorbed by G2. Therefore, the volume of the sodium hydroxide solution will become ~39.9 (39.87) cm^3. This means 1.96 g of sodium hydroxide will be dissolved in ~39.9 cm^3 of water. The relative pressure of this solution is still 0.965 (Perry and Green 1997), as required.

A large solution reservoir could not be put in an NMR tube. Therefore, the samples studied by MRI were prepared in a vial, as described above. When studying the MRI experiment a small amount of solution was placed at the bottom of the NMR tube and a

pellet from the vial was transferred to the NMR tube. The solution in the NMR tube ensured the relative pressure remained constant throughout the MRI experiment. The set up of the NMR tube with a solution and the pellet will now be described in the next sub section.

4.2.4 Suspending the pellets above a solution in an NMR tube

After the sample had reached equilibrium it was transferred to an NMR tube and suspended over the same solution concentration. This process ensured that the established equilibrium between the adsorbed phase and vapour phase was maintained. Initially the pellet was supported above the solution by use of a small glass rod and a susceptibility plug, which is shown in Figure 4.2. However, this method was not appropriate because the solution wicked up the glass rod and contacted the pellet directly (see inset of Figure 4.2).

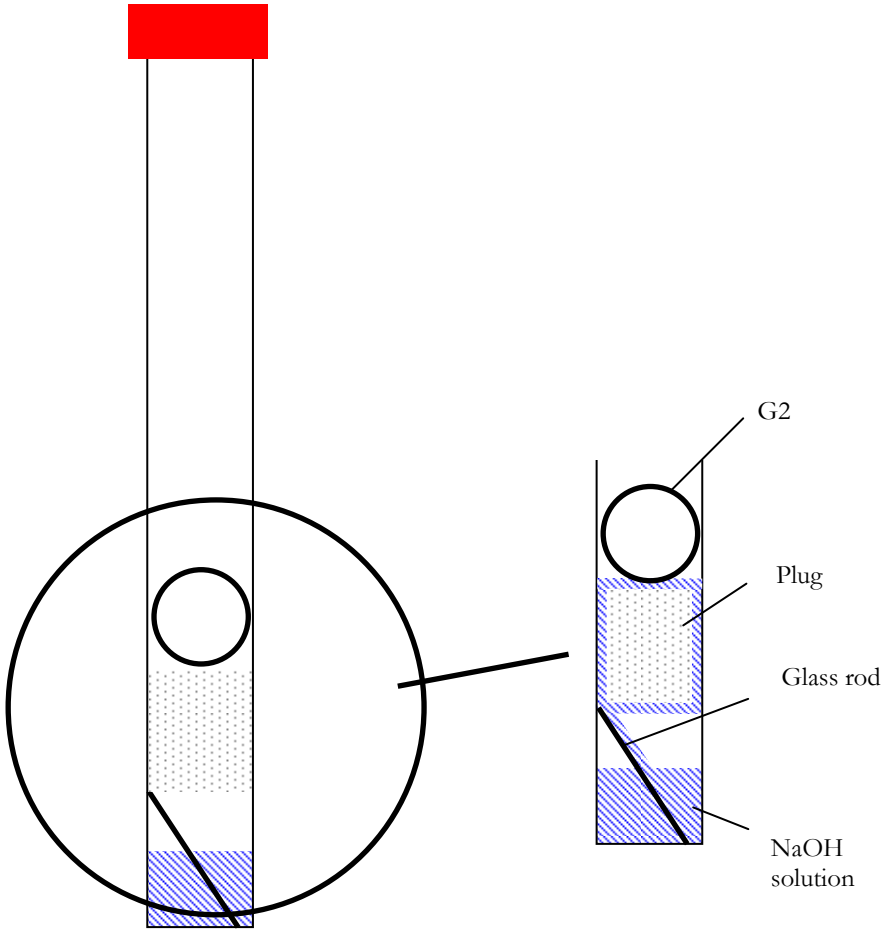

Figure 4.2: Suspending G2 above a solution in an NMR tube using a glass rod and a susceptilbility plug. The inset shows the wicking process

To resolve this problem, nylon wire was supported at the top of the NMR rube and the lower end of the wire was twisted to support the pellet above the solution (Figure 4.3).

This prevented any solution contacting the pellet directly. The NMR tube was then sealed with Parafilm to minimise vapour exchange with the atmosphere.

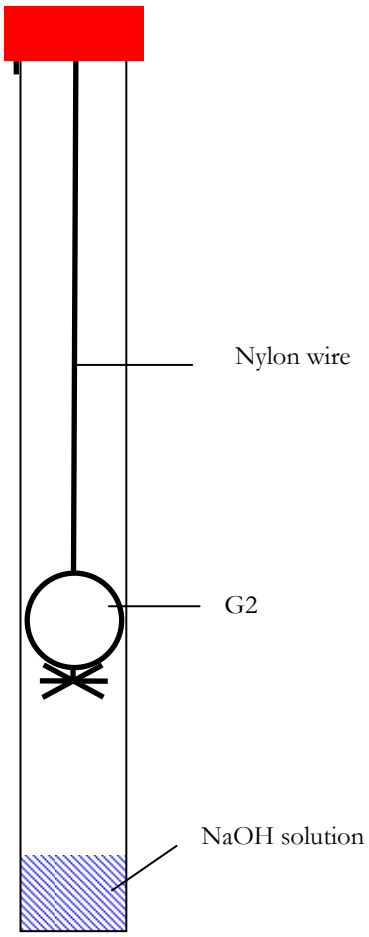

Figure 4.3: Suspending G2 above a solution in an NMR tube using nylon wire

4.2.5 Equilibration time

It was important the samples were suspended above the solutions for a period of time that was long enough for the system to reach equilibrium. To determine the equilibration time, 5 pellets were suspended over water using the set up in Figure 4.1. The mass of the pellets was checked everyday and after 5 days the mass remained constant. This suggested that the pellets had to at least be left for five days for the adsorbed water and gas phase water to reach equilibrium.

4.2.6 NMR phantom

To quantify the amount of water adsorbed in each experiment an NMR phantom was inserted into the NMR tube. A phantom is designed to act in the same way as the sample and if the same phantom is used in each experiment the signal intensities can be normalized using the phantom as a reference. This means each experiment at different

relative pressures can then be compared directly. For the experiments, a 10 wt.% H_2O in D_2O phantom, with copper sulfate added to achieve a $2.0x10^{-3}$ mol dm^{-3} concentration, was inserted into the NMR set up. A Cu(II) complex was added as it has an unpaired electron. The unpaired electron increases the T_1 relaxation time constant for the phantom mixture. The concentration of the phantom was determined by the process of trial and error to produce a T_1 relaxation time constant that was similar to that for the saturated pellet.

4.2.7 MRI sample set up

The 5 mm NMR tube (Figure 4.3) was transferred into a 10 mm birdcage resonator and a CPMG based pulse sequence used to accumulate the data (see Chapter 3). A voxel volume of 79x79x130 μm was achieved. MRI experiments were carried out on a Bruker AVANCE NMR System with static field strength of 7.05 T, yielding a resonance frequency of 300.05 MHz for ^1H nuclei. Temperature stability of ± 0.5 K was maintained throughout all data acquisitions. Transverse relaxation time (T_2) and spin density maps were acquired together using a multi slice multi echo sequence, and employed 90° selective and 180° non-selective pulses. A T_2 imaging sequence with an echo time of 4 ms was used. The number of scans used to ensure a sufficient signal to noise ratio was 600 and the swectral width was 149253 Hz; the acquisition time for one dataset was ~100 h. Data acquisition, initial data transformation, 2-dimensional data processing and workup was handled on an Aspect X32 workstation, running the Pararvision© suite of software (Bruker Analitische Messtechnik Gmbh, Karlsruhe, Germany). The in-plane pixel resolution was 79 μm and the slice thickness was 130 μm.

4.2.8 PFG NMR

PFG NMR experiments were carried out on a Bruker Avance 400 MHz spectrometer with a static field strength of 9.4 T yielding a resonance frequency of 400.13 MHz for ^1H nuclei. The samples were prepared as stated above for MRI and placed in 5 mm NMR tubes. The pulse sequence used was a stimulated echo with bipolar longitudinal eddy current delay (BPLED) (see Chapter 3). The values of δ and τ were 0.002 and 0.001 s and ⊿ was 0.05 or 0.1 s. 12 data points were taken at increasing gradient strengths between 0.674 and 32.030 Gcm^{-1}, and each point was obtained with 16 scans. This particular technique was chosen because, in this study, it is required to examine the spatial distribution of the condensate in regions where pore filling exceeds a thin film. As described by Ardelean and co-workers (2007), thin films with low T_2 values are likely to be invisible in pulsed gradient stimulated echo NMR experiments. The diffusion of water in an NMR tube was also

studied, which enabled the tortuosity values to be calculated.

4.3 Analysis of experimental data

Chapter 3 introduced equations which the raw NMR data in this Chapter will be fitted to. To aid the reader these equations are presented again and all the terms are defined.

The raw PFG-NMR data was fitted to:

$$\frac{I_{NMR}}{I_0} = \exp\left[- D_{PFG}\gamma^2 g^2 \delta^2 \left(\Delta - \frac{\delta}{3} - \frac{\tau}{2} \right) \right] \qquad 4.1$$

where I_{NMR} is the NMR signal intensity, I_0 is the echo intensity in the absence of the gradients, D_{PFG} is the diffusion coefficient, γ is the gyromagnetic ratio, g is the pulsed field gradient strength, δ is the duration of the pulsed gradient, Δ is the diffusion time and τ the correction time for the phasing and dephasing between bipolar gradients.

The measured tortuosity, τ_p, was obtained using:

$$\tau_p = \frac{D(T)}{D_{PFG}} \qquad 4.2$$

where $D(T)$ is the diffusion of bulk water at temperature , T.

The T_2 relaxometry data was fitted to:

$$I_{NMR}(2t_d) = I_0 \exp\left(\frac{-2t_d}{T_2} \right) \qquad 4.3$$

where $I_{NMR}(2t_d)$ is the NMR signal intensity at echo time, $2t_d$.

To process the MR images a Fortran program was used, which was supplied by Dr Sean Rigby. When a pellet was studied at progressively lower relative pressures the signal to noise ratio decreased. Therefore, to fit at least four echoes to equation 4.3, for all studied relative pressures, the odd echoes were used. To ensure fitting the odd or even echoes gave similar transverse relaxation time (T_2) images, the following procedure was carried out. Relaxation time images were calculated for the odd and even echoes separately for a slice

through G2 exposed to a relative pressure of water vapour of 0.980. The frequency histogram for voxels from the transverse relaxation time image calculated using the even echoes is shown in Appendix A1. The analogous histogram for the odd echoes is shown later in this Chapter in Figure 4.10 (c). It can be seen that the histograms of the transverse relaxation time images have very similar form when either the odd or even echoes are used. In addition, previous studies (Rigby *et al.* 2006) used the complete set of echoes. The form of their histogram was very similar to the histograms determined in this thesis when either the odd or even echoes were used. Pixels were only fitted providing their intensity was at least greater than the background noise. The background noise was calculated by averaging a square of pixels intensities (40 x 80), which were outside the region of the pellet. Appendix A2 shows a typical example of a random pixel from sample G2 (at relative pressure 0.965) fitted to equation 4.3 at varying echo times. Appendix A2 additionally shoes a typical log attenuation plot from sample G2 (at relative pressure 0.965).

The lower region of the water sorption isotherm (below relative pressure 0.90) was fitted to the fractal BET equation (equation 4.4) (Mahnke and Mögel 2003). Previous studies (Watt-Smith *et al.* 2005) have used the fractal BET equation to describe the multilayer region in G2 using nitrogen as the adsorbate. The equation in this study has been used only to approximate the amount of multilayer adsorption at relative pressures above ~0.90 (discussed below in the results section). The equation can be expressed by:

$$\log\left[V_{(P/P_0)}\right] = \log\left(V_m\right) + \log\left[\frac{C\left(P/P_0\right)}{1-\left(P/P_0\right)+C\left(P/P_0\right)}\right] - (3-d)\log\left[1-\left(P/P_0\right)\right] \quad 4.4$$

where d is the fractal dimension, V_m is the molar volume, $V_{(P/P0)}$ is the volume adsorbed as a function of P/P_0, P/P_0 is the relative pressure and C the BET constant. The fractal dimension is a structural parameter that quantifies the scaling invariance of self similar systems (Sing and Schüth 2002).

4.4 Results

4.4.1 Water adsorption and desorption isotherms

Figure 4.4 (a) shows the water adsorption and desorption isotherms for batch G2. It can be seen that uptake is very low until a relative pressure of ~0.95 when there is a marked increase in uptake, as capillary condensation commences. This is more clear in Figure 4.4 (b), which shows an enlarged area of Figure 4.4 (a) above relative pressure 0.8. The

adsorption curve is shown by the closed diamonds and the desorption curve by closed squares. The error bars were calculated by studying three batches of pellets and it was found that the amount adsorbed between the batches varied by 6 %. Therefore, the amount adsorbed will be quoted with an error of ±6%. The hysteresis loop is of type H2 (see Chapter 2) and the sharp knee in the desorption isotherm is characteristic of the pore blocking mechanism. Shown in Figure 4.4 (b) are the points on the adsorption isotherm that were studied by MRI.

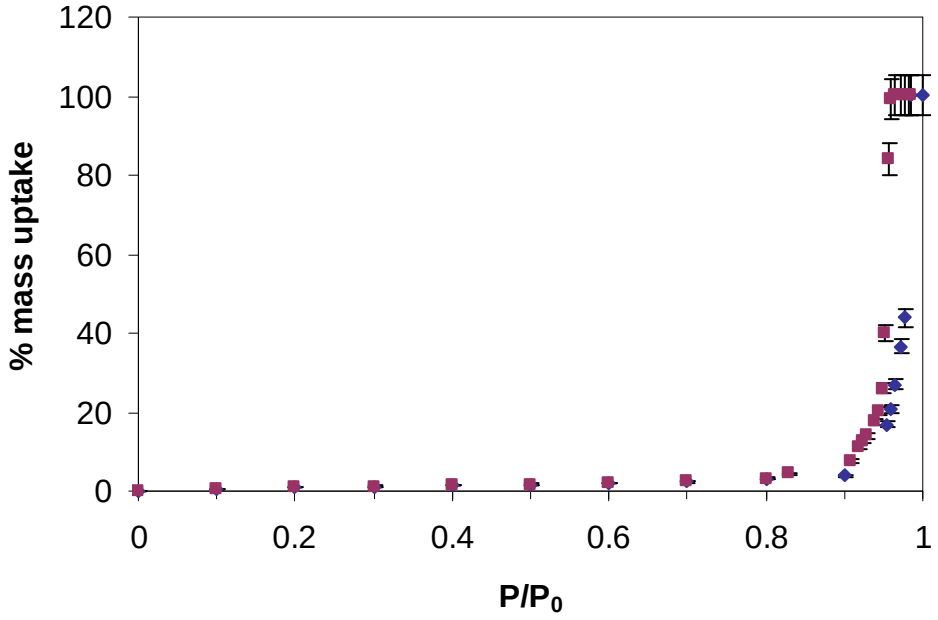

Figure 4.4 (a): Water sorption isotherm for sample G2. Adsorption is shown by closed diamonds and desorption by closed squares

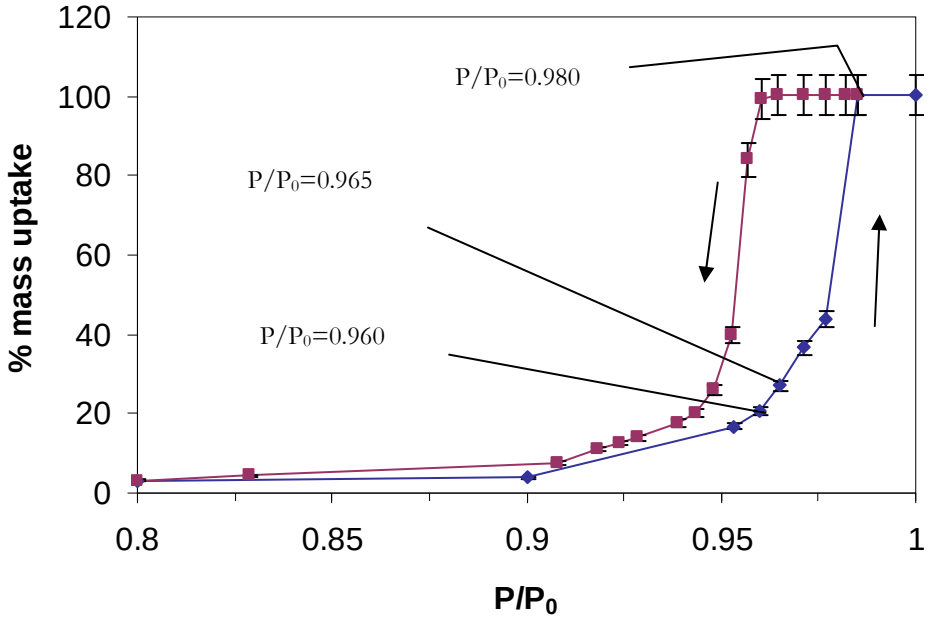

Figure 4.4 (b): An enlarged area of Figure 4.4 (a). Arrows have been added to indicate the direction of the change in pressure. Closed diamonds show the adsorption curve, closed squares show the desorption curve and the line has been added to guide the eye

Figure 4.5 shows a fit of the data in the relative pressure range 0.10-0.90 to the fractal BET isotherm equation (equation 4.4) using the Solver function in Excel. The BET constant was 4.3 and the monolayer capacity obtained was 1.56 % mass uptake, and this value is used below to relate the volume adsorbed from MR images and the gas adsorption isotherm. Also shown in Figure 4.5 is an extrapolation of the fitted fractal BET model to higher relative pressures.

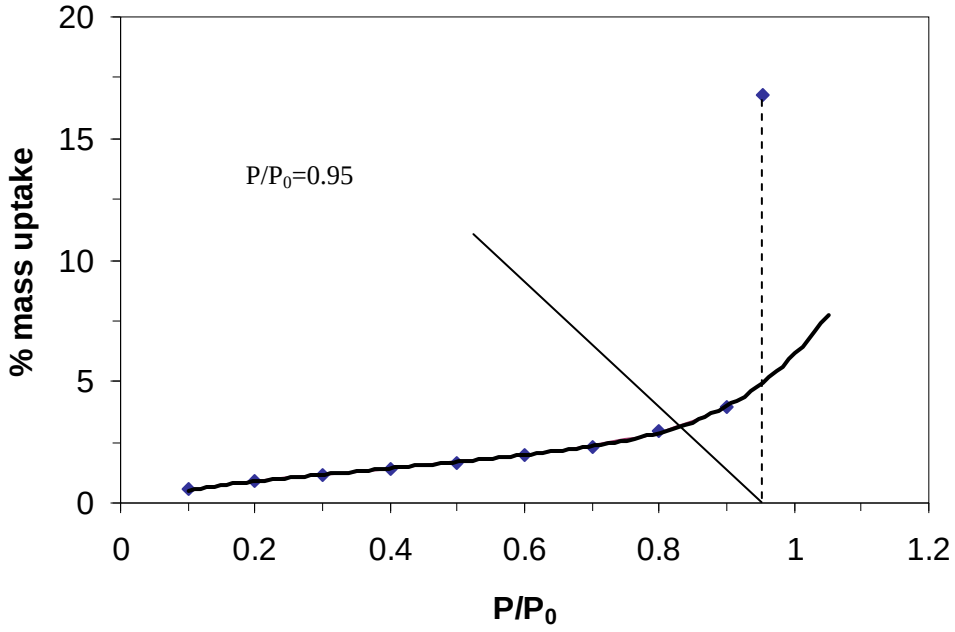

Figure 4.5: Water adsorption isotherm to % mass uptake 20 (closed diamonds). Equation 4.4 has been fitted to the data points below relative pressure 0.9 (fixed line) and the fit has been extrapolated to higher relative pressures

It can be seen that there is a significant deviation from the fractal BET model at relative pressure of 0.95, which suggests capillary condensation has started at this point.

4.4.2 MRI studies of water adsorption and comparing them to the water adsorption isotherm

Figures 4.6-4.8 show the data derived from porosity and transverse relaxation time images for arbitrary equatorial slices through a single pellet sample from batch G2 during equilibrium water adsorption at relative pressures of 0.960, 0.965, and 0.980, respectively.

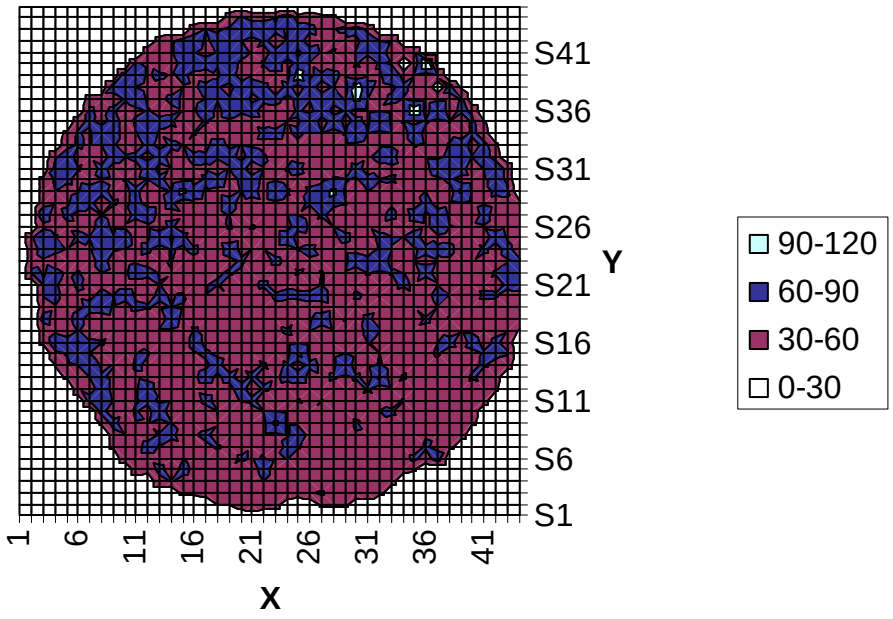

Figure 4.6 (a): Transverse relaxation time (T_2/ms) image for an arbitrary slice through a pellet from batch G2 exposed to a relative pressure of water vapour of 0.980

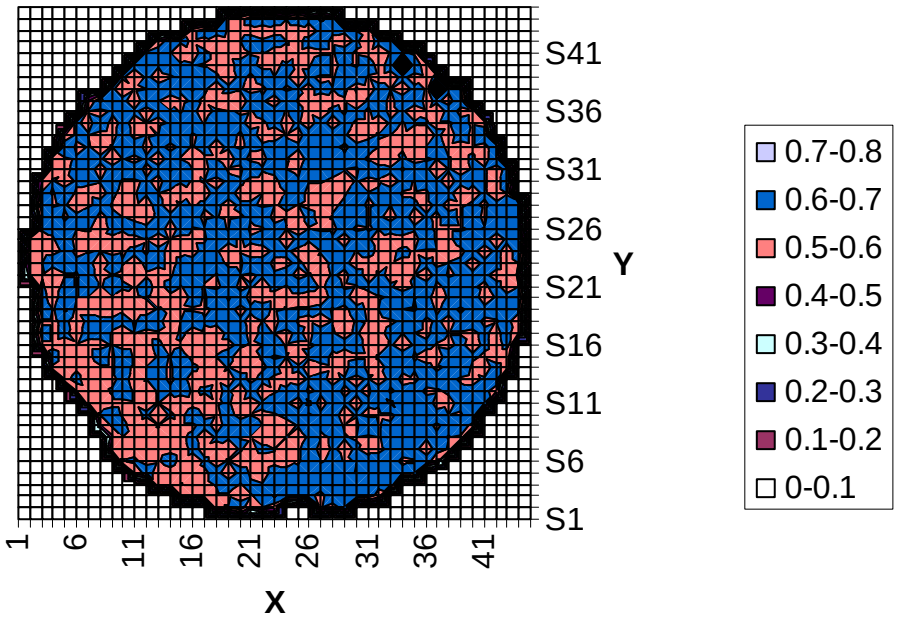

Figure 4.6 (b): Spin density image for an arbitrary slice through a pellet from batch G2 exposed to a relative pressure of water vapour of 0.980. The spin density is given as the fraction of sample volume occupied by water

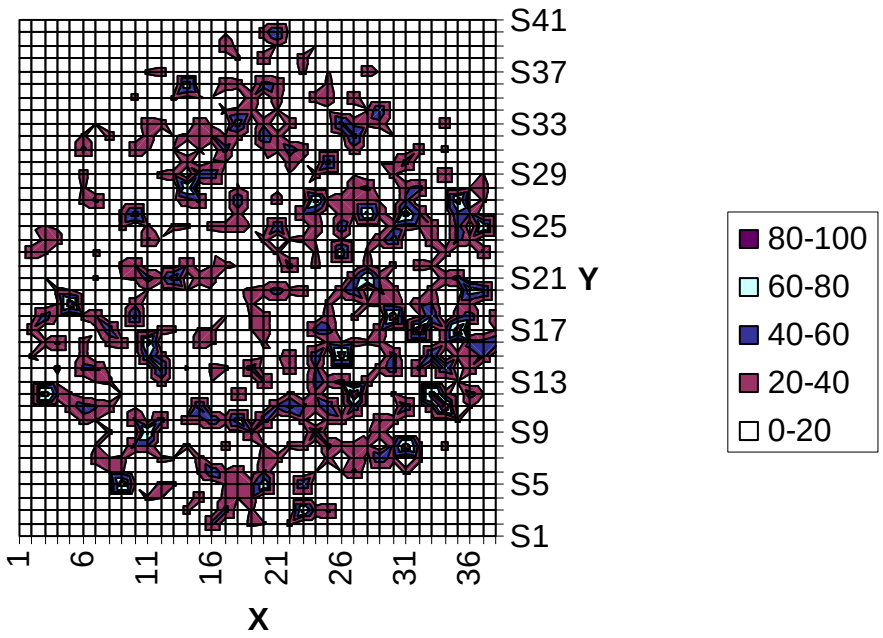

Figure 4.7 (a): Transverse relaxation time (T_2/ms) image for an arbitrary slice through a pellet from batch G2 exposed to a relative pressure of water vapour of 0.965

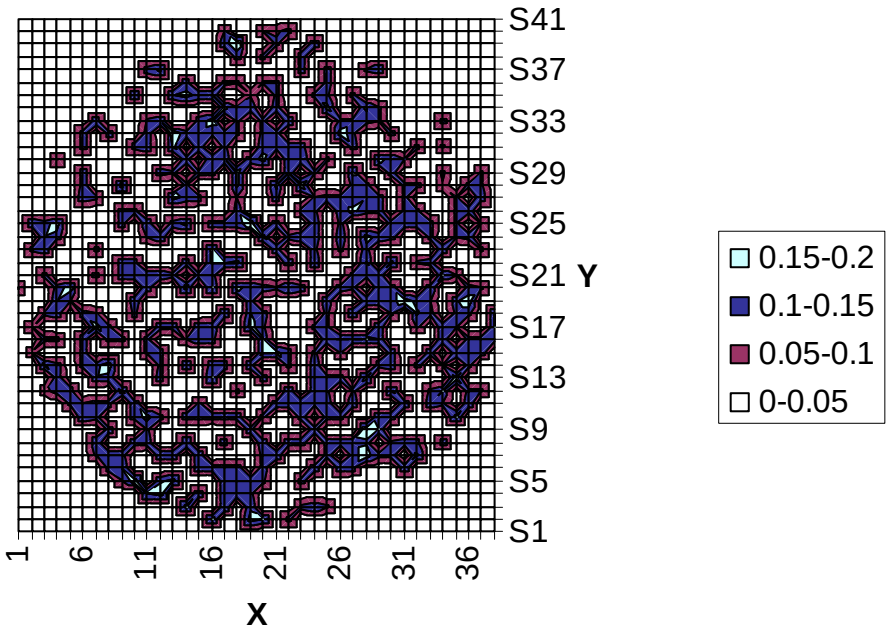

Figure 4.7 (b): Spin density image for an arbitrary slice through a pellet from batch G2 exposed to a relative pressure of water vapour of 0.965. The spin density is given as the fraction of sample volume occupied by water

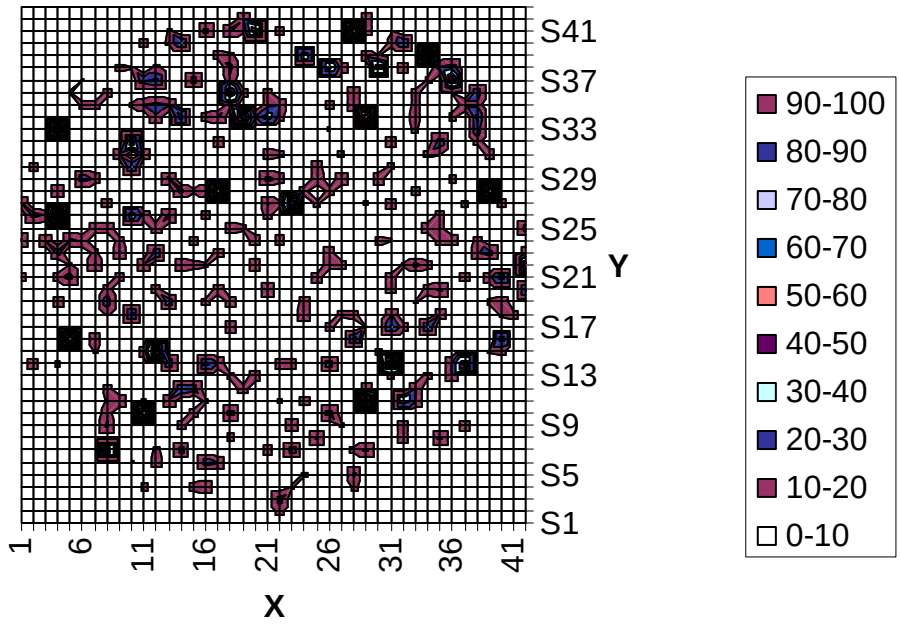

Figure 4.8 (a): Transverse relaxation time (T_2/ms) image for an arbitrary slice through a pellet from batch G2 exposed to a relative pressure of water vapour of 0.965

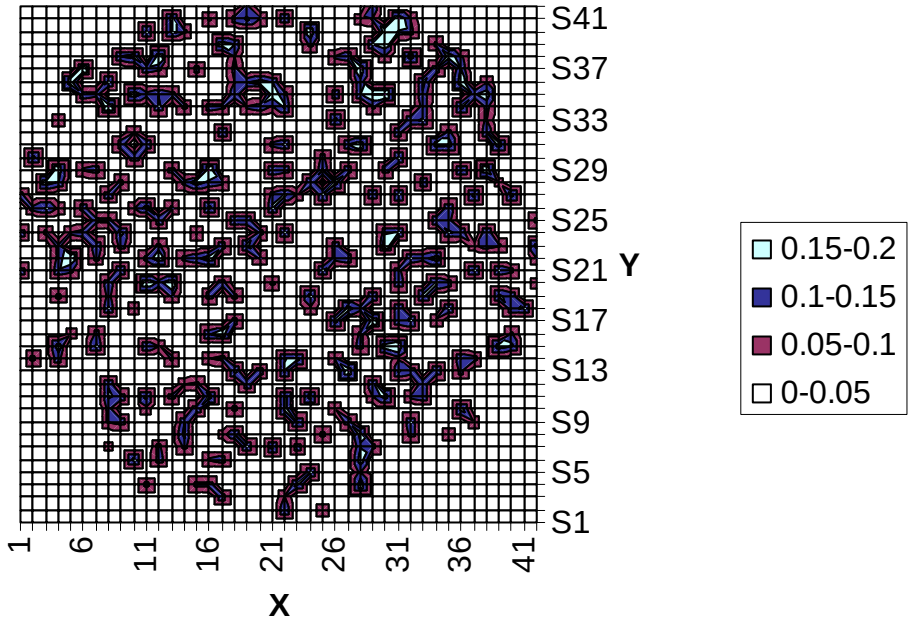

Figure 4.8 (b): Spin density image for an arbitrary slice through a pellet from batch G2 exposed to a relative pressure of water vapour of 0.96. The spin density is given as the fraction of sample volume occupied by water

Due to the short relaxation time of molecules confined to liquid layers nearest the pore wall, regions of the pellet containing just multilayer adsorption will be invisible to MRI with the echo times that are possible to use. Further, as explained in earlier studies (Hollewand and Gladden 1995), even for regions of the void space that are pore-filled, some of the water in layers near the pore wall will be 'invisible' to NMR. The invisible fraction is due to

spins in water which is bound, or close, to the pore surface, that are not averaged over the pore volume by diffusion during the echo time. These are likely to be molecules in the earliest layers of water next to the surface, and are thus present from the very lowest pressure points of the isotherm. This 'invisible' fraction can be determined by comparing the overall average voidage fraction determined from a calibrated spin density image of a fully saturated pellet with the voidage fraction determined in previous studies using mercury pyncnometry (Watt-Smith 2006). For G2 the discrepancy between the MR image at relative pressure 0.980 and from mercury pyncnometry was found to be 0.10±0.02, which is similar to the corresponding value found in earlier MR imaging studies of catalyst support pellets (Hollewand and Gladden 1993 and 1995). Since the typical pore size of G2 is 30 nm, and the thickness of one layer of adsorbed water is ~0.3 nm (D'Orazio 1990), then, averaged over the whole void space, the 10% invisible fraction (Hollewand and Gladden 1993) corresponds to ~2.6 layers of adsorbed water. This is explained using Figure 4.9. Assuming G2 is made up of one pore, if its radius is 15 nm (pore size 30 nm) and the total pore volume is 1 cm^3g^{-1}, the length of the pore can be calculated using the volume of a cylinder equation. By assuming that 10 % of the volume is 'invisible' to MRI (Hollewand and Gladden 1993), this means that MRI would calculate the pore volume to be only 0.9 cm^3g^{-1}. From the calculated pore length (above) and assuming the pore volume detected by MRI is 0.9 cm^3g^{-1}, the radius of the volume of detectable liquid is ~14.2 nm. This means that a layer of water at the pore surface of width ~0.8 nm is not detectable by NMR. This thickness (~0.8 nm) corresponds to ~2.6 layers of water.

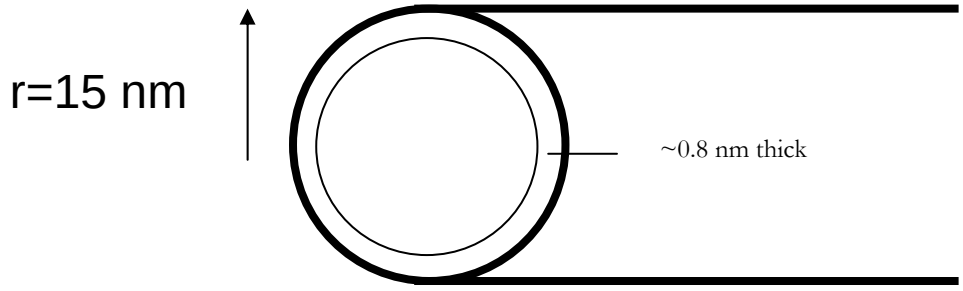

Figure 4.9: Schematic of a 15 nm radius pore showing a thickness layer of ~0.8 nm. The thickness is explained in the text

From the extrapolated multilayer isotherm in Figure 4.5, at relative pressures of 0.960 and 0.965 the amount adsorbed is 5.9 and 6.3 % mass uptake, respectively. This means the multilayer thickness was ~3.8 and ~4 monolayers, respectively, which is very thin, and thus these would be invisible to MRI. To calculate the % mass uptake from the images it will be assumed that a voidage fraction of 0.1 corresponds to 2.6 monolayers for the above

reasons. Hence, from the fitted fractal BET isotherm the voidage fraction occupied in pixels just with multilayer adsorption can be calculated by ratio. For example for relative pressure 0.965 the voidage is ~0.15 (0.1x4/2.6). All of this liquid is considered 'invisible' to MRI. In addition, it was assumed that a voidage fraction of 0.1 occupied by water is invisible to MRI in each pixel that had some visible water, and so this was added to these pixels. Using these assumptions, the average voidage fraction was calculated for the images at relative pressures of 0.960 and 0.965. The % mass uptake from the MR spin density image data could then be determined as 23.6 ± (1.0) % (at relative pressure 0.960) and 25.7 ± (1.1) % (at relative pressure 0.965) of the pore-filled value. The quoted error allows for experimental uncertainty in the void fraction, which was 2.9 % (Watt-Smith 2006) (see Appendix A4 for error calculations). The corresponding values from the water adsorption isotherm (Figure 4.4) are 20.7 ± (1.2) % and 27.0 ± (1.6) %, respectively. Hence, the values estimated from the MRI data are consistent with the water isotherm data.

Figures 4.10 (a)-(c) show the histograms of pixel transverse relaxation times for the pellet slices shown in Figures 4.6-4.8. From the histograms it can be seen that, at a given vapour pressure, the main part of the number distribution of relaxation times consists of a rough bell-shape, but at the lower two relative pressures there is also a long tail of higher relaxation times. At relative pressures of 0.960 and 0.965 the high-end tails consisted of relaxation times in excess of 40 and 50 ms, respectively. As the vapour pressure of water increases, the modal peak of the distribution shifts to larger values of relaxation time and values in the high-end tail increase in frequency. At the highest relative pressure (0.980), the lowest values of relaxation time that were present in the distributions for the lower pressures are absent and the modal peak is sited in the range of values of relaxation time previously making up the high-end tails.

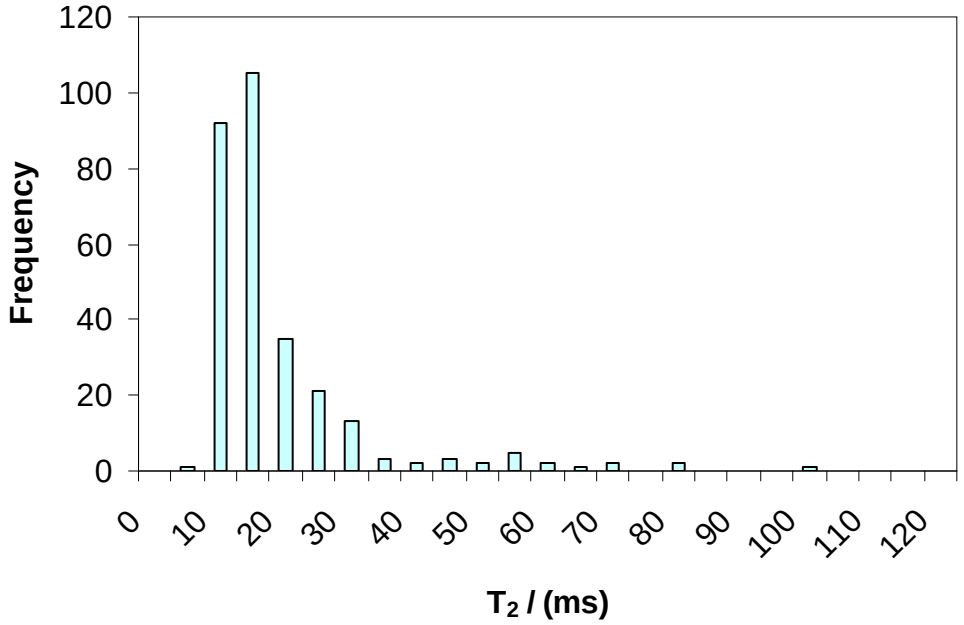

Figure 4.10 (a): Frequency histogram for voxels from the transverse relaxation time (T_2/ms) image obtained of an arbitrary slice through a pellet from batch G2 exposed to a relative pressure of water vapour of 0.960

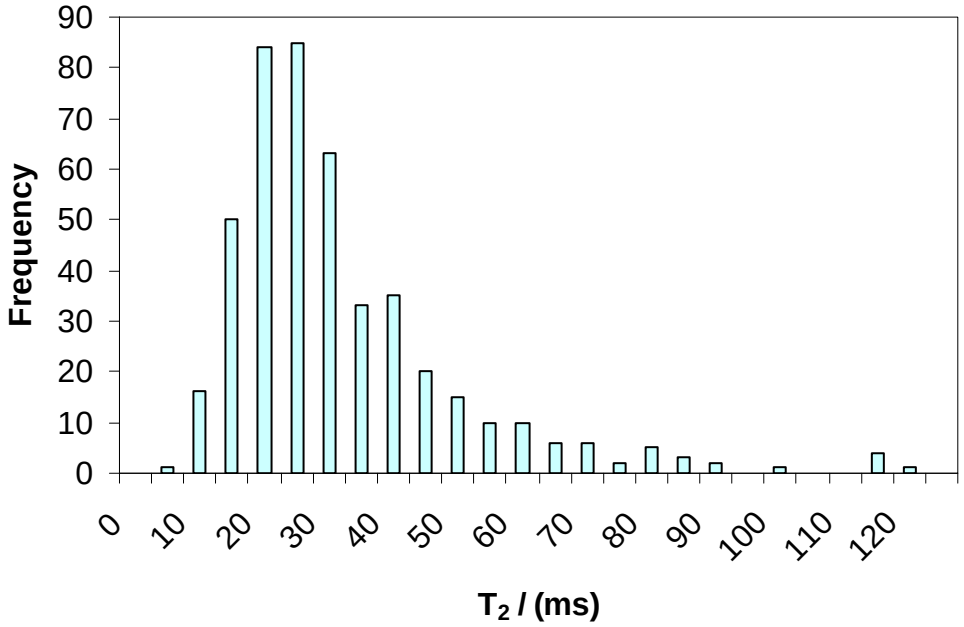

Figure 4.10 (b): Frequency histogram for voxels from the transverse relaxation time (T_2/ms) image obtained of an arbitrary slice through a pellet from batch G2 exposed to a relative pressure of water vapour of 0.965

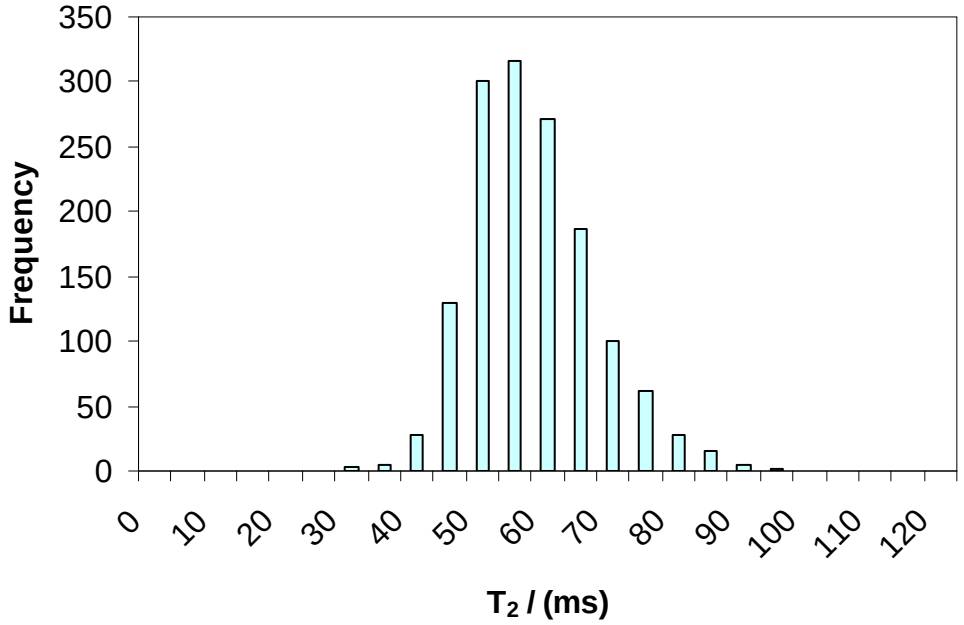

Figure 4.10 (c): Frequency histogram for voxels from the transverse relaxation time (T_2/ms) image obtained of an arbitrary slice through a pellet from batch G2 exposed to a relative pressure of water vapour of 0.980

The images themselves have been used to determine the spatial characteristics of the adsorption process. In the images each pixel has 8 nearest neighbours, including diagonal directions. For relative pressures below 0.980, image pixels containing adsorbed water tended to occur in clusters of other occupied nearest neighbour pixels, separated from other clusters by a continuous sea of unoccupied pixels. The relaxation time for liquid in the surface layers of any adsorbed thin film is so short that the liquid is invisible in MRI. Cluster sizes ranged from single isolated pixels upwards. From a consideration of the values of relaxation time amongst the particular nearest neighbours of each pixel, within its own cluster, it has been found that pixels from the high-end tail of the number distributions are statistically unlikely to be entirely segregated from pixels with values from the main (bell-shaped) body of the distribution. For example, in the transverse relaxation time image obtained at a relative pressure of 0.965, no pixel with a value from the high-end tail of the number distribution was a member of a contiguous cluster within which there were absolutely no pixels with relaxation times from the main body of the number distribution. However, for pixels with transverse relaxation times from the main body of the number distribution 3.1% were totally isolated. This value suggested that the corresponding result for the tail was less than the fraction that might otherwise be anticipated by chance alone. Hence, voxels in the tail are more likely to have an association with a voxel with a T_2 from the peak in the distribution than chance would suggest. This is expected if the voxels in the tails fill by an advanced adsorption mechanism. Shown in

Figure 4.11 is a schematic of a slice through a partially filled pellet. The slice is made up of model ink bottle pores and each neck or body is equivalent to a pixel in an MR image. The T_2 values for the neck would appear in the main (bell-shaped) body of the distribution while the large pore bodies would appear in the high-end tail of the distribution. In the schematic, all the necks and some pore bodies in the ink bottle pores have been filled with condensed gas. There is not an ink bottle pore where the body has become filled with condensed gas but the outer necks are empty. This is because the large pore bodies fill by the advanced adsorption mechanism and require at least one of the outer necks that it is connected to be filled with condensed gas. In addition, experimentally in Figure 4.8 (image at relative pressure 0.960) it was found that a high end tail T_2 (~100 ms) was connected to a T_2 in the main tail with a value of ~20 ms.

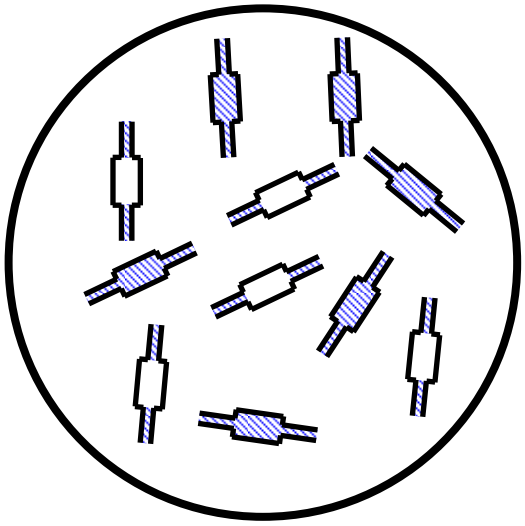

Figure 4.11: Schematic of a slice through a partially filled pellet showing ink bottle type pore models. The shading indicates a capillary filled pore

The spatial distributions of occupied pixels in the MR images have been compared with the random Poisson model. The area of each MR image occupied by the pellet was divided up into squares of size 4×4 pixels, ignoring squares which bridged the pellet boundary and beyond. The number of pixels occupied by condensate in each square was counted. The observed distribution in square occupancy thus obtained was compared with that expected for a Poisson model with the same overall average occupancy rate. Before the results of this study are presented, the Poisson model will first be described and an example used to aid the reader. If the number of filled pixels is, N, that are in any region of area, A, they are said to be randomly dispersed if (Open University 2004):

$$s^2 = \bar{x} \qquad 4.5$$

where s^2 is the sample variance and $\bar{x}$ is the sample mean. The sample mean, $\bar{x}$, can be calculated by (Open University 2004):

$$\bar{x} = \frac{N}{k} \tag{4.6}$$

where N is the total number of pixels filled with condensate and k is the number of squares that the MR image has been divided into. The sample variance, s^2, can be calculated by (Open University 2004):

$$s^2 = \frac{1}{(k-1)}\left(\sum_{i=1}^{k} x_i^2 - \frac{\left(\sum_{i=1}^{k} x_i \right)^2}{k} \right) \tag{4.7}$$

where x_i is the number of filled pixels in square i.

As the MR images in this Chapter are large, it is difficult to demonstrate the test for the reader. Therefore, a smaller sized example is schematically shown in Figure 4.12, which is a large square occupied by 10 dots (N=10). The large square has been divided into 4 smaller squares of equal size (k=4). This is equivalent to the MR images as they were divided into smaller squares (described above) and the filled pixels in the MR images are analogous to the dots in Figure 4.12. Each small square has been labeled i=1-4 in Figure 4.12. The mean, $\bar{x}$, for Figure 4.12 is 2.5 (10/4), which means there is on average 2.5 dots per small square. Table 4.1 summarises the calculations necessary to determine the variance.

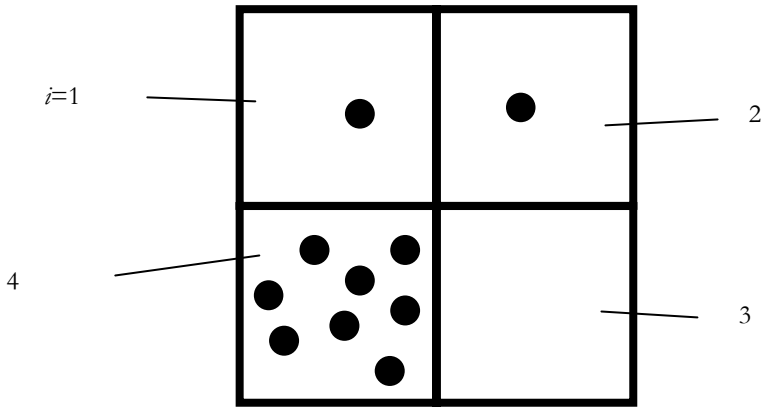

Figure 4.12: Large square filled with dots is split into 4 smaller squares, *i*

i	x_i	x_i^2
1	1	1
2	1	1
3	0	0
4	8	64
	$\Sigma\, x_i = 10$	$\Sigma\, x_i^2 = 66$
	$(\Sigma\, x_i)^2 = 100$	

Table 4.1: Example calculations to calculate the variance in Figure 4.12

Using equation 4.7 the variance is calculated to be 13.7. As the variance does not equal the mean, this suggests that the distribution of dots is non random.

The non random distribution of the dots in Figure 4.12 may have happened by chance and this needs to be ruled out. The chi squared, χ^2, statistic can be used to test whether the pattern of the distributed dots is really non random. The χ^2 statistic can be expressed by (Open University 2004):

$$\kappa^2 = \frac{k}{N}\left(\sum_{i=1}^{k} x_i^2 - \frac{\left(\sum_{i=1}^{k} x_i\right)^2}{k}\right) \qquad 4.8$$

The null hypothesis in the Poisson model is that the distribution of the dots is random. Substituting the values discussed above into equation 4.8, the χ^2 statistic is found to be 16.4. Taking the level of test to be 0.05, the critical region of the test is if χ^2 is less than (or equal to) 0.216 or greater than (or equal to) 9.348 (Open University 2004). The calculated χ^2 is outside this range, which means the probability of Figure 4.12 occurring by chance is

less than 0.05. Therefore, it can be said that the distribution of the dots in Figure 4.12 is non random and this result is statistically significant in a χ^2 test ($p<0.05$). This exact method was used to determine whether the filled pixels in Figures 4.7 (a) and 4.8 (a), which are the T_2 images for the pellet exposed to relative pressures 0.960 and 0.965, were randomly distributed. For both Figures the distribution of the filled pixels was found to be non random and this was statistically significant in a χ^2 test ($p<0.05$). This study indicates that the filled pixels are clustered together instead of being randomly distributed across the pellet. By visual inspection of the MR images this can be seen.

4.4.3 PFG NMR studies of water adsorption

The PFG NMR obtained for the partially saturated samples gave rise to log-attenuation plots that were closely approaching a linear form and were thus fitted to single component diffusion models (see Appendix A2). Table 4.2 shows the variation of tortuosity (for two diffusion times, ⊿) with relative pressure. It can be seen that, at any given relative pressure, the tortuosities obtained at the two different diffusion times, differing by a factor of two, are insignificantly different from each other. This suggests that diffusion is not completely restricted, since, if it were, the apparent tortuosity would be expected to double (or at least substantially increase) as diffusion time is doubled. This suggests that the adsorbed regions of water are continuous over at least the length-scales of the order of the rms displacement of the water molecules (>~10μm). This is consistent with the imaging data that suggests that connected clusters of occupied voxels extend over length scales approaching the order of the size of the pellet. It can also be seen that as the relative pressure is varied from 0.953 to 0.980, corresponding to the region of the steep increase in mass uptake, the tortuosity first increases as far as a relative pressure of ~0.965, and then decreases again.

	Relative pressure					
⊿/s	**0.953**	**0.960**	**0.965**	**0.971**	**0.977**	**0.980**
0.05	1.70	1.98	2.14	2.11	1.96	1.44
0.10	1.77	1.98	2.16	2.13	2.00	1.45

Table 4.2: Average tortuosity values, for self-diffusivity of water within pellets from batch G2, obtained at different relative pressures and diffusion times, ⊿, using PFG NMR

4.5 Discussion

The BET constant obtained from the fit of the water adsorption isotherm to the fractal BET model is 4.3, suggesting that water has only a relatively weak interaction with the

surface of G2 at the temperature the isotherm was carried out (Gregg and Sing 1982). In addition, the MRI data presented above suggests that cooperative adsorption effects can take place between neighbouring pores that differ in size by a factor of 5, and not just the upper limit of 2 suggested by the Kelvin equation (see Chapter 2), when the adsorbate-adsorbent interactions are relatively weak. The statistical analysis of the MR images suggested a non random spatial distribution of condensed phase, as might be expected if advanced adsorption were occurring. This is because if a pore fills, the condensed gas can propagate into neighbouring pores by the advanced adsorption mechanism. It would then be expected that large clusters of adsorbed water would form.

Moving to the PFG NMR data, Naumov *et al.* (2008) have studied the adsorbed phase using PFG NMR during cyclohexane adsorption on Vycor porous glass. They observed a variation in the diffusivity of cyclohexane as the adsorbed amount was increased. It was found that the diffusivity went through a maximum. They attributed this pattern to the presence of three different phases within the sample with different diffusivities that contribute to the measured average diffusivity. First, a slow diffusion contribution from fluid in close contact with the pore walls which makes its largest fractional contribution to the average diffusivity at low pressures. A second fast diffusion contribution comes from the gas-like fluid at the centre of the pores away from the pore walls, making its largest fractional contribution to the average diffusivity over an intermediate range of pressure. Finally, a slow diffusion contribution from fluid in liquid-like states at the centre of pores that makes its contribution at higher pressure. In contrast, for adsorption of water studied here, there is a variation in observed average diffusivity with a minimum (corresponding to a maximum in tortuosity in Table 4.2) at intermediate relative pressures in the range covered. In Table 4.2, the values of tortuosity measured at relative pressures below that required for complete pore filling all exceed that at complete pore filling. Maxwell (cited in Crank) showed that in a two (diffusion) phase system consisting of a suspension of spheres of one phase, *a* (e.g. water), so sparsely distributed in a continuum of the second phase, *b* (vapour), such that any interaction between them is negligible (i.e water is not contiguous), the effective diffusion coefficient of the composite medium, D_{η}, can be written in the form:

$$\frac{D_w - D_b}{D_w + 2D_b} = \nu_a \frac{D_a - D_b}{D_a + 2D_b} \qquad 4.9$$

where υ_a is the volume fraction of the dispersed phase. The coefficient D_{η} is the diffusion coefficient of a hypothetical homogeneous medium exhibiting the same steady-state

behaviour as the two-phase composite. Equation 4.9 would suggest that, if significant exchange was occurring between condensed liquid and vapour, the observed diffusivity would be significantly higher than the purely liquid phase diffusivity at pore filling. However, as seen in Table 4.2, the diffusivity at partial pore filling remains below that at complete pore filling (tortuosity is greater than one). This suggests that the vapour phase is not making any significant contribution to the observed diffusivity (and thus tortuosity), since, otherwise, it would be expected that diffusion would be enhanced relative to solely liquid-phase diffusion. This suggests that the observed variation in tortuosity in Table 4.2 is due to variations in the average tortuosity of the regions making up the void space occupied by liquid at different relative pressures. Given that the MR images suggest that the distribution of condensed water is highly heterogeneous (correlated), and clusters of occupied pixels are macroscopic in dimension, then it seems likely that the area for liquid-vapour exchange is relatively low, and this is why there is no significant contribution of gas phase mass transport to the observed diffusivities.

As noted above, at the highest relative pressure (0.980) imaged, the lowest values of relaxation time present in the distributions for the lower pressures are absent and the modal peak is sited in the range of values of relaxation time previously making up the high-end tails. The lack of the lower values of T_2 in the frequency histograms for higher relative pressure suggest that these values must correspond to partially-filled pores, since, if they had corresponded to completely-filled smaller pores they would still be present in the distribution for images obtained at complete pore filling. However, the lack of restricted diffusion in the corresponding PFG NMR suggests that the water ganglia in the partially filled pores does not occur in isolated blobs of lateral spatial extents less than ~10 μm. Previous findings by Valiullin *et al.* (1997) suggest that the quite linear form of the log-attenuation plots for the PFG NMR data found here (Appendix A2) suggest that diffusion components are not experiencing significant exchange with vapour phase regions. The above findings are thus consistent with the condensed phase, at lower relative pressures, existing as a highly thickened surface layer, with relatively little void space left at the centre of the pores. A progressive thickening of this layer would be consistent with the migration of the modal peak in the distribution of image T_2 values towards higher values. At a relative pressure of 0.960 the modal peak in values of T_2 occurred at ~20-25 ms, while at pore-filling the modal peak occurred at ~60 ms. If values of T_2 of ~20-25 ms at a relative pressure of 0.960 corresponded to the characteristic size of the film (its thickness), and the values of T_2 of ~60 ms at pore-filling correspond to the typical size of a pore, then the relative sizes of these values suggests a thick film of at least ~1/3 of the pore size at a

relative pressure of 0.960. In contrast, the long tail of highest values of T_2 in the frequency histograms, present even at relative pressures of 0.960, included even some voxels with the maximum values of T_2 present in the frequency histogram for the images of the completely saturated (and thus certainly pore-filled) pellet. This suggests that the largest pores containing condensed phase become completely pore-filled at lower pressure than the smaller pores, and thus there is potentially a filling mechanism dependent on pore size or configuration.

Previous work (Grünberg *et al.* 2004; Vyalikh *et al.* 2007) using ^{1}H solid-state NMR to study hydrogen bonding of water confined in MCM-41, SBA-15 and CPG has suggested two different pore filling mechanisms in water adsorption. Grünberg *et al.* (2004) suggested that the mechanism of pore-filling in SBA-15 involved, after initial coverage of the surface, a radial growth in the surface film towards the pore axis. However, for MCM-41 the proposed mechanism of pore-filling involved initial wetting of the surface, then a coexistence of filled pores, or pore segments, with wetted pores, or pore segments, and then further filling occurs as a growth of the filled pores involving an axial filling of the pores. Grünberg *et al.* (2004) suggested that the difference in pore-filling mechanism arose because of the difference in pore sizes between SBA-15 and MCM-41. Subsequently, Vyalikh *et al.* (2007) suggested, based upon ^{1}H-MAS solid state NMR data, that pore filling during the adsorption of water in CPG also occurs by radial growth towards the pore axis. For G2, the migration of the position of the modal peak in the T_2 distribution towards higher values with increased relative pressure suggests that the pore-filling mechanism for G2 is similar to that for SBA-15 and CPG. However, contrary to earlier work (Grünberg *et al.* 2004; Vyalikh *et al.* 2007), for G2 it is the largest pores, rather than the smallest, that have a filling mechanism that is similar to MCM-41. Studies of the pore structure of SBA-15 suggest that it possesses features such as mesoporous connectivity, pore corrugations, hairpin bends, and microporous walls that (at least some) may be shared with CPG but not by MCM-41 (at least not to the same degree). Hence, the differences in filling mechanism observed between SBA-15 and CPG on the one hand, and MCM-41 on the other may be due to other differences between these porous solids besides, or in addition to, pore size.

4.6 Conclusions

This work has shown that the knowledge of the particular spatial connection of pores of different sizes provided by spatially-resolved techniques, like MRI, is essential for

understanding the advanced adsorption processes. MRI data has shown that advanced adsorption effects can happen in neighbouring pores that differ in size by a factor of 5, rather than just up to a factor of 2 as suggested by the Kelvin equation. The variation in the distribution function of T_2 taken from the image data with relative pressure suggests that water adsorption occurs in pores of intermediate and smaller sizes by progressive thickening of an adsorbed film. PFG NMR data has shown that this thick adsorbed film has an extensive lateral spatial extent, and thus adsorption does not occur in isolated pores.

The Chapter to follow will use an integrated gas-mercury-gas experiment to determine the capillary condensation mechanism.

Chapter 5

Determining whether pores fill by cylindrical or hemispherical type menisci using an integrated gas-mercury-gas experiment

5.1 Introduction

Chapter 2 introduced the reader to the concept of advanced adsorption where a pore fills by a hemispherical meniscus instead of a cylindrical meniscus. This Chapter will now introduce an experimental test to determine whether pores fill by hemispherical or cylindrical shaped menisci. As discussed in the previous Chapters, this is important as there is, for example using the Kelvin equation, a factor of 2 error in the predicted pore size compared to the actual pore size if the wrong meniscus geometry is chosen. Currently there are no methods to determine what shape meniscus geometry should be used in advance.

To determine the meniscus geometry in a set of pores, Chapter 5 will combine a nitrogen gas sorption experiment with a mercury porosimetry experiment. This experiment has been termed an integrated gas-mercury-gas experiment (Rigby *et al.* 2008) and is explained as follows using Figure 5.1. Firstly a clean sample (position 1) is studied by a gas sorption experiment, where the gas adsorbs into all accessible pores (position 2). After the gas sorption experiment, the adsorbate is removed from the sample (position 3) and a mercury porosimetry experiment is studied by first intruding mercury into the sample (position 4). When the mercury is extruded, some may become entrapped in the porous material (position 5). Finally a second gas sorption experiment is then studied, with the mercury entrapped in the sample (position 6). By subtracting position 6 from position 2, the adsorption and desorption process in the pores which entrap mercury, can be deconvolved from all the other pores.

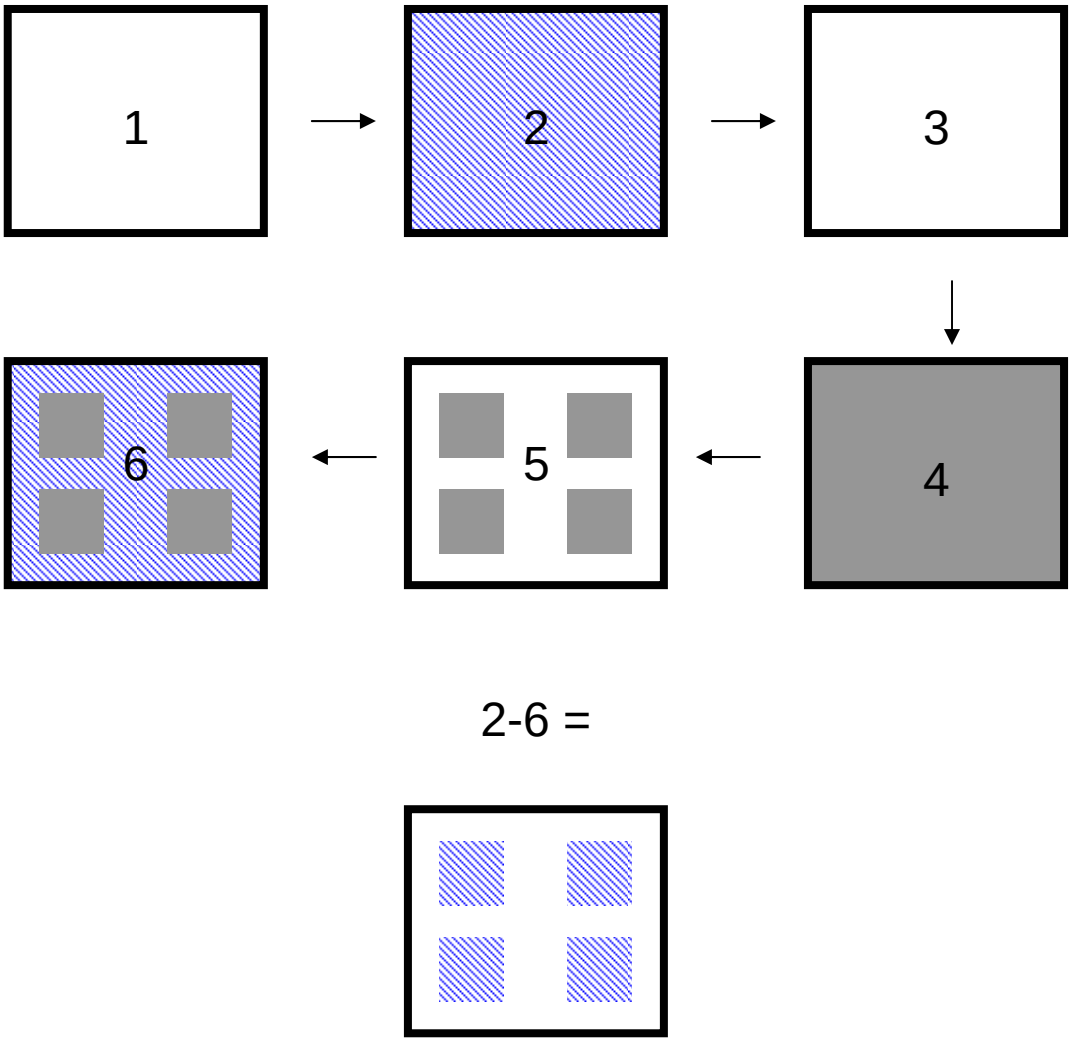

Figure 5.1: Schematic of the integrated gas-mercury-gas experiment. The shading is the adsorbed gas and the grey is mercury

This Chapter will use the difference between the gas sorption experiments, before and after mercury porosimetry, to calculate the size of pores that entrap mercury. In addition, mercury porosimetry experiment results will be analysed to determine which pores entrap mercury. The calculated pore sizes from each method will then be compared to determine the meniscus geometry in the gas sorption experiment.

5.2 Previous studies using the integrated gas-mercury-gas experiment

The integrated gas-mercury-gas experiment has been used by Rigby and co-workers in a select number of publications (Rigby *et al.* 2004a; Rigby and Fletcher 2004; Rigby *et al.* 2004b; Rigby *et al.* 2008; Rigby and Chigada 2009). The experiment has been used to show both pore blocking effects and advanced adsorption and is discussed in detail below.

Early work using the integrated experiments in series has shown pore blocking to exist in pellets from batch G1 (Rigby and Fletcher 2004). G1 is a sol gel silica sphere with a modal pore size of 10 nm. The study compared the gas sorption isotherms before and after mercury porosimetry and it was found that the isotherms overlaid below ~600 $cm^3(STP)g^{-1}$. At ~600 $cm^3(STP)g^{-1}$ the isotherm after mercury porosimetry plateaued, but the isotherm before mercury porosimetry plateaued at a higher total amount adsorbed (~660 $cm^3(STP)g^{-1}$). The difference between the total amount adsorbed before and after mercury porosimetry was equal to the amount of mercury that had been entrapped. This suggested that the mercury became entrapped in only the largest pores. In addition, capillary evaporation before and after mercury porosimetry started at the same relative pressure, which was ~0.85. This suggested that the large pores which entrap mercury could only empty once surrounding narrower necks emptied at relative pressure 0.85. The findings of this study suggested that a pore blocking mechanism exists in sample G1. To further support their findings, Rigby and Fletcher fragmented the sample G1 to deconvolve the large bodies from the necks. The resulting desorption isotherm for the fragmented sample started at a higher relative pressure. This was because the large pore bodies were no longer being blocked by narrow necks and, therefore, could now empty at the equilibrium vapour pressure for a receding meniscus in the pore body.

Advanced adsorption has been observed for pellets from batch S1 using the integrated gas sorption and mercury porosimetry technique (Rigby *et al.* 2008; Rigby and Chigada 2009). S1 is a sol gel silica sphere with a modal pore size of 15 nm; more details are given in the experimental section below. It was found that the spatial arrangement of larger and smaller pores within the region of S1 in which mercury became entrapped was analogous to a through ink bottle pore. Once mercury became entrapped in the larger pores it generated dead ends in the smaller pores. It was found that the relative pressure for condensation in the region of interest for the empty system was the square root of the relative pressure for the reduced condensation occurring in this region following mercury entrapment, and for desorption from the region of interest of the empty sample. This is consistent with the presence of advanced adsorption (and pore blocking), akin to what would be expected for a through ink bottle pore from the Cohan-Kelvin equations, before mercury entrapment in the pore body.

This Chapter will now use the integrated experiment to determine whether the pores at the onset of mercury entrapment fill by a hemispherical or cylindrical shaped meniscus.

5.3 Experimental

5.3.1 Samples studied

Samples studied in this Chapter are S1, EA1 and E2. S1 is a mesoporous sol gel silica sphere of diameter ~3mm. The modal pore diameter is ~15 nm and its BET surface area is ~200 m^2g^{-1}. EA1 is a mesoporous alumina cylindrical tablet of dimensions ~ 3mm. The modal pore size is 25 nm and its BET surface area is ~40 m^2g^{-1}. E2 is an alumina extrudate of length ~5 mm. The modal pore size is ~10 nm and its BET surface area is ~180 m^2g^{-1}.

5.3.2 Nitrogen sorption experiments

Nitrogen sorption experiments were performed at 77 K by use of a Micromeretics Accelerated Surface Area and Porosimetry (ASAP) 2020 apparatus. The sample was placed into a pre-weighed Micromeretics gas sorption tube and a seal frit was placed at the top. The seal frit had two functions. It firstly prevented any sample being evacuated into the manifold of the Micromeretics ASAP apparatus. Secondly, it allowed the Micromeretics gas sorption tube to be removed from the Micromeretics ASAP 2020 apparatus, but keeping the sample inside enclosed in an inert atmosphere of nitrogen. The sample tube (with sample) was attached to the ASAP 2020 and heat treated under vacuum to remove any physisorbed gases. The heat treatment involved heating the sample to 90 °C under a virtual vacuum (relative pressure $1x10^{-5}$) to first remove any physisorbed water. The temperature was then increased to 150 °C and the sample was left for 12 hours. After the heat treatment the sample tube was removed from the ASAP 2020 (seal frit attached) to calculate the dry sample mass. A Micromeretics patented isothermal jacket was then placed around the sample tube and it was reattached to the ASAP 2020. The isothermal jacket ensured a constant thermal profile of 77 K along the length of the sample during the analysis. The gas sorption experiment was fully automated and the relative pressures studied were between 0.004 - 1.00. At each pressure point the saturation pressure was calculated in a cell, which was adjacent to the sample.

5.3.3 Equilibration time

The gas sorption experiment works by dosing an amount of gas, into a fixed volume chamber where the sample (the adsorbent) is situated. The sample, over a period of time, adsorbs the gas and eventually the adsorbed gas (the adsorbate) reaches an equilibrium state with the gas phase. At this point the Micromeretics equipment calculates the amount of gas that has been adsorbed onto the sample and then doses another amount of gas. The

time it takes for the adsorbed gas and the bulk gas to reach equilibrium with one another depends on the adsorbent, the adsorbate, the temperature and the pressure. This period of time can be found by studying the gas sorption isotherm at two different equilibration times. If the amount of adsorbed gas, at a specific pressure, is the same for two times, the system must have reached equilibrium by the shortest time used. If the amount of adsorbed gas is not the same for the two different times used, then it cannot be said that the system is at equilibrium for either of the times. In which case, the experiment would need to be repeated with longer time scales until the amount adsorbed remains unchanged, thus confirming equilibration. The equilibration time used in these studies was tested and found to be 25 s (see Appendix A3).

5.3.4 Mercury porosimetry experiments

Following the gas sorption experiment the sample tube was allowed to reach ambient temperature (~293 K), and the sample was then transferred to a Micromeretics mercury penetrometer. The transfer took place in a small glove box, which was under a dry nitrogen atmosphere. This minimised any adsorption of water from the atmosphere onto the sample when the transfer between sample tubes took place. A mercury porosimetry experiment was then performed using a Micromeretics Auto-pore IV 9450 apparatus. The sample was first evacuated to 6.7 Pa to remove physisorbed water that had adsorbed onto the sample when it was transferred from the gas sorption apparatus. When the system was at vacuum, mercury was allowed to enter the penetrometer and then the pressure was increased toward ambient. The penetrometer was then transferred to a pressure vessel that could reach a maximum pressure of 414 MPa. A fully automated mercury porosimetry experiment was then studied from ambient pressure to 414 MPa using a standard 15 s equilibration time between pressure steps.

5.3.5 The second nitrogen sorption experiment

Following the mercury porosimetry experiment the sample (and mercury) was transferred to a fume cupboard and placed in a crucible. Using tweezers the sample was removed from the mercury and transferred back into the Micromeretics gas sorption tube. The gas sorption tube was reattached to the Micromeretics ASAP 2020 and a filled liquid nitrogen Dewar was raised around the tube to cool the system to 77 K. This set up was left for 30 minutes to ensure all the mercury inside the sample became frozen, before the system was then evacuated to start the next nitrogen sorption experiment. If the mercury was not

frozen, a potential hazard would be introduced, as the vacuum pump used to evacuate the sample at the beginning of the gas sorption experiment was vented into the laboratory.

5.3.6 The number of pressure points

Before the start of the gas sorption experiments the required pressure points were programmed into the Micromeretics software. The region of interest was the capillary condensation part of the isotherm, so a significant number of points were acquired over this pressure range (~60 points). This meant, for long equilibration times (25 s) the total analysis time became ~30-50 hours. The capacity of the liquid nitrogen Dewar used meant the theoretical total analysis time could be a maximum of 60 hours. However, under the experimental conditions it was found that after ~45 hours all the liquid nitrogen in the Dewar had been consumed indicating some loss by evaporation. The reason for the discrepancy was perhaps due to the experiments for this thesis being carried out at a higher ambient temperature, relative to the experiments that had a reported 60 hours analysis time. Therefore, to reduce the total analysis time, fewer pressure points were acquired in the isotherm region before capillary condensation occurred (~15 points).

5.4 Analysis of data

5.4.1 Gurvitsch volume

The amount adsorbed calculated by the Micromeretics ASAP gas sorption machine uses units of $cm^{-3}g^{-1}$ at standard temperature and pressure (STP). To compare the gas sorption data with the mercury porosimetry data, the units were converted into a liquid volume. This was done using the Gurvitsch rule and the conversion is given by (Vansant *et al.* 1995):

$$V_P = 1.547^{-3} V_a \qquad 5.1$$

where V_P is the volume of liquid adsorbate (cm^3) and V_a the volume of adsorbed gas (cm^3(STP)).

5.4.2 Pressure tables

The same pressure points were used before and after the mercury porosimetry experiment so a direct comparison between the two gas sorption experiments could be made. However, there were always small discrepancies between the actual pressure points of each experiment even when the entered pressures were the same. To overcome this problem,

the data points in the second gas sorption experiment were linearly interpolated so the pressure points matched exactly the same pressures in the first isotherm.

5.4.3 Change in incremental amount plots

To understand the location of the entrapped mercury, Rigby *et al.* (2008) used graphs that were termed "change in incremental amount adsorbed plots". These plots will now be explained below. The gas sorption isotherm before mercury porosimetry is analysed by calculating the change in the amount adsorbed between each pressure point. This procedure is then repeated on the gas sorption isotherm following mercury porosimetry. Finally, the change in volume between two pressures following mercury porosimetry is subtracted from the change in volume between the same two pressures before mercury porosimetry.

An example of an adsorption change in incremental amount adsorbed plot is shown in Figure 5.2 and is explained as follows. Between relative pressures 0.7 and 0.85 the plot is at approximately zero. This indicates that before and after mercury porosimetry, the isotherms are the same over this pressure region. Any small fluctuations in this pressure region have previously been explained as noise (Rigby *et al.* 2008). At relative pressure ~0.85 there is a positive signal that continues to relative pressure 1. This positive signal indicates that the gas sorption isotherm following mercury porosimetry adsorbs less gas than the analogous isotherm before mercury porosimetry. This is because following mercury porosimetry some pores have mercury entrapped in them. To distinguish whether the signal in the plot is because of noise or because of the entrapped mercury the following assumption was made. It was assumed that before relative pressure 0.6 no capillary condensation occurred in any of the studied samples. So any fluctuations in the change in incremental amount adsorbed plots in this pressure region were considered to be noise. The standard deviation of the noise was calculated and any fluctuation that was greater than two standard deviations in the noise was deemed to be caused by the entrapped mercury.

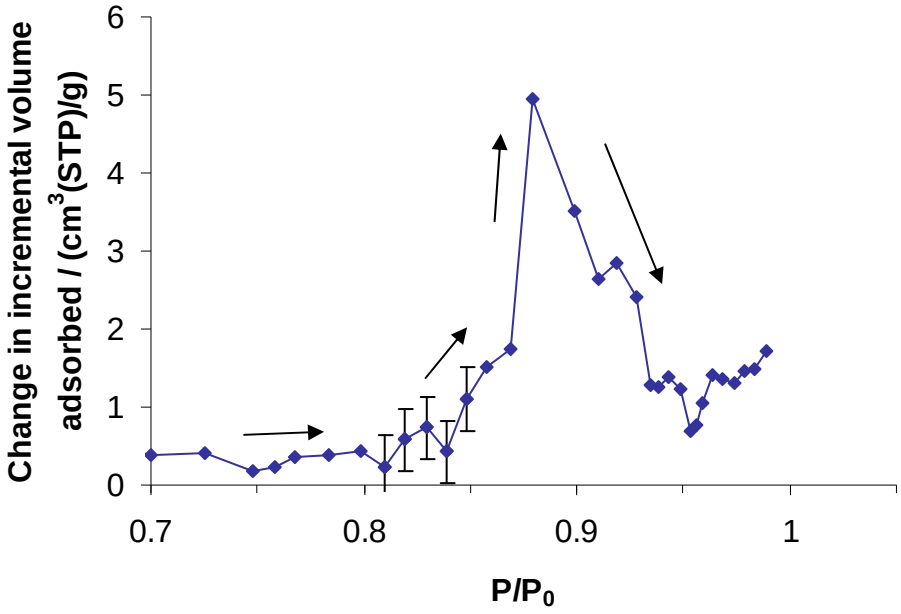

Figure 5.2: An example of an adsorption change in incremental amount adsorbed plot. The arrows show the direction of the change in pressure and the lines are to guide the eye. The error bars are two standard deviations in the noise and are explained in the text

5.4.4 Mercury porosimetry

Mercury porosimetry experiments will be presented in this Chapter and so an introduction to the technique is given as follows. The experiment is used to characterise porous materials that have pore radii ranging from 2 nm to ~3 μm (Lowell and Shields 1984). Unlike nitrogen gas sorption experiments, the imbibed material (mercury) does not wet the sample so it has to be forced in with pressure. The smaller the pore size a greater external pressure is required to force the mercury into the sample. When the external pressure is then lowered the mercury can leave the sample. A relationship between the pressure applied and the pore radii exists (Washburn 1921), and is expressed as:

$$P_{Hg} = -\frac{2\gamma_{ls}\cos\theta}{r} \qquad 5.2$$

where P_{Hg} is the applied pressure, γ_{ls} is the surface tension between the liquid and the solid, θ is the contact angle between the liquid and the solid, and r is the pore radius.

Mercury porosimetry experiments have hysteresis between the intrusion and extrusion pressures, which is known to arise from structural effects and changes in the contact angle. These two points can be explained as follows.

Structural hysteresis: This will be explained using the through ink bottle type pore model. During intrusion, the larger pore should fill first but it is unable to as the outer narrow necks prevent the mercury entering. The large pore body will only fill once sufficient pressure is reached to fill the outer necks. This is analogous to the pore blocking mechanism in gas sorption studies. Using the ink bottle pore model, the extrusion mechanism can now be explained. When the pressure is lowered the small necks should empty first, followed by the large pore body. However, extrusion can happen only if there is a free meniscus. If there is not one, the extrusion process is delayed until at a point when the mercury snaps. When the mercury snaps it generates a meniscus and allows the mercury to extrude from the neck. Moreover, if the pressure cannot be lowered enough to empty the mercury in the large pore body, it becomes entrapped after the mercury porosimetry experiment.

Contact angle hysteresis: When the mercury is forced into the porous material it can have a different contact angle to when it leaves. Due to this difference, the pressure to intrude and extrude the mercury from a pore of radius *r* will be different according to the Washburn equation.

To remove contact angle hysteresis, Rigby and Edler (2002) have suggested using alternative semi-empirical equations to analyse mercury intrusion and extrusion experiments (equation 5.3). By removing contact angle hysteresis it means any remaining hysteresis is because of structural effects. Equation 5.3 is given by (Rigby and Fletcher 2004):

$$r = \frac{-A + \sqrt{A^2 - 2BP_{Hg}}}{P_{Hg}} \qquad 5.3$$

where r is the pore radius (nm) and P_{Hg} the applied pressure (MPa), and A/B are constants that depend on the material and whether the meniscus is advancing or retreating (see Table 5.1). Equation 5.3 has been independently calibrated using electron microscopy (Liabastre and Orr 1978). Additionally, since equation 5.3 has been derived empirically, the calculated error in the pore size is estimated to be ~4-5 % (Kloubek 1981).

	Advancing meniscus		Retreating meniscus	
	A	*B*	*A*	*B*
Silica	-302.533	-0.739	-68.366	-235.561
Alumina	-302.533	-0.739	-40	-240

Table 5.1: Parameters for insertion into equation 5.3. The advancing meniscus values have a pore radius range of 6-99.75 nm and the retreating values have a range from 4-68.5 nm

5.4.5 Gas sorption pore size calculations

In this Chapter, pore sizes will be calculated from gas sorption data using the Kelvin equation (see Chapter 2). By substituting the surface tension of nitrogen, γ, the molar volume of nitrogen, V_m, the ideal gas constant, R, and the temperature, T (77 K), into the Kelvin equation, the pore radius (nm) can be expressed as (Androutsopoulos and Salmas 2000):

$$r(nm) = \frac{0.477}{\ln(P_0 / P)} + t_c \qquad 5.4$$

Equation 5.4 assumes that the meniscus geometry is cylindrical. A modification can be made for a hemispherical meniscus and the Kelvin equation can be expressed as:

$$r(nm) = \frac{0.953}{\ln(P_0 / P)} + t_c \qquad 5.5$$

5.5 Results

The result section will present the data for each sample before and after mercury porosimetry in the sample order EA1, S1 and E2.

When the sample temperature is lowered to 77 K following mercury porosimetry, there is the potential to introduce porosity into the sample. This is because the entrapped mercury will contract in size and generate porosity between it and the pore wall (see Figure 5.3)

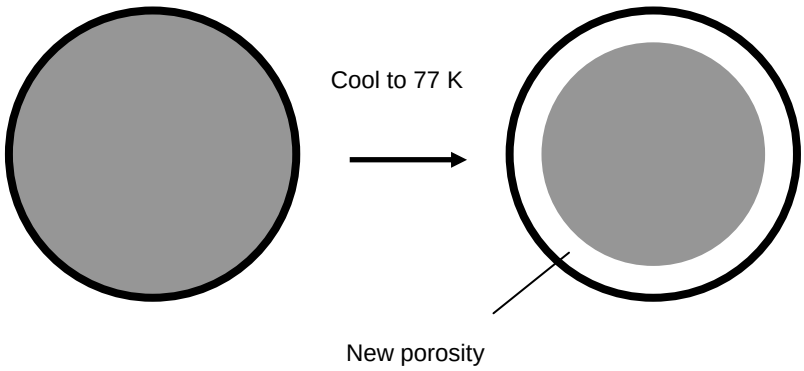

Figure 5.3: Schematic showing the end view of a pore which is occupied by mercury (grey). When the system is cooled to 77 K the mercury contracts causing new porosity between the mercury and the pore wall

If the generated porosity is large, gas can adsorb into it and nucleate adsorption in neighbouring pores by the advanced adsorption mechanism. This adsorption mechanism would not exist in the sample before mercury porosimetry. The potential amount of porosity that can be generated has previously been calculated by Rigby *et al.* (2008) and is explained as follows. It was estimated that when mercury is cooled from 273 K to 0 K it would contract to 0.933 of its original volume. This meant its linear dimension would contract by 2.3 % ($1-\sqrt[3]{0.933}$ as a fraction). Therefore, the mercury has to be entrapped in a cylindrical pore of at least 15.5 nm to create microporosity that would allow a nitrogen molecule to fit (0.354 nm) and 87 nm size pore to create any mesoporosity (mesopore > 2 nm). The samples studied here do not have pores of size 87 nm so it is probable that no mesoporosity is created by the contraction of the mercury. This means it is unlikely that cooling the entrapped mercury will introduce advanced adsorption.

For each studied material, the amount of entrapped mercury (from mercury porosimetry data) was equal to the total loss of pore volume calculated from the gas sorption experiments (Table 5.2). This means that any difference between the gas sorption experiments before and after mercury porosimetry is because capillary condensation cannot occur in the pores which entrap mercury. This suggests the mercury does not guard and, thus, prevent gas accessing pockets of pore volume.

Sample	Pore volume from gas sorption before mercury porosimetry (cm^3g^{-1})	Pore volume from gas sorption after mercury porosimetry (cm^3g^{-1})	Amount of entrapped mercury (cm^3g^{-1})
EA1	0.447 ± 0.004	0.363 ± 0.004	0.081 ± 0.003
S1	1.05 ± 0.003	0.920 ± 0.003	0.133 ± 0.003
E2	0.639 ± 0.003	0.537 ± 0.003	0.100 ± 0.003

Table 5.2: Summary of the pore volume loss attributed to the entrapped mercury. Micromeretics report the error in each gas sorption data point to be ±0.30 cm^3g^{-1} and each mercury porosimetry data point to be 2μlg^{-1}. The quoted errors are cumulative errors; see Appendix A4

5.5.1 Alumina EA1

5.5.1.1 Gas sorption studies before mercury porosimetry

Figure 5.4 shows the gas sorption isotherm for the sample EA1 before mercury porosimetry, and is explained as follows. From a virtual vacuum to relative pressure ~0.7 the amount of gas adsorbed increases and this represents the gas adsorbing onto the surface of EA1. At relative pressure ~0.7, capillary condensation in the pores starts and continues to relative pressure 1. At relative pressure 1, the top of the isotherm has not plateaued, which suggests there are some pores that have not been filled with condensate. This is because these pores are too large for nitrogen at 77 K to condense into at relative pressure 1. The upper pore size limit for a gas adsorption experiments is ~50 nm (Buchmeiser 2003). Since the isotherm does not plateau, this indicates that EA1 must have some pores that are greater than ~50 nm in size. When the direction of pressure changed is reversed (at relative pressure 1) the amount of adsorbed gas decreases immediately and at relative pressure ~0.86 there is a knee point. The knee point is not well defined and has been calculated by extrapolating two straight lines on the desorption isotherm (see Figure 5.5). The point where the two lines intersect has been termed the knee point relative pressure. Capillary evaporation then continues to the closure point of hysteresis at relative pressure ~0.570.

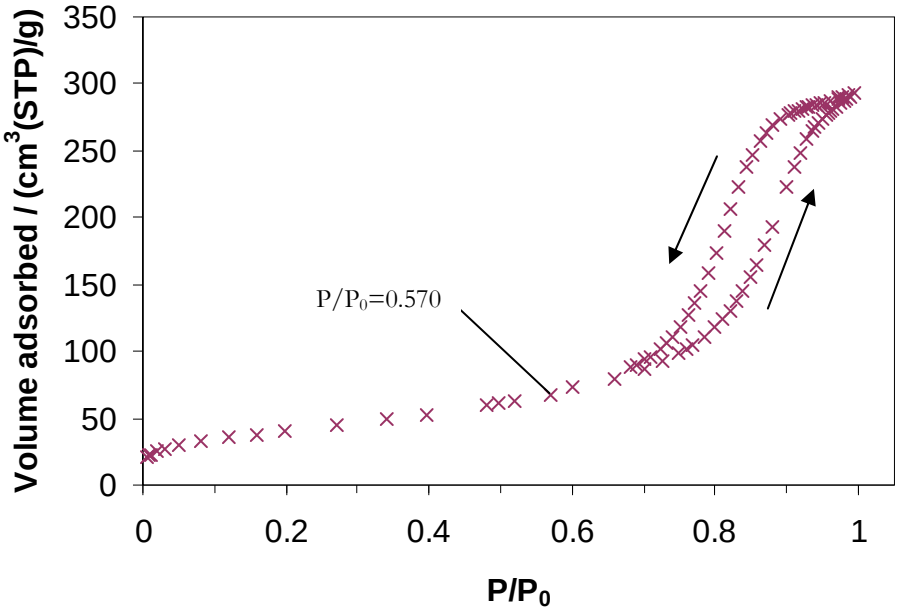

Figure 5.4: Gas sorption isotherm for EA1 (crosses). Arrows have been added to indicate the direction of the change in pressure

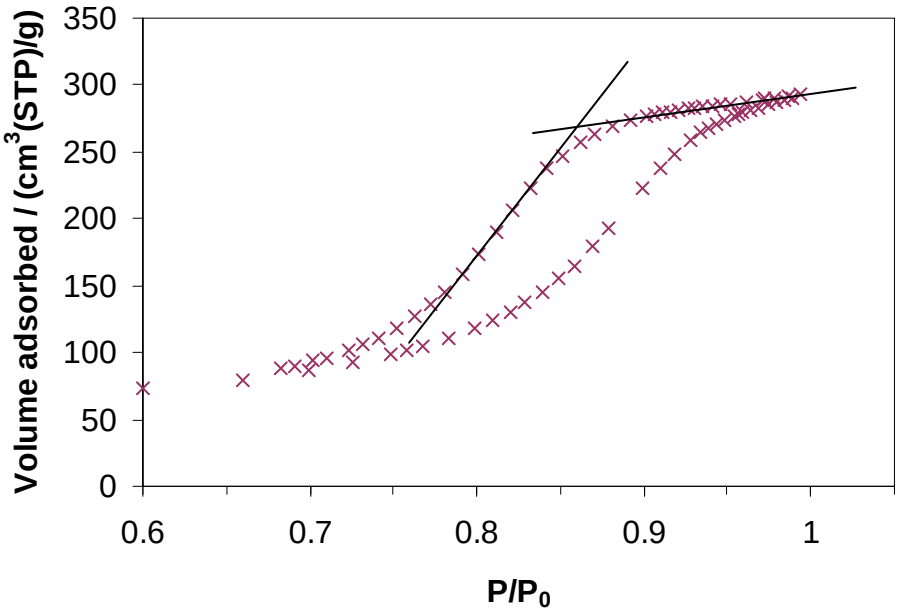

Figure 5.5: An enlarged area of Figure 5.4. The two lines are explained in the text, intersecting at the knee point relative pressure

Since desorption occurs immediately when the direction of pressure is reversed, it must mean there is a reversible adsorption-desorption process. This means that there are sets of pores in EA1 that fill and empty by hemispherical menisci, as this process is reversible.

5.5.1.2 Gas sorption studies following mercury porosimetry

Figure 5.6 shows the gas sorption isotherm for EA1 following the mercury porosimetry experiment. To compare the isotherm with the analogous isotherm before mercury porosimetry, they have both been overlaid in Figure 5.7 (a). In addition, Figure 5.7 (b) shows the same isotherms overlaid, but where the volume adsorbed for all data points, in the isotherm following mercury porosimetry, have been adjusted upwards by 16 cm^3 (STP)g^{-1}. When the isotherm is adjusted upwards by 16 cm^3 (STP)g^{-1} the lower region of the adsorption boundary curve (relative pressure <~0.849) overlays the same region of the isotherm before mercury porosimetry.

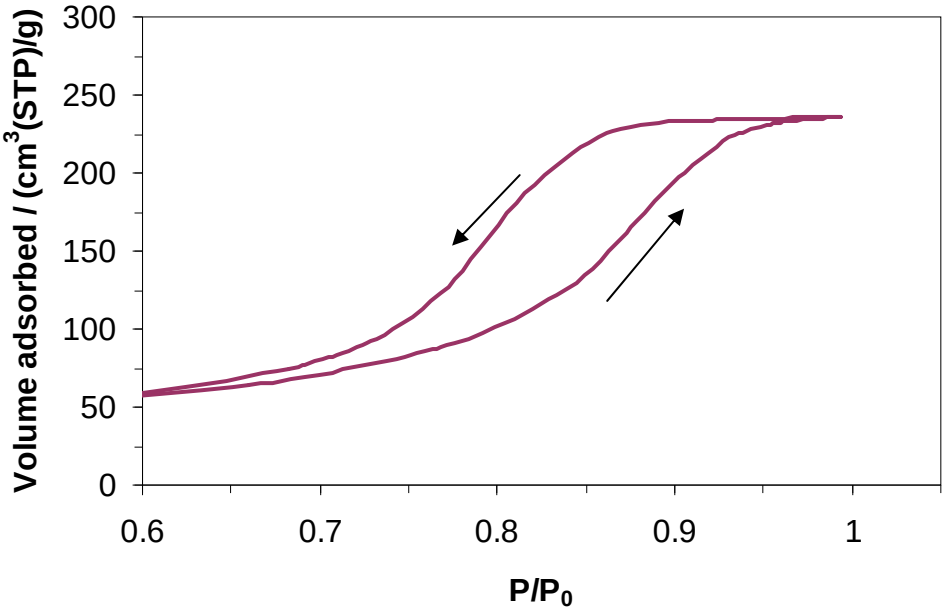

Figure 5.6: Gas sorption isotherm of EA1 following mercury porosimetry. Arrows have been added to indicate the direction of the change in pressure

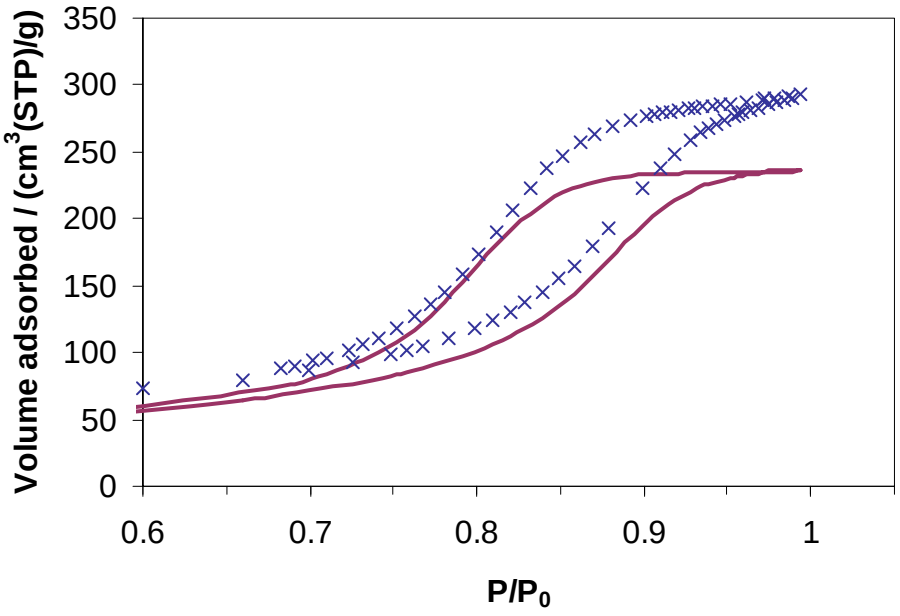

Figure 5.7 (a): Gas sorption isotherm before mercury porosimetry (crosses) and after mercury porosimetry (fixed line)

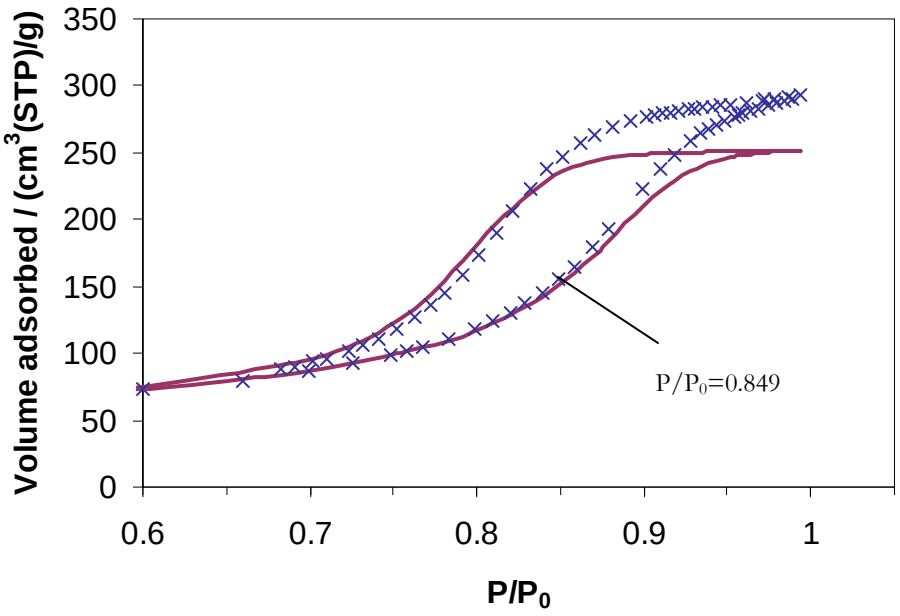

Figure 5.7 (b): Gas sorption isotherm before mercury porosimetry (crosses), and after mercury porosimetry (fixed line where all data points have been adjusted upwards by 16 cm^3 (STP)g^{-1})

Rigby *et al.* (2008) have suggested why there is a difference (16 cm^3 (STP)g^{-1}) in the lower region of the isotherm and this is explained using Figure 5.8. Position 1 shows the multilayer adsorption region in a pore model before mercury porosimetry. The gas is able to adsorb in the pore necks and the large pore body. Position 2 shows the same pore model, but following a mercury porosimetry experiment. Since mercury is entrapped in the large pore body no multilayer adsorption can happen in this pore. This then explains why there is a difference in the amount adsorbed (16 cm^3 (STP)g^{-1}) in lower region of the isotherms.

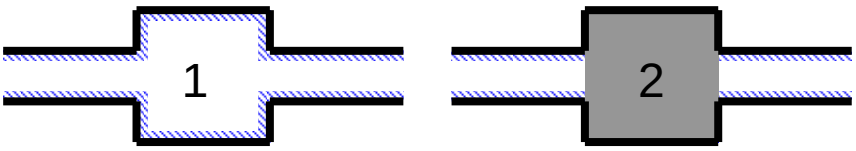

Figure 5.8: A through ink bottle pore schematic before and after mercury porosimetry. The shading shows an adsorbed layer of gas and the grey the entrapped mercury. The text explains the numbers in detail

By adjusting the isotherm following mercury porosimetry upwards by 16 cm^3 (STP)g^{-1}, the adsorption curves only overlay below relative pressure 0.849 and diverge above this pressure. This divergence can be explained using Figure 5.9, which again shows a schematic of a porous material before and after mercury porosimetry. At pressure P1, the necks in the pore model fill with condensate in the system before and after mercury

porosimetry. This means the two isotherms will overlay one another up to pressure P1. At pressure P2 the pore body before mercury porosimetry is able to fill with condensate. However, after mercury porosimetry the pore body has mercury entrapped in it so capillary condensation can no longer occur in this pore. This means at pressure P2 the adsorption isotherm before and after mercury porosimetry will diverge as the system before mercury can adsorb more gas. For EA1 this happens at relative pressure ~0.849.

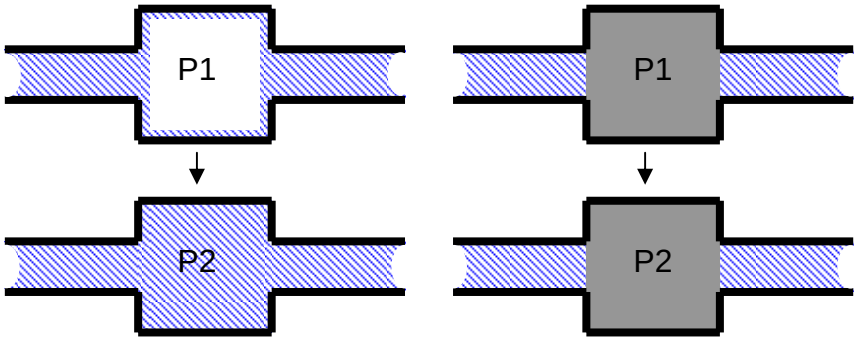

Figure 5.9: A through ink bottle pore schematic before and after mercury porosimetry. The shading shows the condensed gas and the grey the entrapped mercury. P1 and P2 refer to the pressure of the system, where P2>P1, and are explained in the text

The isotherm following mercury porosimetry plateaus at relative pressure 1, which indicates that all the pores accessible by the gas become filled with condensate. This is in contrast to the isotherm before mercury porosimetry, which does not plateau. This indicates that the mercury has become entrapped, at least, in the largest pores that previous could not fill with condensate. In addition, when the direction of pressure change is reversed (at relative pressure 1) to start the desorption process, the amount adsorbed no longer decreases immediately. There is instead a flat region of the isotherm that continues to relative pressure ~0.862 and at this relative pressure capillary evaporation begins. This suggests that the mercury is either entrapped within the pores that desorption could occur from before mercury porosimetry. Alternatively, it is feasible that the entrapped mercury is situated such that it prevents immediate evaporation from these pores when the direction of pressure change is reversed.

To understand where the mercury is entrapped more clearly, change in incremental amount adsorbed plots have been generated for the adsorption and desorption boundary curves (Figure 5.10 (a) and (b)). The fluctuations in the adsorption change in incremental amount adsorbed plot between relative pressures 0-0.7 is noise and has not been shown. At relative pressure 0.849 there is a positive signal, which indicates the smallest pores which entrap

mercury fill at this relative pressure. The positive signal continues to relative pressure 1, which indicates mercury is entrapped in pores that fill over this pressure range.

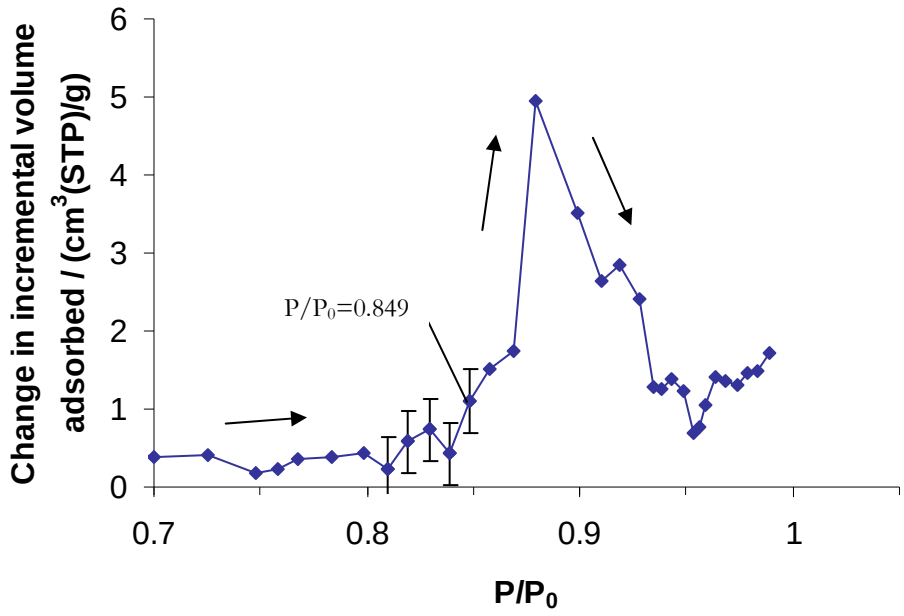

Figure 5.10 (a): Adsorption change in incremental amount adsorbed plot for EA1. The line is to guide the eye and arrows have been added to indicate the direction of the change in pressure. The error bars are explained in Section 5.4.3

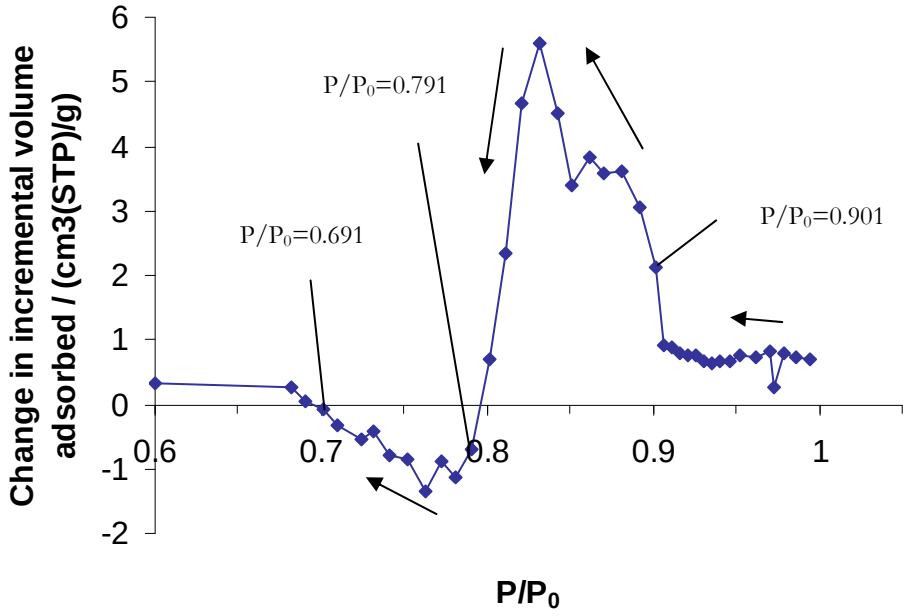

Figure 5.10 (b): Desorption change in incremental amount adsorbed plot for EA1. Arrows have been added to indicate the direction of the change in pressure and lines have been added to guide the eye

The desorption change in incremental amount adsorbed plot (Figure 5.10 (b)) is now discussed. From relative pressure 1 to ~0.90 there is a positive signal. This corresponds to the region in the isotherm before mercury porosimetry where desorption is immediate at the point the direction of pressure change is reversed. At relative pressure 0.901 there is a large positive signal which continues to relative pressure 0.791. It is in this pressure range that the pores which entrap mercury empty. Between relative pressure 0.791 and 0.691 the signal in the plot is negative, which indicates that there is more desorption from the sample following mercury porosimetry over this pressure range. It must be that the mercury becomes entrapped in a set of pores that are part of a critical percolation pathway for desorption. This is explained using Figure 5.11, which is made up of three pores labelled 1, 2 and 3. The left hand schematic is before mercury porosimetry and pores 1 and 2 are filled with condensate. The right hand schematic is the system after porosimetry, where pores 1 and 2 are filled with condensate and pore 3 has mercury entrapped in it. Before mercury porosimetry, when the pressure is lowered pore 2 is able to desorb through pore 3. However, after mercury porosimetry, pore 2 can not empty through pore 3 as it has mercury entrapped in it. In addition, it cannot empty through pore 1 either, as this is filled with condensate. Pore 2 will only be able to empty once the pressure has been lowered for pore 1 to empty. Therefore, in the Figure 5.11, pore 3 is part of the critical percolation pathway, which becomes entrapped with mercury following a mercury porosimetry experiment.

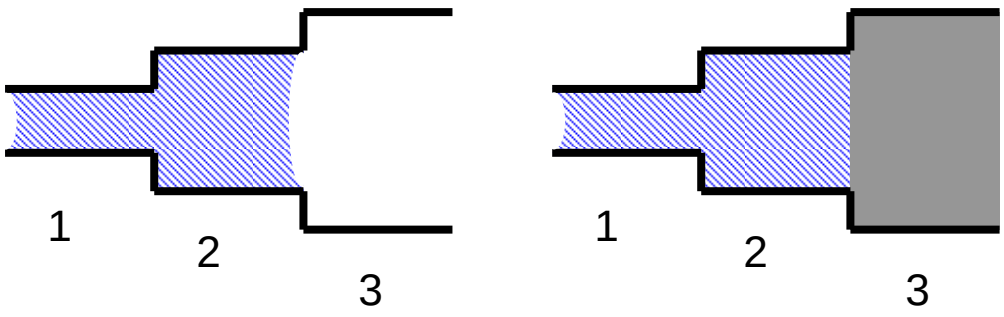

Figure 5.11: Schematic of a pore model before and after mercury porosimetry. The shading is condensed gas and the grey is mercury entrapped following mercury porosimetry. The pore size 3>2>1

5.5.2 Silica S1

This section will now discuss the gas sorption studies using S1 before and after mercury porosimetry. S1 has previously been studied using the integrated gas-mercury-gas experiment (Rigby *et al.* 2008) and the results in this thesis will be related to the previous

work. The experiments using the sample S1 are being repeated as in previous studies the workers failed to ensure that the gas sorption isotherms were at equilibrium.

5.5.2.1 Gas sorption studies before mercury porosimetry

Figure 5.12 shows the gas sorption isotherm before mercury porosimetry for S1. As the region of interest was the capillary hysteresis region, only a few isotherm points were studied below relative pressure 0.7 and so have not been included in Figure 5.12. Arrows have been added to indicate the direction of the change in pressure for the adsorption and desorption boundary curves. Unlike the isotherm for EA1, the isotherm for S1 plateaus before relative pressure 1. This indicates that all pores within S1 become filled with condensate by relative pressure 1.

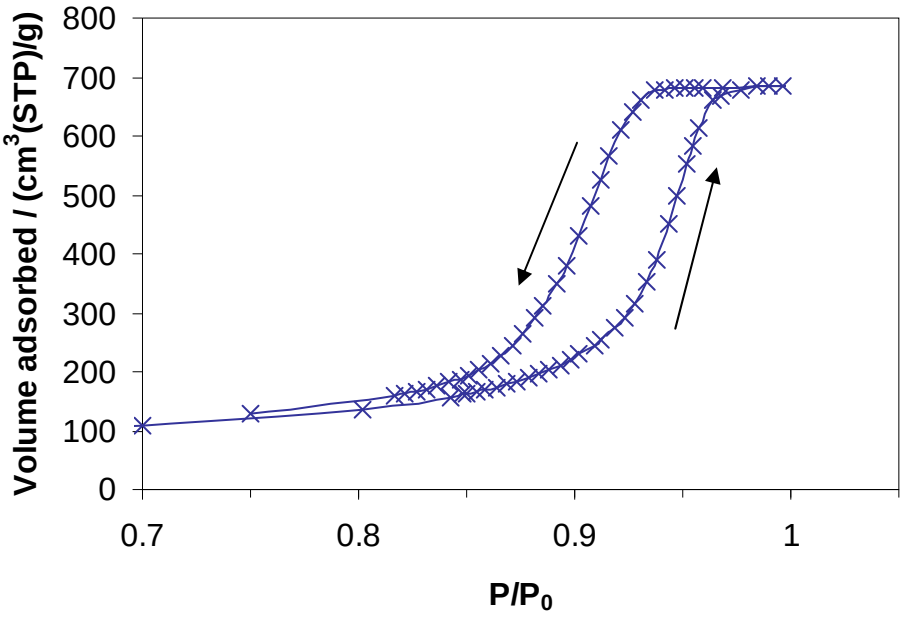

Figure 5.12: Gas sorption isotherm for S1 before mercury porosimetry. Arrows have been added to indicate the direction of the change in pressure and lines to guide the eye

5.5.2.2 Gas sorption studies following mercury porosimetry

The gas sorption isotherm following the mercury porosimetry experiment is shown in Figure 5.13.

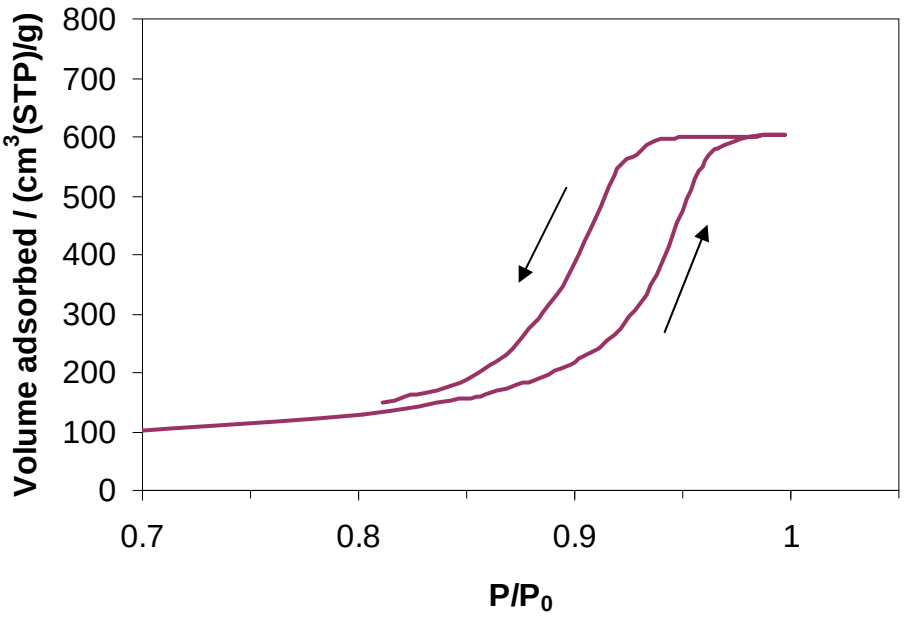

Figure 5.13: Gas sorption isotherm for S1 after mercury porosimetry. Arrows have been added to indicate the direction of the change in pressure

To make a comparison between the analogous isotherm before mercury porosimetry the two isotherms have been overlaid in Figure 5.14 (a) and (b). In the same procedure to the EA1 analysis above, Figure 5.14 (a) shows the isotherms overlaid, but where the volume adsorbed for all data points, in the isotherm following mercury porosimetry, have been adjusted upwards by 3 cm^3 (STP)g^{-1}. Figure 5.14 (b) shows the isotherms overlaid, but where the volume adsorbed for all data points, in the isotherm following mercury porosimetry, have been adjusted upwards by 82 cm^3 (STP)g^{-1}. When the isotherm following mercury porosimetry is adjusted by 3 cm^3 (STP)g^{-1} the lower region of the isotherm (adsorption and desorption boundary curves) overlay below ~300 cm^3 (STP)g^{-1}. In addition, when the isotherm following mercury is adjusted upwards by 82 cm^3 (STP)g^{-1} the top region of the isotherms overlay above ~ 630 cm^3 (STP)g^{-1}. This indicates the pores which entrap mercury do not fill and empty in the upper and lower regions of the isotherm. They instead must fill and empty at intermediate relative pressures, which was found in the previous studies by Rigby *et al.* (2008).

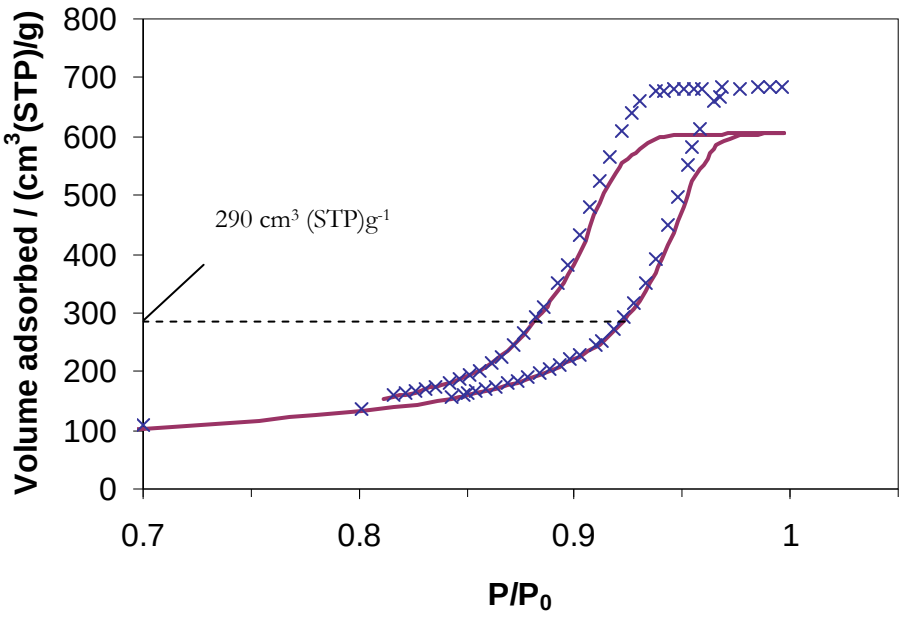

Figure 5.14 (a): Gas sorption isotherm for S1 before mercury porosimetry (crosses), and after mercury porosimetry (fixed line where all data points have been adjusted upwards by 3 cm^3 (STP)g^{-1})

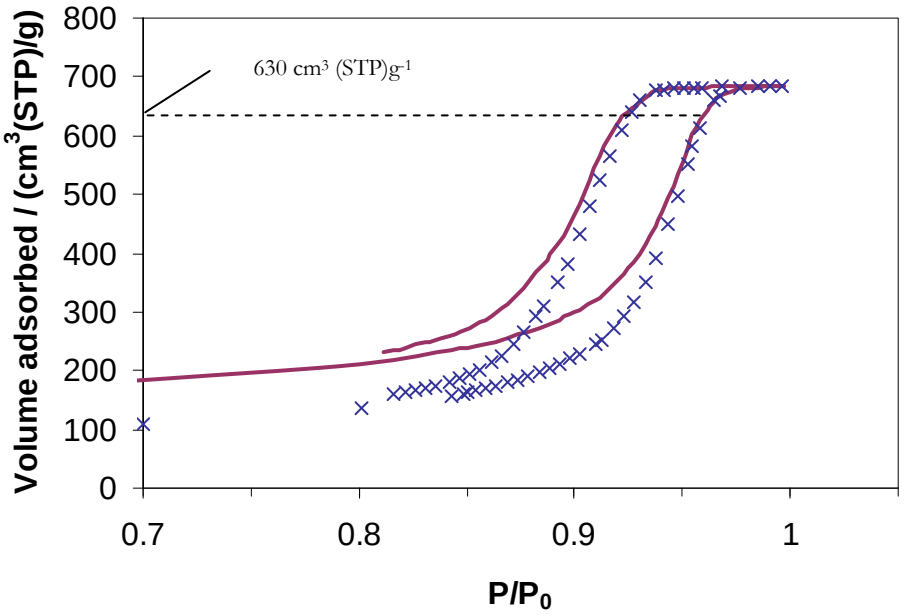

Figure 5.14 (b): Gas sorption isotherm for S1 before mercury porosimetry (crosses), and after mercury porosimetry (fixed line where all data points have been adjusted upwards by 82 cm^3 (STP)g^{-1})

To determine when the pores which entrap mercury fill and empty with condensate, the change in incremental amount adsorbed plots are shown in Figure 5.15 (a) and (b) and are explained as follows. The adsorption change in incremental amount adsorbed plot has a positive signal between relative pressure 0.923 and 0.960. It must be then that the pores which entrap mercury fill in this relative pressure range. This is in close agreement to the previous findings of Rigby *et al.* (2008).

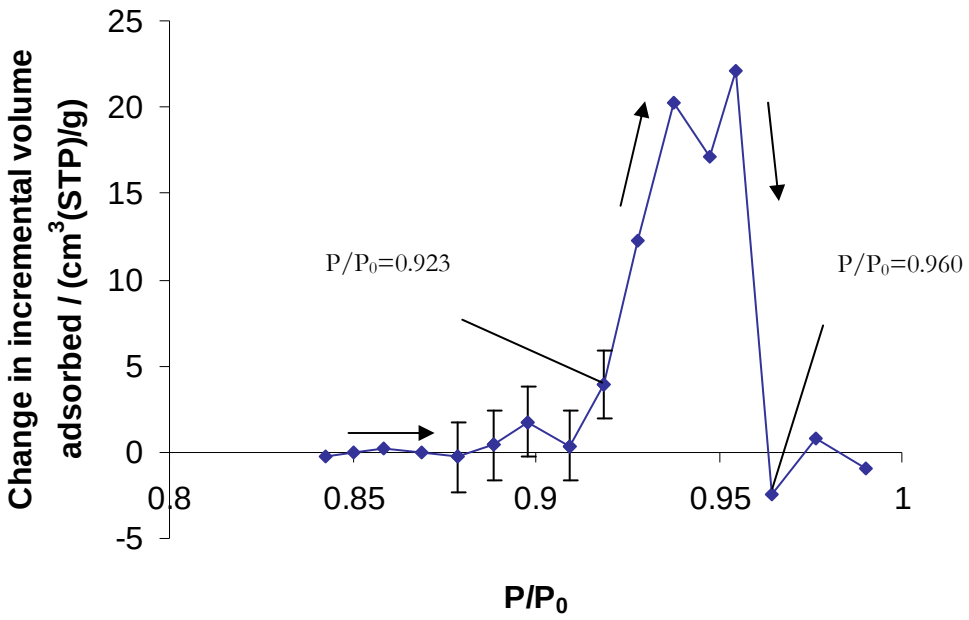

Figure 5.15 (a): Adsorption change in incremental amount adsorbed plot for S1. Arrows have been added to indicate the direction of the change in pressure and lines have been added to guide the eye. The error bars are explained in Section 5.4.3

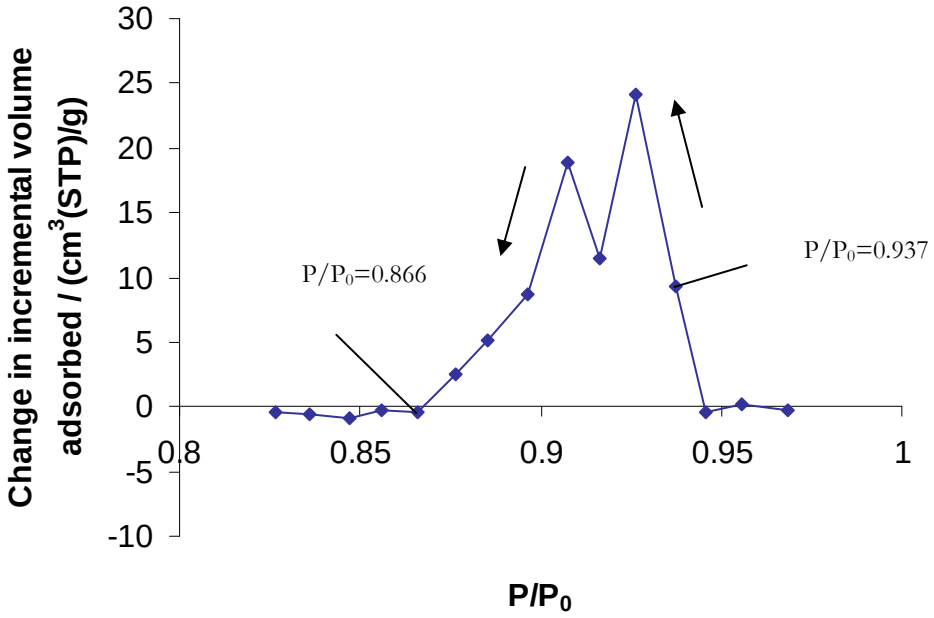

Figure 5.15 (b): Desorption change in incremental amount adsorbed plot for S1. Arrows have been added to indicate the direction of the change in pressure and lines have been added to guide the eye

The desorption change in incremental amount adsorbed plot (Figure 5.15 (b)) has a very similar shape to the analogous adsorption plot (Figure 5.15 (a)) and is described as follows. At relative pressure 0.937 there is a positive signal that continues to relative pressure 0.866. Once more, this suggests that the pores which entrap mercury desorb in this relative

pressure range. The previous studies (Rigby *et al.* 2008), however, report the pores which entrap mercury start to desorb at a lower relative pressure (~0.91) and over a narrower relative pressure range (~0.91-0.88). Their studies though used a 5 s equilibration time, compared to 25 s in this thesis. It is likely then that the delay in desorption for their studies arose from mass-transport limitations. The longer equilibration time used for this thesis provided more time for the nitrogen molecules to diffuse out of the sample and, therefore, desorption started at a higher relative pressure.

5.5.3 E2

This section will now discuss the gas sorption studies using E2 before and after mercury porosimetry.

5.5.3.1 Gas sorption studies before mercury porosimetry

Figure 5.16 shows the gas sorption isotherm before mercury porosimetry for E2. As the region of interest was the capillary hysteresis region, again only a few isotherm points were studied below relative pressure 0.7 and so have not been included in Figure 5.16. Arrows have been added to indicate the direction of the change in pressure for the adsorption and desorption boundary curves. Similar to S1, the isotherm plateaus before relative pressure 1, which indicates that all pores within E2 become filled with condensate by relative pressure 1. The adsorption and desorption isotherms are not smooth curves compared to S1 and EA1. For example, at relative pressure ~0.833 there is a noticeable point of inflexion on the desorption curve, which indicates that the pore structure of E2 is bimodal

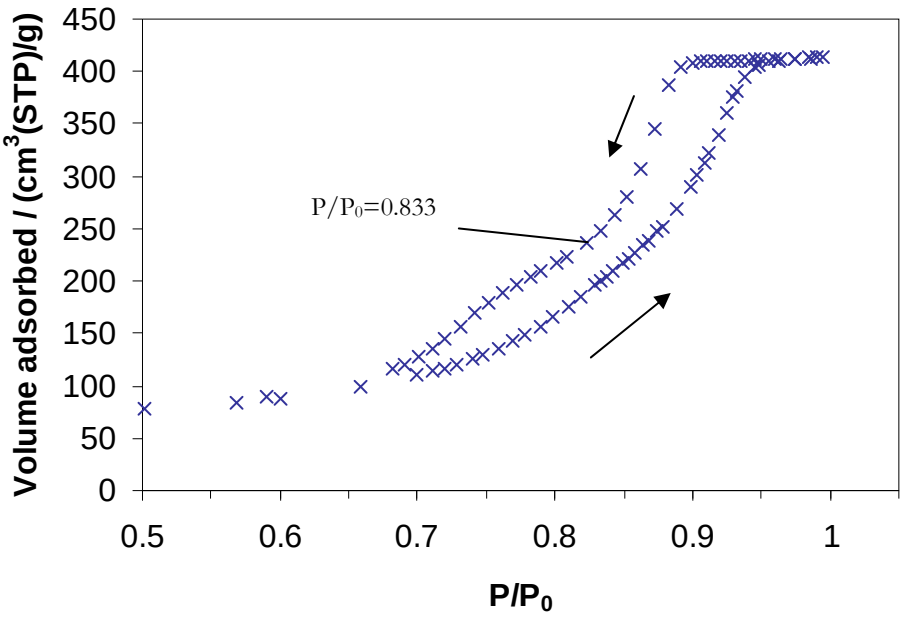

Figure 5.16: Gas sorption isotherm for E2 before mercury porosimetry. Arrows have been added to indicate the direction of the change in pressure

5.5.3.2 Gas sorption studies following mercury porosimetry

The gas sorption isotherm following the mercury porosimetry experiment has been overlaid on the same graph to the analogous isotherm before mercury porosimetry (Figure 5.17 (a) and (b)). Using the same procedure as the other samples analysed above, Figure 5.17 (a) shows the same isotherm overlaid, but where the volume adsorbed for all data points, in the isotherm following mercury porosimetry, have been adjusted upwards by 12 cm^3 (STP)g^{-1}. Figure 5.17 (b) then has the isotherms overlaid, but where the volume adsorbed for all data points, in the isotherm following mercury porosimetry, have been adjusted upwards by 65 cm^3 (STP)g^{-1}. When the isotherm following mercury porosimetry is adjusted by 12 cm^3 (STP)g^{-1} the lower region of the isotherm (adsorption and desorption boundary curves) overlay below ~248 cm^3 (STP)g^{-1}. When the isotherm is adjusted upwards by 82 cm^3 (STP)g^{-1} the top region of the isotherms do not overlay. This indicates the pores which entrap mercury fill and empty in the upper region of the isotherm above ~248 cm^3 (STP)g^{-1}.

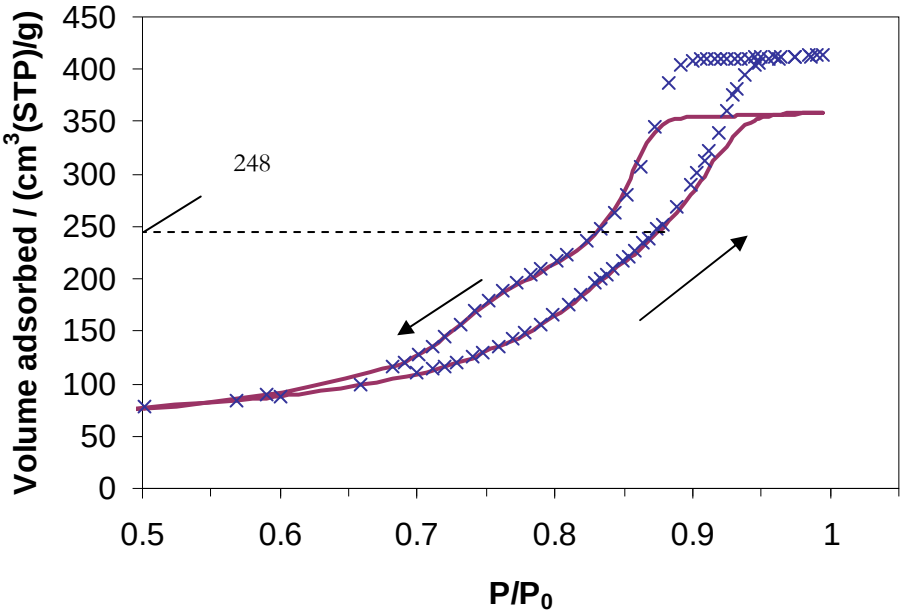

Figure 5.17 (a): Gas sorption isotherm for E2 before mercury porosimetry (crosses), and after mercury porosimetry (fixed line where all data points have been adjusted upwards by 12 cm^3 (STP)g^{-1})

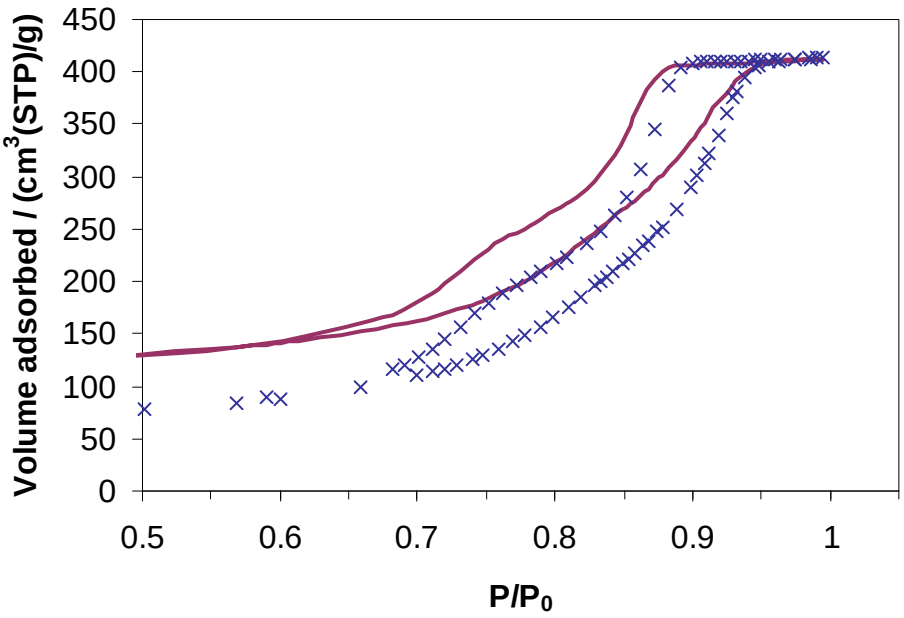

Figure 5.17 (b): Gas sorption isotherm for E2 before mercury porosimetry (crosses), and after mercury porosimetry (fixed line where all data points have been adjusted upwards by 65 cm^3 (STP)g^{-1})

The adsorption and desorption change in incremental amount adsorbed plots for E2 are shown in Figure 5.18 (a) and (b) and are discussed as follows. The adsorption change in incremental amount adsorbed plot has a positive signal between relative pressures 0.878 and 0.955. Again, it must be that the pores which entrap mercury fill in this relative pressure range. The desorption change in incremental amount adsorbed plots has a similar form to the analogous plot for EA1. At relative pressure ~0.901 there is a positive signal

that continues to relative pressure ~0.863. Between relative pressures ~0.863-0.822 the signal becomes negative, which is similar to the desorption change in incremental amount adsorbed plot for sample EA1. To explain this, it was discussed above that the mercury must become entrapped in a set of pores that are part of a critical percolation pathway for desorption (see Figure 5.11).

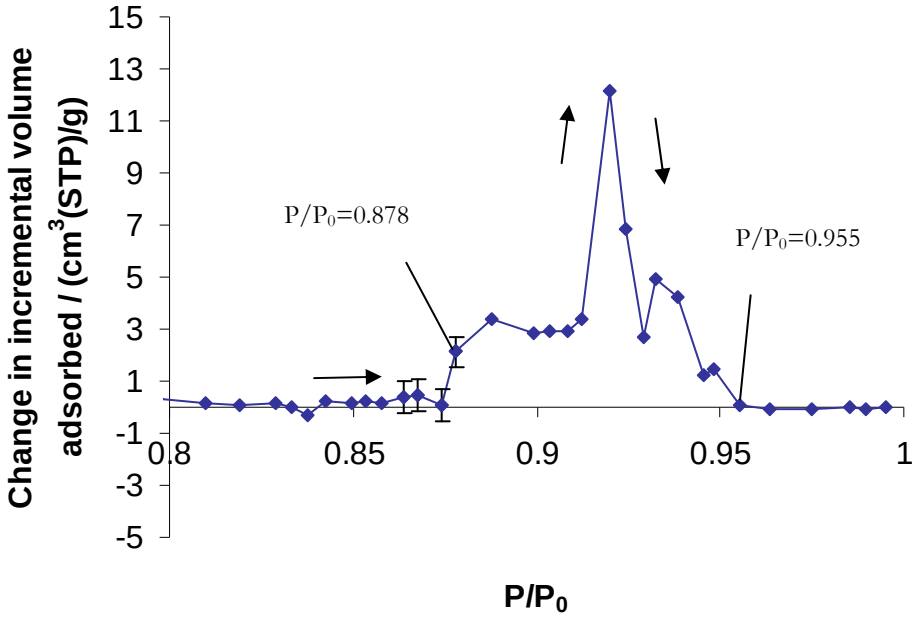

Figure 5.18 (a): Adsorption change in incremental amount adsorbed plot for E2. Arrows have been added to indicate the direction of the change in pressure and lines have been added to guide the eye. The error bars are explained in Section 5.4.3

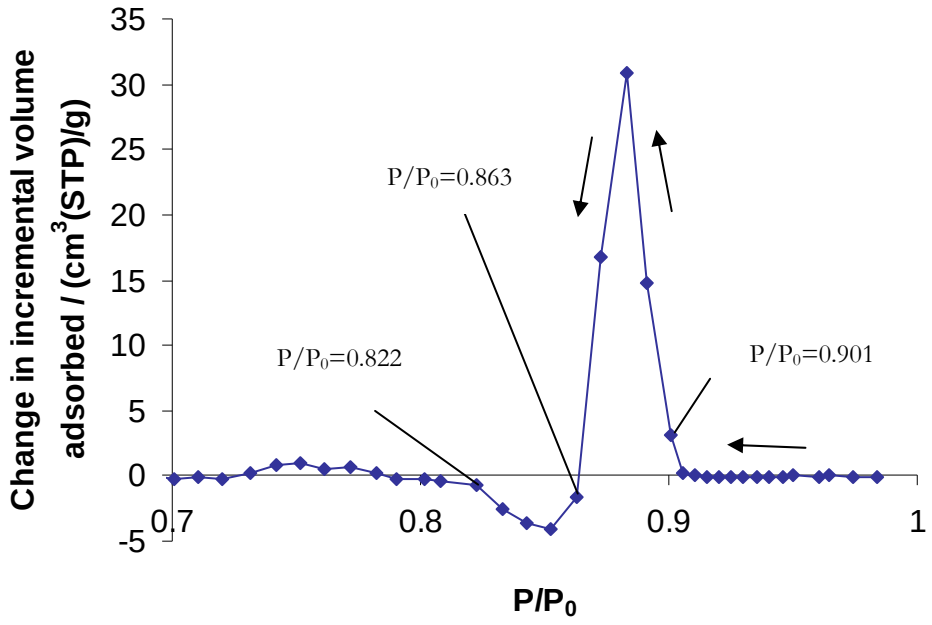

Figure 5.18 (b): Desorption change in incremental amount adsorbed plot for E2. Arrows have been added to indicate the direction of the change in pressure and lines have been added to guide the eye

5.5.4 Mercury porosimetry experiments

This section will present the mercury porosimetry data for the studied samples.

An example of a mercury intrusion and extrusion experiment for EA1 is shown in Figure 5.19. The intrusion curve is shown by the fixed line and the extrusion curve by the crossed squares. For clarity, arrows have been added to indicate the direction of the change in pressure. As you go from low to high pressure the mercury begins to intrude into the sample. At pressure of ~308 MPa no more mercury can intrude into the sample because all pores that are accessible to the mercury have become filled. When the pressure is lowered, there is a flat plateau region before the mercury extrudes from the sample, with the extrusion curve not overlaying the intrusion curve. In addition, at pressures below ~14 MPa, no more mercury extrudes from the sample, resulting in entrapment. Reasons for the hysteresis between the intrusion and extrusion pressures and why there is entrapment were discussed above.

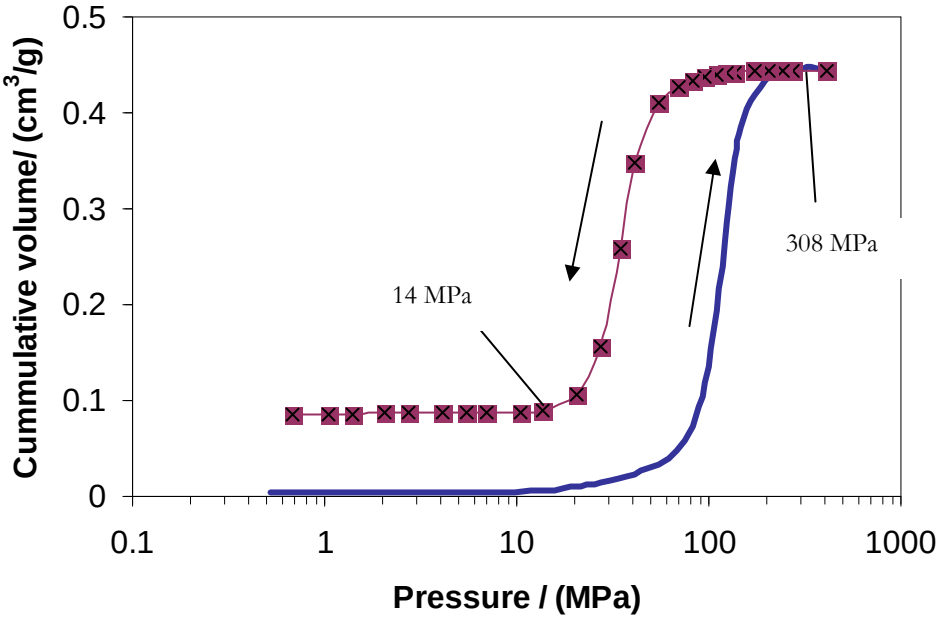

Figure 5.19: The experimental mercury porosimetry data. The intrusion curve (fixed line) and extrusion curve (crossed squares). Arrows have been added to indicate the direction of the change in pressure

To remove the contact angle hysteresis all mercury porosimetry data has been analysed using equation 5.3. The analysed data for EA1 is shown in Figure 5.20, where the x-axis now represents the pore radius (nm). It can be seen that when the contact angle hysteresis is removed the intrusion and extrusion curves overlay below pore radius size ~6 nm. This means for all pore sizes below 6 nm the cause of hysteresis was because of different contact angles between the mercury and the pore wall for the advancing and retreating mercury menisci. When the intrusion and extrusion curves diverge, it indicates that less mercury extrudes from the sample compared to the amount that was intruded. This means the pore size where the curves diverge is when mercury entrapment begins.

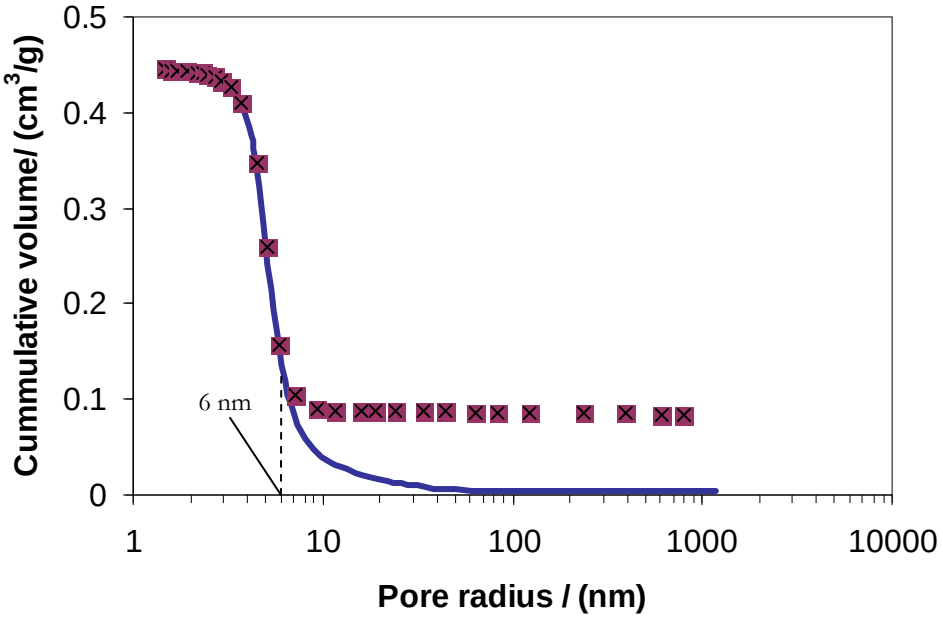

Figure 5.20 (a): Mercury porosimetry data analysed by equation 5.3 for EA1. The intrusion curve (fixed line) and the extrusion curve (crossed squares)

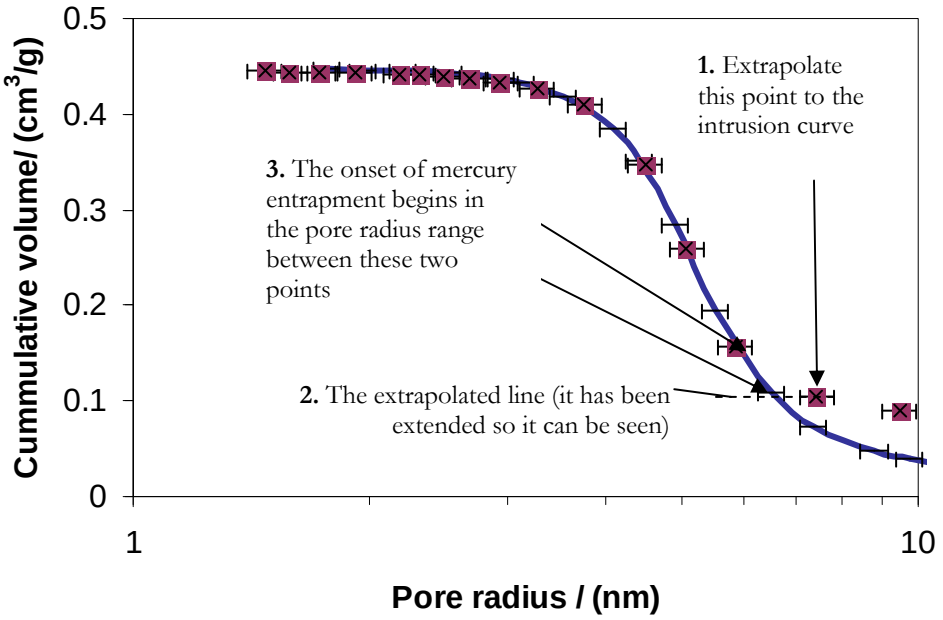

Figure 5.20 (b): An enlarged area of Figure 5.20 (a). The annotations are explained in the text

The exact pore size where the curves diverge cannot be calculated and this is explained as follows using Figure 5.20 (b). It will be assumed that the curves have diverged by the first point on the extrusion curve that is not within the error range of an equivalent volume data point on the intrusion curve. The exact point where the curves diverge will be between the previous extrusion data point and an extrapolated point on the intrusion curve (see Figure 5.20 (b)). It is this pore radius range that will be quoted.

For completeness, the mercury porosimetry data analysed by equation 5.3 is shown for S1 (Figure 5.21) and E2 (Figure 5.22). The pore radius range where mercury entrapment begins for all the studied samples is shown in Table 5.3.

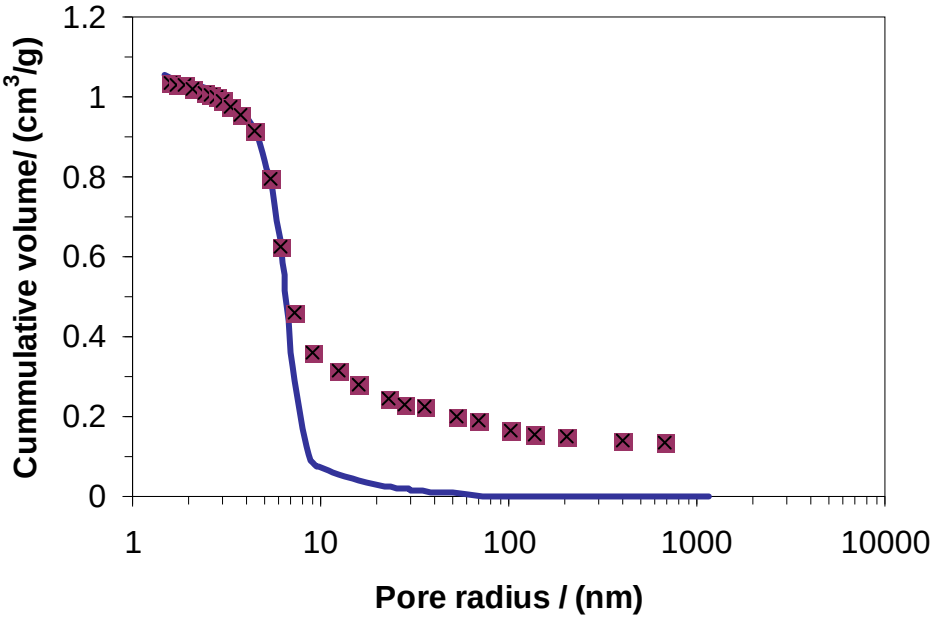

Figure 5.21: Mercury porosimetry data analysed by equation 5.3 for S1. The intrusion curve (fixed line) and the extrusion curve (crossed squares)

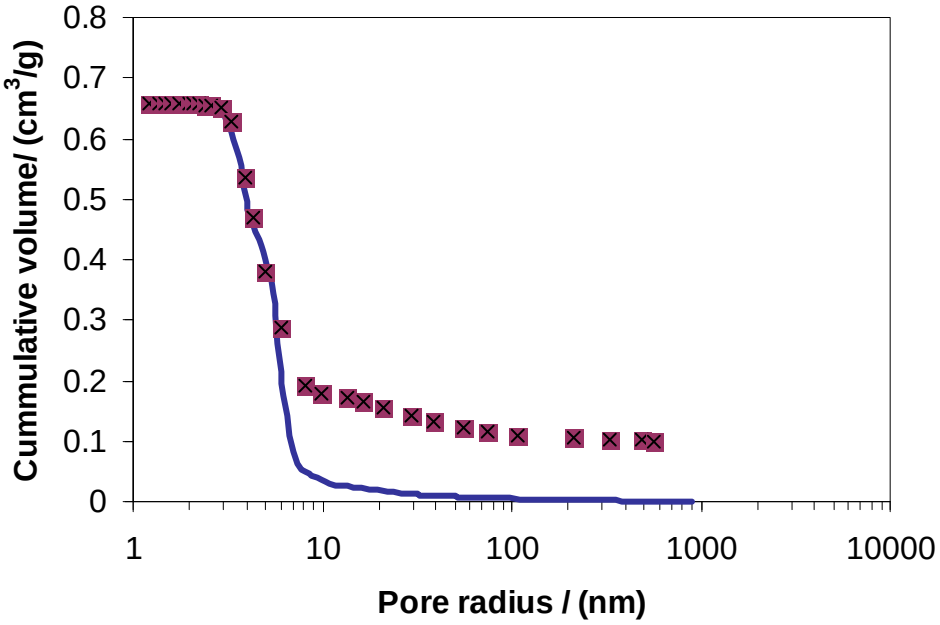

Figure 5.22: Mercury porosimetry data analysed by equation 5.3 for E2. The intrusion curve (fixed line) and the extrusion curve (crossed squares)

Sample	Pore radius size range where mercury entrapment begins/ (nm)
EA1	5.86-6.30
S1	6.17-6.60
E2	6.08-6.27

Table 5.3: The pore size at the onset of mercury entrapment from the analysed mercury porosimetry data using equation 5.3

5.6 Discussion

This Chapter has shown two methods to calculate the pore size where mercury entrapment begins. The two methods will be referred to as Method 1 and Method 2. Method 1 analyses the mercury porosimetry experiment, using the semi-empirical equation 5.3, to remove contact angle hysteresis. The point where the intrusion and extrusion curves diverge corresponds to the pores size where mercury entrapment begins. Method 2 uses the adsorption change in incremental amount adsorbed plot. The point where mercury entrapment begins is indicated by the start of the positive signal in the plot. The relative pressure at this point can then be converted to a pore size using equations 5.4 and 5.5. Since the studied samples in this Chapter are silica and alumina, equation 2.16 (see Chapter 2) will be used to calculate the value of t_c. In previous studies using S1, Rigby *et al.* (2008) found that if the thickness layer was assumed to be one monolayer of nitrogen, equation 5.4 gave a good prediction of the pore sizes which entrap mercury. The size of a nitrogen molecule is 0.354 nm (Rouquerol *et al.* 1999) and this thickness layer correction will also be made. Table 5.4 shows the pore radius size at the onset of mercury entrapment calculated from the change in incremental amount adsorbed plots. To aid the reader, the data from Table 5.3 has been included in Table 5.4.

Sample	P/P_0 at the onset of mercury entrapment	Calculated pore radius from P/P_0 / (nm)		Pore radius from Table 5.3/ (nm)
		Meniscus geometry		
		Cylindrical (equation 5.4)	*Hemispherical* (equation 5.5)	
EA1	0.848	3.25 (1) 4.04 (2)	**6.13** (1) 6.93 (2)	**5.86-6.30**
S1	0.923	**6.31** (1) 7.37(2)	12.25 (1) 13.32 (2)	**6.17-6.60**
E2	0.878	4.02 (1) 4.91 (2)	7.68 (1) 8.57 (2)	6.08-6.27

Table 5.4: The pore size at the onset of mercury entrapment obtained by analysing the adsorption change in incremental amount adsorbed plots using equations 5.4 and 5.5. (1) indicates t_c is equal to 0.354 nm and (2) indicates t_c is calculated using equation 2.16. Data from Table 5.3 has been included. Bold pore sizes show when the analysed gas adsorption data is the same as the analysed mercury porosimetry data

The calculated pore size at the onset of mercury entrapment using the two methods will now be discussed. For EA1, the onset of mercury entrapment using Method 1 was calculated to be in pores of radius 5.86-6.30 nm (Table 5.4). Method 2 calculates that mercury entrapment begins in pores of radius 6.13 nm when equation 5.5 is used with a value of t_c that is equal to a monolayer of nitrogen. This is within the pore size radius range of Method 1. When equation 5.4 is used the pore size radius that corresponds to relative pressure 0.848 is either 3.25 or 4.04 nm and not in the range 5.86-6.30 nm. It must be then that the pores in EA1 which entrap mercury fill by hemispherical menisci. For S1, the onset of mercury entrapment using Method 1 was calculated to be in pores of radius 6.17-6.60 nm (Table 5.4). Method 2 calculates that mercury entrapment begins in pores of radius 6.30 nm when equation 5.4 is used with a value of t_c that is equal to a monolayer of nitrogen. If equation 5.5 is used the calculated pore radius size at the onset of mercury entrapment is greater than 12 nm. It must be then that the smallest pores which entrap mercury in S1 fill by cylindrical shaped menisci. For E2, however, there appears to be no relationship between Method 1 and Method 2 to calculate the pore size where mercury entrapment begins. It is feasible that the pore shape in E2 is not cylindrical and so the Kelvin equation for a cylindrical shape pore cannot be used. When calculating a pore size distribution, it is common to use the BJH method assuming the pores are cylindrical in shape. This experimental test has shown that the experimental gas sorption data for E2 should not be analysed using the BJH method. In addition, the BJH method commonly uses equation 2.16 to account for the multilayer adsorption region. For samples S1 and EA1 it has been shown that when equation 2.16 is used the pore size is over estimated.

5.7 Conclusions

The test described in this Chapter has shown a method to determine whether a set of pores fill by hemispherical or cylindrical shaped menisci. It is important to determine the meniscus geometry as there is a potential factor of two error between the predicted pore size and actual pore size if the wrong meniscus geometry (in the Kelvin equation) is used. There are currently no other methods to determine the shape of the meniscus geometry.

The described method probes only the pores which entrap mercury. For the samples studied in this Chapter this accounts for ~ 15 % of the void volume. In Chapter 7, the reader will be introduced to scanning curve and scanning loop experiments, which can be used to determine the pore filling and emptying mechanisms in the pores which do not entrap mercury.

Chapter 6

Testing the single pore hysteresis mechanism

6.1 Introduction

Chapter 2 introduced the single pore hysteresis mechanism, which is summarised as follows. Cohan (1938) hypothesised that hysteresis was caused by the different shapes of menisci during adsorption and desorption in an open cylindrical pore. It was suggested that for capillary condensation gas adsorbs on pore walls, forming cylindrical shaped menisci, which propagate towards the centre of pores. Desorption, however, occurs from the pore ends and the shape of the menisci are said to be hemispherical.

Chapter 6 will now test the single pore hysteresis theory using the integrated gas-mercury-gas experiment. It will be shown that the pores in S1 which entrap mercury appear to fill and empty as independent cylindrical pores. In addition, it will be proposed that the theory suggested by Cohan (1938) over estimates the width of hysteresis in cylindrical pores. For background on single pore hysteresis the reader is diverted to Chapter 2.

6.2 Experimental

6.2.1 Samples studied

The sample studied in this Chapter will be the sol gel silica S1. S1 has a modal pore size of ~15 nm and a BET surface area of ~200 m^2g^{-1}. S1 is being used because the adsorption and desorption change in incremental amount adsorbed plots, seen in Chapter 5, are of similar shape. This is discussed in detail below.

6.2.2 Integrated gas-mercury-gas experiment

The integrated experimental procedure was identical to the previous Chapter, but argon sorption at 87 K was also studied. The integrated experiment was as follows:

1. Nitrogen sorption experiment at 77 K
2. Argon sorption experiment at 87 K
3. Mercury porosimetry experiment
4. Nitrogen sorption experiment at 77 K

5. Argon sorption experiment at 87 K

This procedure was also studied with the order of steps 1/2 and 3/4 reversed, with the reason for this change discussed below. The same sample was used in all the experiments to remove inter-batch variability. This means any difference between the nitrogen and argon experiments are because of the different properties of the two adsorbates.

6.2.3 Reasons for using argon as an adsorbate

In previous studies, argon has been used as an adsorbate to characterise porous solids because it is non-polar and so it has non-specific interactions with the adsorbent (Rouquerol *et al.* 1989). This means that if the adsorbent has localised polar groups, such as hydroxyl groups on silica, the argon molecules will not preferentially interact with either the oxygen or hydrogen atom. Nitrogen molecules, however, have a permanent quadrupole moment so they have a specific interaction with the hydroxyl groups. Argon, as an alternative adsorbate to nitrogen, has not been widely utilized in the literature because there is insufficient knowledge of its adsorption behaviour. For example, there is a limited amount of multilayer adsorption thickness data available (Gregg and Sing 1982; Kruk and Jaroneic 2000; Lowell *et al.* 2004), which means pores sizes cannot be correctly calculated. Morishige and Nakamura (2004) and Thommes *et al.* (2006) have used argon to improve the understanding of capillary hysteresis in mesoporous materials. For example Thommes *et al.* (2006) have compared argon desorption studies with nitrogen studies to determine whether desorption is controlled by pore blocking or cavitation. Morishige and Nakamura (2004) demonstrated that capillary condensation in cylindrical pores occurs at equilibrium by studying argon sorption experiments at different temperatures. These two studies were discussed in greater depth in Chapter 2 and the reader is referred back to this Chapter for more details. In the current Chapter, integrated argon-mercury-argon studies will be compared to the analogous nitrogen experiments to determine whether there are any differences between their capillary condensation and evaporation processes.

6.3 Analysis of data

The data in this Chapter will be analysed using the change in incremental amount adsorbed plots, as described in Chapter 5.

6.4 Results and discussion

The results and discussion section will first compare the adsorption and desorption change in incremental amount adsorbed plots that were presented in the previous Chapter for S1. Following this the results of the analogous argon experiments will be presented.

6.4.1 Nitrogen adsorption and desorption change in incremental amount adsorbed plots

The adsorption and desorption change in incremental amount adsorbed plots for S1, from the previous Chapter, have been overlaid in Figure 6.1. The area and shape of the positive deviations are approximately the same for the adsorption and desorption plots. The only difference appears to be that the adsorption change in incremental amount adsorbed plot is shifted to higher relative pressures. This is expected because $P_{adsorption}>P_{desorption}$, where P is pressure. The similar shapes would indicate that the pores which entrap mercury capillary fill and empty like independent pores and this can be explained using a counter example. The counter example will assume that the pores which entrap mercury capillary fill as independent pores, but the pores empty by a pore blocking mechanism. If this was the case, it would be anticipated that the desorption process would occur over a narrower pressure range. Experimentally this is not observed and therefore it must be that the adsorption and desorption processes, in the pores which entrap mercury, capillary fill and empty like independent (open) cylindrical pores.

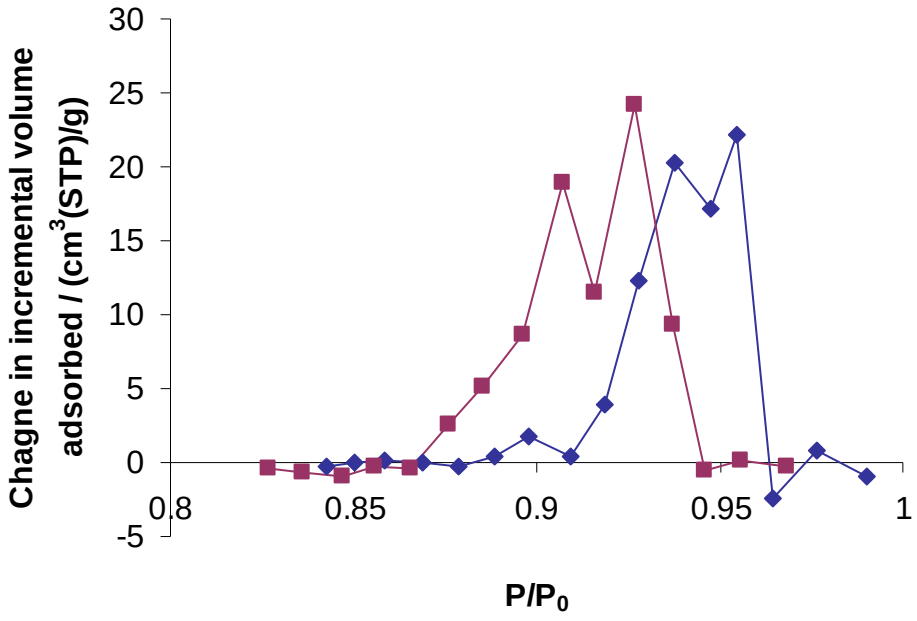

Figure 6.1: Adsorption (closed diamonds) and desorption (closed squares) change in incremental amount adsorbed plots for N_2 at 77 K. Lines have been added to guide the eye

In Chapter 2, the reader was introduced to the single pore hysteresis mechanism using the Kelvin-Cohan equations (Cohan 1938). Implicit in the equations, is the conception that, upon adsorption in an open cylindrical pore, gas adsorbs on the pore wall and capillary condensation occurs by the adsorbed gas propagating toward the pore centre (cylindrical meniscus). Desorption, however, can occur from both ends of the pore by hemispherical menisci. Due to the adsorption and desorption menisci geometries there is a relationship between the adsorption and desorption relative pressures, which is expressed as:

$$\left(\frac{P_{Desorption}}{P_0}\right) = \left(\frac{P_{Adsorption}}{P_0}\right)^2 \qquad 6.1$$

This relationship was discussed in Chapter 2.

Moreover, in previous studies Perkins *et al.* (2008) have demonstrated, using the cryoporometry technique (see Chapter 8), that the pores in S1 are cylindrical in shape. Therefore, the relationship in equation 6.1 can be tested using the pores in S1 which entrap mercury. This test has been carried out using the following method. All the pressures in the adsorption change in incremental amount adsorbed plot (closed diamonds in Figure 6.1) have been squared and the resultant plot has been overlaid with the desorption change in incremental amount adsorbed plot (Figure 6.2 (a)).

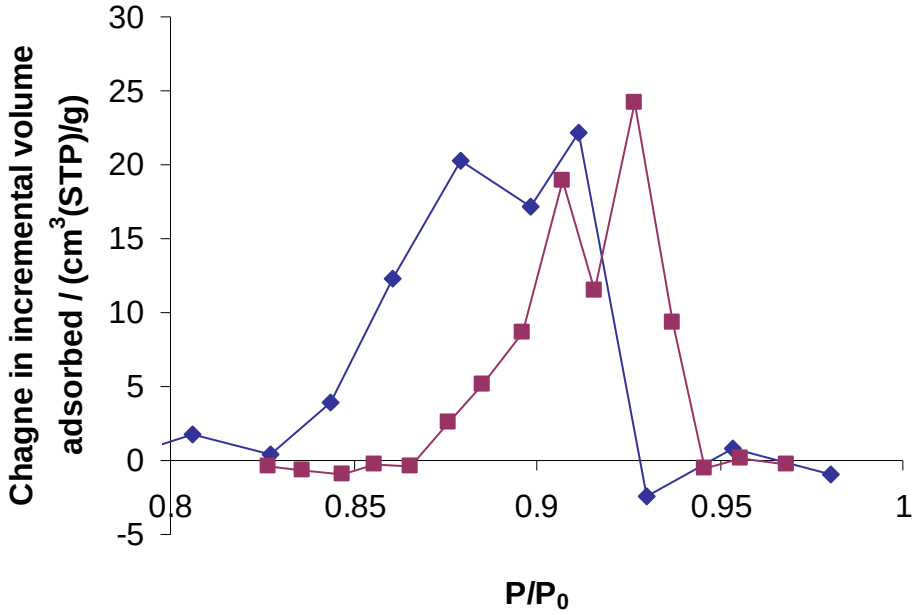

Figure 6.2 (a): The adsorption (closed diamonds) change in incremental amount adsorbed plot, for N_2 at 77 K, where all relative pressures have been squared. The desorption (closed squares) change in incremental amount adsorbed plot. Lines have been added to guide the eye

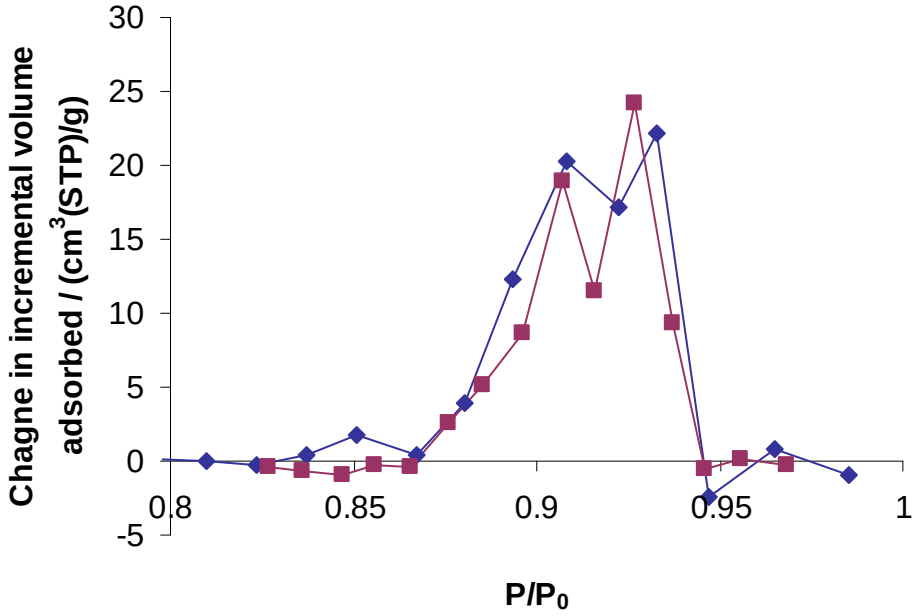

Figure 6.2 (b): The adsorption (closed diamonds) change in incremental amount adsorbed plot, for N_2 at 77 K, where all relative pressures have raised to the power 1.5. The desorption (closed squares) change in incremental amount adsorbed plot. Lines have been added to guide the eye

It can be seen in Figure 6.2 (a) that the adsorption change in incremental amount adsorbed plot now becomes shifted to lower relative pressures compared to the analogous desorption plot. This indicates that the width of hysteresis in the pores which entrap

mercury is narrower than what is predicted by the Kelvin-Cohan equations. Experimentally, it has been found, by the process of trial and error, that the relationship between the adsorption and desorption relative pressures, in the pores which entrap mercury, can be expressed by:

$$\left(\frac{P_{Desorption}}{P_0}\right) = \left(\frac{P_{Adsorption}}{P_0}\right)^{1.5} \qquad 6.2$$

This relationship is demonstrated in Figure 6.2 (b), which shows the adsorption change in incremental amount adsorbed plot overlaying the desorption plot.

Reasons why the experimental data does not obey the relationship in equation 6.1 have been discussed previously in Chapter 2. For example, it may be because the Kelvin-Cohan equations do not correctly predict the capillary condensation and evaporation processes in pores less than ~ 20 nm in diameter (Neimark and Ravikovitch 2001). This is because the Kelvin-Cohan equations are based on macroscopic properties such as the surface tension and contact angle between the liquid meniscus and the pore wall. It is believed that these assumptions are inappropriate for pores less than ~ 20 nm in diameter. Due to this, studies by Neimark and Ravikovitch (2001) advocate the use of DFT to calculate the size of cylindrical pores from experimental gas sorption studies. This is because DFT provides a microscopic model of the gas sorption process taking into account gas-gas, gas-liquid, gas-solid and liquid-solid interactions as well as the pore geometry. To verify their theoretical approach they have compared their studies to experimental gas sorption experiments using templated mesoporous materials such as MCM-41 (Ravikovitch *et al.* 1995) and SBA-15 (Ravikovitch and Neimark 2001). They report that there is a quantitative agreement between the theoretical isotherms, using DFT, and the experimental studies. This would then indicate that the DFT method can be used to correctly predict pore sizes from experimental gas sorption studies. However, there is an inherent problem with their method to check the theoretical approach, which is explained as follows. All their experimental studies use MCM-41 and SBA-15 materials that have pore sizes such that capillary condensation and evaporation occur in the relative pressure range ~0.4-0.7. The DFT calculations have not been compared to experimental data for larger pores where capillary condensation and evaporation happens above relative pressure 0.7. This is because there are no templated materials with pores which capillary fill and empty at these high relative pressures. Therefore, the DFT method to calculate pore sizes should not be used for systems where capillary hysteresis happens above relative pressure ~0.7. From the

discussions above it appears that the pores which entrap mercury in S1 capillary fill and empty as independent pores. Moreover, capillary condensation and evaporation in these pores happens above relative pressure 0.85. This means that S1 has suitably sized pores that can test the DFT calculations at relative pressures higher than ~0.7.

Neimark and Ravikovitch (2001) have calculated, using DFT, the adsorption and desorption isotherms in cylindrical pores of sizes 2-100 nm. In their studies they have plotted the capillary condensation relative pressures and capillary evaporation relative pressures for the different pore sizes. The data for their study was processed using the Data Thief programme and is shown in Figure 6.3 (a). The closed diamonds represent the capillary condensation transitions for the different size pores and the open squares represent the corresponding capillary evaporation transitions. Figure 6.3 (b) shows an enlarged area of Figure 6.3 (a), between relative pressures 0.85-1. By the process of trial and error the width of the hysteresis predicted by DFT has been tested. It has been found in this study that the relationship between the adsorption relative pressures and desorption relative pressures can be expressed by:

$$\left(\frac{P_{Desorption}}{P_0}\right) = \left(\frac{P_{Adsorption}}{P_0}\right)^{1.8} \qquad 6.3$$

This relationship is shown by the fixed line in Figure 6.3 (b). This means the width of hysteresis predicted by DFT in cylindrical pores is narrower than what the Kelvin-Cohan equations predict. However, the width of hysteresis predicted by DFT is wider than what is experimentally found for the pores in S1 which entrap mercury. If the width of hysteresis in S1 was determined by a pore blocking mechanism it would be anticipated that the hysteresis width would be wider than what is predicted by DFT. Experimentally, as stated, it has been found that the hysteresis is instead narrower for S1. This suggests that DFT does not correctly predict the adsorption and desorption processes in cylindrical pores that capillary fill and empty above relative pressures 0.85. This is the first time that experimental data has been used to test DFT calculations in pores that capillary fill and empty above relative pressure ~0.7.

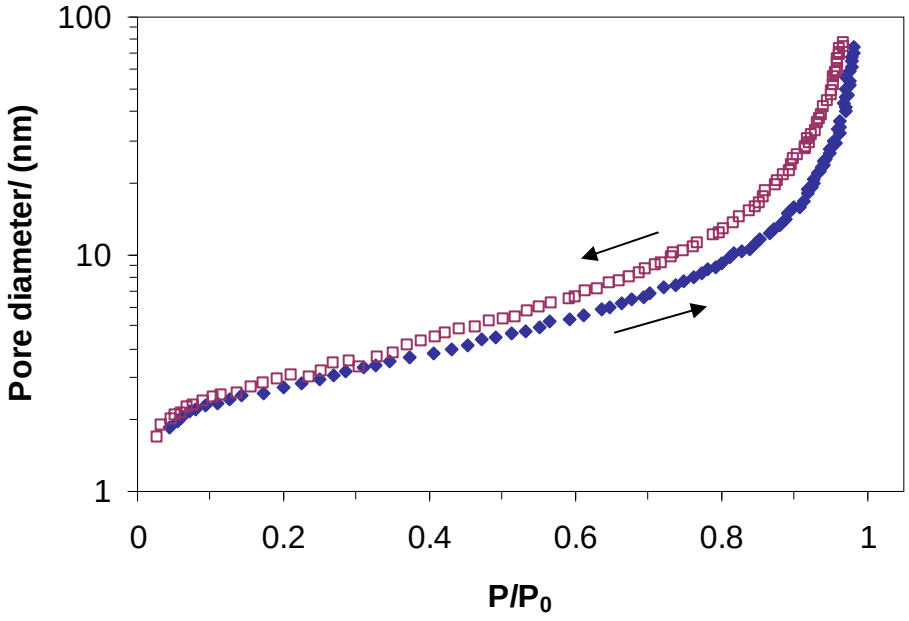

Figure 6.3 (a): This data is from Neimark and Ravikovitch (2001): Capillary hysteresis of N_2 in cylindrical pores at 77 K. The closed diamonds show the spinodal condensation pressure and the open squares the equilibrium desorption pressure. Arrows have been added to show the direction of the change in pressure

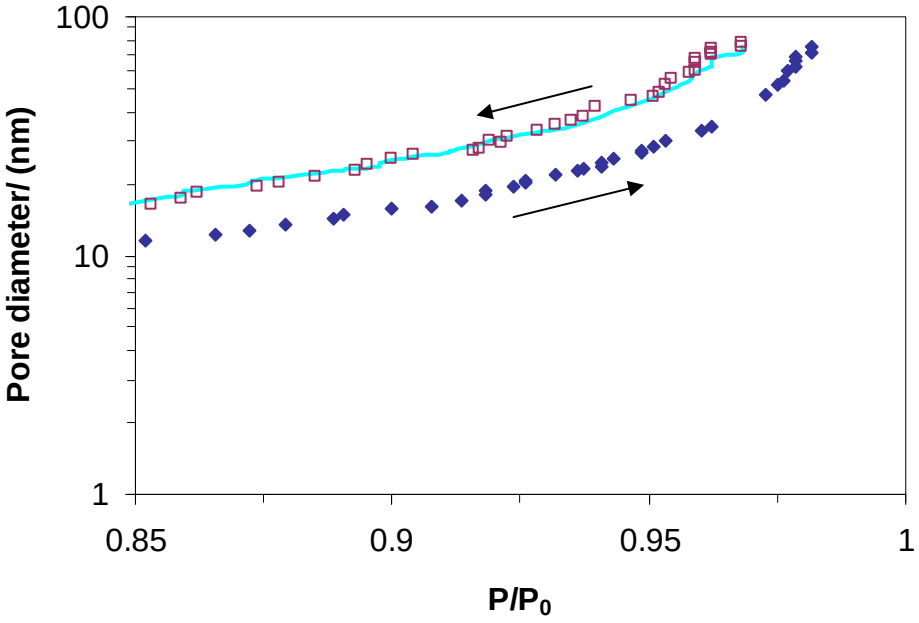

Figure 6.3 (b): An enlarged region of Figure 6.3 (a). The fixed line represents the relationship in equation 6.3. Arrows indicate the direction of the change in pressure

6.4.2 The hysteresis loop for the pores which entrap mercury

Using the adsorption and desorption change in incremental amount adsorbed plots the adsorption and desorption boundary curves, for the pores which entrap mercury, can be generated. This is done by cumulatively adding the adsorption change in incremental amount adsorbed or by cumulatively subtracting the desorption change in the incremental

amount adsorbed, for the adsorption and desorption curves respectively. The procedure to generate the adsorption curve is shown as follows. The adsorption change in incremental amount adsorbed plot in Figure 6.1 has been tabulated in Table 6.1 and the calculations to generate the adsorption curve (amount adsorbed) have been shown. Plotting the relative pressures against the amount adsorbed in Table 6.1 generates the adsorption boundary curve for the pores which entrap mercury. A similar procedure can be carried out to generate the desorption curve. The adsorption and desorption boundary curves for the pores which entrap mercury are shown in Figure 6.4. The hysteresis loop is of Type H1 (see Chapter 2), as the adsorption and desorption boundary curves are parallel. This is expected for a system that is made up of independent (open) cylindrical pores.

Starting amount at start (P/P_0=0.878) of the adsorption curve / $cm^3(STP)g^{-1}$	**Change in incremental amount adsorbed / $cm^3(STP)g^{-1}$**	**Calculation / $cm^3(STP)g^{-1}$**	**Adsorption curve (amount adsorbed) for the pores which entrap Hg / $cm^3(STP)g^{-1}$**
0	0.0	0.0+0.4	0.4
	1.8	0.4+1.8	2.2
	0.4	2.2+0.4	2.6
	4.0	2.6+4.0	6.6
	12.2	6.6+12.2	18.8
	20.3	18.8+20.3	39.1
	17.1	39.1+17.1	56.2
	22.1	56.2+22.1	78.3
	0.0	78.3+0.0	78.3
	0.0	78.3+0.0	78.3
	0.0	78.3+0.0	78.3

Table 6.1: Calculations showing how to generate the amount adsorbed for the adsorption boundary curve from the adsorption change in incremental amount adsorbed plot

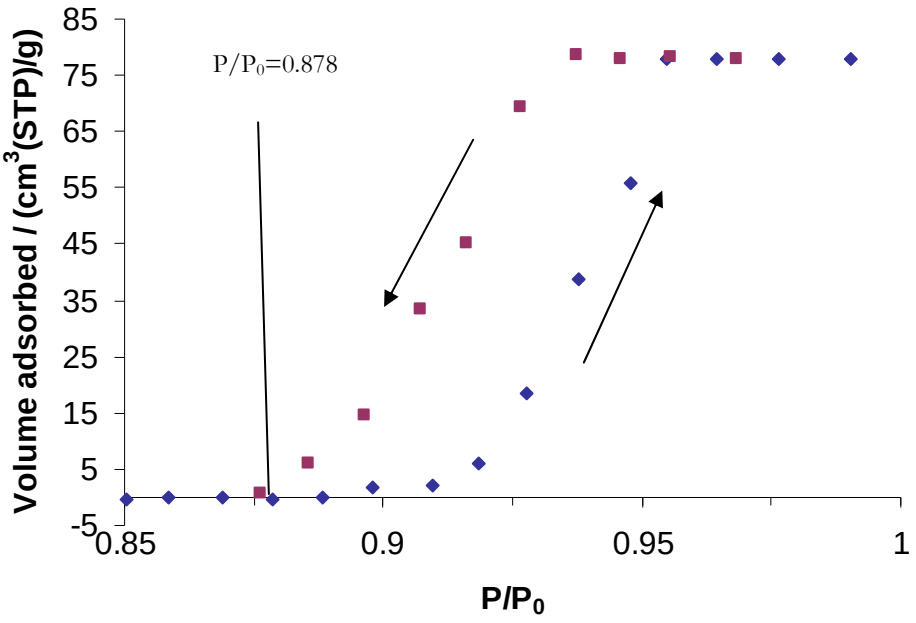

Figure 6.4: The adsorption (closed diamonds) and the desorption (closed squares) boundary curves for the pores which entrap mercury. The arrows have been added to indicate the direction of the change in pressure

6.4.2 Comparing argon gas sorption studies with the analogous nitrogen studies

The argon sorption isotherms before and after mercury porosimetry (between relative pressures 0.6-1) are shown in Figure 6.5. It is noted that the hysteresis regions are very similar to the analogous nitrogen isotherms for S1 (see previous Chapter). This suggests that the capillary condensation and evaporation mechanisms are similar for both adsorbates.

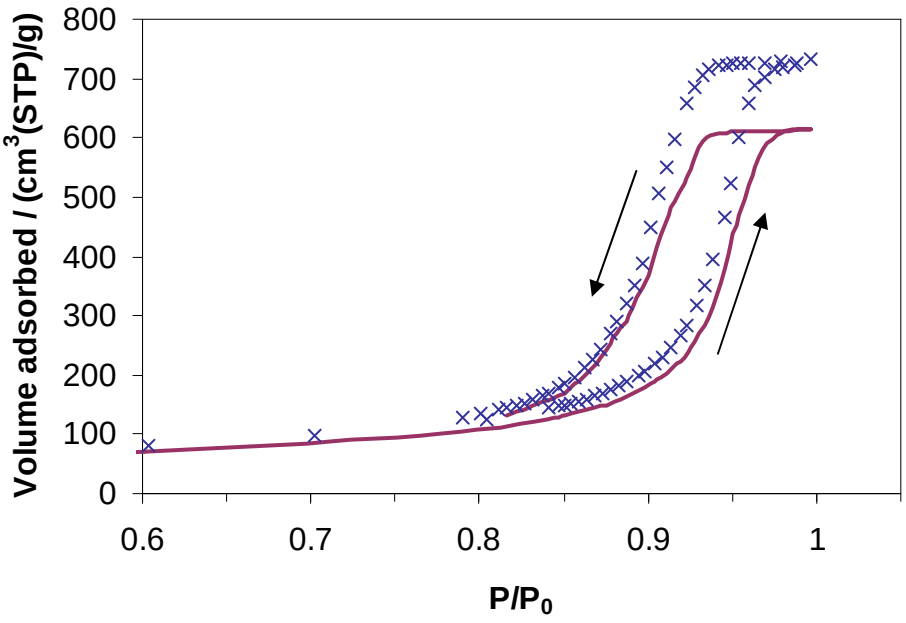

Figure 6.5: The hysteresis loop region of the argon 87 K gas sorption isotherm before (crosses) and after (fixed line) mercury porosimetry. Arrows have been added to indicate the direction of the change in pressure

The adsorption and desorption change in incremental amount adsorbed plots for argon are shown in Figure 6.6 (a) and (b). The adsorption change in incremental amount adsorbed plot is explained as follows. At relative pressure 0.913 there is a positive signal that continues to relative pressure 0.954. At relative pressure 0.959 the signal becomes negative which is not the same as the analogous nitrogen plot (see Figure 6.1). The desorption change in incremental amount adsorbed plot is of similar form to the adsorption plot and is explained as follows. At relative pressure 0.933 there is a negative signal and as the pressure is lowered the signal becomes positive (relative pressure 0.922). The signal remains positive until relative pressure 0.872. The negative signal indicates that following the mercury porosimetry experiment there are now more pores that fill at a higher relative pressure. This would then suggest that following mercury porosimetry there are larger pores in the sample. It is feasible that larger pores were created during the experimental procedure by a freeze thaw mechanism. When the sample is transferred from the mercury porosimeter to the gas sorption apparatus it will adsorb water from the atmosphere. This adsorbed water cannot be removed by heating the sample under vacuum as there is now mercury in the sample. Therefore, when the sample is studied by nitrogen gas sorption the water will freeze when the sample is cooled to 77 K. Following the nitrogen experiment the adsorbed water can thaw and this freeze thaw process may cause the sample to crack generating larger pores. To ensure that this was not the cause of the negative signal an experiment was carried out where the argon gas sorption experiment was studied before

the nitrogen gas sorption experiment. This would eliminate the freeze thaw mechanism before the argon gas sorption experiment. When the integrated gas-mercury-gas experiment was studied in this order the argon change in incremental amount adsorbed plots still had a negative signal while the analogous nitrogen plot did not. These plots are shown in Appendix A5. This indicates that the cause of the negative signal has to be because of difference in adsorbate-adsorbent interactions rather than a freeze thaw cycle generating larger pores.

A feasible explanation for the negative signal would be that the contact angle between mercury and argon is greater than the contact angle between the silica surface and argon. This can be explained in more detail using the Kelvin equation, introduced in Chapter 2, which is expressed as:

$$\ln(\frac{P}{P_0}) = -\frac{2\gamma V_m \cos\theta}{RT(r_p)} \qquad 6.4$$

Assuming that argon wets the surface of the silica the contact angle will be 0° and so the cosθ term in equation 6.4 is 1. Following mercury porosimetry, if the contact angle increases the cosθ term becomes less than 1. This means for a given pore radius the capillary condensation and evaporation process would occur at a higher relative pressure following mercury porosimetry. This would then explain why there is a negative signal in both the adsorption and desorption change in incremental amount adsorbed plots. For the analogous nitrogen plots there is no negative signal. This would indicate that the contact angle between silica and nitrogen and mercury and nitrogen are similar. Therefore, it must be that the sensitivity of argon at 87 K and nitrogen at 77 K to changes in surface chemistry are different.

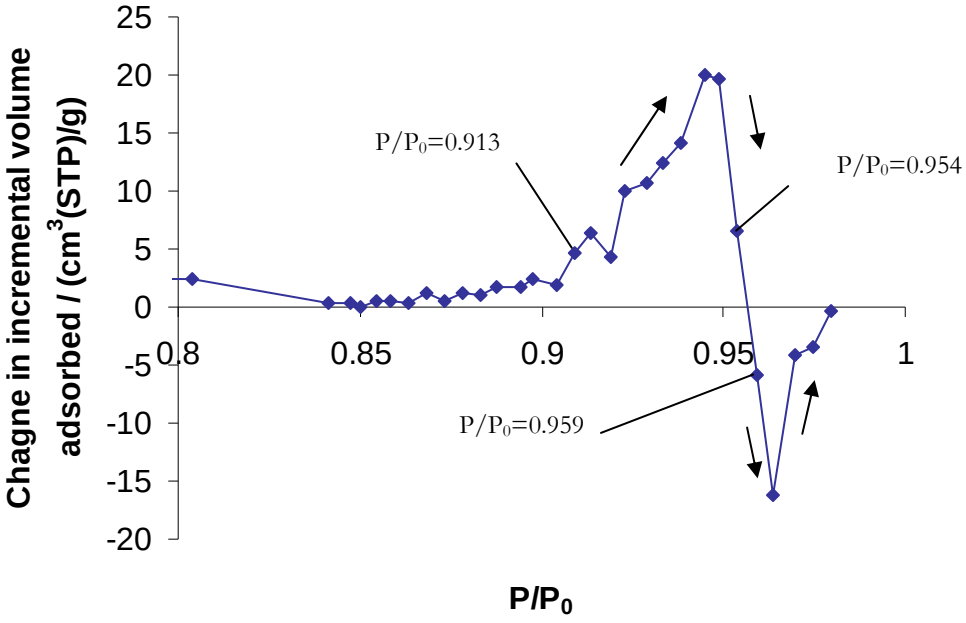

Figure 6.6 (a): The adsorption change in incremental amount adsorbed plot for argon at 87 K. Arrows have been added to indicate the direction of the change in pressure and lines to guide the eye

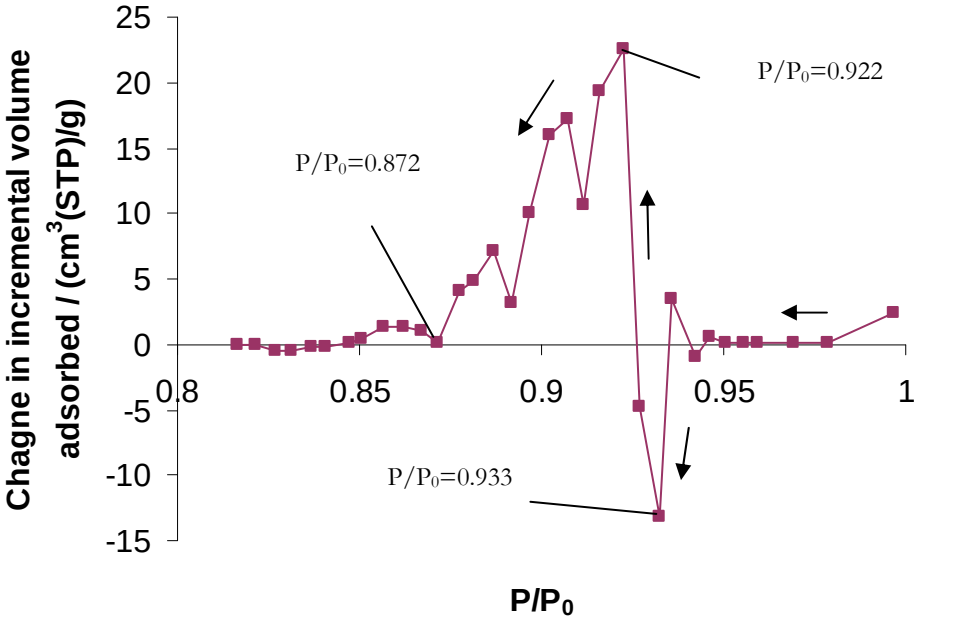

Figure 6.6 (b): The desorption change in incremental amount adsorbed plot for argon at 87 K. Arrows have been added to indicate the direction of the change in pressure and lines to guide the eye

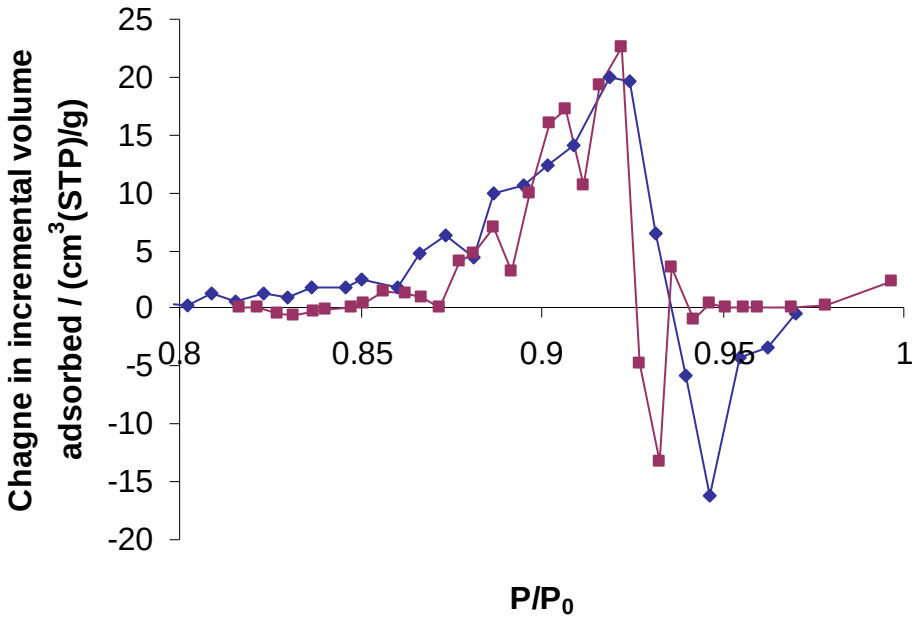

Figure 6.6 (c): The adsorption (closed diamonds) change in incremental amount adsorbed plot where all relative pressures have raised to the power 1.5. The desorption (closed squares) change in incremental amount adsorbed plot. Lines have been added to guide the eye

Due to the comparable shapes of the adsorption and desorption change in incremental amount adsorbed plots, they have both been overlaid in Figure 6.6 (c). In Figure 6.6 (c), all the pressures in the adsorption change in incremental amount adsorbed plot have been raised to the power 1.5. It can be seen that the positive deviation of the adsorption and desorption plots approximately overlay one another, but the negative deviations do not. This would be anticipated if the contact angle for the pores that contribute to the positive and negative deviations were different.

6.5 Conclusions

Using the integrated gas-mercury-gas experiment, it has been shown that the pores which entrap mercury in S1 appear to fill and empty as independent pores. The theories of both the Kelvin-Cohan equations and DFT calculations in open cylindrical pores have been tested. It has been found that the experimental width of hysteresis is narrower that what the two theories predict.

The integrated gas-mercury-gas experiment has been studied using argon and nitrogen. It has been shown that the adsorption and desorption mechanisms must be different for the two adsorbates used.

Chapter 7

Studies of gas adsorption-desorption scanning curves and scanning loops

7.1 Introduction

From Chapter 2, implicit in the Kelvin-Cohan equations (Cohan 1938), is the concept that, upon adsorption in an open cylindrical pore, gas adsorbs on the pore wall and capillary condensation occurs by the adsorbed phase propagating toward the pore centre. Chapter 2 then introduced the reader to an adsorption mechanism, originally put forward by de Boer (1958), termed advanced adsorption (Esparza *et al.* 2004). The mechanism suggests it can be possible for an open cylindrical pore to fill via a hemispherical meniscus, if a neighbouring pore becomes filled with condensate. In addition, from the Kelvin-Cohan equations, a pore that fills by a hemispherical meniscus will be twice the size of a pore that fills by a cylindrical meniscus, at the same pressure (see Chapter 2). It is, therefore, necessary to detect the advanced adsorption mechanism before interpreting gas adsorption data.

To test the theory of advanced adsorption, Chapter 4 used a spatially resolved technique (MRI). T_2 relaxation images showed that some of the largest pores of G2 (a sol gel silica sphere) were filled at a pressure where only approximately a third of the void space was filled with condensate. In addition, because the method was spatially resolved, it could be seen that the large pores, which had become filled with condensate, were connected to smaller necks. This supported the advanced adsorption mechanism, which occurs when small pores (necks) fill with condensate and then form hemispherical menisci that can ingress into large pore bodies. To help industry elucidate the pore filling mechanism more quickly, a new technique was introduced in Chapter 5. Gas adsorption experiments were studied before and after mercury porosimetry, and two independent methods were used to calculate the smallest pore size that entrapped mercury. Method 1 analyses the mercury porosimetry experiment using the Kloubek equations to determine the pore size at which mercury entrapment begins. Method 2 uses the change in incremental amount adsorbed plots, described in Chapter 5. The pore sizes, which entrap mercury, can then be calculated using, for example, the Kelvin equation, assuming either a cylindrical or hemispherical meniscus geometry. For S1 (a sol gel silica sphere), Method 1 calculated that mercury entrapment began in ~13 nm sized pores, which was the same as Method 2 when a

cylindrical meniscus geometry was assumed in the Kelvin equation. For EA1 (an alumina pellet), Method 1 calculated mercury entrapment began in ~12 nm sized pores, which was the same as Method 2 when a hemispherical meniscus geometry was assumed in the Kelvin equation. The test used in Chapter 5 was able to quickly determine whether a cylindrical or hemispherical meniscus geometry should be used in the Kelvin equation, to calculate a pore size.

Chapter 7 will now provide the reader with another experimental check to determine whether pores fill by cylindrical or hemispherical type menisci. The Chapter will demonstrate explicitly that S1 consists of pores that fill and empty via advancing and retreating hemispherical menisci, and that hysteresis can be virtually purged because of this mechanism. The types of experiments employed in Chapter 7 are termed gas sorption scanning curves and scanning loops (Tompsett *et al.* 2005). This Chapter will now define what scanning curves/loops are and it will then provide background literature to explain why they are used in gas sorption studies. Following this, the experimental studies for Chapter 7 will be presented and discussed.

7.2 Defining gas sorption scanning curves

Scanning curves in gas sorption studies are achieved through reversing the direction of pressure change at some point, on either of the boundary sorption curves. To distinguish between adsorption and desorption scanning curves, they will be defined in the following way. A desorption scanning curve will be achieved when the direction of the change in pressure is reversed on the adsorption boundary curve, before the upper closure point of hysteresis has been reached. For simplicity, each desorption scanning curve that is presented in this thesis will use open square shaped symbols, unless stated otherwise. An analogous reversal in pressure can take place on the desorption boundary curve, before the lower closure point of hysteresis has been reached, and this will be termed an adsorption scanning curve. Again, to help the reader, all adsorption scanning curves presented will use open diamond shaped symbols, unless stated otherwise. Figure 7.1 (a) and (b) show examples of adsorption and desorption scanning curves.

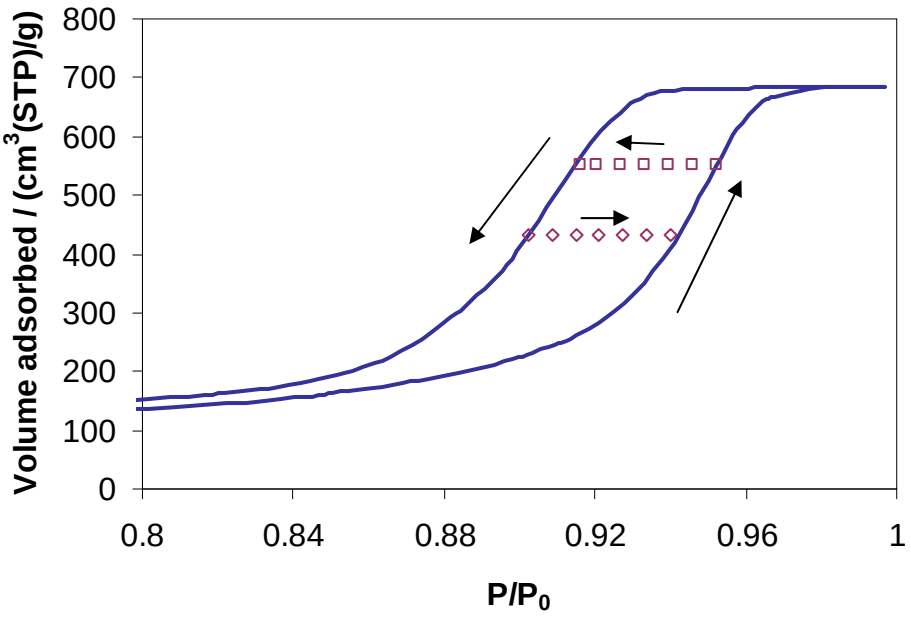

Figure 7.1 (a): Schematic of a crossing adsorption (open diamonds) and crossing desorption (open squares) scanning curves. Arrows are added to indicate the direction of the change in pressure. The boundary curves are shown by the fixed line

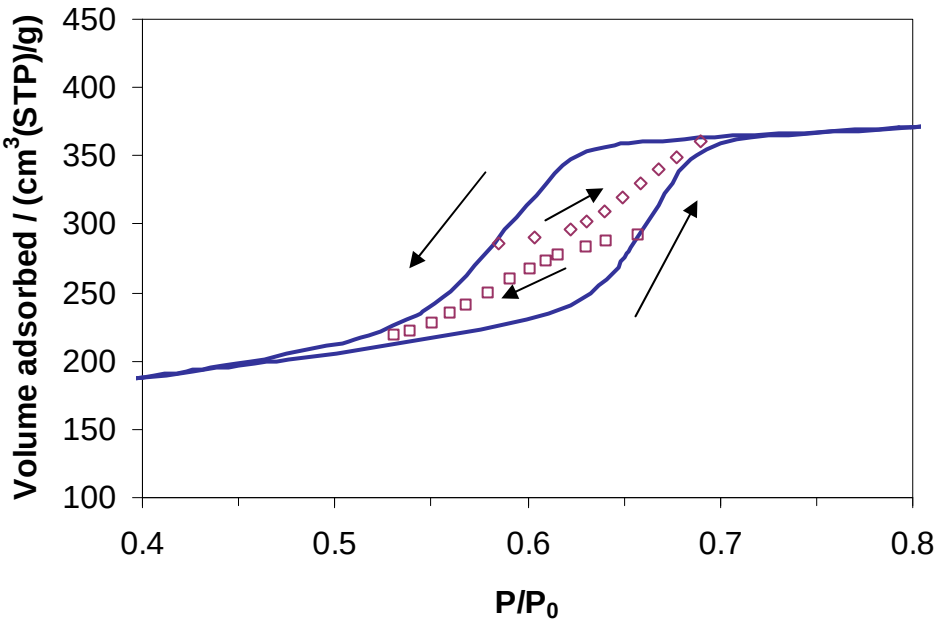

Figure 7.1 (b): Schematic of a converging adsorption (open diamonds) and converging desorption (open squares) scanning curves. Arrows are added to indicate the direction of the change in pressure. The boundary curves are shown by the fixed line

The scanning curves in Figure 7.1 (a) cross from one boundary curve to another and these scanning curves will be termed crossing scanning curves. For example, a desorption scanning curve that crosses from the adsorption boundary curve to the boundary desorption curve is a crossing desorption scanning curve. The adsorption and desorption

scanning curves in Figure 7.1 (b) converge to the upper and lower closure points of hysteresis respectively. These types of scanning curves will be termed converging scanning curves. For example, a desorption scanning curve that converges to the lower closure point of hysteresis is a converging desorption scanning curve.

In addition, it is not always the case that both the adsorption and desorption scanning curves cross between the boundary curves, or converge to the closure points of hysteresis. It is possible that adsorption scanning curves cross while the desorption scanning curves converge to the lower closure point of hysteresis. Such an example has been presented by Grosman and Ortega (2008) using SBA-15 as the adsorbent. Alternatively, the adsorption scanning curves can converge to the upper closure point of hysteresis while the desorption scanning curves cross. Tompsett *et al.* (2005) have reported this scenario when they studied scanning curves using MCM-41 as the adsorbent.

The next section will explain why scanning curves have been used in the literature and an explanation why scanning curves cross between boundary curves or converge to the closure points of hysteresis will follow.

7.3 Using gas sorption scanning curves to support pore models

Chapter 2 discussed the main theories that have been proposed to explain hysteresis, such as different adsorption and desorption mechanisms (Kelvin-Cohan equations) or pore blocking effects (McBain 1938). Moreover, it was shown that attempts, in the literature, have been made to link experimental results to the causes of hysteresis in models of the structure of porous materials. For example, it was discussed that Neimark and Ravikovitch (2001) simulated gas sorption experiments (DFT) in cylindrical type pore models to explain the experimental hysteresis in MCM-41 and SBA-15. In other studies, scanning curve experiments have been theoretically simulated and then compared to experimental scanning curves to validate hysteresis causes (Everett 1967; Mason 1988; Ball and Evans 1989; Kierlik *et al.* 2001). Typically, simulated scanning curve experiments are compared only qualitatively to experimental work, and if the simulated data looks "strikingly similar to those observed experimentally" (Kierlik *et al.* 2001) it is concluded that the simulation provides a description for the hysteresis phenomena.

7.4 An explanation of scanning curves

An early theory proposed to explain scanning curve experiments is termed independent domain theory, which developed over a number of publications (Everett and Whitton 1952; Everett and Smith 1954; Everett 1954; Everett 1955). Independent domain theory describes porous materials as being made up of microscopic domains, which are voids that are connected to adjacent domains. Each domain has a particular volume and will fill at a particular vapour pressure, P_a, and will empty at a vapour pressure, P_d. Each domain can only be filled or empty and so the theory ignores the multilayer adsorption of gas. The vapour pressure a domain fills at is greater than the pressure a domain empties ($P_a > P_d$), and this is the only cause of hysteresis in independent domain theory. This is because it is assumed that each domain does not interact with any of its neighbouring domains and, thus, the theory ignores pore blocking or advanced adsorption. Later work by Everett (1967) recognised independent domain theory was not the only explanation for hysteresis. This finding was based on studies by Brown (1963 cited by Everett 1967) on gas sorption scanning curve experiments for xenon on porous glasses. The experimental scanning curves were not qualitatively similar to the theoretical scanning curves from independent domain theory. Independent domain theory predicts that scanning curves should cross directly between the boundary sorption curves. However, the experimental adsorption and desorption scanning curves presented by Brown converged to the upper and lower closure points of hysteresis respectively. Everett, therefore, concluded that pore blocking effects (McBain 1938) had to play a significant role in hysteresis.

The next sub-sections will present to the reader theoretical scanning curve work that has been studied in the literature, using different pore models. This will explain why scanning curves either cross between the boundary curves or converge to the closure points of hysteresis. With this background knowledge, the experimental scanning curves studied for this thesis will then be presented.

7.4.1 Converging scanning curves

This sub-section will discuss scanning curves where the adsorption and desorption scanning curves converge to the upper and lower closure points of hysteresis respectively.

Mason (1988) used the pore blocking mechanism to explain why scanning curves converge at the closure points of hysteresis. In his studies, Mason used a pore model that consisted of cavities, which were connected to four other cavities by differently sized narrow necks. Mason assumed that each neck and cavity could fill independently of one another and so

ignored the advanced adsorption mechanism. However, for desorption, a cavity could not empty if all of the necks that it was connected to were filled, which is the pore blocking mechanism. Mason found, for his pore model, that the calculated adsorption and desorption scanning curves converged to the upper and lower closure points of hysteresis respectively. In addition, they were qualitatively compared to the experimental scanning curves of Brown (1963 cited by Everett 1967), discussed above, and were found to be very similar. Mason, therefore, concluded that the pore blocking effect was the reason why scanning curves converged at the closure points of hysteresis.

Mason ignored advanced adsorption, but later studies have calculated scanning curves that have accounted for both advanced adsorption and pore blocking effects (Coasne *et al.* 2005; Rojas *et al.* 2002). Coasne *et al.* used a pore model consisting of an assembly of dead end pores with an irregular cross section. To aid the reader, a schematic of a pore with an irregular cross section is shown in Figure 7.2, with each section labelled p1, p2, p3 and p4. Section p1 is closed at one end (dead end) and the cross section diameter of p2>p4>p1>p3. Coasne *et al.* assumed, for example, if p3 became filled with condensate and the neighbouring pore p4 was less than twice the size of p3, p4 would fill by advanced adsorption. In addition, if p1, p2 and p3 were filled, p2 and p1 would only empty once p3 had become empty (pore blocking). For such a pore model, the study calculated that both adsorption and desorption scanning curves would converge to the upper and lower closure points of hysteresis respectively.

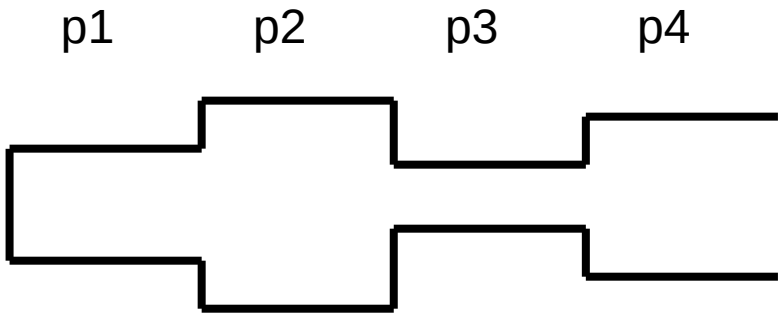

Figure 7.2: An example of a pore with an irregular cross section

Rojas *et al.* (2002) apply the same rules (as Coasne *et al.*) for advanced adsorption and pore blocking effects, but used a 3-dimensional network of cavities connected by narrow necks. They also calculated adsorption and desorption scanning curves for their pore model and the scanning curves converged to the upper and lower closure point of hysteresis respectively.

7.4.2 Crossing scanning curves

This sub-section will discuss scanning curves where both the adsorption and desorption scanning curves cross between the boundary curves.

It is generally thought that crossing scanning curves occur, in pore systems, when the pores fill and empty independently. This was originally predicted by independent domain theory (Everett 1954). To explain this in detail, a simple model will be used (Figure 7.3) and the corresponding gas sorption schematic, for the pore model, is presented in Figure 7.4. The pore model is made up of three domains, p1, p2 and p3, where the diameter of p3>p2>p1 and the volume of each domain is the same. The domains, although connected, do not interact with one another, so each domain will fill and empty independently. Furthermore, the domains will fill in order of increasing size, empty in order of decreasing size and the adsorption pressure is greater than the desorption pressure.

The corresponding gas sorption schematic (Figure 7.4) is now explained. The x-axis is the relative pressure, P/P_0, and the y-axis is the amount adsorbed, n^a. As the pressure is increased p1 becomes filled with condensate, which is indicated by position A. As the pressure is increased further p2 (position B) and then p3 (position C) become filled with condensate. On lowering the pressure p3 empties (position E), and on lowering the pressure further p2 empties (position F). The point where the pore model is completely empty of condensate has not been shown, in Figure 7.4, to improve the clarity of the schematic. In addition, desorption scanning curves can be achieved by reversing the direction of pressure change at positions A and B on the adsorption curve. Alternatively, adsorption scanning curves can be achieved by reversing the direction of pressure change at positions E and F on the desorption curve. The desorption scanning curve from position B to E will now be described in detail. At position B on the adsorption curve domains p1 and p2 are filled. On reversing the direction of pressure change, to start the desorption scanning curve, domain p2 will not empty until at least position E has been reached. The desorption scanning curve will therefore cross directly from the adsorption boundary curve to the desorption curve between positions B and E. An analogous explanation can be used to explain that the adsorption scanning curves will cross from positions E and F to positions B and A respectively.

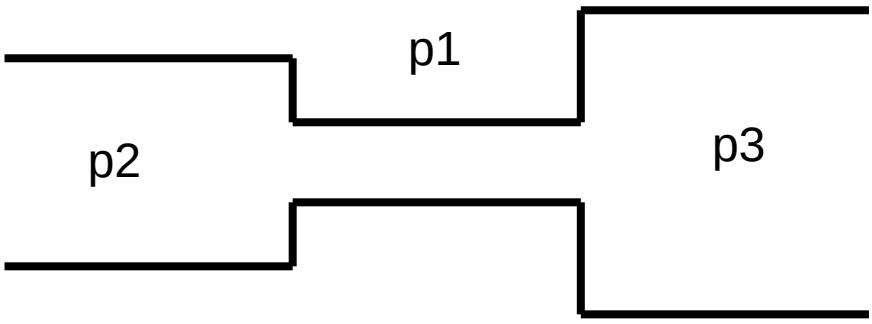

Figure 7.3: Pore model made up of domains. The diameter of domain p3>p2>p1

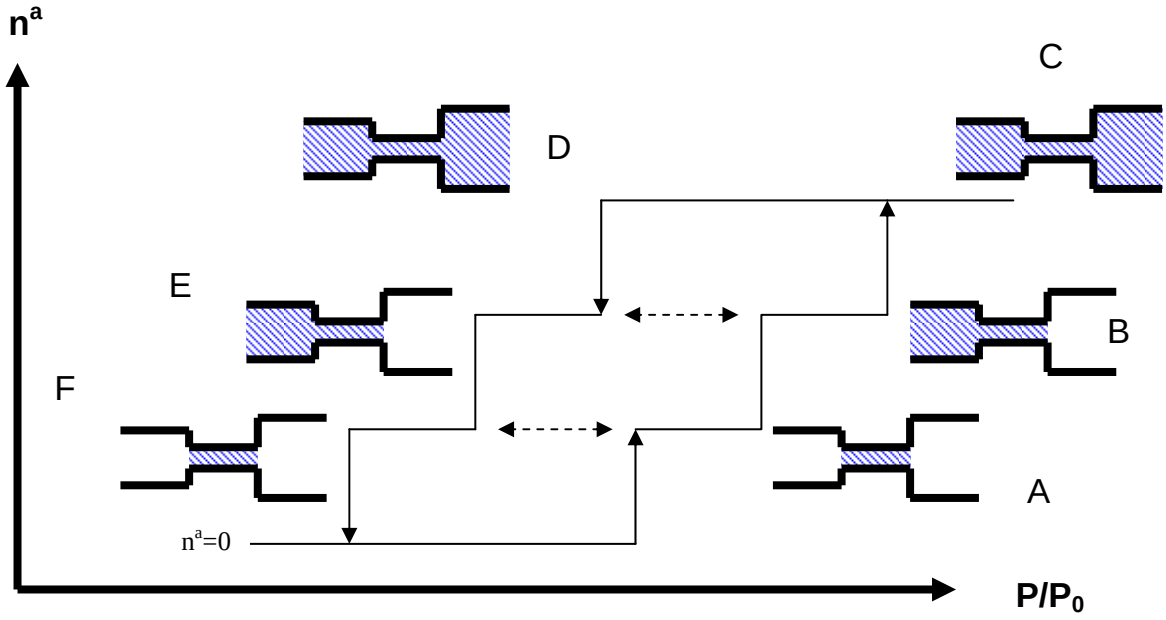

Figure 7.4: Gas sorption schematic for the pore model in Figure 7.3. The shading shows condensed gas and the text explains the schematic. For simplicity hemispherical menisci have not been shown, but the reader is referred back to Figures 2.2 and 2.3, if necessary, to understand the direction of the hemispherical shape

Tompsett *et al.* (2005) have explained that desorption scanning curves can also cross when pore blocking effects occur. This is now explained using the pore model shown in Figure 7.5, and its corresponding gas sorption schematic (Figure 7.6). The pore model (Figure 7.5) is made up of four domains, where the diameter of p3>p2=p2'>p1. In this pore model it is assumed that domains can interact, and they do so in the following way. Once p1 becomes filled with condensate a hemispherical meniscus can then ingress into the neighbouring domain, p2', which is the advanced adsorption mechanism. The domains p1, p2 and p3 will fill independently and so are not filled by an advanced adsorption mechanism. For desorption, p3 can empty only if p2 is empty of condensate and p2' can empty only if p1 is empty of condensate. In addition, the void volume of each domain is the same.

The gas sorption schematic is now explained as follows. As the pressure is increased p1 becomes filled with condensate, which fills p2' by an advanced adsorption mechanism (position A). As the pressure is increased further, p2 fills (position B) followed by p3 (position C). On lowering the pressure from position C, the condensate in p3 becomes metastable, as it is prevented from emptying by p2. When the pressure has been lowered to a point where p2 empties (position E), p3 will automatically empty as the pressure to empty this domain has already been passed. In addition, at position E the condensate in p2' is in a metastable state as it is blocked from emptying by p1. When the pressure is lowered further, p1 empties and p2' will then automatically empty. An example of a desorption and adsorption scanning curve, between positions A and E, is now explained as follows. At position A, p1 has become filled with condensate and p2' has filled by the advanced adsorption mechanism. The desorption scanning curve between positions A and E is achieved by reversing the direction of pressure change at position A. The desorption scanning curve will cross directly to position E, as the pressure at which p1 empties still has not been reached. In addition, p2' will not empty as it is blocked by p1. The adsorption scanning curve will also cross from position E to position A because the pressure to fill p2 will not be surpassed until position B. This is, therefore, an example of how scanning curves can cross between the boundary curves when domains interact with one another.

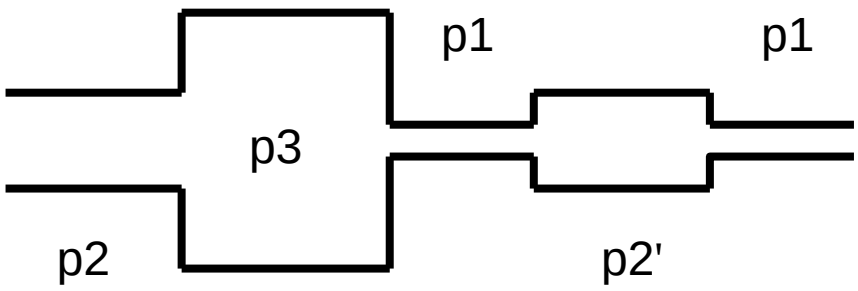

Figure 7.5: Pore model made up of domains. The diameter of domain p3>p2=p2'>p1

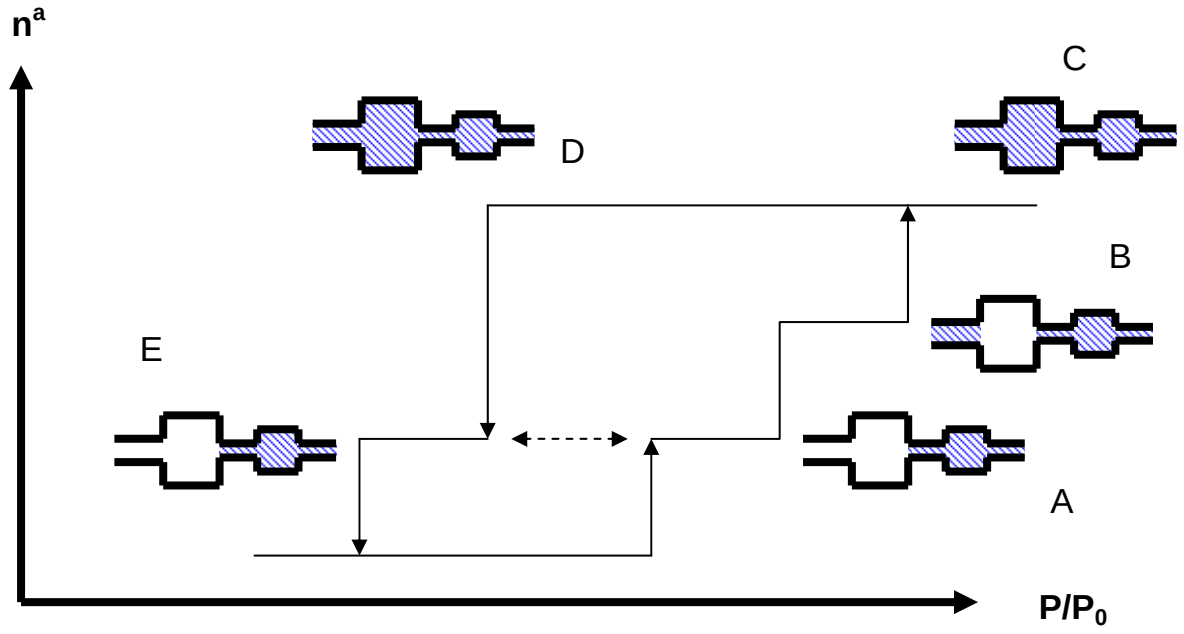

Figure 7.6: Gas sorption schematic for the pore model in Figure 7.5. The shading shows the condensed gas and the text explains the schematic. For simplicity hemispherical menisci have not been shown, but the reader is referred back to Figures 2.2 and 2.3, if necessary, to understand the direction of the hemispherical shape

Crossing desorption scanning curves have been shown experimentally by Ravikovitch and Neimark (2002). They studied the desorption scanning curves of a silica, termed FDU-1, which is made up of cavities that are surrounded by microporous necks. To explain the experimental result they used an ink bottle pore model (see Chapter 2), where the pore body was spherical shaped. They then studied the gas sorption process using the pore model, by DFT, and found that the desorption scanning curves crossed from the adsorption boundary curve to the desorption boundary curve. This was because the condensate in the spherical pore bodies was blocked from emptying by the narrow necks. In addition, because the necks were so small, the desorption scanning curves were able to cross to the desorption boundary curve before the pressure, at which the necks emptied, had been reached.

The above studies have shown that scanning curves that cross between the boundary curves are not necessarily because of thermodynamically independent pores. Morishige (2009), for example, experimentally studied desorption scanning curves for different CPGs and showed crossing desorption scanning curves. Morishige concluded that this showed the CPG could be described as a collection of thermodynamically independent pores. However, Ravikovitch and Neimark (2002) have shown that desorption scanning curves can cross even when there are cooperative effects between pores and Figure 7.6 has been used to aid the explanation.

7.4.3 Mixed scanning curves

Mixed scanning curves are when either of the following occurs: the desorption scanning curve converges to the lower closure point of hysteresis while the adsorption scanning curve crosses to the boundary adsorption curve. Alternatively, the adsorption scanning curve converges to the upper closure point of hysteresis and the desorption scanning curve crosses to the boundary desorption curve.

At the time of writing, only one study could be found where converging and crossing scanning curves were simulated at the same time (Puibasset 2009). The study used a pore model with an irregular cross section. Each different sized cross section was a domain and each domain could interact with its neighbouring domain. Puibasset then simulated a gas sorption experiment, using Monte Carlo simulations, and found the desorption scanning curve converged to the lower closure point of hysteresis, while the adsorption scanning curve crossed.

7.4.4 Summary of scanning curves

An explanation for scanning curves was originally proposed by Everett known as independent domain theory. However, this theory does not account for cooperative effects between pores and proposes an incorrect gas sorption mechanism, which assumes pores to be either filled or empty. Therefore, other works have been presented above, which have studied scanning curves and accounted for advanced adsorption and pore blocking mechanisms. These studies, conclude that scanning curves that converge to the closure points of hysteresis are due to cooperative effects between pores. However, scanning curves that cross can be either accounted for by independent pores or simple network effects.

7.5 Defining gas sorption scanning loops

A more complex scanning curve would be a scanning loop where the pressure is reversed, once more, but on the scanning curves. For example, using Figure 7.7, if the direction of pressure change is reversed on the adsorption boundary curve at position A, a desorption scanning curve would be initiated. If then the direction of pressure change is reversed once more at position B, before the scanning curve has reached either the desorption boundary curve or the lower closure point of hysteresis, a scanning loop is generated. This type of loop will be termed a desorption scanning loop. To help the reader, all desorption scanning loops in this thesis will be represented by closed square shapes, unless stated

otherwise. An analogous scanning loop can originate from the desorption boundary curve and will be termed an adsorption scanning loop. In this thesis all adsorption scanning loops will be represented by closed diamond shapes, unless stated otherwise.

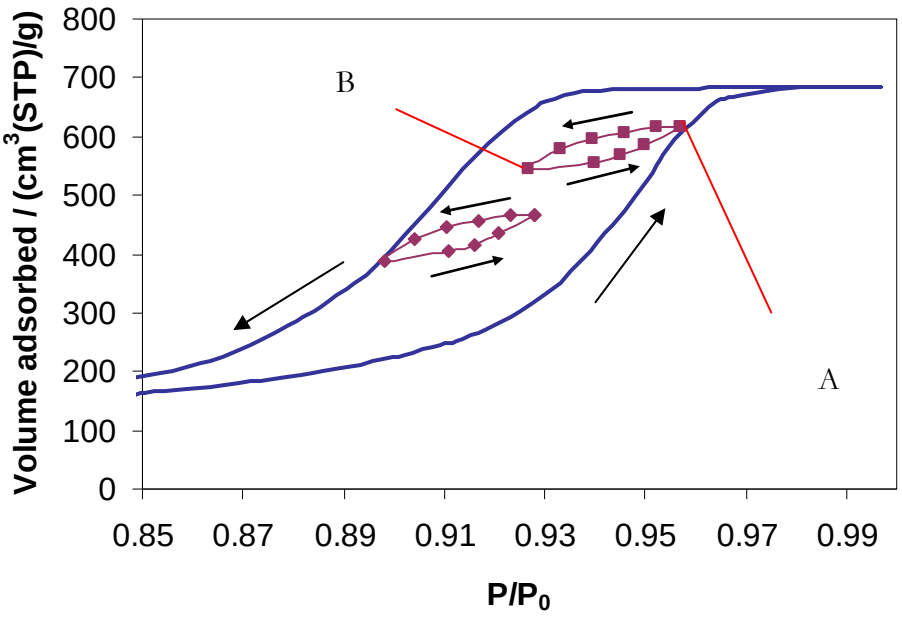

Figure 7.7: Schematic of an adsorption (closed diamonds) and desorption (closed squares) scanning loops. Arrows are added to show the direction of the change in pressure and the letters are referred to in the text

Grosman and Ortega (2008) have used scanning loops to determine whether SBA-15 is made up of independent cylindrical shaped pores. SBA-15 was introduced in Chapter 2, and is thought to consist of a 2-dimensional hexagonal array of cylindrical type pores, which are interconnected by micropores. Due to its structure, it is believed that each mesopore will fill and empty independently and, therefore, SBA-15 has been used as model porous materials to study gas sorption (Neimark and Ravikovitch 2001). If a porous material is made up of independent pores they will fill at, say, pressure P_a and empty at pressure P_d. Therefore, if a desorption scanning loop and an adsorption scanning loop span the same pressure range, the shape and size of the loops should be identical. If two shapes can be transformed into one another by translations or rotations they are said to be congruent. This test for congruent scanning loops was put forward by Everett and Smith (1954) as part of the independent domain theory. Grosman and Ortega (2008) used this test and found that desorption and adsorption scanning loops for SBA-15, studied over the same pressure range, were not congruent. From this result, they concluded that the pores of SBA-15 do not fill and empty independently. This test will explained in detail below and used to test whether the pores in S1 fill and empty independently.

7.6 Experimental

7.6.1 Studied materials

S1 and SBA-15 were studied for this Chapter. S1 is a sol gel silica sphere with a pellet size of ~3 mm. It has a modal pore size of ~15 nm and a BET surface area of ~200 m^2g^{-1}. SBA-15 is a silica material of powder form. It has a modal pore size of ~6 nm and a BET surface area of ~300 m^2g^{-1}. The SBA-15 sample was supplied by Prof. Alexei Lapkin and the preparation of the material is described in Lapkin *et al.* (2003).

7.6.2 Procedure

The gas sorption experimental procedure to study S1 was identical to the procedure in Chapter 5 and so the reader is referred back to this Chapter for details. However, in Chapter 7 the Micromeretics Scanning Loop software was used. The normal Micromeretics software only allows the user to reverse the direction of pressure change once. This means that adsorption scanning curves and scanning loops can not be studied using the normal software. The Micromeretics Scanning Loop software allows the user to reverse the direction of pressure change more than once and so allowed the study of scanning curves and scanning loops.

Within our research group, the characterisation of SBA-15 had previously not been studied and so suitable experimental conditions were unknown. In the literature, SBA-15 samples are heated to temperatures that vary from 120 °C (Grosman and Ortega 2005) to 300 °C (Tompsett *et al.* 2005). It therefore seemed reasonable to use the S1 experimental procedure for SBA-15. The equilibration time used for the SBA-15 sample was 20 s, and is explained as follows. The variation in the amount adsorbed, for a 20 and 40 s equilibration time, was studied for SBA-15. Both sorption results are overlaid in Figure 7.8 and the curves are within the experimental error of one another. The error bars have not been included because they are smaller than the symbols used for each data point. A 20 s equilibration time was therefore used for the SBA-15 sample.

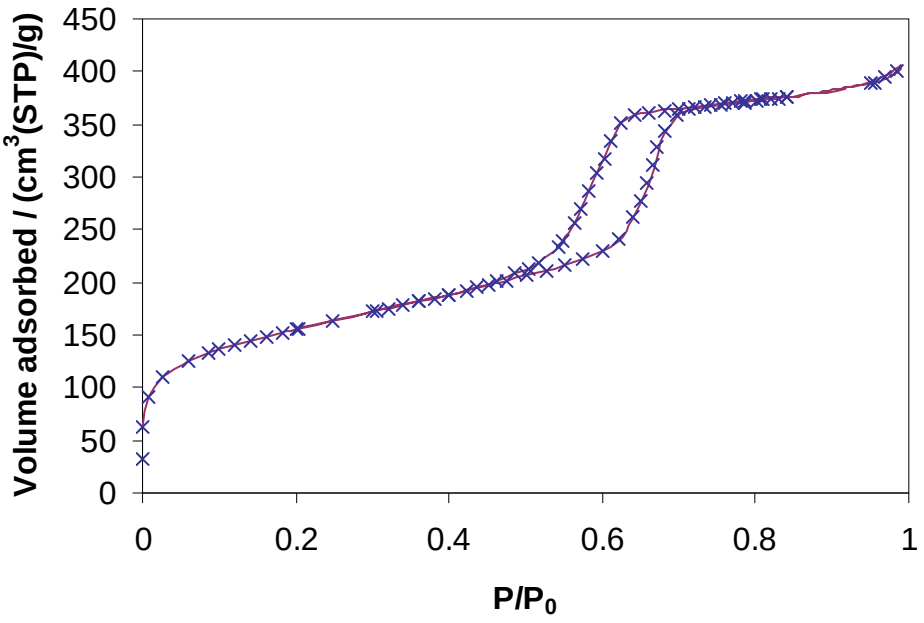

Figure 7.8: Gas sorption isotherm for SBA-15 using a 40 second equilibration time (fixed line) and 20 second equilibration time (crosses)

In addition, it was unknown whether the equilibration time used for the boundary curves was long enough for the scanning curves too. To check whether it was, adsorption and desorption scanning curves for SBA-15 were studied at different equilibration times (20 and 40 s) (Figure 7.9). The adsorption and desorption scanning curves overlaid for the two equilibration times. This indicated that an equilibration time of 20 s was long enough to study the scanning curves.

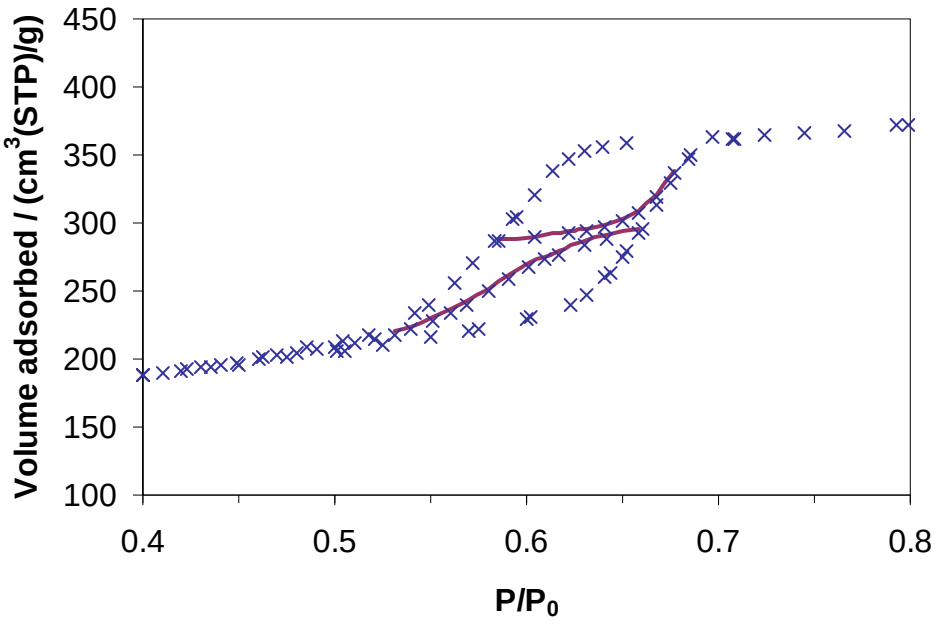

Figure 7.9: Gas sorption scanning curve isotherm for SBA-15 using a 40 second equilibration time (fixed line) and 20 second equilibration time (crosses)

7.6.3 Integrated gas-mercury-gas experiment

S1 was studied by the integrated gas-mercury-gas experiment. The experimental procedure presented in Chapter 5 is the same procedure used in Chapter 7.

SBA-15 was not studied by the integrated experiment as it was in powder form, making it impossible to be extracted from the mercury following a mercury porosimetry experiment. S1 is in pellet form and so can easily be extracted from the mercury using tweezers.

7.7 Results

The first set of results presented will be the gas sorption studies on SBA-15. The experimental results will be compared to similar SBA-15 studies from the literature.

Following the SBA-15 results, scanning curve and loop studies on S1 will then be presented to the reader. In addition, scanning curve experiments following mercury porosimetry will be compared to the analogous scanning curve experiments before mercury porosimetry.

7.7.1 Scanning curve results using SBA-15 as the adsorbent

As discussed in Chapter 2, SBA-15 is a mesoporous templated material that is thought to have a 2-dimensional hexagonal array of cylindrical pores that are interconnected by

micropores (Kruk *et al.* 2000; Ryoo *et al.* 2000). Therefore, it has been used as model pore materials to test the theories of gas sorption hysteresis (Neimark and Ravikovitch 2001).

The gas sorption isotherm obtained for SBA-15 is shown in Figure 7.10 (a) and (b), and the hysteresis loop has a H1 shape. The capillary condensation region will now be explained as follows, using Figure 7.10 (a), which has been annotated. At approximately relative pressure 0.623 capillary condensation begins and the closure point of hysteresis is approximately at relative pressure 0.711. When the direction of pressure change is reversed, to start the desorption process, capillary evaporation started at approximately relative pressure 0.622. Capillary evaporation continued to the lower closure point of hysteresis, which was at approximately relative pressure 0.461. Using equation 5.5 and a thickness layer that is equal to 0.354 nm, relative pressure 0.461 corresponds to a ~3.2 nm sized pore. This pore size is greater than the size of a micropore. Therefore, the micropores of SBA-15 must have remained filled with condensate at all pressures associated with the capillary hysteresis region. Thus, the micropores do not affect the capillary condensation and evaporation process in the mesopores (Grosman and Ortega 2005). The mesopores of SBA-15 should therefore fill and empty as thermodynamically independent pores. From the discussions above (Figure 7.4), this means the adsorption and desorption scanning curves, for SBA-15, should cross between the boundary curves.

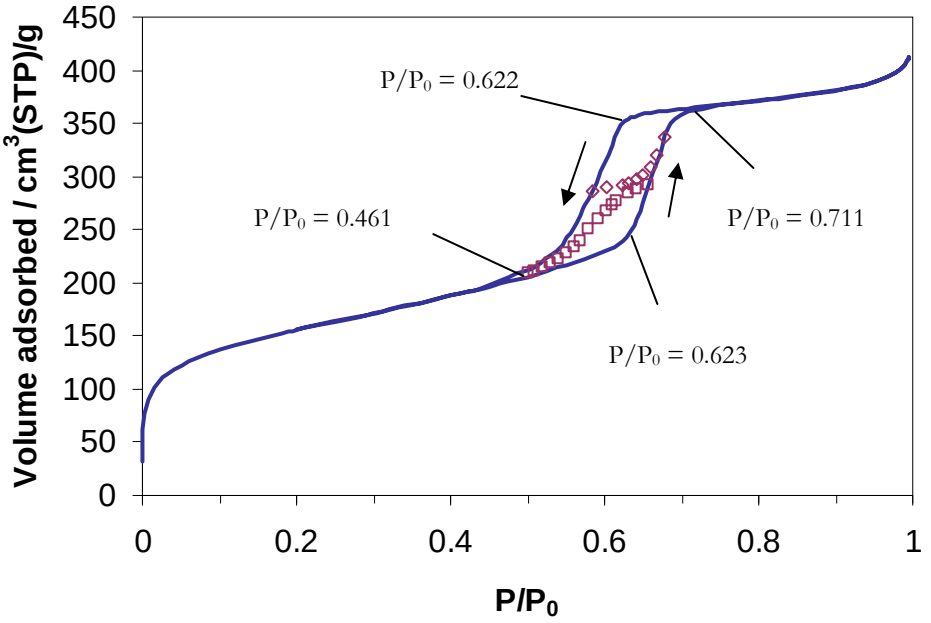

Figure 7.10(a): Boundary curves (fixed line) and desorption (open squares) and adsorption (open diamonds) scanning curves for SBA-15. Arrows have been added to indicate the direction of the change in pressure

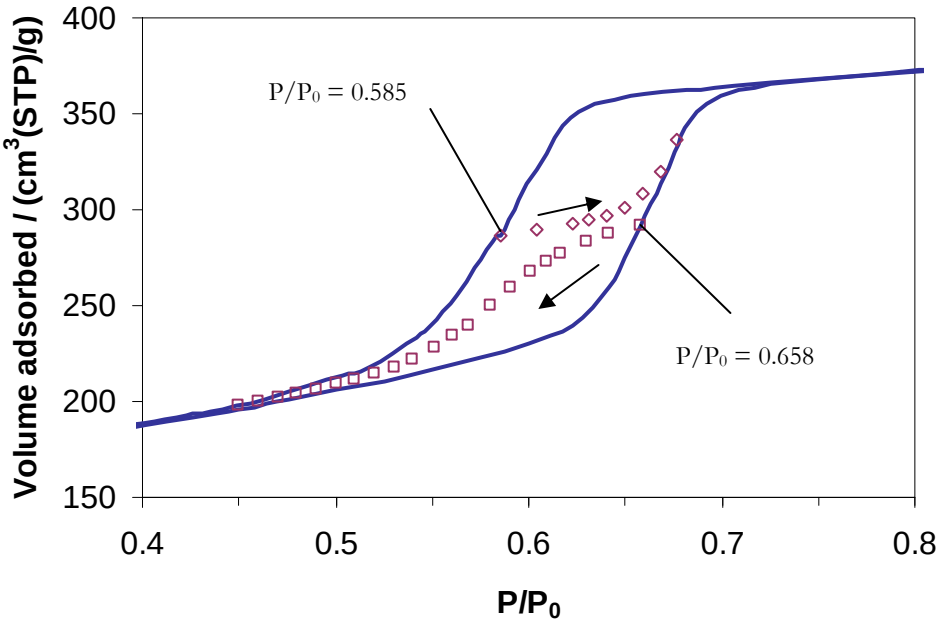

Figure 7.10(b): Boundary curves (fixed line) and desorption (open squares) and adsorption (open diamonds) scanning curves for SBA-15. Arrows have been added to indicate the direction of the change in pressure

Figure 7.10 (b) is of an enlarged area of Figure 7.10 (a) and will now be used to explain the adsorption and desorption scanning curves obtained for SBA-15. The desorption scanning curve (open squares) started at relative pressure 0.658 on the adsorption boundary curve, while the adsorption scanning curve (open diamonds) started at relative pressure 0.585 on the desorption boundary curve. It can be seen in Figure 7.10 (b) that the adsorption scanning curve crosses between the boundary curves. However, the desorption scanning

curve converges at the lower closure point of hysteresis. Theses results are in agreement with other work in the literature that studied scanning curves using SBA-15 as the adsorbent (Esparza *et al.* 2004; Grosman and Ortega 2005; Tompsett *et al.* 2005). From the discussions above, Puibasset (2009) suggested mixed scanning curves, of this form, occur for tubular type pores that have an irregular cross section. This would suggest that the mesopores in the studied SBA-15 sample have this pore structure. In addition, Esparza *et al.* (2004) earlier explained scanning curves for SBA-15, of this form, by suggesting the mesopores had an "undulating cross section nature". This meant that both advanced adsorption and pore blocking effects could occur in the each mesopore, which is explained as follows using Figure 7.11. Figure 7.11 shows an example of a pore with an irregular (undulating) cross section, where the diameter of section p4>p3>p2>p1. The advanced adsorption mechanism can occur if for example p1 fills with condensate first by a cylindrical type meniscus. This means that there is a hemispherical meniscus at either end of p1 that could potentially ingress into p3 or p4 by the advanced adsorption mechanism. Moreover, the pore blocking effect would occur if p1, p2, p3 and p4 were filled with condensate. On lowering the pressure, the condensate in p4 would be blocked from emptying until the condensate in p2 has emptied. Therefore, the type of pore structure proposed by Esparza *et al.* (2004) would potentially have cooperative effects for both adsorption and desorption processes. Thus, this would explain why the mesopores of SBA-15 do act as independent pores and why the scanning curves do not cross directly between the boundary curves. The experimental result of this thesis and those reported in the literature (Esparza *et al.* 2004; Tompsett *et al.* 2005), would suggest the mesopores of SBA-15 do not fill and empty as independent pores. In Chapter 2 it was discussed that Neimark and Ravikovitch (2001) have compared theoretical gas sorption data to experimental SBA-15 data. This was because they believe SBA-15 is made up of smooth independent cylindrical pores. The scanning curves studied here, and in previous studies (Esparza *et al.* 2004; Tompsett *et al.* 2005), indicate that the mesopores in SBA-15 do not fill and empty as independent cylindrical pores. This suggests experimental gas sorption studies using SBA-15 are not suitable to compare to theoretical gas sorption studies using cylindrical shaped pore models

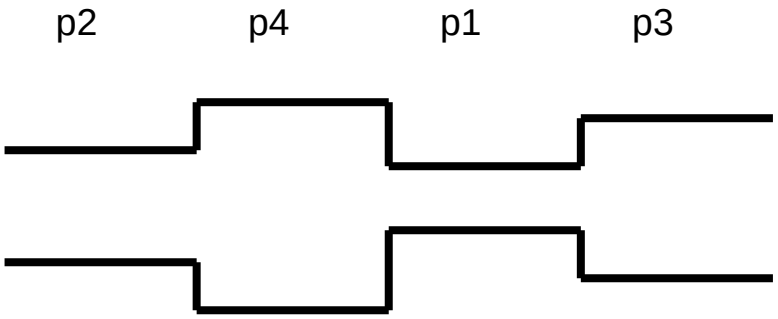

Figure 7.11: Pore model with an irregular cross section

7.7.2 Scanning curve results using S1 as the adsorbent

Boundary gas sorption studies on S1 were discussed in Chapter 5 and so only scanning curve/loops studies will be discussed in this Chapter.

Figures 7.12 and 7.13 show examples of various desorption and adsorption scanning curve experiments (open squares and diamonds respectively) for S1, together with the surrounding boundary sorption curves.

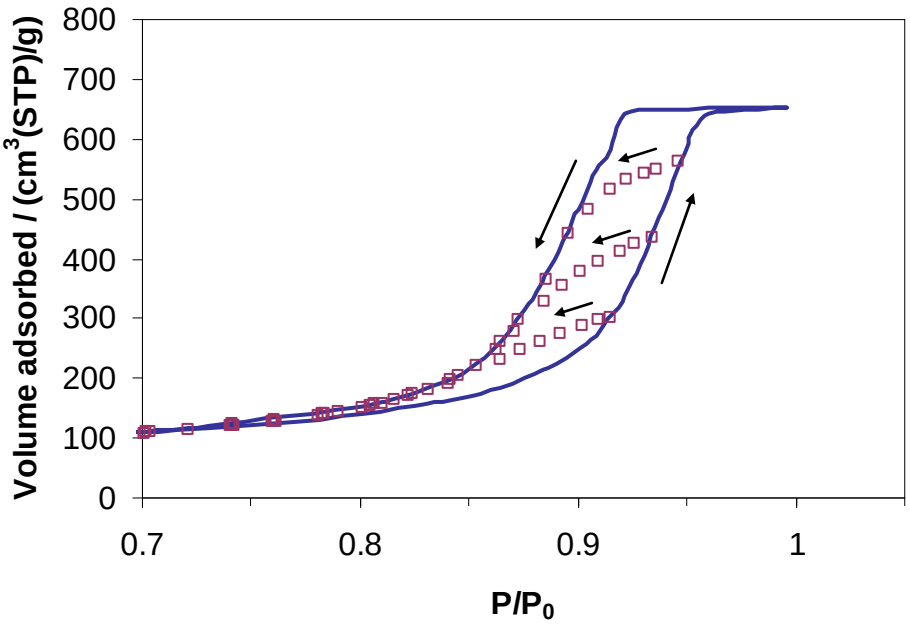

Figure 7.12: Desorption scanning curves (open squares) and the boundary curve (fixed line) for S1. Arrows are added to indicate the direction of the change in pressure

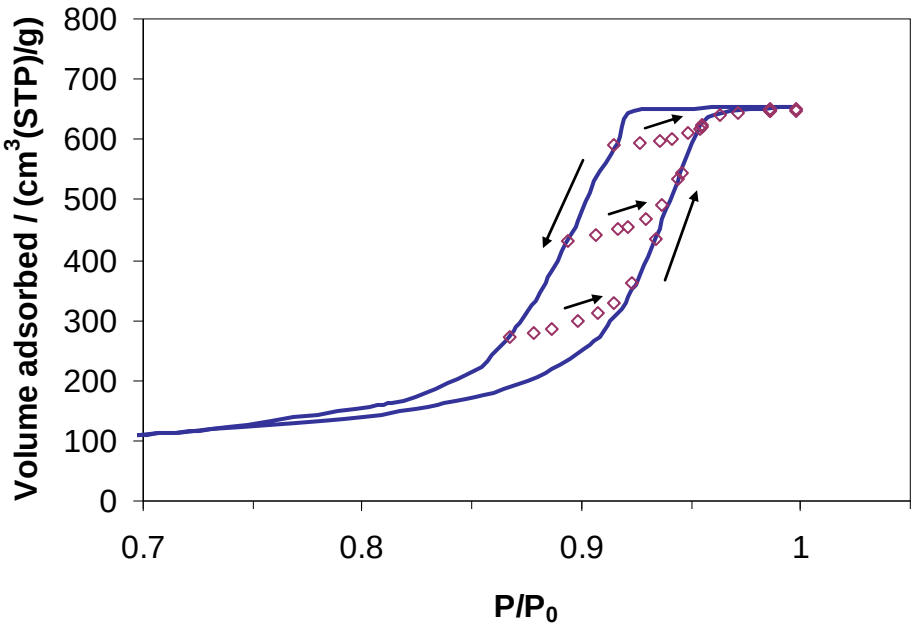

Figure 7.13: Adsorption scanning curves (open diamonds) and the boundary curve (fixed line) for S1. Arrows are added to indicate the direction of the change in pressure

A detailed description of a desorption scanning curve (Figure 7.14) is now given. On increasing the pressure from a virtual vacuum (relative pressure $5x10^{-5}$) to relative pressure 0.934, the direction of the change in pressure was reversed. At relative pressure 0.934 S1 was only partially saturated with condensate. On lowering the pressure, from relative pressure 0.934, the amount of adsorbed gas decreased immediately, which differed from the boundary desorption curve. Therefore, at the start of the desorption scanning curve there is, at least, one meniscus from which desorption can initiate from. Moreover, the immediate desorption indicates that some pores must be filling and emptying reversibly. This implies that these pores are filling and emptying by a hemispherical meniscus, as this filling and emptying mechanism is reversible. The rate of decrease in the amount adsorbed with respect to the change in pressure was not as great as for the boundary desorption curve. Therefore, the desorption scanning curve crossed to the boundary desorption curve at relative pressure ~0.871. The desorption scanning curve and boundary curve continued, from this pressure, to follow identical paths.

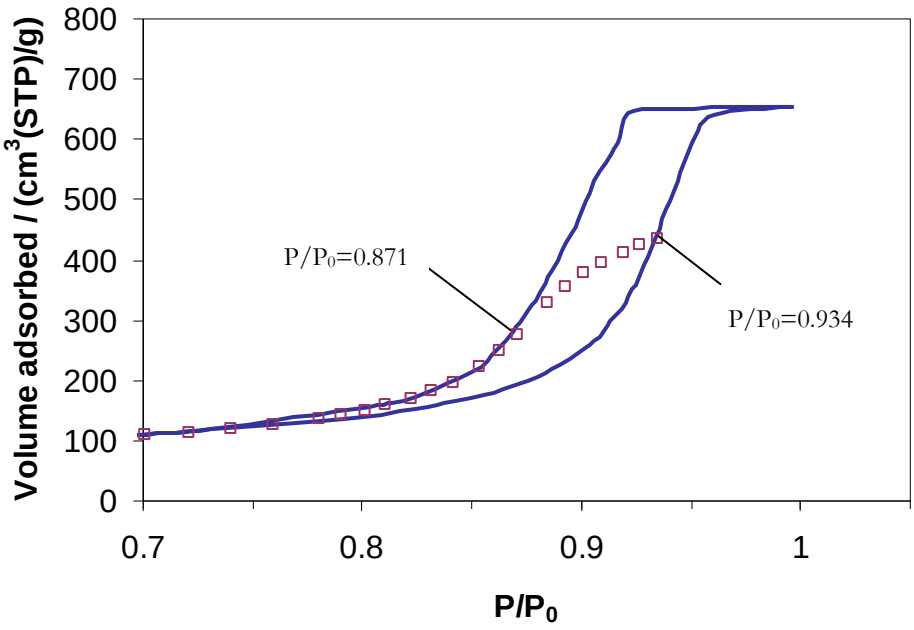

Figure 7.14: Desorption scanning curve (open squares) and the boundary curve (fixed line) for S1. A detailed explanation is given in the text

The form of the adsorption scanning curves, shown in Figure 7.13, are comparable to the desorption scanning curves. A detailed description of an adsorption scanning curve, shown in Figure 7.15, will now be given. On complete pore filling (relative pressure 1) the pressure of the system was lowered to relative pressure 0.894 and at this pressure the direction of the change in pressure was reversed. At relative pressure 0.894, S1 was partially filled with condensate. When the pressure was increased the amount of adsorbate increased immediately and the scanning curve crossed to the boundary adsorption curve at relative pressure 0.946.

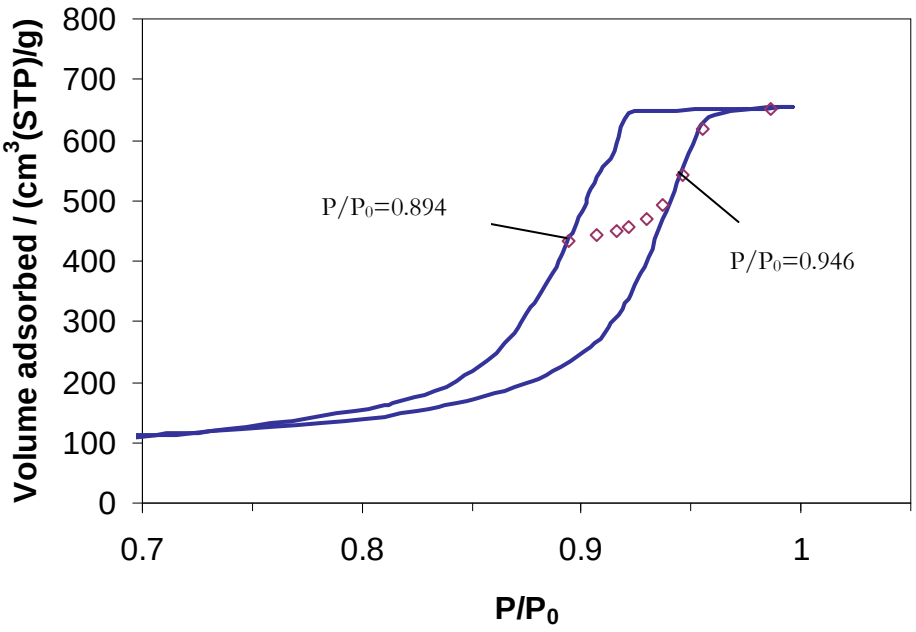

Figure 7.15: Adsorption scanning curve (open diamonds) and the boundary curve (fixed line) for S1. A detailed explanation is given in the text

Moreover, the pressure range over which the adsorption scanning curve spanned corresponded to a region on the adsorption boundary curve where there was capillary condensation. This is in contrast to the desorption scanning curve, as the boundary desorption scanning curve was flat at the start of the desorption scanning curve (Figure 7.14). This led to the suggestion above that there were pores which were filling and emptying reversibly at the start of the desorption scanning curves. A similar conclusion cannot be drawn for the adsorption scanning curve. This is because it is feasible, if pores do not fill and empty with incremental size, that the adsorption scanning curve corresponds to the filling of the same set of pores that fill on the boundary adsorption curve, over the same pressure range. Alternatively, it may be that the amount adsorbed, immediately after the direction of pressure change was reversed, corresponded to an advanced adsorption mechanism. This is reasonable because when the direction of pressure change is reversed, S1 is partially filled with condensate. Therefore, hemispherical menisci would exist at the ends of filled pores and could ingress into neighbouring pores when the direction of the change in pressure was reversed. From the adsorption scanning curves alone it was not possible to disambiguate the different mechanisms involved so further studies were required.

7.7.3 Scanning loop results using S1 as the adsorbent

To further understand the mechanism involved in gas sorption studies, of S1, more complex scanning curve experiments, scanning loops, were investigated. Figure 7.16 (a) shows two scanning loops that have been studied in this work and a detailed description of the scanning loops in Figure 7.16 (b) are given as follows. The desorption scanning loop: the pressure was increased from a virtual vacuum to relative pressure 0.935. At this relative pressure the direction of the change in pressure was reversed to start a normal desorption scanning curve and the amount adsorbed decreased immediately. At relative pressure 0.904 the direction of pressure change was reversed once more and the amount adsorbed immediately increased. As the pressure was increased further, the scanning loop path intersected the starting point of the scanning loop and then continued to follow the adsorption boundary curve. An analogous explanation is now given for the adsorption scanning loop: at relative pressure 0.904, on the desorption boundary curve, the direction of the change in pressure was reversed. As the pressure was increased the amount of adsorbed gas increased immediately. The pressure was increased to relative pressure 0.936 and at this point the direction of pressure change was reversed again. When the pressure was reduced the amount adsorbed immediately decreased. In addition, as the pressure was lowered further, the scanning loop trajectory intersected the start position of the scanning loop and it then continued to follow the path of the desorption boundary curve.

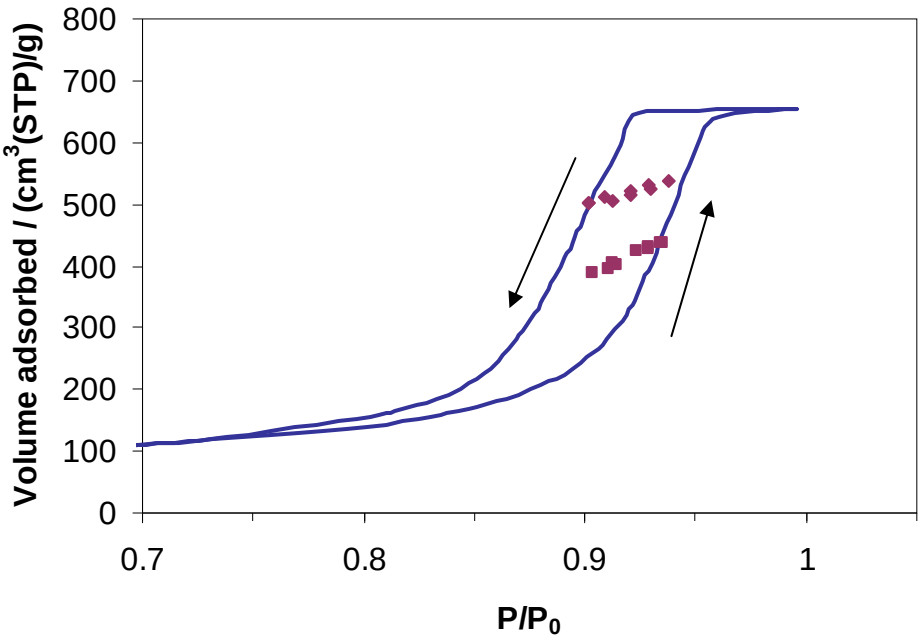

Figure 7.16 (a): Adsorption scanning loop (closed diamonds) and a desorption scanning loop (closed squares) within the boundary curve (fixed line) for S1. Arrows are added to indicate the direction of the change in pressure

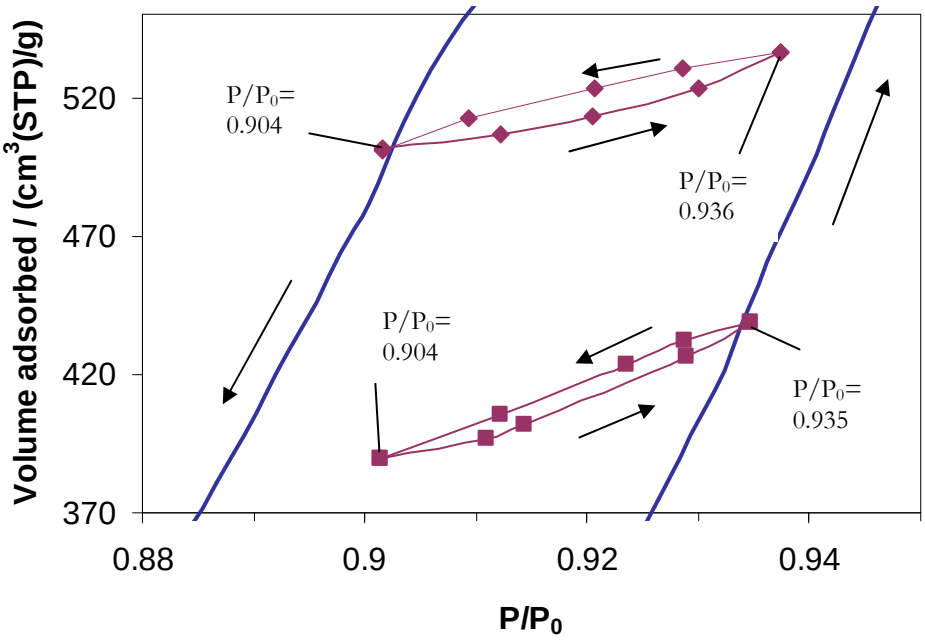

Figure 7.16 (b): An enlarged area of Figure 7.16 (a). Lines have been added to the scanning loop data points to guide the eyes. Arrows are added to indicate the direction of the change in pressure

In the preceding section, it was unclear whether the adsorption mechanism at the start of the adsorption scanning curves was due to pores filling by hemispherical menisci, in the advanced adsorption mechanism, or by cylindrical menisci. Scanning loop studies will now

be used to show that it must be due to pores filling by hemispherical menisci. Shown in Figure 7.17 is an adsorption scanning loop that spans the pressure range 0.883 to 0.917 and a desorption scanning curve that starts at relative pressure 0.917. It is clear that there is significant hysteresis between the adsorption boundary curve and the desorption scanning curve. However, there is virtually no hysteresis within the adsorption scanning loop. Therefore, it must be that different pores were filling during the adsorption scanning loop over the same pressure range as the adsorption boundary curve. Moreover, because the hysteresis is negligible on the adsorption scanning loop, this would suggest that the filling and emptying mechanism is an advancing and retreating hemispherical menisci. This is because this mechanism is reversible.

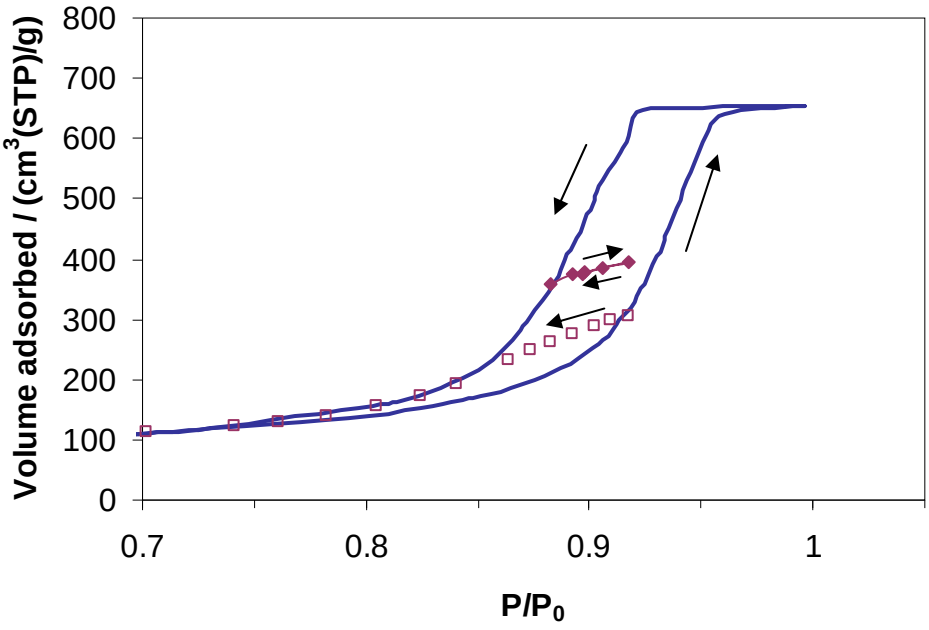

Figure 7.17: Desorption scanning curve (open squares) and adsorption scanning loop (closed diamonds) for S1. The boundary curve is shown by the fixed line. Arrows are added to indicate the direction of the change in pressure

7.7.4 Spiral Scanning loops

This section will show that hysteresis can be virtually purged in a gas sorption experiment, which indicates a reversible adsorption/desorption mechanism.

Extensive studies on desorption scanning loops were carried out, where the scanning loops were repeated over smaller and smaller pressure ranges to form a scanning spiral. The desorption scanning loop spiral is shown in Figure 7.18 (a) and for clarity, the closed square symbols, to indicate desorption scanning loops, have not been used.

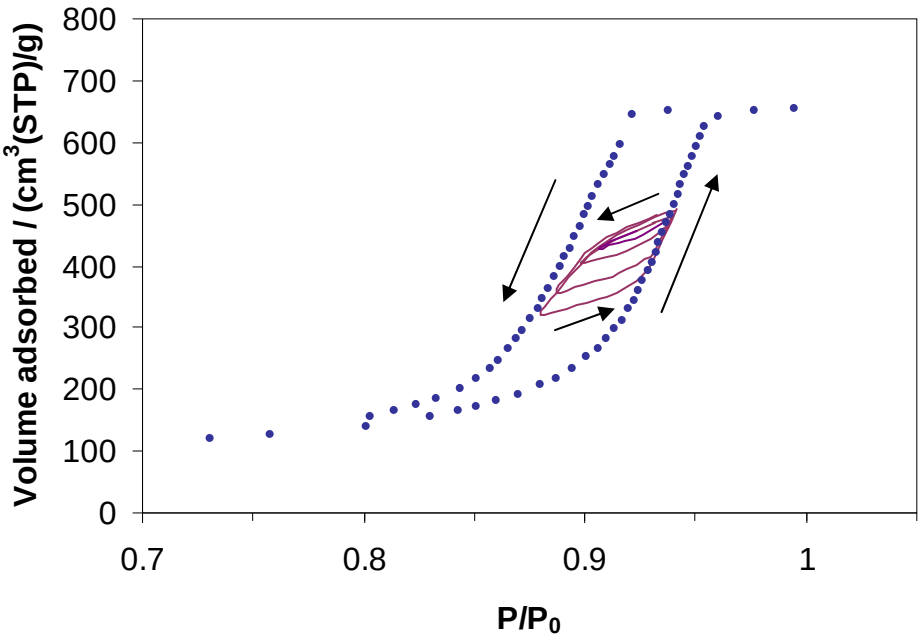

Figure 7.18 (a): Spiral scanning loops (fixed line) within the boundary curve (dots) for S1. Arrows have been added to indicate the direction of the change in pressure

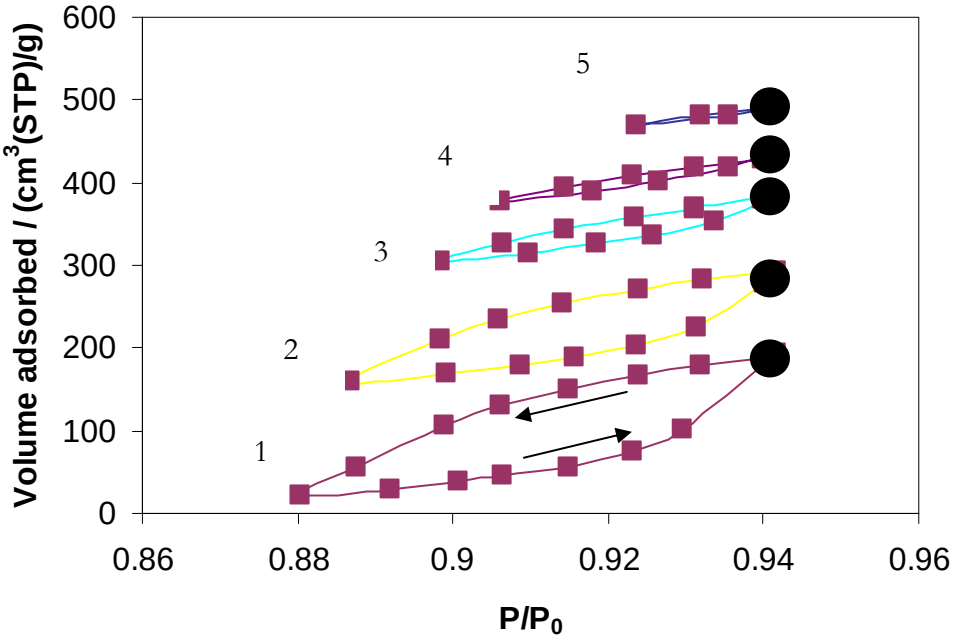

Figure 7.18 (b): For clarity the boundary curve has now been removed and each successive scanning loop (1-5), of the spiral, has been vertically offset upwards in the amount adsorbed, by an arbitrary amount, from its predecessor. The closed circle indicates the start of each scanning loop. Arrows have been added to indicate the direction of the change in pressure

To make the scanning loops (1-5) clearer, each successive scanning loop of the spiral has been vertically offset upwards in the volume adsorbed, by an arbitrary amount, from its

predecessor (see Figure 7.18 (b)). Also, the start of each desorption scanning loop is shown by a closed circle and scanning loop 1 has been labelled with arrows, to indicate the direction of the change in pressure.

The spiral scanning loop study, shown in Figures 7.18 (a) and 7.18 (b), will now be discussed in detail. As you move from scanning loop 1 to scanning loop 5, the pressure range that each scanning loop spans becomes less. As the pressure range was reduced, hysteresis between the adsorption and desorption branch, of each loop, was progressively purged, to the point where it became negligible (scanning loop 5). Since hysteresis is purged in scanning loop 5, this must correspond to adsorption by advancing hemispherical menisci and desorption by retreating hemispherical menisci, as this process is reversible.

7.7.5 Hysteresis in desorption scanning loops

The cause of the hysteresis for the larger scanning loops (scanning loops 1-4 in Figure 7.18 (b)) can potentially be explained through single pore hysteresis, such as the theory put forward in the Kelvin-Cohan equations. This suggests that adsorption in an open cylindrical pore occurs by a cylindrical type meniscus and desorption by a hemispherical meniscus. Alternatively, hysteresis could be explained through structural effects, such that the pore blocking mechanism was a cause of hysteresis. The following section will now show that the cause of hysteresis cannot be single pore hysteresis, using Figure 7.19.

Figure 7.19 shows scanning loop 1 (closed diamonds) and scanning loop 3 (closed squares). Scanning loop 1 starts at relative pressure 0.942 and the direction of pressure change is reversed at relative pressure 0.880. Scanning loop 1 then returns to the starting point before the next desorption scanning loop, of the scanning spiral, begins. The third scanning loop (closed squares) starts at the same beginning point, as scanning loop 1, and follows the trajectory of scanning loop 1, until its direction of pressure change is reversed. When the pressure is increased adsorption starts immediately and scanning loop 3 returns to the starting point. Since scanning loops 1 and 3 start at the same point and follow initially the same trajectory, it is suggested that desorption occurs from the same set of pores for both scanning loops. If the cause of hysteresis, in scanning loops 1 and 3, was single pore hysteresis, the trajectory of scanning loop 3 should follow the path of the closed triangles and join scanning loop 1 at relative pressure 0.930. Scanning loops 1 and 3 would then follow identical paths again, indicating the same sets of pores are filling. These pores would correspond to the sets of pores that emptied at the start of scanning loops 1

and 3. Scanning loop 3 does not follow this path and so there must be an alternate explanation for the hysteresis.

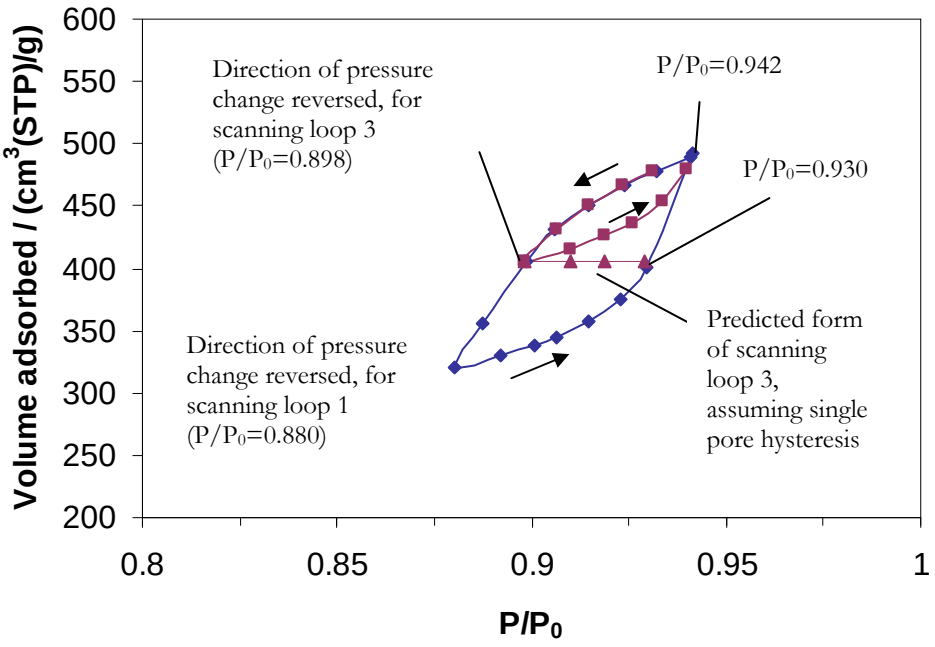

Figure 7.19: An overlay of scanning loop 1 (closed diamonds) and 3 (closed squares) of the scanning loop spiral. Triangles predict the form of scanning loop 3 assuming single pore hysteresis. Arrows have been added to indicate the direction of the change in pressure

An alternative explanation for the hysteresis, and the one propounded here, is that the adsorption and desorption processes are based upon a hemispherical meniscus entering and leaving S1 through different size constrictions (depicted in Figure 7.20) and the mechanism includes advanced adsorption and pore blocking. Initially on the desorption branch of the desorption scanning loop, evaporation can occur immediately from a large pore, whose neighbouring pore is empty, via a hemispherical meniscus (position 1). Evaporation is, however, halted by a narrow constriction (position 2) and the pressure has to be lowered further for more evaporation to occur. Once the pressure is lowered again evaporation can continue, and beyond the narrow constriction evaporation in any pores of larger radii that were shielded by the constriction will occur (position 3). As the desorption scanning loop can be stopped at different points it suggests still further narrow constrictions. At the point where the pressure is reversed to initiate the adsorption branch, condensate will be in a narrow constriction that neighbours a larger empty pore. Condensation is initially delayed until the pressure is increased to fill the neighbouring larger pore with condensate via an advancing hemispherical meniscus. On reaching the necessary pressure, condensation will advance through any pore of this radius or less, and will be halted on reaching a large radius pore (position 4). To initiate condensation further,

the pressure needs to rise once more and the system is returned to the same point at the start of the desorption scanning loop (position 1). Therefore, hysteresis is explained from the structural effects that at different points halt the retreating and advancing menisci for desorption and adsorption. The progressive disappearance of the adsorption-desorption hysteresis shown in Figure 7.18 (b) is also consistent with the adsorption and desorption mechanism proposed, in Figure 7.20, as follows. When the scanning loop spans only a small pressure range, only a small number of pores, accessible by the retreating hemispherical meniscus, will desorb. On reversing the pressure, these pores can adsorb immediately, initiated by a hemispherical meniscus originating from the pseudo-dead end type pores created by adjoining filled pores.

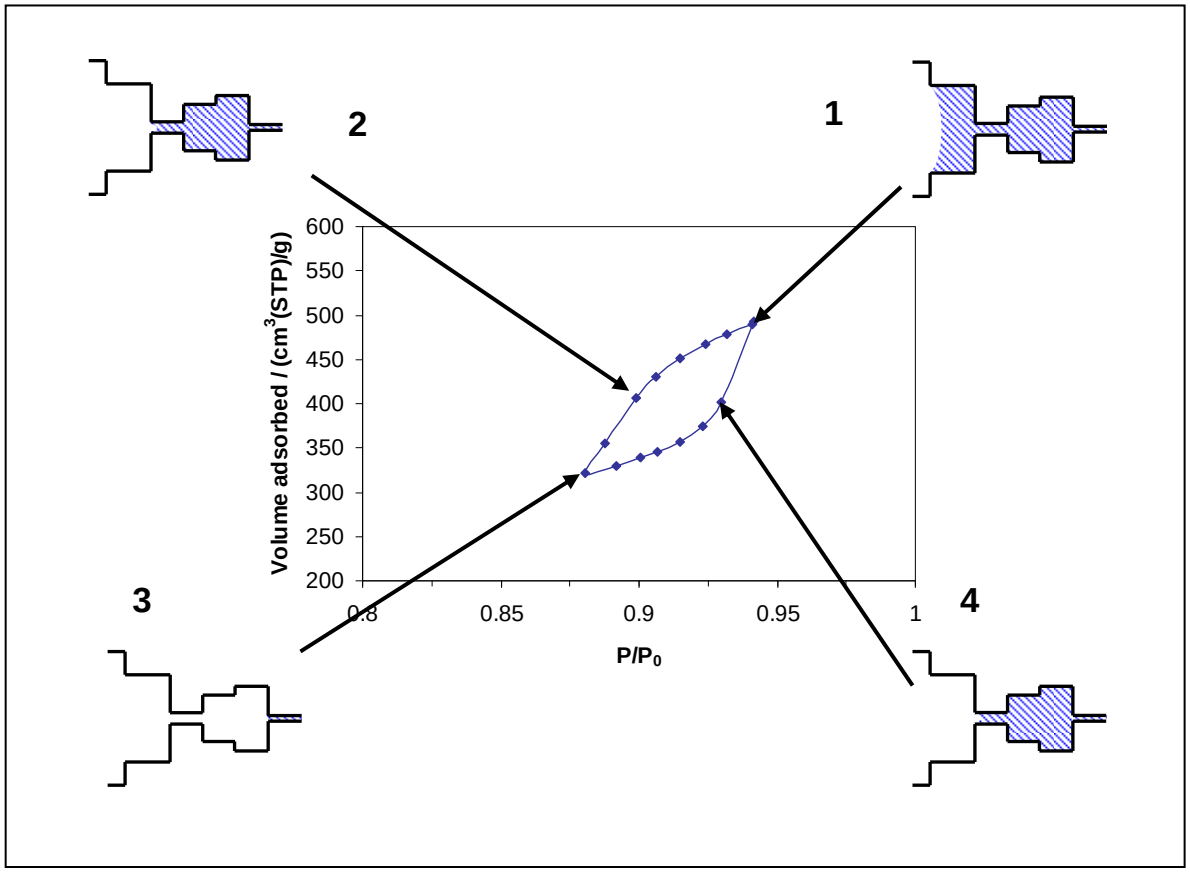

Figure 7.20: A schematic representation of desorption and adsorption, occurring by hemi-spherical menisci, at various points around a desorption scanning loop performed on a shielded pore network. Desorption and adsorption are delayed through structural effects. The shading represents filled pores, and white (no) shading represents empty pores

Moreover, an analogous desorption scanning loop spiral experiment was studied for SBA-15 (Figure 7.21). The pattern where hysteresis was progressively purged as the scanning loop spanned smaller pressure ranges, was the same for the SBA-15 sample. Therefore, the same explanation is used to explain the hysteresis in the desorption scanning loops of SBA-15. This is reasonable since, as discussed above, Esparza *et al.* (2004) suggest

the mesopores in SBA-15 are tubular in shape with an irregular cross section. The pore model in Figure 7.20, used to explain the desorption scanning loops for S1, uses a tubular shape pore with an irregular cross section.

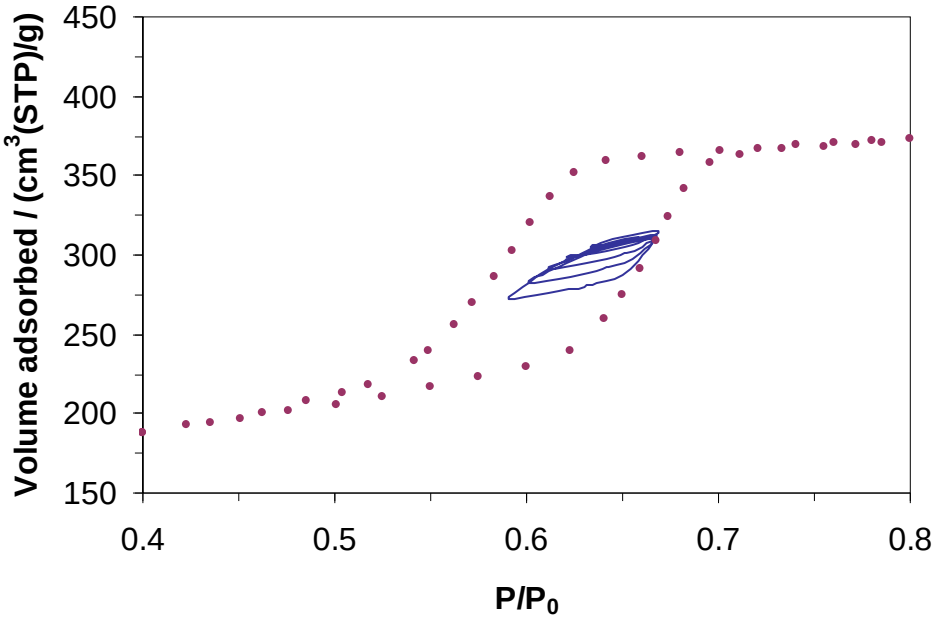

Figure 7.21: Desorption scanning loop spiral experiment (fixed line) using SBA-15 as the adsorbent. The boundary curve is shown by the dots

7.7.6 The spatial configuration of the adsorbate

The gas sorption isotherm is 1-dimensional, so the spatial configuration of the adsorbate is not clear. For example, the spatial configuration of the adsorbed gas, at positions of the same amount adsorbed, on the adsorption and desorption boundary curves, may be different. In Chapter 4, a spatially resolved method (MRI) was able to determine the spatial configuration of the adsorbed gas at different pressures and was used to confirm the advanced adsorption mechanism. The following section will now use gas sorption scanning loops and scanning curves to probe the different spatial configurations of the adsorbed gas.

Figure 7.22 (a) and (b) shows an example where a desorption scanning curve and adsorption scanning loop intersect the same point on the isotherm (relative pressure 0.900 and volume adsorbed 378 cm^3(STP)/g) . In addition, the direction of the change in pressure is the same for both the desorption scanning curve and, the desorption part of the adsorption scanning loop. However, their trajectories differ even though they intersect the same point on the isotherm. It has to be that the configuration of the adsorbate on, the

desorption part of, the adsorption scanning loop, and the desorption scanning curve are different. The difference can be explained by their histories to get to the intersection point. The history of the adsorption scanning loop is as follows: going from a virtual vacuum the sample becomes completely saturated at relative pressure 1. The pressure of the system is then lowered, which starts the desorption boundary curve. At relative pressure 0.883 and then 0.911, the direction of pressure change is reversed to generate the adsorption scanning loop. The history of the desorption scanning curve is as follows: going from a virtual vacuum the pressure is increased to relative pressure 0.934. At this pressure, the direction of the change in pressure is reversed to start the desorption scanning curve. Presumably though, a same set of pores is filled, at the point of intersection, for both the desorption scanning curve and the adsorption scanning loop. This is because below relative pressure 0.853, the adsorption scanning loop and desorption scanning curve follow identical trajectories. However, the rate of change in the amount adsorbed with respect to pressure, at the point of intersection, is greater for the desorption scanning curve. It is most likely then that, at the point of intersection, there are a fewer number of pores that can desorb, on the adsorption scanning loop, which indicates pores are blocked from desorbing. Thus, at the point of intersection then, there must be less pore blocking for the desorption scanning curve compared to the desorption part, of the adsorption scanning loop.

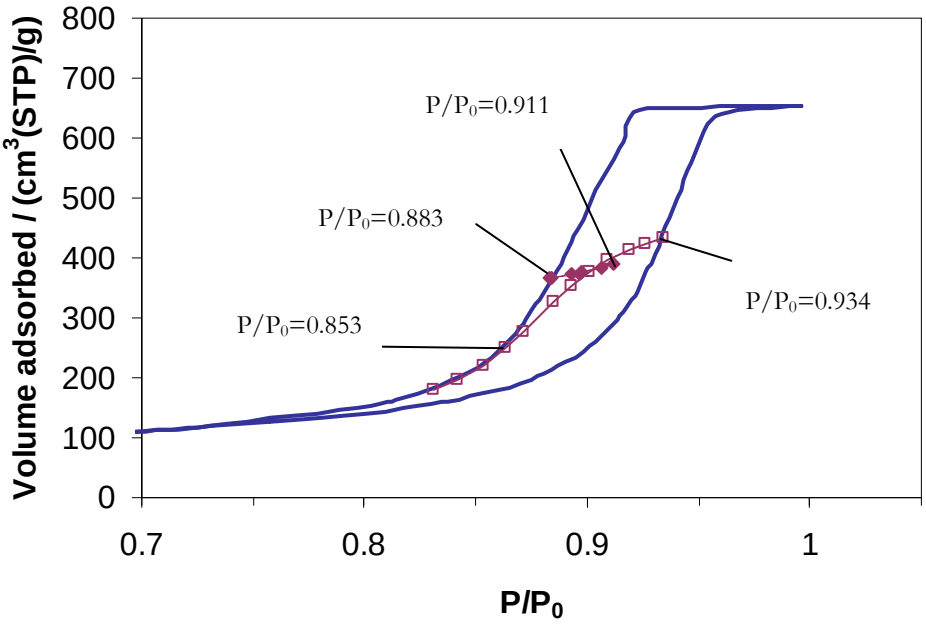

Figure 7.22 (a): Intersecting desorption scanning curve (open squares) and adsorption scanning loop (closed diamonds) for S1. The boundary curves are shown by the fixed line

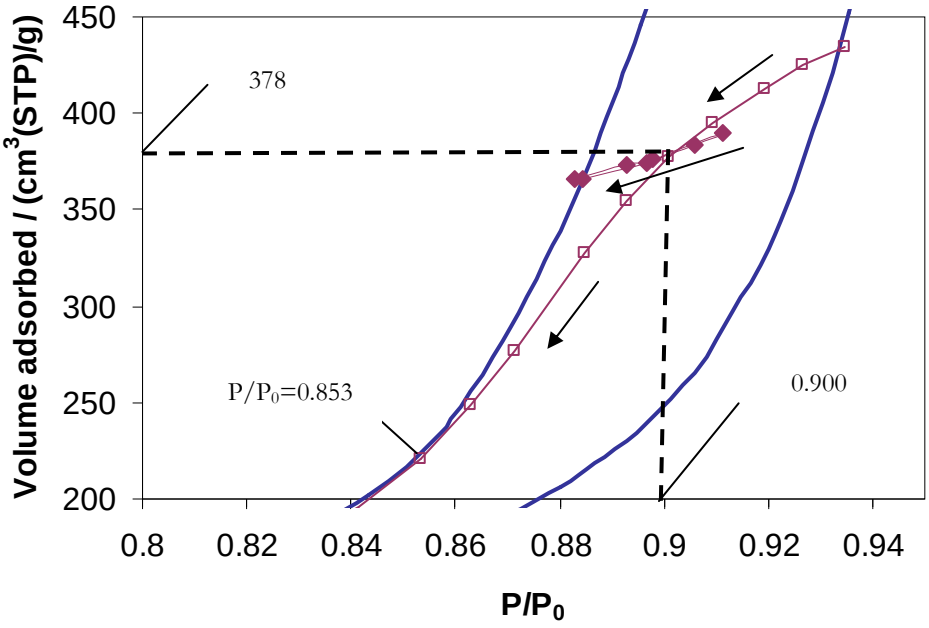

Figure 7.22 (b): An enlarged area of Figure 7.22 (a). Arrows have been added to indicate the direction of the change in pressure

7.7.7 Further tests for independent pores

The scanning loop congruency test, proposed by Everett and Smith (1954), was discussed above, but will now be explained in greater detail. A scanning loop represents a set of pores which empty and fill, or fill and empty, depending on whether it is a desorption or adsorption scanning loop. Based on independent domain theory, if sets of domains fill and empty, two scanning loops, spanning the same pressure range, should represent the filling and emptying of the same sets of pores. This would mean that the two scanning loops should be the same size and shape (congruent).

The test can be carried out by studying an adsorption scanning loop and a desorption scanning loop. Two adsorption or two desorption scanning loops could never span the same pressure range and so the test would not work. Importantly, the test proposed by Everett and Smith (1954) has to be adapted to a gas sorption experiment. This is because independent domain theory assumes that each domain is either filled or empty of condensate and so ignores the multilayer adsorption process. In a gas sorption experiment, the pores that have not been filled with condensate will still contribute to the change in the total amount adsorbed, as their multilayer thickness will change with pressure. To test the congruency of scanning loops, the change in the multilayer thickness must be accounted for, as the change will be different for the two studied loops. This is because the

adsorption scanning loop, although it spans the same pressure range as the desorption scanning loop, will be at a higher total amount adsorbed compared to the desorption scanning loop. Therefore, there will be less empty pores in the system, during the adsorption scanning loop, so the contribution to the change in multilayer adsorption will be less.

The method used, in this thesis, to account for the change in multilayer adsorption is explained as follows, with the help of Figure 7.23. The lower portion of the isotherm, before capillary condensation, was fitted to the fractal BET equation (equation 7.1) (Mahnke and Mögel 2003). This was used in Chapter 4. Additionally, previous studies (Rigby *et al.* 2008) have used the fractal BET equation to describe the multilayer region in S1, and so it has been used in this thesis.

$$\log\left[V_{(P/P_0)}\right] = \log\left(V_m\right) + \log\left[\frac{C\left(P/P_0\right)}{1-\left(P/P_0\right)+C\left(P/P_0\right)}\right] - (3-d)\log\left[1-\left(P/P_0\right)\right] \quad 7.1$$

The fractal BET equation was initially fitted in the multilayer region between relative pressures 0.3 and 0.4. The equation describes the multilayer region of the isotherm and so should not be fitted to the capillary condensation region. To determine the upper cut off point of the fit (before capillary condensation started), the multilayer fit was progressively extended to higher pressures to determine if there were systematic changes in the parameters using the Solver function in Microsoft Excel. It was found for S1 that capillary condensation started at relative pressure ~0.7, so the fractal BET equation was fitted below this relative pressure. A polynomial expression was then be fitted to the multilayer isotherm model and extrapolated, beyond relative pressure ~0.7, to relative pressures 1. This extrapolation, shown in Figure 7.23 as a fixed line, represents the multilayer isotherm for S1 if no capillary condensation occurred. At the start of the scanning loops, capillary condensation has occurred in some pores, so only the fraction that have not been filled with condensate will contribute to the multilayer adsorption. The fraction of pores that have not been filled can be calculated from the BJH pore size distribution, which was introduced in Chapter 2. From the BJH pore size distribution, the volume of each pore size can be calculated and, thus, the surface area of each pore size can be determined. This means the fraction of surface area of the pores that have not been filled with condensate, which are the pores that contribute to the change in multilayer adsorption, can be found.

Therefore, the scanning loops can be corrected for the change in multilayer adsorption using this method.

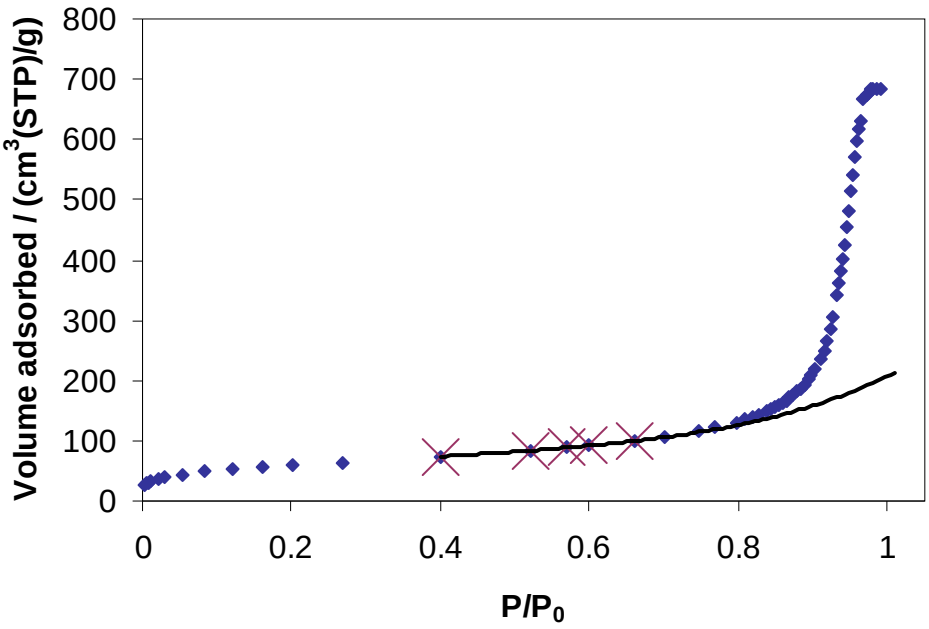

Figure 7.23: Boundary adsorption curve (diamonds), fitted points to the multilayer equation (crosses) and the predicted multilayer adsorption (fixed line) for S1

Figure 7.24 shows the desorption loop that has been corrected for the change in multilayer adsorption (crosses) and the corresponding uncorrected scanning loop overlaid (fixed line). The overlay for the adsorption scanning loop has not been shown and because of the reasons stated above; the correction for the adsorption scanning loop is even less. The congruency test between the two corrected loops is shown in Figure 7.25. A fixed line has been drawn through the upper and lower points of the adsorption (closed diamonds) and desorption (closed squares) scanning loops. The fixed line that goes through the desorption scanning loop has been shifted upwards by 98 cm^3(STP)/g, which is shown by the broken line. By comparing the broken line with the fixed line that goes through the adsorption scanning loop, it can be seen that the loops are not congruent. This suggests that at least some pores in S1 do not behave as independent pores.

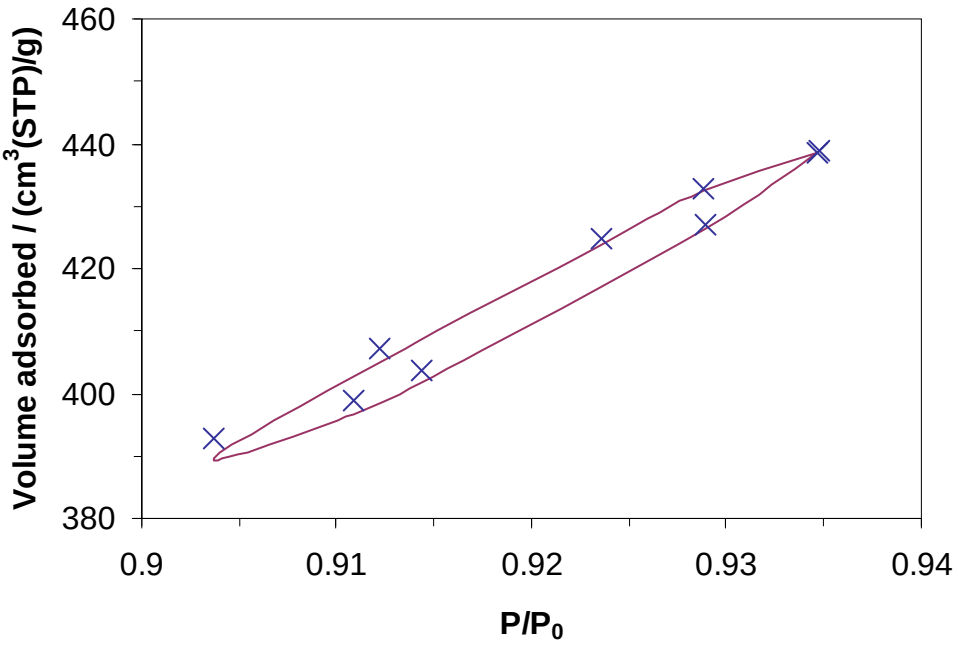

Figure 7.24: Desorption scanning loop (fixed line) and scanning loop corrected for the change in multilayer adsorption (crosses) for S1

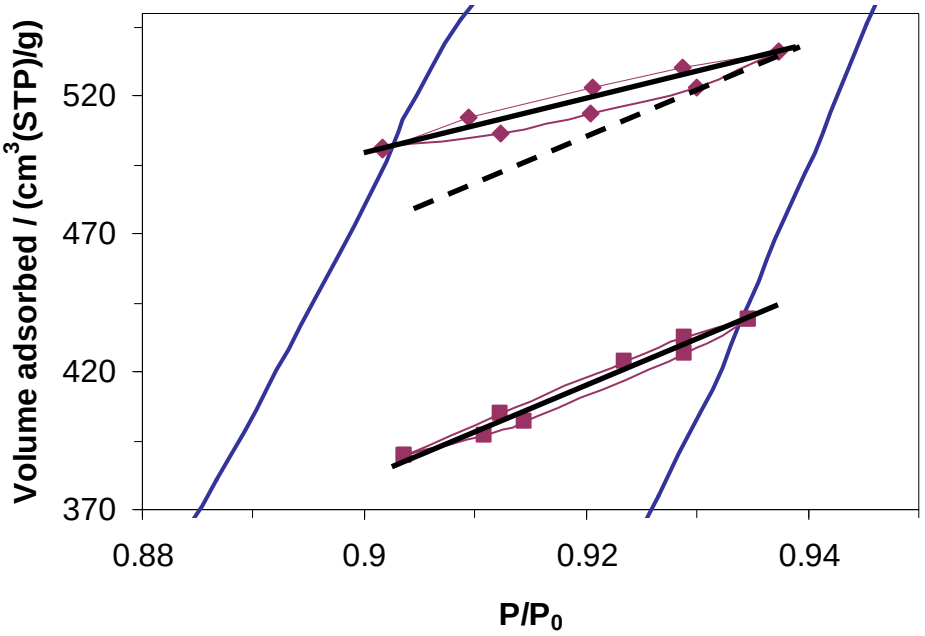

Figure 7.25: Enlarged region of Figure 7.16 (a). Fixed lines are added to show the different gradients of the scanning loops, such that the loops are not congruent. The broken line is discussed in the text

7.7.8 Scanning curve and loop studies following mercury porosimetry

The work presented, thus far, in Chapter 7 has indicated at least some pores fill and empty, in S1, by an advancing and retreating hemispherical meniscus. To further probe the pore structure of S1, and elucidate the scanning curve studies more, gas sorption scanning curves were obtained for S1 following mercury porosimetry. They have then been compared directly with analogous data obtained for S1 before mercury porosimetry. Previously in Chapter 6, it was demonstrated that the pores, which become entrapped with mercury, fill and empty like independent pores. This was because the adsorption relative pressure of the pores, which entrap mercury, could be related to the desorption relative pressure by a power of 1.5. If the pores, which entrap mercury, are thermodynamically independent, the shape of the adsorption and desorption scanning curves, for these pores, should reflect this by crossing between the boundary curves directly. The reason for this was discussed above, using Figure 7.4.

7.7.8.1 Scanning curves following mercury porosimetry

From Chapter 5 (change in incremental amount adsorbed plots), the pores which entrap mercury fill in the relative pressure range ~0.876-0.946 and empty in the relative pressure range ~0.920-0.964. The studied desorption scanning curves following mercury porosimetry therefore started in the relative pressure range 0.876-0.946 and the start point of the adsorption scanning curves was in the relative pressure range ~0.920-0.964. Therefore, the scanning curves spanned the pressure range that corresponded to the point where pores that entrap mercury fill and empty with condensate.

Figure 7.26 shows the desorption (open squares) and adsorption (open diamonds) scanning curves, for S1 following mercury porosimetry. Qualitatively, the scanning curves appear similar to the adsorption and desorption scanning curves in Figures 7.12 and 7.13, which are the analogous scanning curves before mercury porosimetry. This would indicate that the pores, which entrap mercury, do not influence the capillary condensation and evaporation processes.

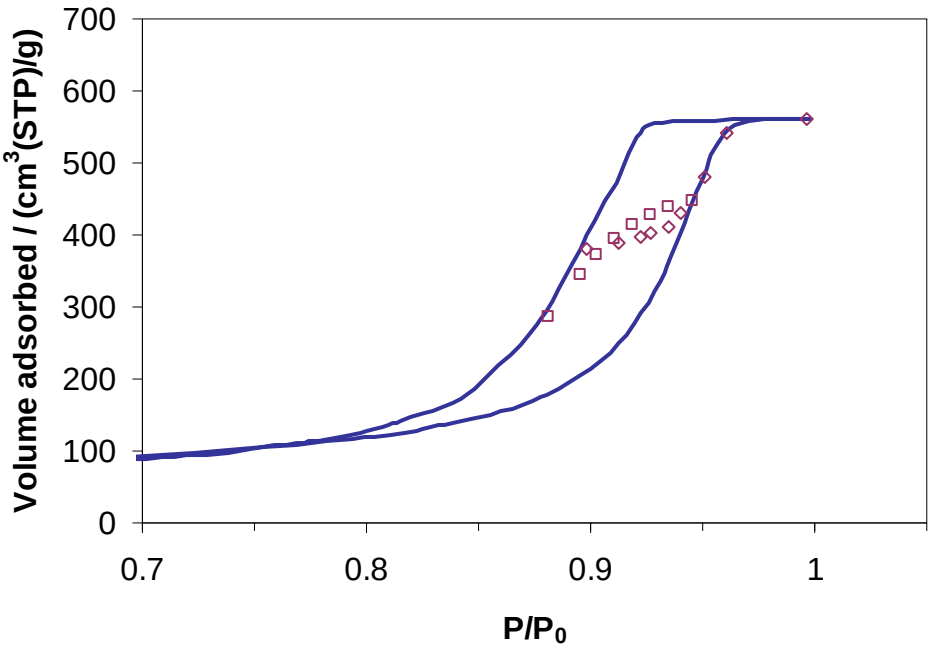

Figure 7.26: Desorption (open squares) and adsorption (open diamonds) scanning curves for S1following mercury porosimetry. The boundary curve is shown by the fixed line

7.7.8.2 Comparing desorption scanning curves before and following mercury porosimetry

To compare the desorption scanning curves, before and after mercury porosimetry, they have been overlaid in Figure 7.27. The desorption scanning curve before mercury porosimetry is shown by the open square symbols and the desorption scanning curve following mercury porosimetry by the fixed line. For clarity no boundary curves have been included, but arrows have been to indicate the direction of the change in pressure. The difference in the total amount adsorbed, between the scanning curves, is because less gas is adsorbed onto the sample when mercury is entrapped.

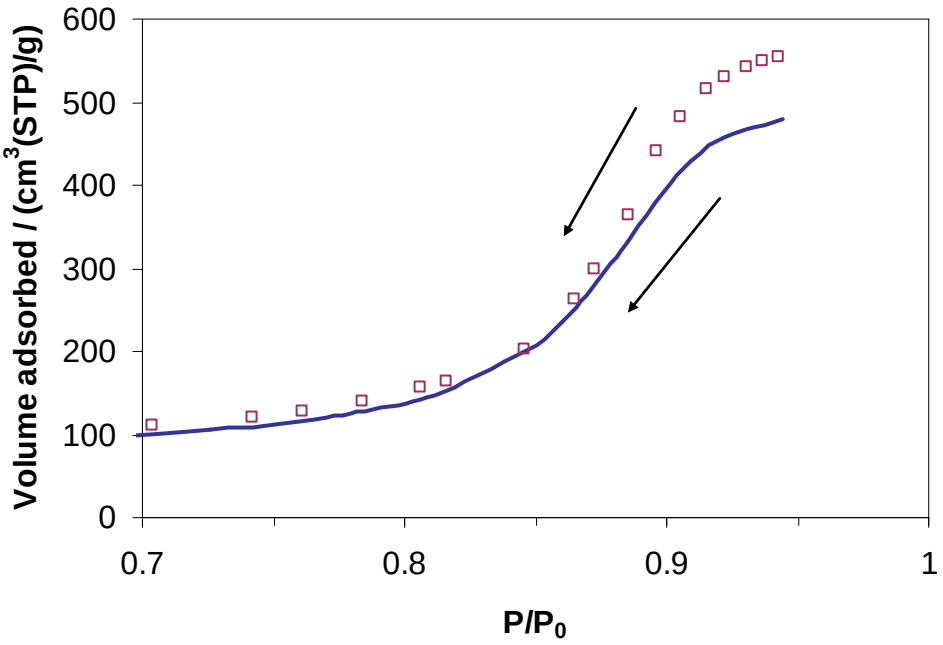

Figure 7.27: Desorption scanning curve before mercury porosimetry (open squares) and desorption scanning curve following mercury porosimetry (fixed line) for S1. The arrows indicate the direction of the change in pressure

Figure 7.28 (a) and (b) show a comparison of the same desorption scanning curves, but where the volume adsorbed for all data points, in the desorption scanning curve following mercury porosimetry, have been adjusted upwards by 12 or 75 cm^3 (STP)/g. When the scanning curve is adjusted upwards by 12 cm^3 (STP)/g, the lower region of the scanning curve (below relative pressure ~0.872) overlays the same region of the scanning curve before mercury porosimetry. Similarly, when the desorption scanning curve, following mercury porosimetry, is adjusted upwards by 75 cm^3 (STP)/g, the top region of the desorption scanning curve (above relative pressure ~0.905) overlays the same region of the scanning curve before mercury porosimetry.

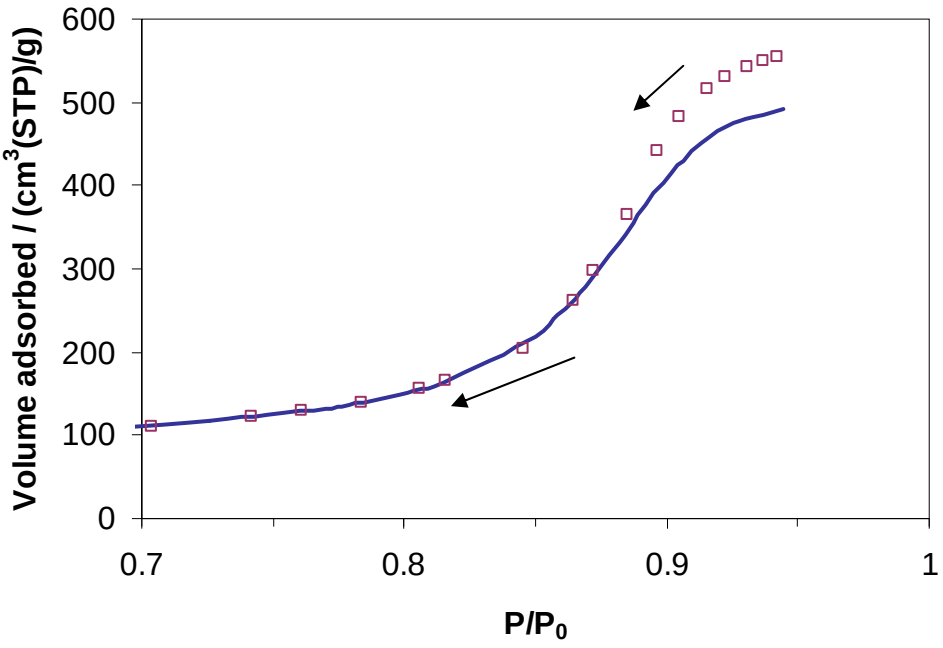

Figure 7.28 (a): The desorption scanning curve following mercury porosimetry (fixed line) has been adjusted upwards by 12 cm^3(STP)/g and the desorption scanning curve before mercury porosimetry (open squares) for S1. Arrows have been added to indicate the direction of the change in pressure

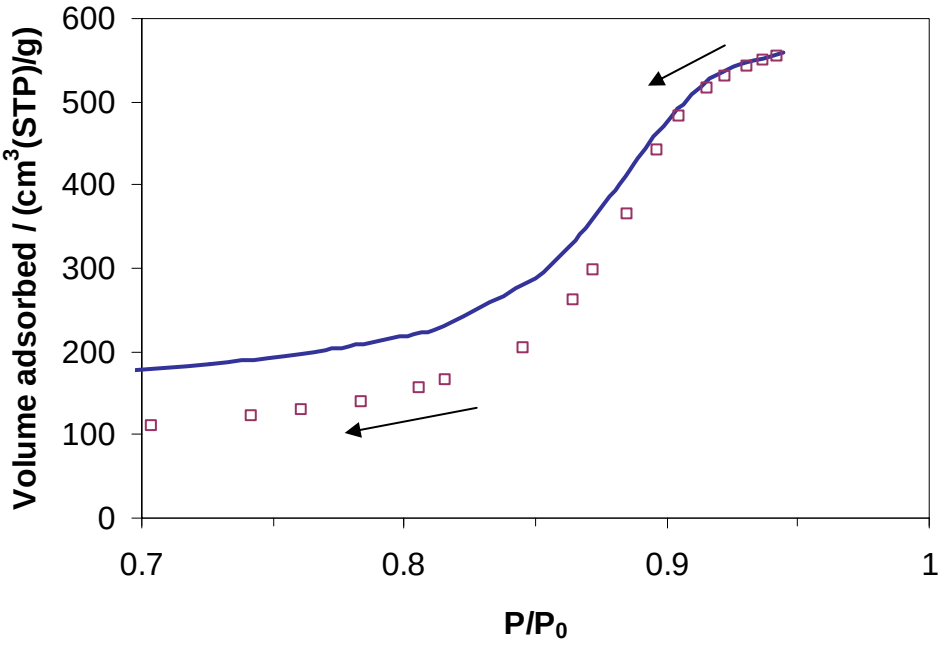

Figure 7.28 (b): The desorption scanning curve following mercury porosimetry (fixed line) has been adjusted upwards by 75 cm^3(STP)/g and the desorption scanning curve before mercury porosimetry (open squares) for S1. Arrows have been added to indicate the direction of the change in pressure

This finding suggests that the pores which entrap mercury have no influence on the capillary evaporation process in the upper and lower regions of the desorption scanning

curve. Since the desorption scanning curves, before and after mercury porosimetry, diverge between relative pressures ~0.872-0.905, it is in this pressure range that the pores which entrap mercury empty.

7.7.8.3 Comparing adsorption scanning curves before and following mercury porosimetry

The adsorption scanning curve, before and following mercury porosimetry, have been studied in an analogous way to the desorption scanning curves. First, the adsorption scanning curves have been overlaid in Figure 7.29. The adsorption scanning curve before mercury porosimetry is shown by the open diamonds, while the adsorption scanning curve following mercury porosimetry is shown by a fixed line. Similar to Figure 7.27, the boundary curves have been omitted for clarity, but arrows have been added to indicate the direction of the change in pressure for the two adsorption scanning curves.

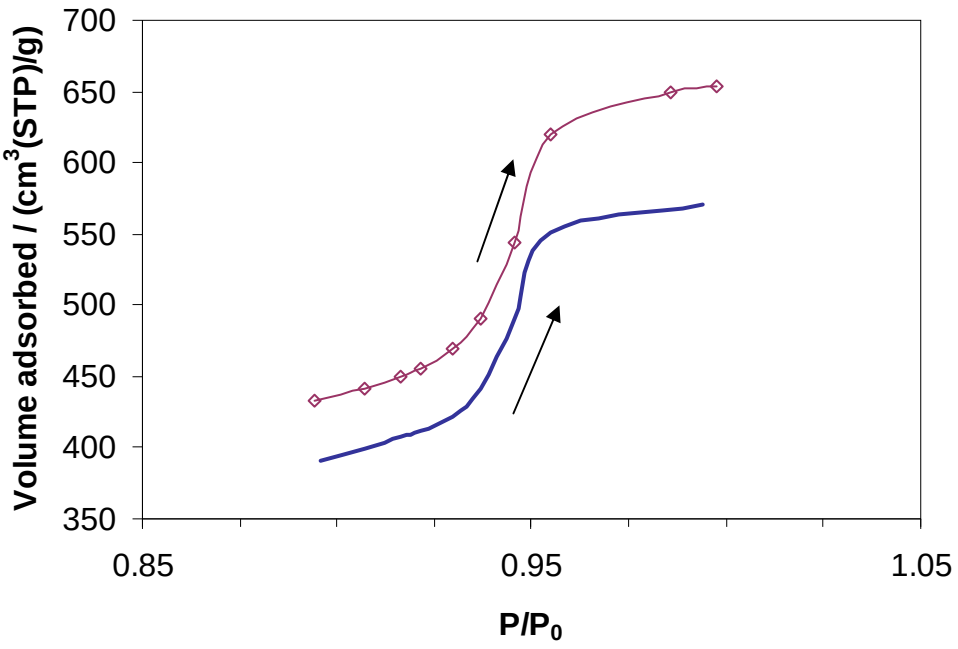

Figure 7.29: The adsorption scanning curve before mercury porosimetry (open diamonds with a line to guide the eye) and adsorption scanning curve following mercury porosimetry (fixed line) for S1. Arrows have been added to indicate the direction of the change in pressure

Figure 7.30 (a) and (b) show a comparison of the same adsorption scanning curves, but where the volume adsorbed for all data points, in the adsorption scanning curve following mercury porosimetry, have been adjusted upwards by 41 or 85 cm^3 (STP)/g. When the scanning curve is adjusted upwards by 41 cm^3 (STP)/g, the lower region of the scanning curve (below relative pressure ~0.929) overlays the same region of the scanning curve

before mercury porosimetry. Similarly, when the adsorption scanning curve, following mercury porosimetry, is adjusted upwards by 85 cm^3 (STP)/g, the top region of the adsorption scanning curve (above relative pressure ~0.955) overlays the same region of the scanning curve before mercury porosimetry.

This finding suggests that the pores, which entrap mercury, have no influence on the capillary condensation process in the upper and lower regions of the adsorption scanning curve. Since the adsorption scanning curves, before and after mercury porosimetry, diverge between relative pressures ~0.929-0.955, it is in this pressure range that the pores which entrap mercury fill.

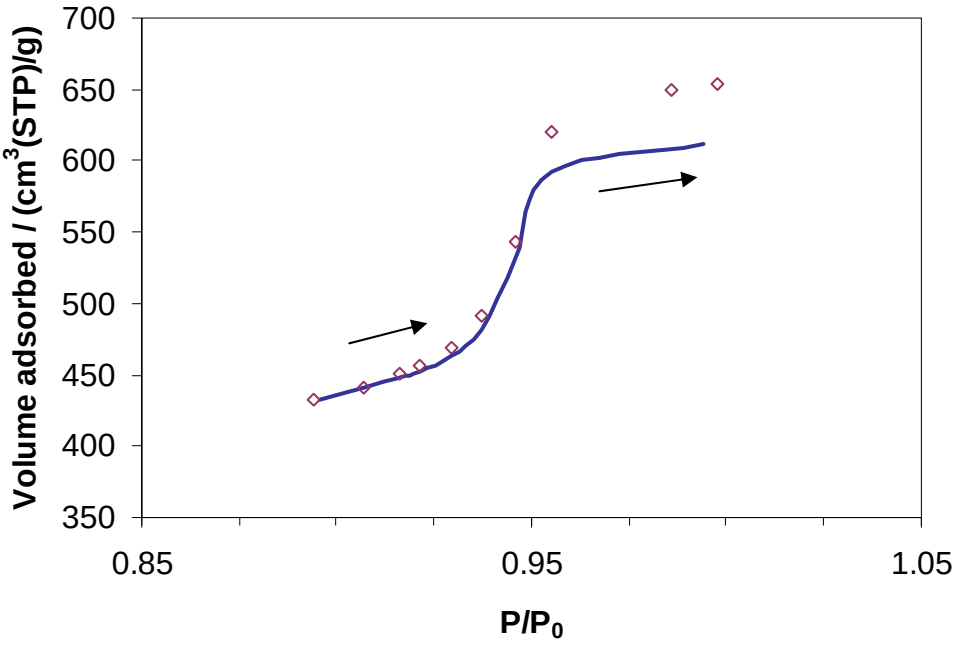

Figure 7.30 (a): The adsorption scanning curve following mercury porosimetry (fixed line) has been adjusted upwards by 41 $cm^3(STP)g^{-1}$ and the adsorption scanning curve before mercury porosimetry (open diamonds) for S1. Arrows have been added to indicate the direction of the change in pressure

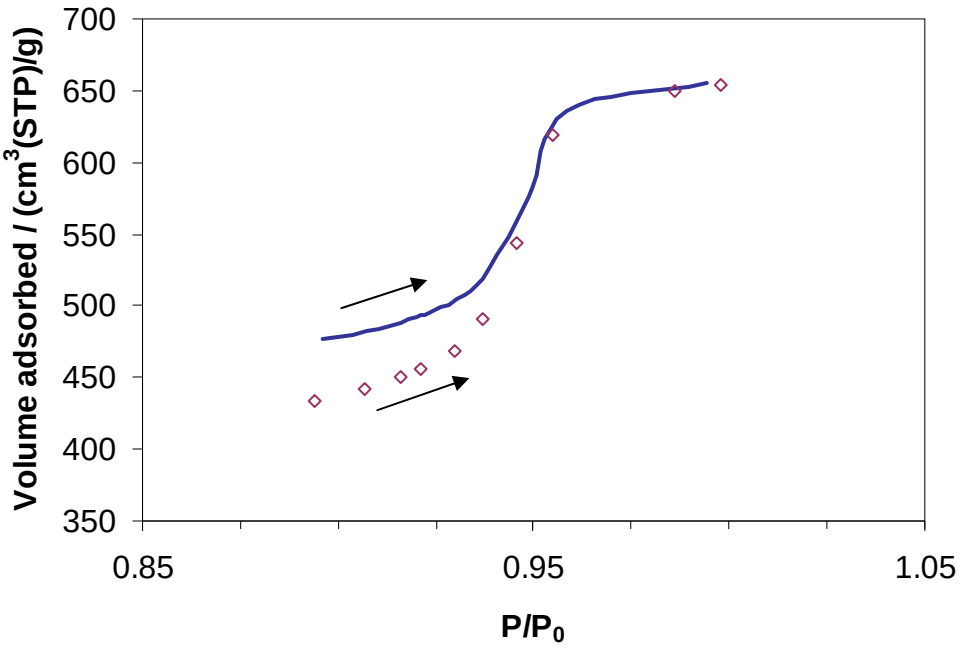

Figure 7.30(b): The adsorption scanning curve following mercury porosimetry (fixed line) has been adjusted upwards by 85 $cm^3(STP)g^{-1}$ and the adsorption scanning curve before mercury porosimetry (open diamonds) for S1. Arrows have been added to indicate the direction of the change in pressure

7.7.8.4 Deconvolving the gas sorption process in the pores that mercury became entrapped in

The adsorption and desorption scanning curves following mercury porosimetry, which are shown in Figure 7.26, represent the adsorption and desorption processes, respectively, for all pores minus those which entrap mercury. To generate scanning curves that are associated only with the pores that become entrapped with mercury, change in incremental amount plots can be subtracted or added to the starting point of the desorption or adsorption scanning curve respectively. To explain this in detail, Figure 7.31 represents the change in incremental amount adsorbed plot for the desorption scanning curves (before and after mercury porosimetry) from Figure 7.27.

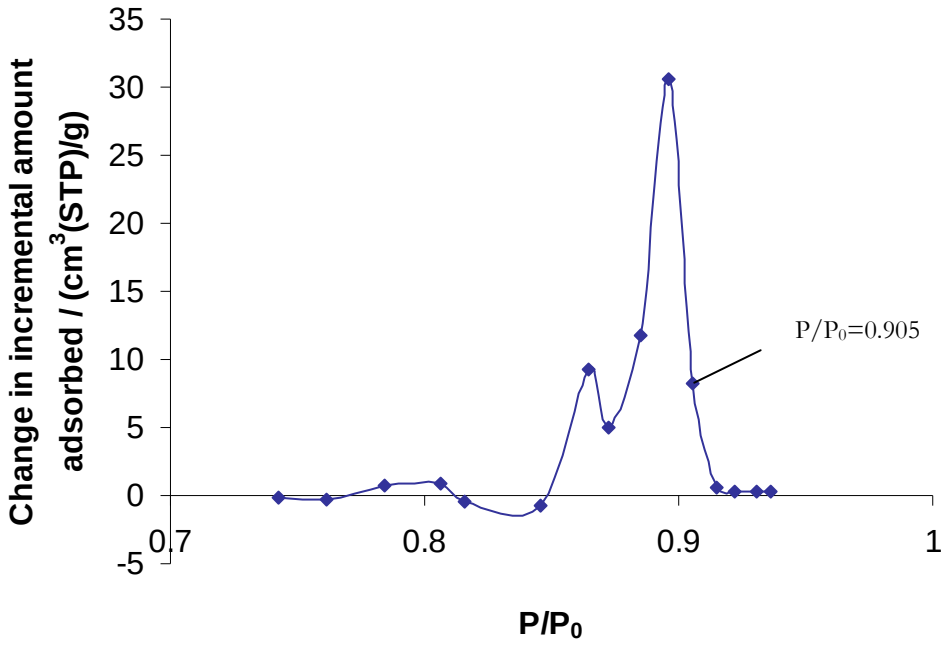

Figure 7.31: Change in incremental amount adsorbed plot for the desorption scanning curves. A line has been added to guide the eye

At the start of the change in incremental amount adsorbed plot (Figure 7.31), between relative pressure 0.948 and 0.915, the change in incremental amount adsorbed is approximately zero. This indicates the region where the desorption scanning curves, before and after mercury porosimetry, overlay in Figure 7.28 (b). At relative pressure 0.905, there is a positive deviation (~8 cm^3(STP)/g), and it is at this pressure that the pores which entrap mercury begin to empty. To generate a desorption scanning curve, which represents only the pores which entrap mercury, the change in incremental amount adsorbed plot is cumulatively subtracted from the starting point of the desorption scanning curve before mercury porosimetry (see Table 7.1). An analogous procedure can be carried out for the adsorption scanning curves, but the change in incremental amount adsorbed plot is cumulatively added instead.

Starting amount at start of the desorption scanning curve / $cm^3(STP)g^{-1}$	**Change in incremental amount adsorbed / $cm^3(STP)g^{-1}$**	**Calculation / $cm^3(STP)g^{-1}$**	**Desorption scanning curve (amount adsorbed) for the pores which entrap Hg / $cm^3(STP)g^{-1}$**
561	0.251	561 - 0.251	560.750
	0.353	560.750 - 0.353	560.396
	0.316	560.396 - 0.316	560.080
	0.580	560.080 - 0.580	559.500
	8.174	559.500 - 8.174	551.326
	30.624	551.326 - 30.624	520.702
	11.782	520.702 - 11.782	508.920
	5.003	508.920 - 5.003	503.917
	9.192	503.917 - 9.192	494.725
	-0.7543	494.725 – (-)0.7543	495.479

Table 7.1: Calculating the desorption scanning curve for the pores which entrap mercury

Figure 7.32 (a) shows the desorption scanning curves, starting at relative pressure 0.948, for all filled pores in S1 (fixed line) and for those which entrap mercury (closed squares). Also, Figure 7.32 (b) shows the adsorption scanning curves, starting at relative pressure 0.894, for all empty pores in S1 (fixed line) and for the pores which entrap mercury (open diamonds). The adsorption and desorption scanning curves, for the pores which entrap mercury, cross directly between the boundary curves. As discussed above, this result is anticipated for independent pores.

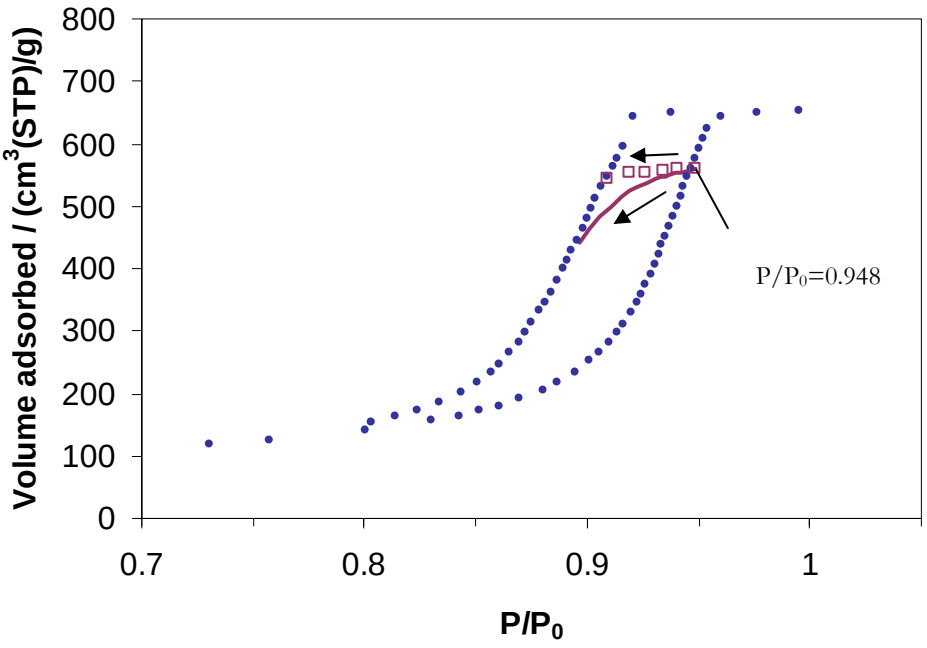

Figure 7.32 (a): The desorption scanning curve for all pores (fixed line) and pores that became entrapped with mercury (open squares) for S1. Arrows have been added to indicate the direction of the change in pressure

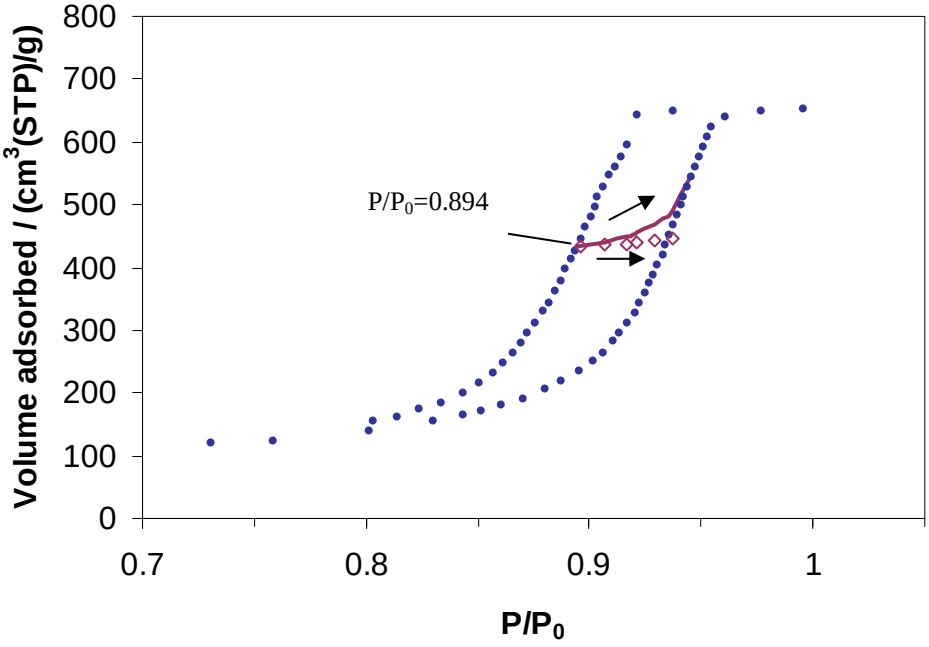

Figure 7.32 (b): Adsorption scanning curve for all pores (fixed line) and pores that became entrapped with mercury (open diamonds) for S1. Arrows have been added to indicate the direction of the change in pressure

7.8 Discussion

Previously, independent domain theory has been used as a way to explain why adsorption and desorption scanning curves cross between the boundary curves (Everett and Smith 1954). Moreover, experimental crossing scanning curve studies are then interpreted based on these theoretical studies (Morishige 2009). However, Tompsett *et al.* (2005) have suggested (discussed in detail above) that desorption scanning curves can cross if there are pore blocking effects. As will now be seen below, the experimental study of scanning curves before and after mercury porosimetry, indicate that scanning curves cross because of pore blocking effects

Referring to the experimental scanning curve studies and the schematic representation depicted in Figures 7.4 and 7.6, this can be explained as follows. From the experimental studies above, the adsorption and desorption scanning curves, for the pores which entrap mercury in S1, cross directly between the boundary curves. This experimental result can be explained using either Figure 7.4 or Figure 7.6. Figure 7.4 is of a system that is made up of independent domains, such that each domain does not interact with its neighbouring domain. It was shown above that adsorption and desorption scanning curves would cross directly between the boundary curves for such a system. Figure 7.6 though, is of a system where domains can interact such that pore blocking effects can occur. Due to the pore blocking effect, desorption scanning curves are able to cross directly between the boundary curves. Importantly, the pores which show the crossing scanning curves in S1 are the pores which entrap mercury. Therefore, the pore model used to explain the experimental crossing scanning curves must account for entrapping mercury. In Chapter 5, mercury porosimetry was introduced to the reader and a through ink bottle pore model was used to explain how mercury becomes entrapped following a mercury porosimetry experiment. Giesche (2008) has however suggested that mercury can become entrapped in independent cylindrical pores and entrapment does not rely on structural effects. By studying a mercury porosimetry experiment in a straight channel of diameter 1.5 mm, Giesche found that the mercury could still become entrapped following a porosimetry experiment. Extensive mercury entrapment studies using S1, were carried out by Rigby *et al.* (2008). They showed that when S1 was fragmented to a particle size of 60-90 μm, the pore system no longer entrapped mercury following a porosimetry experiment. This means that the mercury which becomes entrapped in S1 is because of structural heterogeneities over length scales of 90 μm (Rigby *et al.* 2008). So the pore model to explain the experimental crossing scanning curves for S1 should be able to entrap mercury when whole and not entrap

mercury when it is fragmented. If the pore model in Figure 7.3 is made up of independent domains which are able to entrap mercury, by fragmenting the system the domains would still be independent. Therefore, it would be anticipated that the system would still entrap mercury when it becomes fragmented. On the other hand, the pore model in Figure 7.5 is made up of interacting domains, which could become independent domains when the pore model is fragmented. It is feasible then for the pore model of Figure 7.5 to entrap mercury when whole, and not entrap mercury when it is fragmented. It is therefore proposed that the desorption crossing scanning curves for the pores which entrap mercury are a result of pore blocking effects. This means that the pores which entrap mercury in S1 do act as independent pores.

Chapter 6 indicated that the pores which entrap mercury do fill and empty like independent pores. This was because the adsorption relative pressure raised to the power 1.5 was equal to the desorption relative pressure for these pores. To account for this result it must mean that the pores which entrap mercury fill by the advanced adsorption mechanism but also empty by the pore blocking mechanism. To explain this, a simple pore model is presented in Figure 7.33 which also shows the capillary condensation and evaporation mechanisms for the pore model. The pore model is made up of three pores, A, B and C, and following a mercury porosimetry experiment pore C becomes entrapped with mercury. The size of pore C>pore B>pore A, and the pressure of the system is shown as P0 or P1, where P1>P0. At pressure P0 no gas has condensed in the pore model. As the pressure is increased to P1, pore A fills with condensed gas by a cylindrical type meniscus. Since pore B now has a closed end, the condensed gas in pore A can ingress into pore B and pore C by the advanced adsorption mechanism. This means pore C, which entraps mercury (following mercury porosimetry) fills at the same pressure as pore A. When the pressure is lowered, pore C and B will only empty once the condensed gas in pore A evaporates. This is the pore blocking mechanism and pore A will empty at pressure P0 by a hemispherical meniscus. This means that pore C, which entraps mercury (following mercury porosimetry) empties at the same pressure as pore A. Therefore, pore C would appear as an independent pore in a gas sorption experiment. Moreover, the capillary condensation and evaporation in pore C would happen at pressures anticipated for a pore of size A.

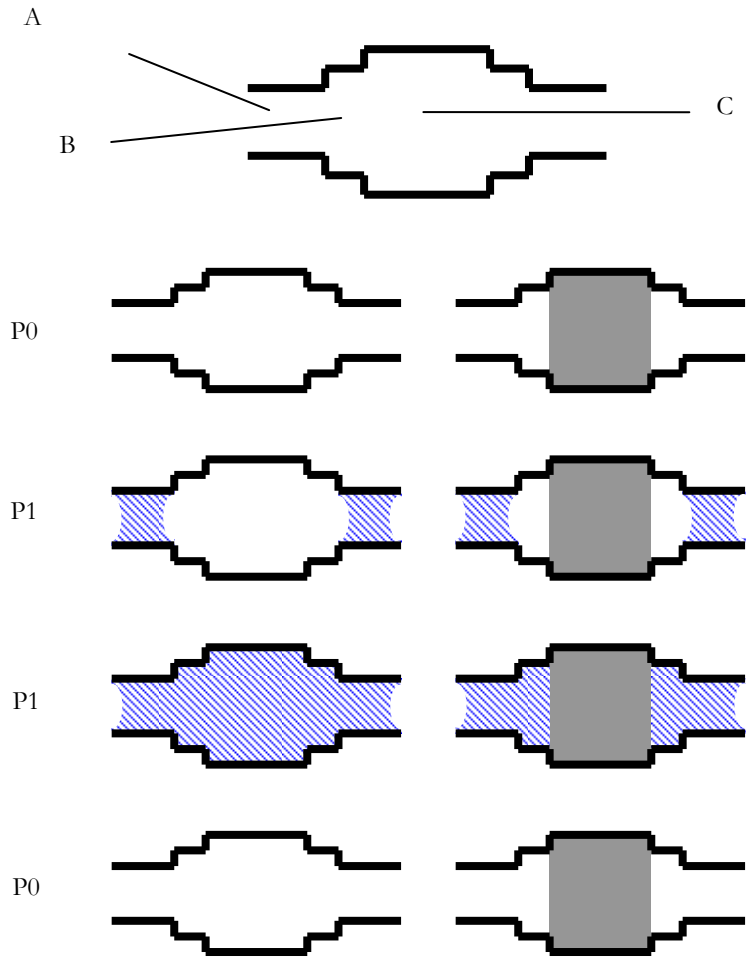

Figure 7.33: A pore model where pore size C>B>A and a gas sorption process is also shown. Condensed gas is shown by the shading and entrapped mercury is shown by the grey. The schematic is explained in the text

The experimental results from this Chapter, Chapter 6 and previous studies by Rigby *et al.* (2008) would indicate that the gas sorption experiment is less sensitive to changes in the pore size compared to mercury porosimetry, which is explained as follows. Previously, Rigby *et al.* (2003) have described S1 as "a void space network with a correlated, spatial arrangement of mesopores analogous to a macroscopic ink bottle". By fragmenting S1 the macroscopic necks and bodies become disconnected, which means mercury no longer becomes entrapped following a porosimetry experiment. The difference in size between the macroscopic necks and bodies is the reason why mercury becomes entrapped in S1 (whole sample) following mercury porosimetry. This means mercury porosimetry distinguishes between the macroscopic bodies and necks. However, a gas sorption experiment cannot distinguish between these necks and bodies. This is because the pore bodies, which entrap mercury, capillary fill and empty at the pressure of the necks. This is because the pore bodies fill and empty due to advanced adsorption and pore blocking

respectively. Therefore, as stated, the gas sorption technique cannot distinguish between the necks and bodies as the filling and emptying mechanisms are controlled only by the necks.

7.9 Conclusions

Scanning curve and loop experiments have been studied on S1 before and after mercury porosimetry. The scanning curves before mercury porosimetry have indicated that the pore filling and emptying mechanisms, in some pores, occur by advancing and retreating hemispherical menisci. This is because adsorption and desorption occurred immediately when the direction of pressure change was reversed at the start of the scanning curves. This mechanism was supported by the scanning loop experiments. When the scanning loops were studied over small pressure ranges it was found that hysteresis could be purged. By removing hysteresis, it indicated that the pore filling and emptying mechanisms were reversible. Again, this suggests that capillary condensation and evaporation in S1 occurs by advancing and retreating hemispherical menisci. When the scanning loops were studied over larger pressure ranges hysteresis occurred. The hysteresis was explained by structural effects, which delayed the retreating and advancing hemispherical menisci when the pressure was lowered or increased. These results mean that cooperative effects between pores in S1 occur for both adsorption and desorption processes. Therefore, S1 cannot be described as a collection of thermodynamically independent pores and, thus, its gas sorption data should not be analysed by assuming that it is.

Scanning curves are used as a test to determine whether a porous system is made up of a collection of thermodynamically independent pores. If scanning curves cross directly between the boundary curves it is believed the system is made up of independent pores. The integrated gas-mercury-gas experiment has been used to show that crossing scanning curves are not necessarily because of thermodynamically independent pores. Tompsett *et al.* (2005) previously suggested that scanning curves can cross due to pore blocking effects. The work in this Chapter has demonstrated this idea experimentally. The scanning curves for the pores which entrap mercury were found to cross between the boundary curves, which indicate thermodynamically independent pores. However, the pores which entrap mercury cannot be described as thermodynamically independent pores. This is because mercury becomes entrapped in S1 due to structural effects. Therefore, it was discussed that the scanning curves crossed due to pore blocking effects.

Chapter 8

Cryoporometry: an alternate pore characterisation technique

8.1 Introduction

The previous Chapters have shown that there is a potential error of 100 % in derived pore size from gas sorption data. This 100 % error occurs because of the advanced adsorption mechanism. Chapter 8 will therefore introduce the reader to an alternate characterisation technique known as cryoporometry. It is a technique that investigates pore sizes by monitoring the depression of the melting/freezing points of an imbibed liquid using, commonly, either NMR, or differential scanning calorimetry (DSC) techniques (Gane *et al.*, 2004). The NMR method is a static procedure that allows the study of the molten fraction of an imbibed material at a given temperature, relying on the solid fraction having a much faster NMR relaxation rate than the molten fraction, while DSC cryoporometry, on the other hand, is a dynamic measurement, which studies the heat flow to and from the sample. The basic cryoporometry experimental method freezes an imbibed material inside a porous sample and then melts it. Generally, the temperature at which the imbibed material freezes to a solid and subsequently melts, detected by NMR or DSC, is dictated by the pore size. However, analogous to both mercury porosimetry and gas sorption studies, hysteresis between the melting and freezing processes, of an imbibed material, is observed in cryoporometry (Denoyel *et al.*, 2004).

This Chapter will first introduce the reader to the theory of cryoporometry and will discuss related background work in the literature. The theory will explain how a pore size calculation can be found from the cryoporometry data and an explanation as to why there is hysteresis between freezing and melting points will be given. In addition, reasons why the cryoporometry technique is more advantageous than current methods such as gas sorption will be described and commented on. Following this introduction Chapter to cryoporometry, Chapters 9 and 10 will present the experimental cryoporometry work that has been conducted for this thesis.

8.2 Background to cryoporometry

The theory of cryoporometry is based on the works of W. Thomson (Thomson 1871, cited by Mitchell *et al.* 2008) and J.J. Thomson (Thomson 1888, cited by Mitchell *et al.* 2008), which was later developed by J.W. Gibbs (Gibbs 1928, cited by Mitchell *et al.* 2008). They established that the melting point for a small crystal is depressed relative to the bulk melting point, and the extent it is depressed by varies inversely with the crystal size. This relationship can be expressed by (Jackson and McKenna 1996):

$$\Delta T_m = T_m - T_m(x) = \frac{4\sigma_{sl} T_m}{x \Delta H_f \rho_s} \qquad 8.1$$

where, ΔT_m is the melting point depression, T_m the melting point of crystals of diameter infinity, $T_m(x)$ the melting point of crystals of diameter x, σ_{sl} the surface energy of crystal-liquid interface, ΔH_f the bulk enthalpy of fusion and ρ_s the bulk density of the crystal. Hereafter, equation 8.1 will be referred to as the Gibbs-Thomson equation.

The Gibbs-Thomson equation was originally derived to explain the melting of a crystal within a liquid of the same material. If it is to be applied to a crystal confined in a pore an account of the interaction between the crystal and pore wall needs to be made. This can be achieved by incorporating the meniscus contact angle, θ, with the pore wall (Mitchell *et al.* 2008), and the Gibbs-Thomson equation can then be expressed as:

$$\Delta T_m = T_m - T_m(x) = \frac{4\sigma_{sl} T_m}{x \Delta H_f \rho_s} \cos\theta \qquad 8.2$$

The interaction between the confined solid and the pore wall is assumed to be weak (Mitchell *et al.* 2008) and the contact angle is typically taken as 180° (Jackson and McKenna 1990), which implies that the solid crystal and pore wall are not in contact with one another. This can be explained by having a liquid like layer that does not freeze between the solid crystal and pore wall (Quinson and Brun 1988; Jackson and McKenna 1990; Schmidt *et al.* 1995; Schreiber *et al.* 2001), which is shown in Figure 8.1.

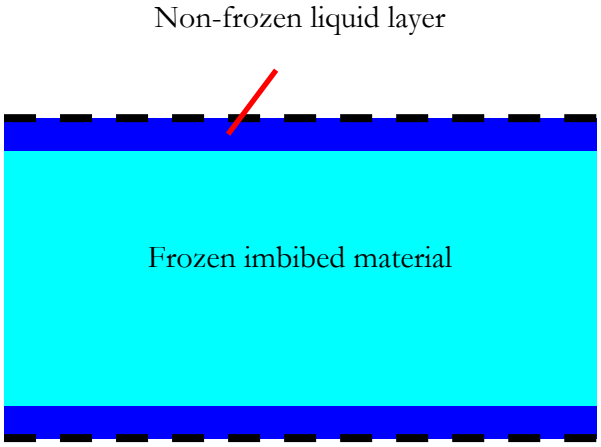

Figure 8.1: Schematic of a frozen imbibed material (light shading) inside a pore (broken line). Between the frozen imbibed material and the pore wall is a non-frozen liquid like layer (dark shading)

This non-frozen layer has been confirmed experimentally by Overloop and Vangerven (1993). They noted, using NMR, that when the imbibed liquid became frozen in their porous system there still remained detectable magnetisation. This magnetisation decreased smoothly with decreasing temperature, and it was not associated with hysteresis when the temperature was then raised. Moreover, the relaxation of a solid was expected to be much faster, thus precluding its signal. From this they concluded that the change in magnetisation could not be from freezing and melting of the imbibed material, but must be due to a liquid layer that does not freeze. This non-frozen layer is analogous to the *t* layer in gas sorption studies, which was discussed in Chapter 2.

However, because the interaction strength between the frozen crystal and pore wall will vary between different imbibed liquids and different porous materials, the contact angle will vary. Thus, to solve Equation 8.2 accurately a measurement of the contact angle would need to be made for each experiment. To resolve this, Strange *et al.* (1993) suggested combining the parameters in the Gibbs-Thomson equation and deriving them experimentally. The Gibbs-Thomson equation can then be expressed as:

$$\Delta T_m = T_m^o - T_m(x) = \frac{K_{GT}}{x} \qquad 8.3$$

where K_{GT} is the Gibbs-Thomson calibration constant, determined empirically, and accounts for adsorbate-adsorbent interactions.

8.2.1 Determining the Gibbs-Thomson constant

The empirical method to determine the Gibbs-Thomson constant is explained as follows. By using samples with a known pore size, a plot of the melting point depression against the inverse median pore size is made. According to Equation 8.3 there should be a linear relationship where the gradient is the Gibbs-Thomson constant. However, non-linear relationships between the melting point depression and the inverse pore size are reported. Hansen *et al.* (1997) suggested that this was because the enthalpy change and the solid-liquid interface tension changes with temperature. Schreiber and co-workers (2001), however, suggested a simple modification to the Gibbs-Thomson equation should be made that accounts for the non-frozen layer, of thickness *t*, between the ice crystal and pore wall to explain the deviation. Equation 8.3 can then be modified and expressed as:

$$\Delta T_m = \frac{K_{GT}}{x - 2t} \qquad 8.4$$

This empirical method relies on the accuracy of the known pore size, which is commonly calculated from gas sorption studies (Baba *et al.* 2003; Hansen *et al.* 2005). Therefore, any error in the gas sorption pore size will be transferred into the Gibbs-Thomson constant. Chapter 2 has discussed the potential inaccuracies from calculating pore sizes from gas sorption studies, which include possible errors from the Kelvin equation (Neimark and Ravikovitch 2001) and potential cooperative effects between pores such as advanced adsorption (Esparza *et al.* 2004). Despite these known problems the described method is still used to calculate the Gibbs-Thomson constant (Webber *et al.* 2001; Baba *et al.* 2003; Dore *et al.* 2004; Hansen *et al.* 2005). In fact a recent publication has even described the Gibbs-Thomson constant as "approximately 50 K nm" and uses this value to convert the depressed melting points in a pore size (Ryu *et al.* 2010). A more accurate method for determining the Gibbs-Thomson constant was therefore necessary, which would allow an accurate pore size to be found from cryoporometry. Perkins (2009) proposed an alternate method for calculating the Gibbs-Thomson parameter and is explained as follows. The work compared the freezing curve of a fragmented sol gel silica (S1) with the corresponding mercury intrusion curve corrected by the Kloubek equations. By fragmenting the sample Perkins (2009) ensured cooperative effects between pores had been removed. The Gibbs-Thomson parameter and the thickness of the non-frozen layer were found to be 48 nmK and 0.4 nm respectively, which were comparable to other values found in the literature, summarised by Petrov and Furó (2009). The method described by Perkins (2009) is more accurate compared to the other method as it accounts for the

possibility of pore-pore interactions from the mercury intrusion and extrusion data. These effects have been ignored by others (Webber *et al.* 2001; Baba *et al.* 2003; Dore *et al.* 2004 and Hansen *et al.* 2005).

8.2.2 The probe liquid

Cryoporometry studies reported in the literature have used a wide variety of probe liquids including acetonitrile (Wulff 2004), benzene (Dosseh *et al.* 2003), chloromethane (Morishige 1999), cyclohexane (Booth and Strange 1998), cyclooctane (Petrov and Furó 2009), heptane (Jackson and McKenna 1990), naphthalene (Strange *et al.* 2003), nitrobenzene (Khokhlov *et al.* 2007) and water (Hansen *et al.* 1996). The choice of the probe liquid is important, and reasons for selecting different probe liquids are as follows. The chosen liquid should wet the surface of the material, which means all the pores will fill spontaneously. If only some pores fill it would mean the calculated pore size distribution would not represent those that are unfilled. Having a wetting probe liquid additionally means the outer surface of the material will be wetted allowing both freezing and melting studies to be made. This point is explained further below.

It is also preferable that when the imbibed liquid freezes it becomes crystalline. In the introduction it was mentioned that the NMR cryoporometry method replies on the solid fraction having a much faster relaxation time compared to the molten fraction. Therefore, in the NMR cryoporometry experiment the contribution to the NMR signal from both the solid fraction and liquid fraction can be separated. This is made easy for a material that becomes crystalline upon freezing, such as water (Webber 2010). It has been reported (Booth and Strange 1998) that cyclohexane, however, has an intermediate non crystalline phase, which makes it harder to define the solid and liquid fractions. For such imbibed materials the liquid to solid (or solid to liquid) transition temperature is therefore less clear, and it is the temperature of this transition that is used to determine a pore size.

Probe liquids can also be chosen to have high Gibbs-Thomson constant. This is because a higher constant means larger pores can be probed using the cryoporometry method (see Equation 8.4). The magnitude of the Gibbs-Thomson constant depends heavily on how the imbibed fluid wets the surface of the material, as shown by the work of Dosseh *et al.* (2003). They compared the melting point depressions of cyclohexane in SBA-15 and a CPG which had the surface hydroxyl groups removed by grafting the surface with trimethylsilyl (TMS) groups. Grafting the surface meant it became more hydrophobic

and so the cyclohexane wetted it more. It was then found that for a ~8 nm sized pore the melting point depression for cyclohexane in SBA-15 was 60 °C compared to 20 °C for the TMS grafted CPG sample. An example of a probe liquid that has been used to probe large pores is octamethylcyclotetrasiloxane (OMCTS) (Vargas-Florencia *et al.* 2007), which was used to probe pores up to 1 μm in diameter. Moreover, they claimed that OMCTS can wet silica and has a distinct crystalline phase in pores as small as 10 nm. Therefore, it appears a suitable probe for cryoporometry experiments. Of further importance, its melting point of 290.4 K (Hunter *et al.* 1946), means there is little reliance on cryogenic cooling to freeze the liquid when it is imbibed in pores (Vargas-Florencia *et al.* 2007).

For industry one of the most desirable probe liquids is water because it is non-toxic, non-volatile, abundant and wets catalyst supports such as silica and alumina. However, there can be circumstances where the porous material has both a hydrophobic and hydrophilic surface. Such an example would be a coked catalyst, where the un-coked regions would potentially be hydrophilic while the coke regions hydrophobic. In this instance water would not be appropriate as a probe liquid. A probe liquid that wets both hydrophobic and hydrophilic surface is therefore required. Examples of such liquids are cyclohexane and cyclooctane, which have been used to wet coked Pt-ZSM-5 zeolite catalysts (Chua 2010), while Vargas-Florencia *et al.* (2007) report octamethylcyclotetrasiloxane will wet both hydrophilic and hydrophobic surfaces. Water also has the additional draw back that it expands on freezing so may cause stress on the pore walls (Scherer 1999). If the stress is sufficient, the frozen water will damage the pore wall structure making pore size calculations inaccurate. A check can be made to determine whether the pore structure is damaged by repeating the freeze-thaw cycles (Perkins *et al.* 2008). If the freeze-thaw cycles overlay it suggests the process does not damage the pore structure. If there is a difference it would mean an alternate probe liquid to water needs to be found.

8.2.3 Hysteresis in cryoporometry

Alluded to in the introduction of this Chapter, the depressed freezing and melting temperatures of an imbibed liquid are different. This difference in temperature is referred to as freeze-thaw hysteresis. A discussion of freeze-thaw hysteresis is given by Denoyel *et al.* (2004). They studied the hysteresis in cryoporometry experiments and commented on the similarities with hysteresis found in gas sorption studies claiming that gas adsorption-desorption mechanisms are analogous to the melting-freezing mechanisms in

cryoporometry. However, they do not give a detailed thermodynamic explanation of hysteresis.

Since then, several theories have been proposed to account for hysteresis in cryoporometry (Petrov and Furó, 2006), which are detailed as follows. One mechanism proposed suggests that when there is no nucleation source to seed freezing at the equilibrium freezing point, the confined liquid becomes super-cooled. This is analogous to what occurs for bulk liquids, and super cooling continues until homogeneous nucleation finally initiates ice formation. However, the melting process can occur more readily because the non-frozen liquid like layer can initiate melting. Another potential explanation for hysteresis is when the freezing is nucleated by a solid (ice) phase already formed, which is termed heterogeneous nucleation. However, the crystalline (ice) front can potentially be prevented from freezing a pore if its access to the pore is blocked by a narrower pore neck. Therefore, the penetration of an exterior crystalline (ice) front is delayed until the temperature is lowered to the value required by the Gibbs-Thomson relationship for the narrow neck to freeze. This type of mechanism is analogous to the pore blocking mechanism described in Chapter 2 for gas desorption studies. A third potential explanation considers how the solid-liquid interface propagates during freezing and melting. It is believed that freezing occurs along the axis of the pore, from a nucleation site at one end, while melting occurs from the non-frozen layer at the pore surface towards the pore centre (see Figure 8.2). The melting process is however delayed until the energy barrier required to initiate melting is overcome. For example, if there is a pore where the imbibed material is frozen, the pore system is at a local minimum energy. On melting the imbibed material, the pore system, once more, is at a local minimum energy. However, to get to the new minimum energy an activation barrier has to be overcome, and it is this energy barrier that is the reason for hysteresis. This is similar to the adsorption and desorption mechanism proposed by Cohan (1938). The freezing process occurs via a hemispherical meniscus (analogous to the desorption mechanism) while the melting process occurs via a cylindrical sleeve type meniscus (analogous to the adsorption mechanism). As stated, these processes are shown in Figure 8.2.

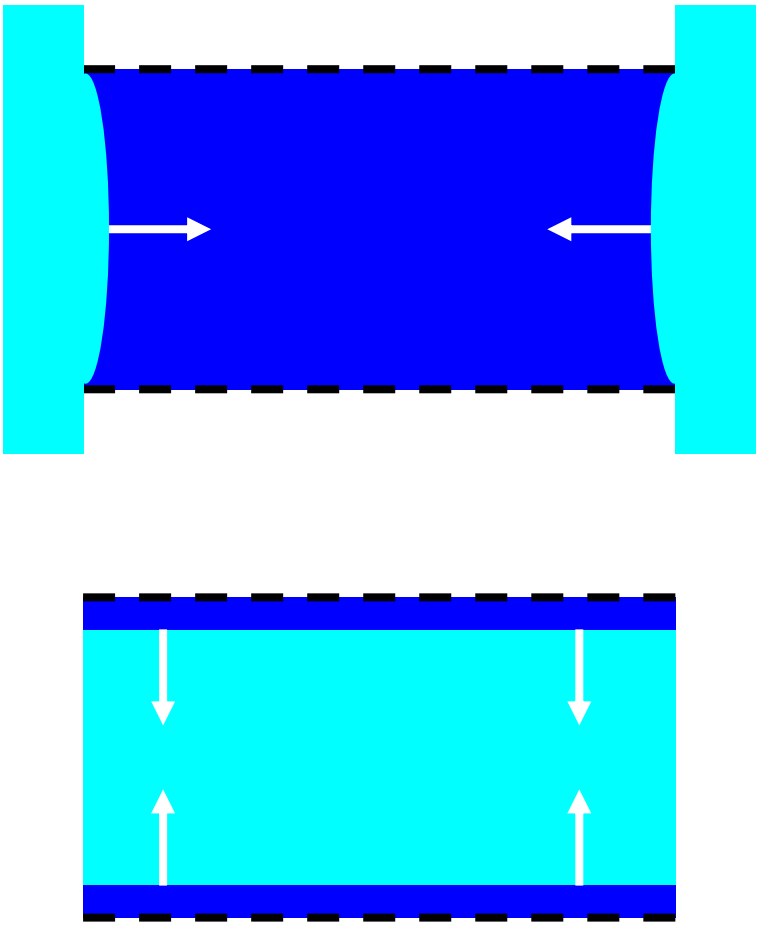

Figure 8.2: The top schematic shows the crystalline (ice) front entering the pore, filled with the same liquid, axially; this is termed axial freezing and occurs by a hemispherical meniscus. The lower image shows the liquid like layer acting as the nucleation source to melt the crystalline (ice); this is radial melting and occurs by a cylindrical sleeve meniscus. The dark shading indicates the liquid phase (including the non-frozen layer), the light shading shows the frozen imbibed material and the broken line is the pore wall.

In addition, Petrov and Furó (2006) showed that the freezing point depression is dependent on the surface to volume ratio and can be expressed by:

$$\Delta T_f \cong -\frac{V_m \gamma_{sl} T^0}{\Delta H} \frac{S}{V} \qquad 8.5$$

where V_m is the molar volume, γ_{sl} is the surface tension, T^0 is the bulk melting point, ΔH is the latent heat of melting, S is the surface area of the pore and V is the volume of the pore. The melting point depression, however, was shown to be dependent on the curvature of the pore surface given by:

$$\Delta T_m \cong -\frac{V_m \gamma_{sl} T^0}{\Delta H} \frac{\partial S}{\partial V} \qquad 8.6$$

The workers then related the melting point depression to include the mean curvature of the surface, κ

$$\Delta T_m \cong -\frac{V_m \gamma_{sl} T^0}{\Delta H} 2\kappa \qquad 8.7$$

By combining Equations 8.5 and 8.7 the melting point and freezing point depressions can then be related by:

$$\Delta T_m = \Delta T_f \frac{2\kappa V}{S} \qquad 8.8$$

This explanation of hysteresis by Petrov and Furó explains hysteresis in a single pore. Hereafter it will be termed cryoporometry single pore hysteresis to differentiate it from gas sorption single pore hysteresis, discussed in Chapter 2.

The pore blocking freezing mechanism has been indirectly verified by Khokhlov *et al.* (2007). They electrochemically etched out two ink bottle model pore structures from silicon wafers with varying pore diameters and conducted cryoporometry experiments using nitrobenzene. Pore model PM1 had the smallest necks on the outside of the pore structure while pore model PM2 had the smallest necks on the inside. The work found that the freezing curve for pore model PM1 froze at a single temperature corresponding to the freezing point of the outer neck size. The freezing curve for PM2 had two steps. The first step corresponded to freezing the larger pore body and the next step, at a lower temperature, corresponded to the narrower neck freezing. They concluded that the freezing mechanism of pore model PM1 was controlled by the outer neck, which is analogous to the pore blocking mechanism in gas sorption. Perkins *et al.* (2008) carried out similar work, but used S1 which has a spatial arrangement of mesopores like a macroscopic ink-bottle (Rigby *et al.* 2003). They compared the freezing curves of the whole sample with the corresponding fragmented sample. By fragmenting the sample the necks and bodies became separated and, thus, all pores became accessible to the exterior bulk water. Therefore, the ice front could advance into each pore as they became below their freezing point. When the sample was whole, the ice front could not advance to the large pores

deeply buried in the pellet if, to access them, it had to go through a narrow neck. To test the pore blocking theory they calculated the tortuosity at the same molten fraction for both the whole and fragmented sample and found a difference. They concluded that this had to be because the advancing ice front was blocked in the whole sample. This meant a different set of pores were frozen in the whole and fragmented sample, at the same molten fraction. Therefore, there must have been a pore blocking mechanism for S1.

Unlike gas sorption studies, there is still only a limited amount of work in the literature that has tested the theories to explain freeze-thaw hysteresis. Therefore, there is uncertainty over whether the freezing or melting curve should be used to calculate a pore distribution. According to Mitchell *et al.* (2008) the melting curve has commonly been used for calculating pore sizes as this removes complications such as the super cooling effect discussed above. The super cooling effect can be removed by keeping an outer frozen layer around the sample during the cryoporometry experiment (Petrov and Furó 2006), and is explained as follows using Figure 8.3. At position 1 the sample (white square) is imbibed with a liquid and there is also a bulk liquid layer on the outside of the sample. The system temperature is lowered and because there is no nucleation source the liquid is super cooled and freezes by homogeneous nucleation (position 2). The sample is then heated and only the imbibed material melts. The outer bulk layer is equivalent to bulk solid and will melt at a higher temperature. Therefore, the intra-particle material can be molten while the outer layer is kept frozen (position 3). When the system is cooled again, the outer frozen layer can now act as a nucleation source to freeze the intra-particle liquid (position 4). Therefore, the intra-particle liquid is no longer super cooled before it freezes.

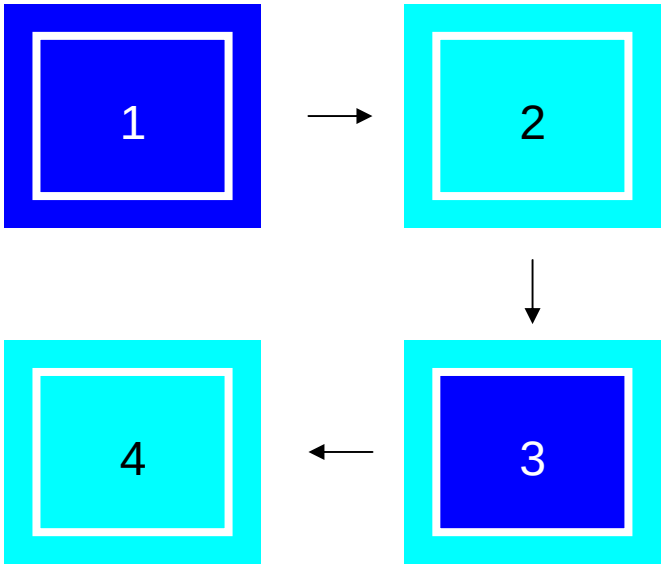

Figure 8.3: Schematic of the freeze-thaw cycle when there is always a frozen layer of liquid on the outside of the sample (white square). The dark shading indicates liquid and the light shading indicates the (frozen) solid. See text for an explanation

Despite current literature suggesting the melting curve gives a true pore size, the experimental work in Chapter 10 will discuss the possibility of an advanced melting mechanism, which is analogous to advanced adsorption (Chapter 2). The effect of this mechanism leads to inaccurate pore size distributions.

8.2.4 Pore connectivity and shape

Chapter 2 introduced the Kelvin-Cohan equations and discussed that there is a square relationship between the adsorption relative pressure and the desorption relative pressure for an independent cylindrical pore. If this relationship occurs then information regarding the pore shape can be found. Cryoporometry can similarly be used to gain information about pore shape (Petrov and Furó 2006; Perkins *et al.* 2008; Petrov and Furó 2010). From equation 8.8 (Petrov and Furó 2006) the value of $2\varkappa V/S$, for example, for a cylindrical shaped pore is 1/2, while for a spherical shaped pore it is 2/3. Therefore, information about the pore geometry is attainable from cryoporometry freeze-thaw hysteresis. Perkins *et al.* (2008) were first to experimentally demonstrate the theory by comparing the melting and freezing curves of water imbibed in a fragmented sample of S1. They found that the depressed melting point temperatures were exactly 1/2 of the depressed freezing point temperatures. This suggested that all pores of S1 had a cylindrical geometry. Petrov and Furó (2010) have similarly tested their theory on a selection of whole CPGs using water, cyclohexane, cyclooctane and benzene. They found that the ratio between the freezing and

melting point depressions suggested some samples had cylindrical shaped pores while others had spherical shaped pores.

8.2.5 Further applications and advantages of cryoporometry

The above sections have introduced the reader to the pore characterisation technique termed cryoporometry. This section will now introduce the reader to the advantages cryoporometry offers over current methods:

Sample preparation- To prepare samples for cryoporometry experiments they are imbibed with the liquid, which is to be detected either by NMR or calorimetric methods. If the liquid wets the sample, impregnation can be done simply by adding the sample to the chosen liquid. Gas sorption and mercury porosimetry studies, on the other hand, require extensive heat treatments which is time consuming. In addition, these heat treatments may cause artificial changes to the pore structure for some materials.

Imbibed liquid- The liquid that is analysed can be as simple as water. For hydrophilic samples with mesoscopic pore diameters, water is ideal because it wets the surface and it is cheap and non toxic. Methods such as mercury porosimetry require mercury which is toxic.

Pressure- If the liquid wets the surface no high pressure equipment is required to imbibe the liquid. Mercury is a non wetting technique and requires high pressure equipment, which is expensive, to intrude the mercury into the samples. In addition, gas sorption studies require low pressure (vacuum) equipment, which is equally expensive.

Experimental time- In addition to the sample preparation time, the experimental time is short too. Analysis can be completed within 2-6 hours, while gas sorption analysis studies in this thesis took ~ 30 hours. This is important for industrial applications as it enables a fast throughput of samples.

8.3 Conclusions

Chapter 8 has introduced the reader to cryoporometry and explained the theoretical background to the technique. The method requires calibration from other characterisation methods, such as gas sorption studies, but the method offers advantages over gas sorption and mercury porosimetry such as faster analysis and preparation time periods. However, as

for these other techniques, there is also hysteresis, in the case associated with the melting and freezing processes. This means an understanding of the freeze-thaw thermodynamics must be known to accurately calculate pore sizes.

Chapter 9 will now compare experimentally the NMR and DSC techniques to study cryoporometry. As there are two different experimental methods to study cryoporometry, industry needs to know which method is the 'best'. This will be followed by Chapter 10 that will probe the thermodynamics of the freeze-thaw hysteresis, and demonstrate that there is an analogous mechanism to advanced adsorption (Esparza *et al.* 2004), which is termed advanced melting.

Chapter 9

An experimental comparison between DSC cryoporometry and NMR cryoporometry

9.1 Introduction

Chapter 8 has introduced the reader to the cryoporometry characterisation technique, which can be studied using either NMR or DSC methods. The NMR method is a pseudo static one that studies the molten fraction of an imbibed material at a given temperature, relying on the solid fraction having a much faster NMR relaxation rate than the molten fraction. The DSC method, however, is a dynamic technique that studies the heat flow to and from the sample for melting and freezing respectively.

Industry is taking an interest in the cryoporometry technique as current pore characterisation techniques have possible errors, such as advanced adsorption that was discussed in Chapters 2, 4-7. Another advantage is that the technique is significantly faster as samples do not require long preparation periods, such as in gas sorption and mercury porosimetry experiments. The initial experimental cryoporometry work in this thesis will focus only on the two different experimental methods- NMR and DSC. Both methods will be used to analyse S1 (defined below) with the pore size distributions from both sets of data calculated.

9.2 Experimental sample preparation

9.2.1 Samples studied

S1 will be characterised in this Chapter and water will be the imbibed material. S1 is a sol gel silica sphere with a pellet diameter of ~3 mm. It has a modal pore size of ~15 nm and a BET surface area of ~200 m^2g^{-1}. Due to the hydroxyl groups in S1, water readily wets the surface. Additionally, the size of pores results in a significant, observable, melting point depression relative to bulk water. Therefore, it is a suitable material to be analysed by cryoporometry.

9.2.2 Impregnation of S1 with water

Pellets of S1 were impregnated with demineralised water in a three step procedure. Initially the pellets were exposed to the atmosphere to adsorb water vapour to an equilibrium level. The next stage involved placing them on a damp filter paper and then they were fully immersed into demineralised water. If the pellets were immersed immediately into water some appeared to crack. This may be because the samples have been calcined at high temperatures, which de-hydroxylates the surface. Therefore, when immersing them directly into water the fast re-hydroxylation of the surface may cause them to crack. The more gradual three step procedure described appeared to prevent the pellets from cracking and was therefore used throughout the thesis.

9.3 Experimental procedures

Previous work in the Rigby group has extensively explored the experimental set-up for NMR cryoporometry experiments (Perkins 2009). In this work, Perkins suggested a thermocouple should be inserted into the NMR tube to accurately record the sample temperature during the cryoporometry experiment. This then enabled an accurate pore size calculation from equation 8.4. The work in this thesis will use the experimental procedure described by Perkins (2009), which will be described below. The DSC method has not previously been used in the group and this thesis will describe the method development in greater detail.

9.3.1 NMR Cryoporometry procedure

NMR experiments were carried out on a Bruker Avance 400 MHz spectrometer with a static field strength of 9.4 T, yielding a resonance frequency of 400.13 MHz for ^{1}H nuclei. Two pellets of S1 were removed from the water and placed into a 5 mm NMR tube. It was ensured that a sufficient amount of bulk water remained on the outside of the pellets to allow the freezing curve to be studied. Two susceptibility plugs either side of the sample were used to fill the void space preventing the sample drying by evaporation. This also helped to reduce the temperature gradient across the sample (Perkins 2009). To cool the sample, a gas flow of cool nitrogen gas (from liquid nitrogen) was passed over the outside of the NMR tube. The temperature of the nitrogen gas was controlled by a heating element inside the NMR machine. To monitor the temperature accurately a calibrated thermocouple was inserted through the top susceptibility plug and positioned to touch the top pellet. The position of the thermocouple was not in the region of the detection coil and so it did not affect the collected free induction decay (FID). A schematic of the

bottom of the NMR tube is shown in Figure 9.1. Temperature control was achieved using a Bruker BVT3200 temperature control unit. The temperature stability was ±0.1 K, while the accuracy was ±0.2 K due to the temperature gradient across the sample (Perkins 2009). The temperature was changed in a stepwise manner and a proton spin echo spectrum was acquired at each temperature. To allow the molten water and frozen water to reach equilibrium the sample was held at each temperature for 20 minutes. Perkins (2009) had previously carried out cryoporometry studies on S1 and found 20 minutes was a sufficient period of time for the molten water and frozen ice fronts to reach equilibrium. The spin echo pulse sequence used was "$90°_x$ - t_d - $180°_y$ - t_d – acquire", with an echo time, $2t_d$, of 2 ms (see Chapter 3) and a 90° pulse length of 10.75 μs. The number of scans used for each dataset was 4 and the spectral width was 11990 Hz.

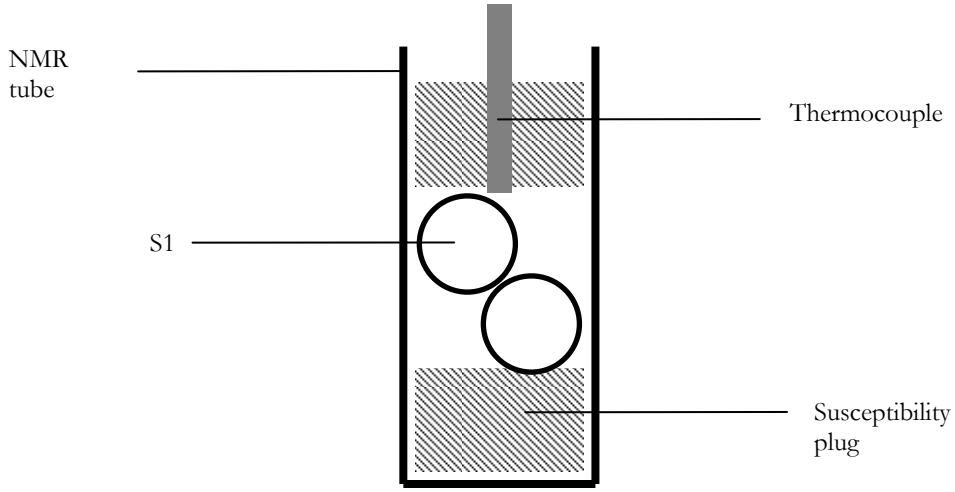

Figure 9.1: Bottom of the NMR tube. Two pellets of S1 are situated between two susceptibility plugs and a thermocouple is inserted to record the temperature

9.3.2 The external NMR thermocouple and its calibration

A Bruker t-type thermocouple (copper constantan) was used and calibrated against the melting points of decane, dodecane, tetradecane, water and the sublimation temperature of carbon dioxide (see Table 9.1). The melting points were obtained from the material safety data sheets provided by Alfa Aesar.

Material	Melting point / (°C)
Decane	-29.7
Dodecane	-9.6
Tetradecane	5.5
Water	0.0
Sublimation of CO_2 is at -78 °C	

Table 9.1: Melting points of different liquids used to calibrate the thermocouples. Included is the sublimation temperature of CO_2

9.3.4 DSC set-up procedure

The DSC apparatus used was a Perkin-Elmer machine with a liquid nitrogen cooling unit that again passed gas over the sample to freeze the water. The temperature stability was ±0.01 K, while the accuracy was ±0.1 K, according to the product specifications. A single pellet imbibed with water was placed on an aluminium pan and covered with a lid. The approximate total mass for the system for each experiment was 20 mg. The sample was initially cooled to -25 °C and heated at a variety of ramp rates. The different ramp rates are discussed throughout the text below.

9.3.5 DSC thermocouple calibration

Decane, dodecane, tetradecane and water were standard materials used to calibrate the DSC equipment (Table 9.1).

9.4 Results

9.4.1 Results: Preliminary note

As there was no previous experience using the DSC method the results section is, at first, a method development for DSC. All stages of the method development are presented.

After the DSC method development, data obtained by this technique is then compared to that from NMR. The NMR procedure was previously developed by Perkins (2009).

9.4.2 Introducing the thermograms

The DSC data is presented as thermograms that show the amount of heat being released and used by the system as the water was frozen and melted respectively. Figure 9.2 shows a typical example of a recorded thermogram for the melting and freezing process in S1, while Figure 9.3 shows the initial super cooling process. Arrows have been added to both Figures to indicate the direction of the change in temperature and they are described as

follows. The sample, with water, is loaded into the DSC machine at ~ 25 °C and the temperature is lowered. The freezing process is exothermic and, therefore, energy is released from the system which is shown by the positive amount of heat in Figure 9.3. Due to the super cooling effect the sample does not freeze at 0 °C, but ~ -15 °C for all studied samples. This is clear in Figure 9.3 where there is a large amount of heat released from the system, which subsequently results in the temperature of the system rising. Once all the water freezes no more energy is released from the system and it begins to cool once more. At -20 °C the temperature change is reversed to start heating the sample, and the melting process is observed (see Figure 9.2). At this reversal temperature the system adsorbs energy that relates to the specific heat capacity of the system at this specific temperature. As the temperature is further increased the ice begins to melt. This process requires energy in excess of that associated with raising the temperature of the sample, and the endotherm associated with this process is seen (Figure 9.2) and peaks at approximately -3 °C. The then flat region on the melting endotherm between -2 and 0 °C is when all the intra-particle water is molten but there remains the frozen outer bulk layer of ice. If the temperature is reversed at 0 °C the outer bulk water layer remains frozen and acts as a nucleation seed to freeze the intra-particle water, when the freezing point is reached according to the Gibbs-Thomson equation. The process to freeze the intra-particle water releases energy and is seen (Figure 9.2) by the exotherm that peaks at approximately -7 °C. Alternatively, instead of reversing the temperature at 0 °C the system can be heated to melt the outer bulk water, and the endotherm associated with this transition occurs approximately between 0 and 4 °C in Figure 9.2.

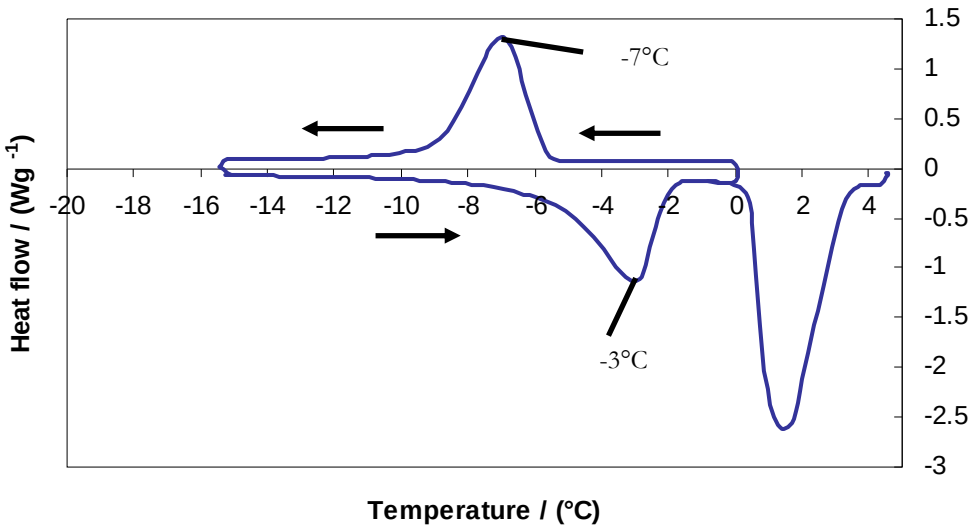

Figure 9.2: Example of the freezing exotherms and melting endotherms for S1. The x-axis label is shown below Figure 9.2 for clarity. Arrows are added to indicate the direction of the change in temperature

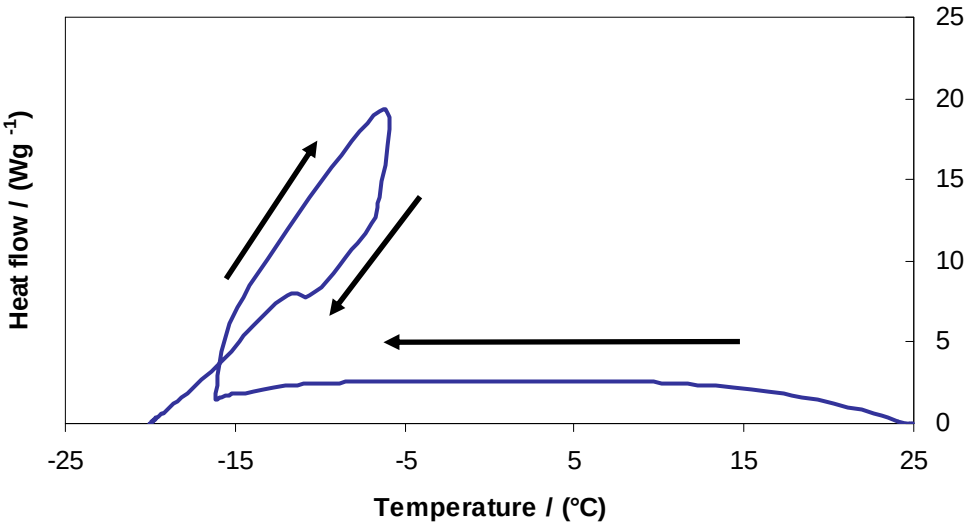

Figure 9.3: Super cooling exotherm. Arrows indicate the direction of the change in temperature

Since the freezing exotherm for S1 shows a single signal (Figure 9.2), it suggests that there is only heterogeneous nucleation occurring. DSC cryoporometry studies on MCM-41 (Janssen *et al.* 2004) have shown that the freezing exotherm has two overlapping signals, which was explained in terms of both heterogeneous and homogeneous nucleation processes. This was because the studied MCM-41 sample had pores of diameter ~ 3-4 nm, and heterogeneous nucleation for these sized pores occurs at temperatures where homogeneous nucleation begins. This resulted in two exotherms at approximately the same temperature. The pore diameters of S1 are much larger than the MCM-41 material studied by Janssen *et al.* (2004), and so only a single exotherm signal is observed (Figure 9.2). Perkins *et al.* (2008) have previously proposed that once there is an ice layer on the

outside of S1, the freezing processes will nucleate from there. The single signal observed in Figure 9.2 must therefore be due to heterogeneous nucleation.

9.4.3 Ensuring all intra-particle water became frozen

Perkins (2009) had previously shown, using NMR, that super cooling of the intra-particle water continued to approximately -15 °C, and at this temperature all the intra-particle water froze. To check this using the DSC method, two experiments were studied where the same sample was cooled to two different temperatures. Initially the sample was cooled to -60 °C and the temperature was increased with a heating rate of 0.5 °C min^{-1} until all the ice, including the outer bulk layer, became molten (Figure 9.4). Following this the system was cooled to - 20 °C and then once more heated at 0.5 °C min^{-1} (Figure 9.4). It can be seen that the endotherms for each run overlay from ~-19 °C, which suggested -20 °C was sufficiently low to freeze all the intra-particle water.

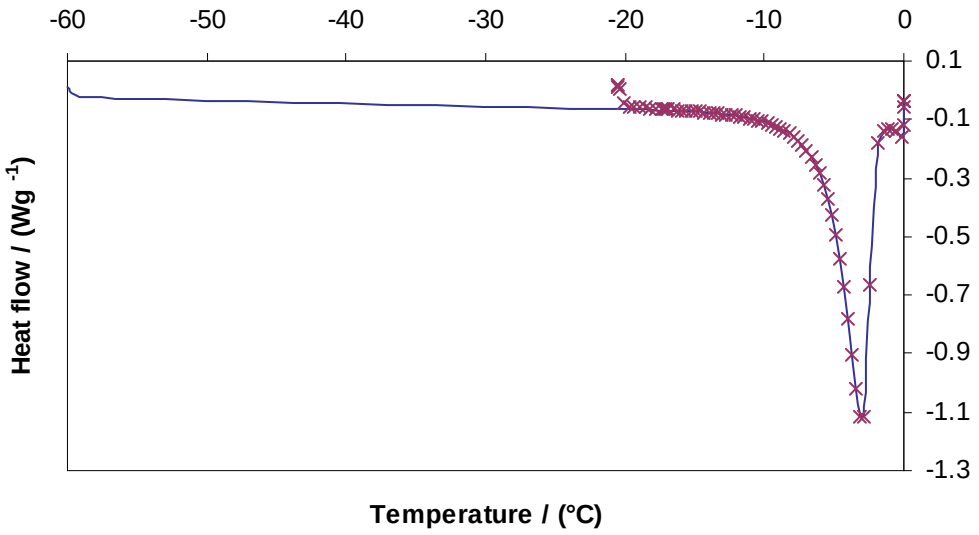

Figure 9.4: A comparison of an endoderm starting at -60 °C (fixed line) and one at -20 °C (crosses)

9.4.4 Evaporation of water during the experimental procedure

The DSC equipment used was unable to crimp together the pan and its lid. There was therefore the potential for liquid to evaporate during the course of the DSC experiment. To minimise the effect of evaporation from the system during the experiment the pan lid was still placed over the sample. In addition, the outer flow of nitrogen, which could not be turned off, was kept at a minimum rate of 2 ml min^{-1}. To ensure that this set-up was effective in preventing evaporation of the intra-particle water from the system, several freezing and melting cycles were performed, keeping the outer bulk layer frozen, on the same sample. It is clear from these results, presented in Figure 9.5 that the exotherms and

endotherms overlay, which proving the same amount of energy is being released and used by the system, respectively, for each freezing and melting cycle. Therefore, the precautions to prevent evaporation of water were sufficient during the experimental time scale.

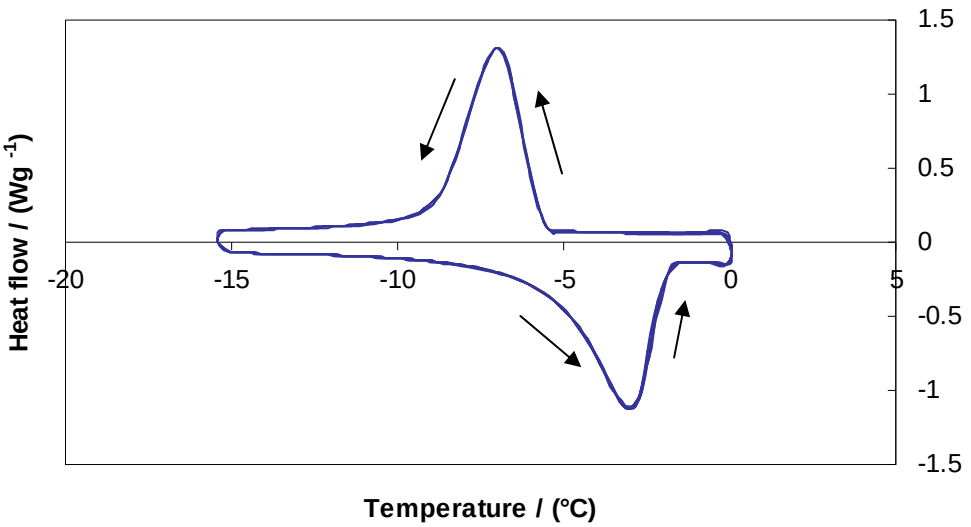

Figure 9.5: Cycles of freezing exotherms and melting endotherms. Arrows indicate the direction of the change in pressure

A similar experiment was then conducted, but the outer bulk liquid was also melted. Figure 9.6 shows the melting endotherms corresponding to this experiment and it can be seen on successive melting cycles less energy was used by the system. This can be explained by a loss of mass, which is due to evaporation of water during the course of the experiment. As there became less water, less energy was required to melt the water in the system. The reason why the exotherms were not studied and presented in Figure 9.6 is because all the water became molten. Therefore, there was no nucleation source (outer bulk layer) to initiate freezing.

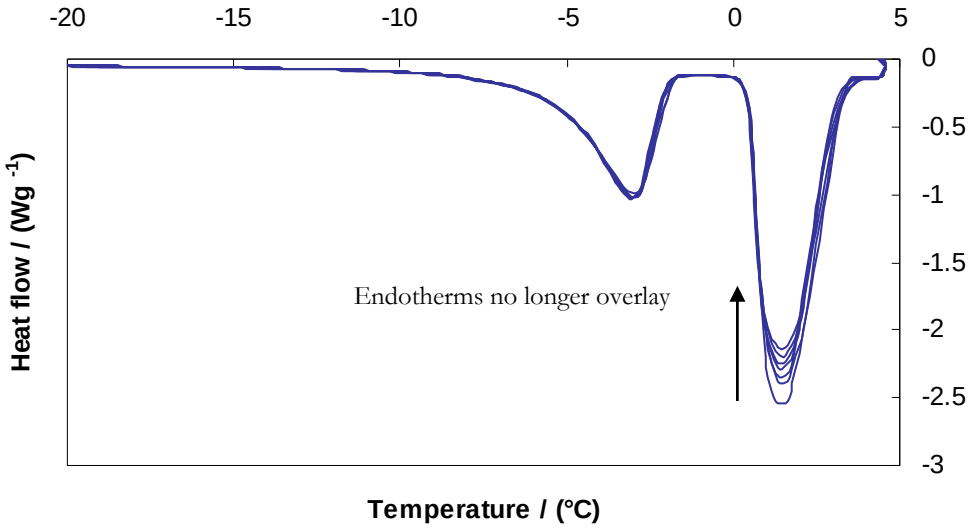

Figure 9.6: Cycles of melting endotherms where the bulk water is also melted. The arrow indicates the endotherms do not overlay

9.4.5 Sample cracking

Perkins *et al.* (2008) demonstrated, through repeating freezing and melting cycles, that S1, during NMR cryoporometry experiments, does not chemically degrade over the experimental time period and the freeze-thaw cycles of water do not destroy the pore walls. Since the exotherms and endotherms overlay (Figure 9.5) it suggests that the experimental conditions during the DSC experiments, similarly, did not cause fractures of the pore walls during the expansion and contraction of water.

9.4.6 Equilibration

The Gibbs-Thomson equation is used to convert melting and freezing point depressions into a pore size, but the equation assumes the system is at equilibrium. The NMR cryoporometry method allows the user to hold the sample at a temperature and allows the system to reach equilibrium and, therefore, the Gibbs-Thomson equation can be used. However, for the DSC experiments the heating is continuous. Therefore, if the melting and freezing processes are non-instantaneous, it means that the melting and freezing temperatures are higher and lower, respectively, than they apparently should be. The lag time effect can be seen in Figure 9.2 and explained as follows. At 0 °C the melting of the outer bulk frozen layer starts but the endotherm continues to ~ 4 °C. In theory bulk water should all melt at 0 °C but because there is a lag time effect the endotherm is instead a broad signal.

To minimise the lag time effect slower ramp rates can be used. However, the ramp rate needs to be high enough for the DSC to be able to detect the heat being consumed or released by the system. To understand how the ramp rate affected the melting process studies were conducted and are explained as follows. A measurement was first carried out using a stepwise change in temperature profile (Gane *et al.* 2004) where every 1 °C the heating was interrupted and the system held at a temperature for 15 minutes. This is shown in Figure 9.7 and overlaid is an endotherm where the ramp rate was continuous at 0.5 °C min^{-1}. It appears that the annealing caused no significant change to the shape of the endotherm and it may be assumed that the system is near equilibrium during the continuous ramp rate experiments.

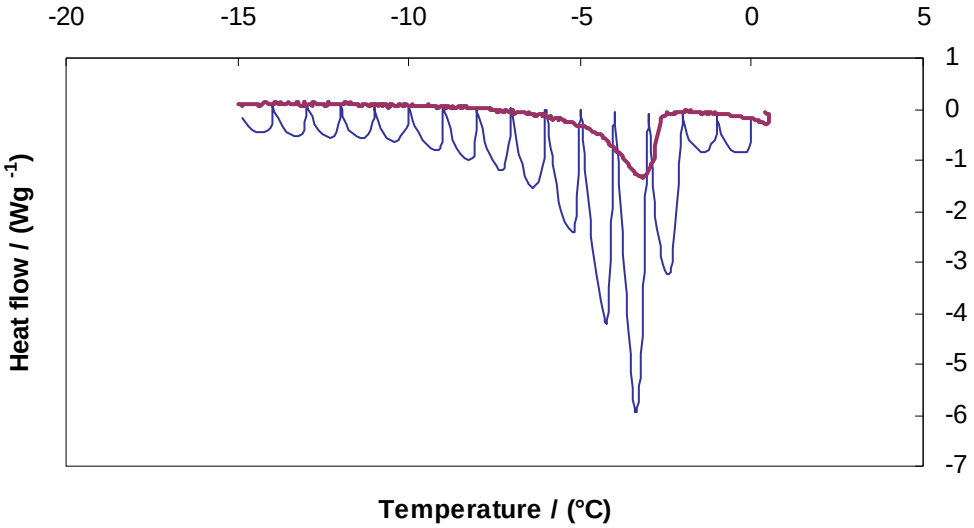

Figure 9.7: Melting endotherm for continuous melting (maroon line) and melting endotherm for when the sample is annealed every degree (blue line)

To see the effect of different heating and cooling ramp rates an experiment was studied which froze and melted only the intra-particle water, using ramp rates that ranged from 0.2-1.4 °C min^{-1} (Figure 9.8). The higher ramp rate experimental runs can be distinguished in Figure 9.8 by more heat being released and consumed by the system for the exotherms and endotherms respectively. If there is a lag time effect between heat being released and consumed by the system it would be anticipated that the exotherms would be shifted to lower temperatures while the endotherms shifted to higher temperatures. This was observed experimentally (Figure 9.8) as the exotherms were progressively shifted to lower temperatures when the ramp rate was increased. In addition, the endotherms were shifted to higher temperatures when the ramp rate was increased.

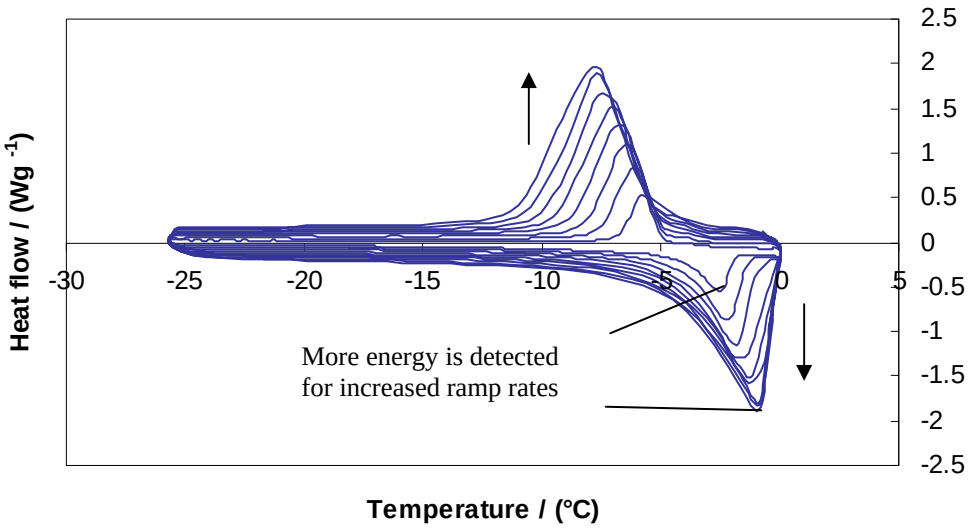

Figure 9.8: The freezing exotherms and melting endotherms for different ramp rates. The arrows show the increasing ramp rates for the exotherms and endotherms

It is proposed that by extrapolating the ramp rates to 0 °C min^{-1} you could achieve a theoretical exotherm and endotherm at a ramp rate of 0 °C min^{-1}. This theoretical exotherm and endotherm would remove the lag time effect and potentially represent the system at equilibrium. However, Figure 9.9 reports how the onset melting temperature and the maximum endotherm peak melting temperatures vary with the heating ramp rates used. It is clear that the temperature where the endotherm reaches a maximum has a linear relationship with the ramp rate that is different to the onset melting point relationship with the ramp rate. It is unclear why there are different temperature dependencies. However, it is clear that to recalibrate the melting endotherm to a ramp rate of "zero" the correction function is itself a function of temperature. Therefore, it was decided not to extrapolate the endotherms and exotherms to a theoretical ramp rate of 0 °C min^{-1}.

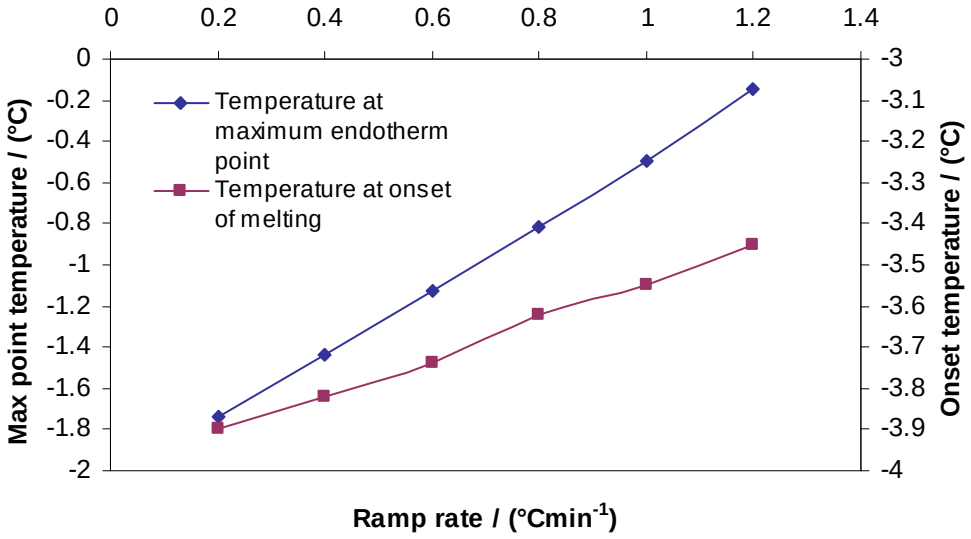

Figure 9.9: The melting onset and maximum endotherm temperatures for different ramp rates

9.4.7 NMR cryoporometry

An example of a typical NMR cryoporometry data set is presented in Figure 9.10 and is explained as follows. The fraction of the molten phase (Figure 9.10) is relative to the total intra-particle water and is proportional to the NMR signal (Mitchell *et al.* 2008). The sample is placed into the NMR machine (280 K) and the relative signal intensity (crosses) corresponds to the intra-particle molten water and the outer bulk molten water. As the temperature is lowered the NMR signal increases according to the Curie Law (Mitchell *et al.* 2008). In addition, because of the super cooling effect the water does not freeze at 0 °C (273.15 K) and there remains signal until freezing is initiated at ~ 262 K when the NMR signal disappears. The system is then heated and the intra-particle water melts, which is shown by the closed diamonds, but the outer bulk layer was kept frozen. The region over which the intra-particle liquid is molten, but the bulk is frozen, is indicated by the plateau in molten volume fraction over the temperature range of ~271-273 K. To freeze the system the temperature change is reversed (closed squares), and when the temperature became low enough the intra-particle water started to freeze. This is indicated by the decrease in the NMR signal. Perkins *et al.* (2008) demonstrated, through repeating the freeze-thaw cycles, that the expansion of water during the NMR cryoporometry experiment did not damage the pore structure of S1. Indeed, the expansion of water on freezing decreases with temperature, and thus freezing point depression will reduce thermal expansion problems (Perkins *et al.* 2008).

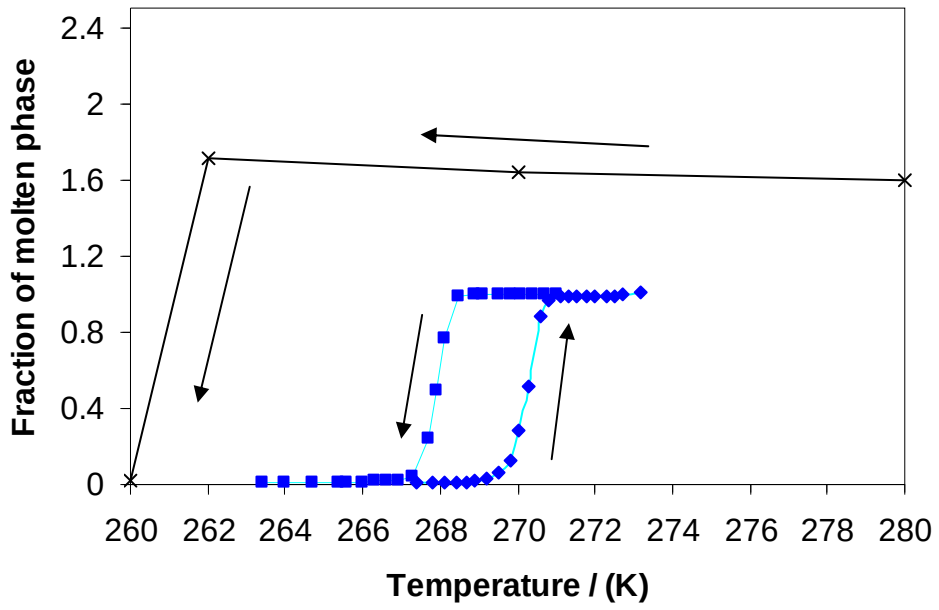

Figure 9.10: NMR cryoporometry boundary freezing (closed squares) and melting (closed diamonds) curves with the super cooling curve (crosses). Arrows are added to show the temperature direction change and lines are to guide the eyes. The molten fraction is set to one when only the intra-particle material is molten

9.5 Discussion

This Chapter so far has presented the experimental cryoporometry results for S1 using the DSC method and NMR method. The discussion section will convert the experimental data into a pore size distribution to enable a comparison between the two methods.

Before this is presented, an explanation of how the pore size distributions are found using cryoporometry data is given as follows. On increasing the temperature the amount of molten liquid is proportional to the NMR signal intensity (Mitchell *et al.* 2008), I_{NMR}, or the heat, Y, recorded by the calorimeter (Iza *et al.* 2000). In addition, according to the Gibbs-Thomson equation, the amount of molten liquid, v, at a given temperature will be in pores of size x or less. Therefore, when the temperature is increased over a small range, the change in the molten volume, which is proportional to dI_{NMR} or dY, will occur in pores of size $x + dx$. Strange *et al.* (1993) and Iza *et al.* (2000) have proposed methods to calculate a pore size distribution, $\frac{dv}{dx}$ as a function of x, from the NMR and DSC methods respectively. The NMR method employed by Strange *et al.* (1993) uses the chain rule expressed by:

$$\frac{dv}{dx} = \frac{dI_{NMR}}{dx} = \frac{dI_{NMR}}{dT_m(x)} \cdot \frac{dT_m(x)}{dx} \qquad 9.1$$

From the Gibbs Thomson expression $dT_m(x)/dx=K_{GT}/x^2$, so equation 9.1 can be expressed as:

$$\frac{dI_{NMR}}{dx} = \frac{dI_{NMR}}{dT_m(x)} \cdot \frac{K_{GT}}{x^2} \qquad 9.2$$

Iza *et al.* (2000) expressed $\frac{dv}{dx}$ as:

$$\frac{dv}{dx} = \frac{k}{K_{GT}} \cdot \frac{(\Delta T)^2}{W(T)} Y \qquad 9.3$$

where $W(T)$ is the energy of solidification of water as a function of temperature and k the heating rate.

9.5.1 Comparison of pore size distributions from DSC and NMR methods

Pore size distributions have been calculated for both the DSC and NMR methods using the melting curves (Mitchell *et al.* 2008). In addition, $\frac{dv}{dx}$ has been renormalised to 1, which is defined as P(d).

P(d) as a function of pore size for the DSC method has been presented for two different ramp rates, which are 0.5 °C min^{-1} (Figure 9.11) and 1 °C min^{-1} (Figure 9.12). For both ramp rates there is a monodisperse pore size, but for the higher ramp rate the distribution is shifted to larger pores. This is because of the lag time between the heat being used by the system and the heat change being detected by the thermocouples, as discussed above.

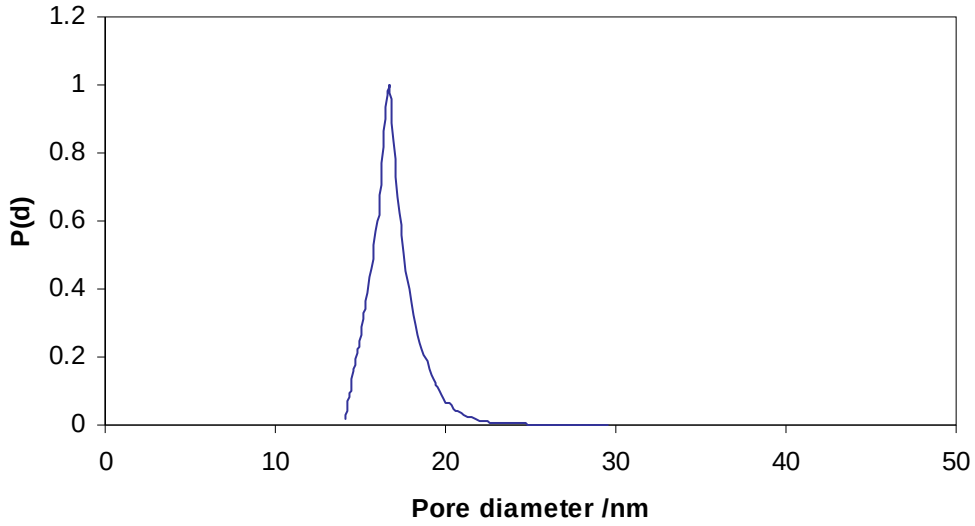

Figure 9.11: Normalised PSD from DSC data when the ramp rate is set at 0.5 °C min^{-1}

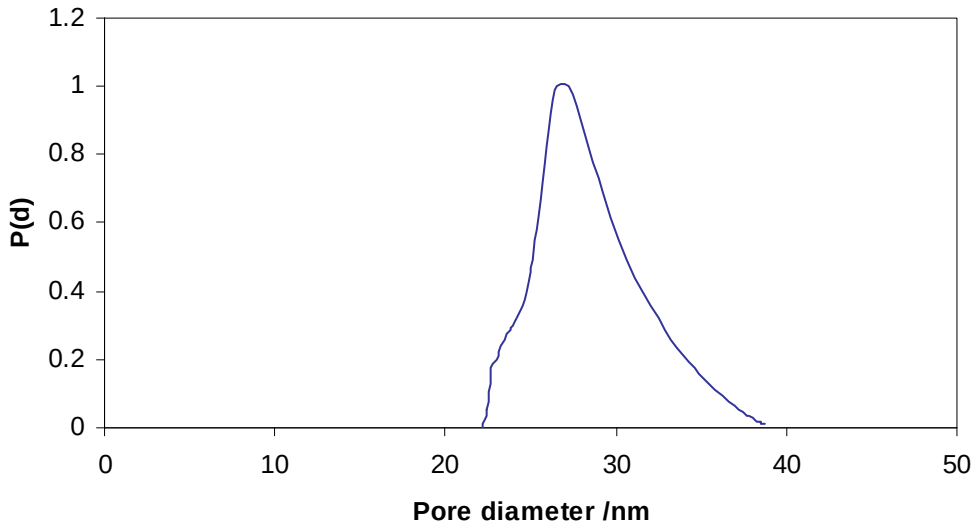

Figure 9.12: Normalised PSD from DSC data when the ramp rate is set at 1 °C min^{-1}

In Figure 9.13, P(d) as a function of pore size from the cryoporometry NMR data set is presented, which gives again a monodisperse distribution of pores. An overlay of the PSD from the DSC method using a 0.5 °C min^{-1} has been made. Incorporated in the PSD curves are the error bars calculated from the temperature gradient across the samples. Perkins (2009) calculated this to be ± 0.2 K for the NMR method while the DSC method is ± 0.1 K from the manufacturer's specifications. The median pore sizes from the two experimental methods are identical within the experimental error. However, it appears the PSD from the DSC method is systematically narrower compared to the PSD from the NMR method.

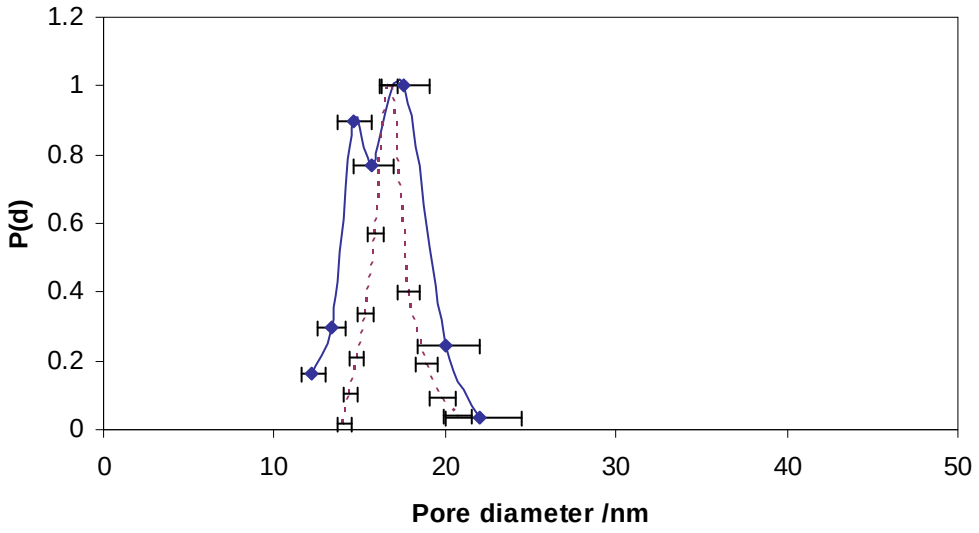

Figure 9.13: Normalised PSD from NMR cryoporometry data (closed diamonds) and the normalised PSD from the DSC data using a 0.5 °C min^{-1} ramp rate (dotted line)

9.6 Conclusions

The NMR cryoporometry method is a static one so the liquid-ice interface can be allowed to reach equilibrium. The DSC method, however, uses a continuous ramp rate so there is always a lag time between the heat change and the detection by the thermocouples. However, there does appear to be agreement between both the NMR and DSC methods for analysing S1 (see Figure 9.13), when the set ramp rate for the DSC is low and the total system mass is low (20 mg). For larger samples there may be an increased lag time effect between the heat change and the thermocouples detecting the change. Therefore, if the DSC method is used instead of the NMR method a check that the ramp rate is sufficiently low must be carried out.

9.7 Direction of cryoporometry work

It appears the DSC method is a suitable alternative to the NMR method for calculating a pore size distribution. However, the NMR method has an advantage over the DSC method as some NMR machines can probe the molten fraction further by diffusion studies and relaxation studies (Perkins *et al.* 2008). The next Chapter will focus solely on the NMR method to study the freeze-thaw mechanisms. The work indicates that there is an analogous mechanism to advanced adsorption in cryoporometry that is termed advanced melting.

Chapter 10

Studies of freezing-melting hysteresis in cryoporometry scanning loop experiments using NMR diffusometry and relaxometry

10.1 Introduction

Chapter 8 has introduced the reader to the background theory of cryoporometry and discussed the different mechanisms that have been proposed to explain freeze-thaw hysteresis. Following this Chapter 9 compared the two different experimental methods, DSC and NMR, and found they give similar pore size distributions using the calculations proposed by Strange *et al.* (1993) and Iza *et al.* (2000).

The aim of this Chapter is to utilise scanning loop and curve experiments on S1, to test the various theories of freeze-thaw hysteresis more rigorously. Scanning loop experiments have been used extensively in gas sorption studies to probe sorption hysteresis models, and the reader is referred back to the work in Chapter 7 for an in-depth discussion. For clarity, a brief summary of gas sorption scanning curve work is given as follows. In gas sorption, scanning curves are achieved by reversing the progressive increase, or decrease, in pressure on the adsorption, or desorption, curve, respectively, while the sample is still partially saturated in the capillary condensation region. An early model, developed by Everett and Smith (1954), and commonly referred to as independent domain theory, has been found to account for many of the findings. The main idea of the theory is that each pore space can fill and empty independently of the state of its neighbour. Therefore, for pores that can act independently, it is expected that desorption and adsorption scanning curves should cross directly from the adsorption and desorption boundary curves respectively. Conversely, for pores that do not act independently, the scanning curves will meet the hysteresis loop at its closure point. Cryoporometry also potentially represents an excellent test for independent domain theory, since a possible mechanism for melting involves initiation from the ubiquitous, non-frozen layer at the pore surface (Quinson and Brun 1988; Jackson and McKenna 1990; Schmidt *et al.* 1995; Schreiber *et al.* 2001), where the liquid-solid meniscus propagates from the surface towards the pore bulk. In such a case, each pore can melt independently, and, thus, a melting scanning curve should cross directly between melting and freezing boundary curves. However, it is also possible that an advanced melting

mechanism, analogous to advanced adsorption (de Boer, 1958), may also arise, involving initiation of melting from the molten phase within an adjoining pore. The occurrence of this mechanism would thus probably lead to marked changes in the form of the melting scanning curve. Moreover, since the mechanism for heterogeneous nucleation of freezing relies upon the state of the neighbouring pore, then the shape of a freezing scanning curve should, therefore, also contrast markedly with that of a melting scanning curve for pores melting independently.

10.2 Previous studies

Some previous work has been conducted on cryoporometry scanning curves. Kondrashova *et al.* (2010) conducted cryoporometry experiments with nitrobenzene imbibed in Vycor porous glasses where they partially melted the imbibed material and then refroze the system. Similarly, melting scanning curves were performed where the system was only partially frozen and then re-melted. Kondrashova *et al.* (2010) claimed that, since the scanning freezing and melting loops intersected at particular points, but followed different paths to get there, then there must be different solid-liquid configurations existing at the same point on each loop. These workers, however, did not directly demonstrate that the configuration of the molten fraction was different at the curve intersection point. However, the size of the pores, within which the molten fraction resides, can be probed by relaxometry, and the configuration and connectivity of the pores containing molten phase can be probed with pulsed-field gradient (PFG) NMR. PFG NMR has previously (Perkins *et al.* 2008) been used to demonstrate percolation effects in freezing. Hence, in this work PFG NMR and relaxometry will be used to probe the distribution and connectivity of molten phase at various points within scanning loops in order to assess how well the various theories of hysteresis can account for these observations. In particular, the presence of dead-end pores has been invoked previously (Kondrashova *et al.* 2010) to explain the shape of cryoporometry scanning loops and the viability of this explanation will also be assessed. This Chapter will aim to study advanced melting effects, as they may impact adversely on the accuracy of pore size distributions obtained from melting curves if neglected. It has also been suggested (Kondrashova *et al.* 2010) that the removal of hysteresis by axial freezing and melting has not been observed. In this Chapter it will be explicitly demonstrated that hysteresis can be virtually removed from cryoporometry data, which indicates axial freezing and melting, which means advancing and retreating hemispherical menisci. This is instead of melting by cylindrical sleeve menisci (see Chapter 8).

10.3 Experimental

The material studied in this Chapter is S1. The material has been run in whole and fragmented states, with a powder particle size of 25 μm for the latter. Previous work (Rigby 2000) has shown that fragmentation does not damage the mesoporous structure.

10.3.1 NMR cryoporometry

The NMR cryoporometry procedure for whole samples was detailed in Chapter 9. In this Chapter fragmented samples have been used too. To fragment the samples, 20 whole dry S1 pellets were crushed using a pestle and mortar. The approximate sizes of the particles were determined by a microscope and they were greater than ~ 25 μm. The fragmented particles were then water imbibed as described in Chapter 9. The NMR experiments were carried out on the fragmented samples as they were for the whole samples (see Chapter 9).

10.3.2 PFG-NMR Diffusion studies

The PFG-NMR experiments were carried out during the NMR cryoporometry experiment. The pulse sequence used was a stimulated echo with bipolar longitudinal eddy current delay (BPLED) developed by Wu *et al.* (1995) (see Chapter 3). The values of δ and τ were 0.002s and 0.0001s respectively and four different values of Δ were used, which were 0.2, 0.15, 0.1 and 0.05s. For each diffusion experiment, 10 data points were taken at increasing gradient strengths between 0.674 and 33.143 G cm^{-1}, and each point was obtained with 16 scans.

10.3.3 T_2 studies

The T_2 experiments were carried out during the NMR cryoporometry experiment. The pulse sequence used was the Carr-Purcell Meiboom-Gill (CPMG) sequence (see Chapter 3). The values of t_d used varied between 0.6 and 1 ms.

10.4 Analysis of experimental data

Chapter 3 introduced equations which the raw NMR data in this Chapter will be fitted to. To aid the reader these equations are presented again and all the terms are defined.

The raw PFG-NMR data was fitted to:

$$\frac{I_{NMR}}{I_0} = \exp\left[- D_{PFG}\gamma^2 g^2 \delta^2 \left(\Delta - \frac{\delta}{3} - \frac{\tau}{2} \right) \right] \qquad 10.1$$

where I_{NMR} is the NMR signal intensity, I_0 is the echo intensity in the absence of the gradients, D_{PFG} is the diffusion coefficient, γ is the gyromagnetic ratio, g is the pulsed field gradient strength, δ is the duration of the pulsed gradient, Δ is the diffusion time and τ the correction time for the phasing and dephasing between bipolar gradients.

The measured tortuosity, τ_p, was obtained using:

$$\tau_p = \frac{D(T)}{D_{PFG}} \qquad 10.2$$

where $D(T)$ is the diffusion of bulk water at temperature , T.

The T_2 relaxometry data was fitted to:

$$I_{NMR}(2t_d) = I_0 \exp\left(\frac{-2t_d}{T_2} \right) \qquad 10.3$$

where $I_{NMR}(2t_d)$ is the NMR signal intensity at echo time, $2t_d$.

As will be shown below, during various freezing and melting mini loops, several PFG experiments and T_2 relaxation studies were carried out at points where the sample contained the same fraction of frozen water. This enabled a direct comparison of diffusion/T_2 relaxation data following different thermal histories but at an equivalent relative signal intensity. The diffusion coefficients and T_2 relaxation constants for the molten water were calculated from the signal attenuation observed during the experiments (see Chapter 3 for the method). To account for the temperature dependency of the water

diffusion coefficient, a calibration curve was used based upon literature data. This was discussed in Chapter 3 and the calibration curve was determined by Perkins (2009). The tortuosity factor at different temperatures could then be calculated according to equation 10.2. To account for the temperature dependency for the T_2 relaxation, the following procedure was carried out. T_2 relaxation studies in the region over which the intra-particle water is molten, but the bulk is frozen were probed. This region was discussed in Chapter 8 but for completeness a typical NMR cryoporometry data set has been presented in Figure 10.1 and a rectangle shows this region. The variation in T_2 relaxation constants with temperature over this region are presented graphically in Figure 10.2. Figure 10.2 will be referred to in the Results section to correct the T_2 relaxation time constants for temperature effects.

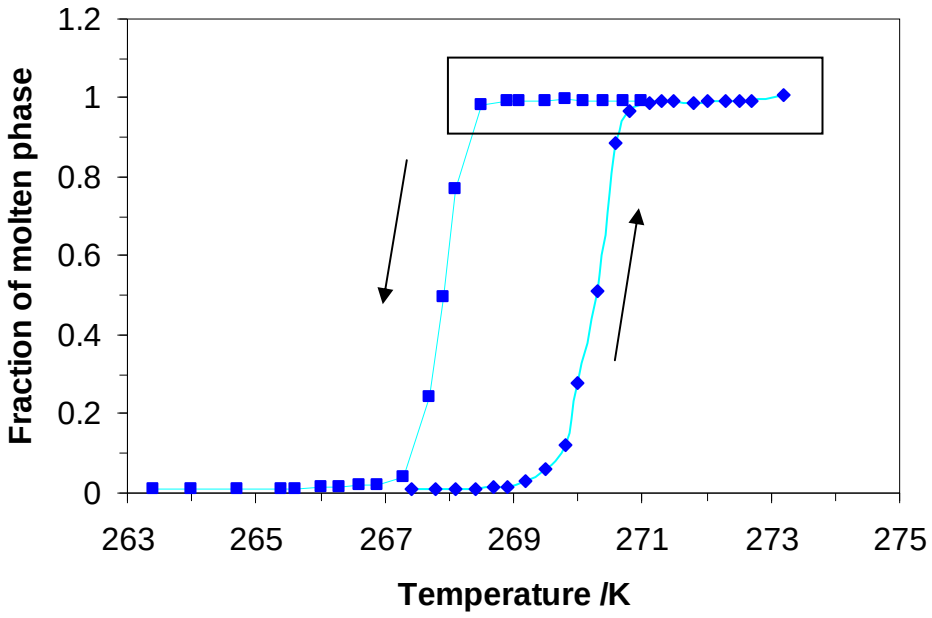

Figure 10.1: Typical boundary freezing and melting curves for a typical whole pellet sample from batch S1. The closed squares depict the boundary freezing curve, the closed diamonds depict the boundary melting curve, and arrows shown are to guide the eye. The rectangle is described in the text

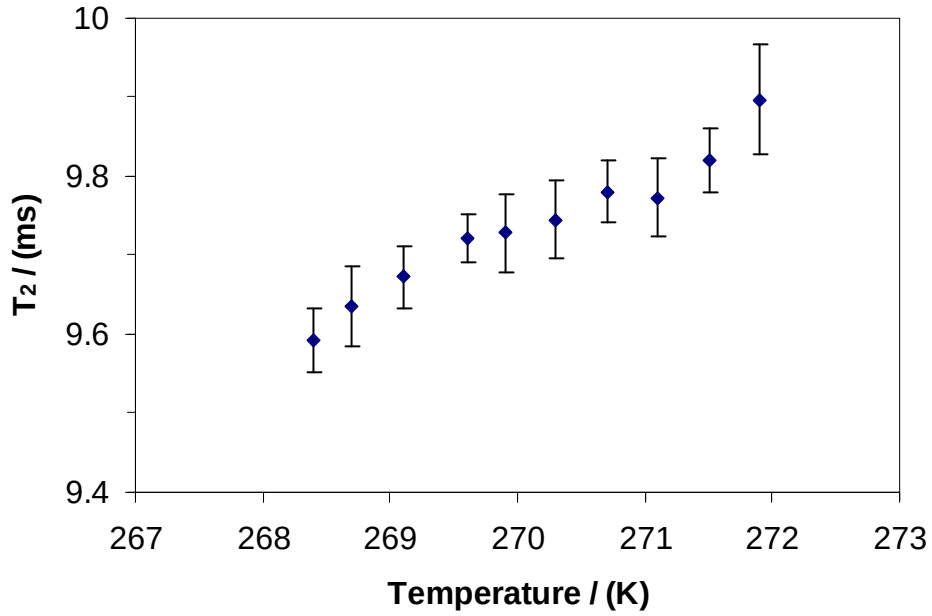

Figure 10.2: Variation of T_2 relaxation constants over the plateau region in Figure 10.1. The error bars were calculated using the non linear curve function in Origin

10.5 Results

10.5.1 NMR cryoporometry scanning curves

Melting and freezing scanning curves were achieved through only partial melting, or freezing, of the pore fluid, and then cooling, or warming, the system, respectively. Figure

10.3 shows the results of various examples of melting and freezing scanning experiments (open diamonds and squares respectively) for water in S1, together with the surrounding boundary melting and freezing curves (closed diamonds and squares respectively). Following initial freezing, where the temperature was decreased to 265.2 K until all significant NMR signal had disappeared, the temperature on the subsequent melting curve was raised to 270.2 K, where the sample was only partially melted. On reversing the temperature at 270.2 K, the NMR signal decreased immediately (open squares), differing from the boundary freezing curve (closed squares), which is delayed through pore blocking (Perkins *et al.* 2008). This initial decrease in the NMR signal on reversing the temperature suggests that, for the scanning freezing curve, there is already an ice front within the pore network that can propagate through the pore system immediately without being delayed by narrow pore necks at the exterior. To indirectly support this idea, it is noted that the freezing scanning curve is similar in shape to the boundary freezing curve of the fragmented sample (see closed squares in Figure 10.4), which has had pore blocking effects removed (Perkins *et al.* 2008).

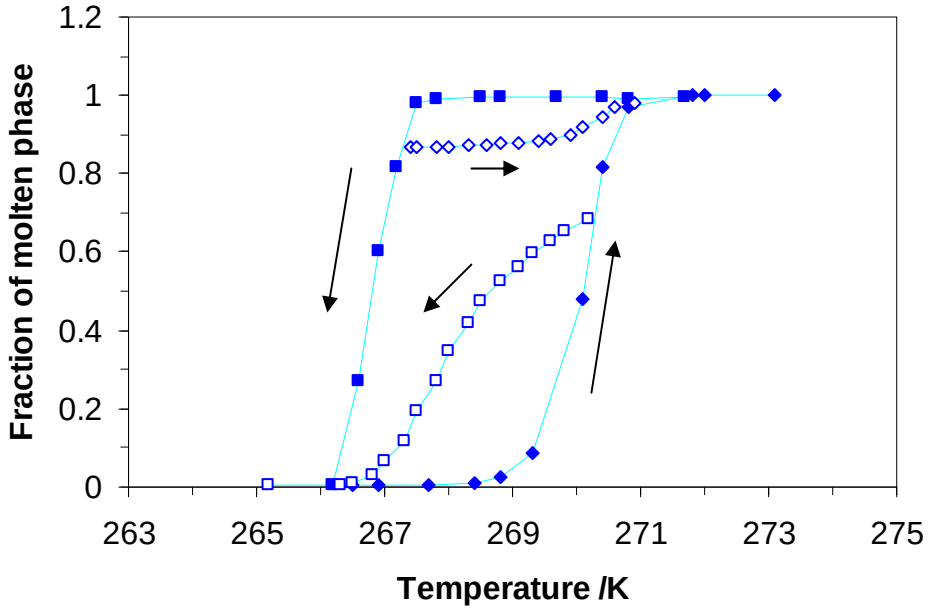

Figure 10.3 (a): Examples of freezing (open squares) and melting (open diamonds) scanning curves inside the boundary curves (closed squares and diamonds), for whole pellet samples from batch S1. The arrows shown are to guide the eye

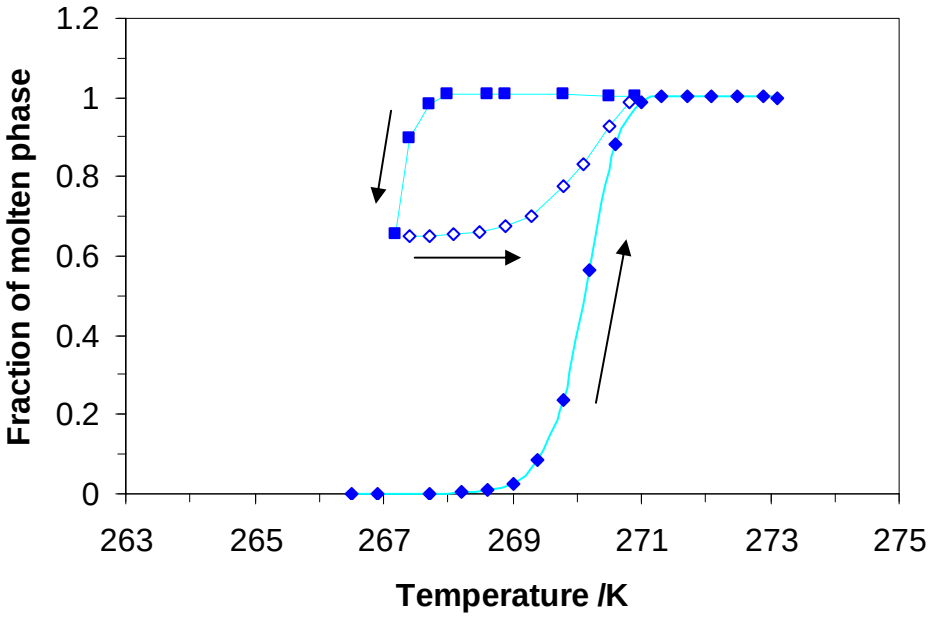

Figure 10.3 (b): Further example of a melting scanning curve (open diamonds) inside the boundary curve for a whole pellet sample from batch S1. The arrows shown are to guide the eye

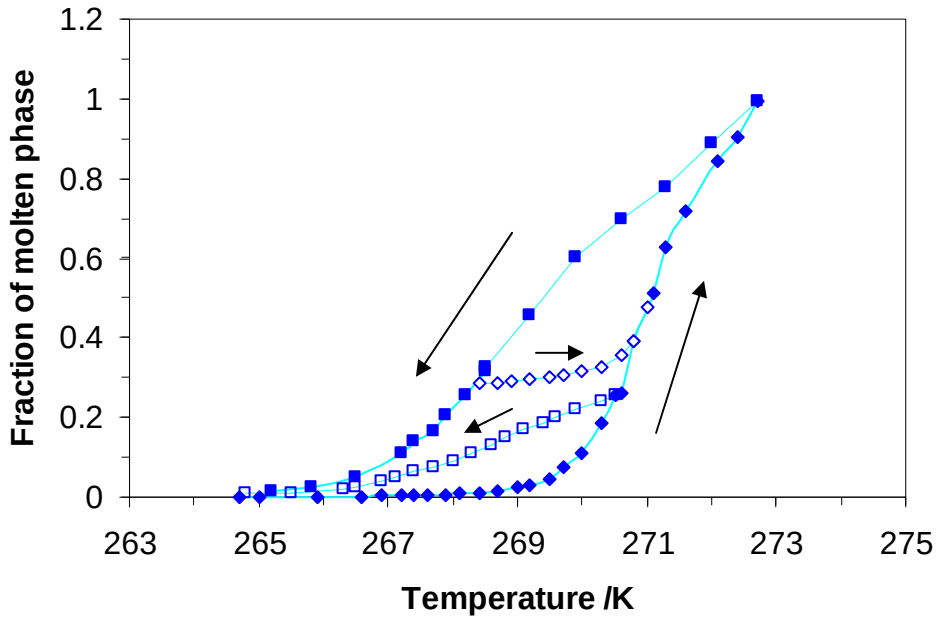

Figure 10.4: Examples of freezing (open squares) and melting (open diamonds) scanning curves inside the boundary loop (closed squares and diamonds) for a fragmented sample from batch S1. The arrows shown are to guide the eye

In Figure 10.3, the form of the melting scanning curves is remarkably different to that of the freezing scanning curve. Following complete melting of the imbibed pore liquid (closed diamonds), the temperature was decreased to partially freeze the sample. At an arbitrarily chosen molten fraction the temperature was then raised, where the melting scanning curve is depicted by open diamonds. On incrementally increasing the temperature, the molten fraction did not initially increase. This feature is consistent with the theory of cryoporometry single pore hysteresis in cylindrical pores, where melting is nucleated from the liquid-like layer arising between the frozen liquid and the pore wall. This theory predicts that the melting scanning curve should cross from the boundary freezing curve directly to the boundary melting curve. However, Figure 10.3 (a) shows that, at 269 K, the molten fraction increases on the melting scanning curve, and the scanning curve subsequently joins the upper closure point of hysteresis. The temperature, of 269 K, at which the molten fraction increases on the scanning curve is within the range of temperatures over which the molten fraction is increasing on the boundary melting curve. This result is consistent with what would be expected if pore blocking was present, as proposed by Perkins *et al.* (2008) for S1, and is explained as follows. On the boundary freezing curve, freezing is only started once the temperature of the system has been lowered to freeze the outer narrow necks of S1. Since it is feasible to stop the boundary freezing curve at various points, to perform different melting scanning curves, this is suggestive of a range of particular narrow neck

sizes in S1 guarding access to different regions, and the propagation of the ice front through each of these regions is held up until the temperature has been progressively further lowered to reach the freezing point for each particular guarding neck size. The form of the melting scanning curve is consistent with either an independent pore, or an advanced melting, mechanism. If the pores were melting independently, the first pore to melt, via a cylindrical sleeve meniscus, following reversal of temperature would be the smallest frozen neck. Subsequently, as the temperature is raised, progressively larger and larger pores could melt via a cylindrical sleeve meniscus. If the pores are melting independently, the temperature range of melting for the scanning curve must be within the range of temperatures where melting also occurs on the boundary melting curve. A small pore neck could conceivably shield some, but not necessarily, all of the pores larger than itself, and thus the path of the melting scanning curve would represent the distribution of necks shielded by the particular neck size corresponding to the temperature at reversal. Since this might include representatives from all bins in pore size in the overall distribution, the scanning curve would then meet the boundary curve at the upper hysteresis closure point, as observed experimentally. Conversely, if advanced melting were a possibility, this would not necessarily mean that melting would be initiated immediately, via an hemispherical meniscus, following a reversal in temperature, since the smallest frozen pores may, themselves, be surrounded by ice, even if molten fronts existed elsewhere in the pore structure next to much larger pores. Melting would not then occur until the temperature reached that required for melting via a cylindrical sleeve meniscus in the smallest frozen pores, or via a hemispherical meniscus for larger pores neighbouring a molten front. It is also conceivable that, even if advanced melting was possible, a void space region that becomes frozen may also be isolated from the rest of the void space that remains molten by solid walls, and thus, in the absence of dead-ends, would still initiate melting only via a cylindrical sleeve meniscus of the smallest frozen pore. Hence, further information is required to distinguish between these various potential interpretations of these ambiguous melting scanning curves.

10.5.2 Scanning curves on fragmented S1

In order to elucidate the melting mechanisms operating for scanning curves, scanning experiments were also performed on a fragmented sample. Since S1 is macroscopically heterogeneous, with long-range, spatial correlations in pore sizes (Hollewand and Gladden 1995b), the shielding of the larger pores by exterior pore necks can be removed by fragmentation of the whole pellets. Figure 10.4 shows an example of a melting scanning

curve (open diamonds) for a fragmented sample of S1. It can be seen from Figure 10.4 that the melting scanning curve now crosses more directly between the freezing and melting boundary curves, and this is consistent with what would be expected for cryoporometry single pore hysteresis, within a cylindrical pore, arising because fragmentation has now removed adjacent pores that remained molten (and could thus initiate advanced melting) from immediate proximity to the frozen pores.

10.5.3 NMR cryoporometry scanning loops

More complex scanning experiments can also be used to disambiguate the interpretation of basic scanning curve data. Within a scanning curve it is possible to effect a further reversal in the direction of the temperature change, and such an experiment will be subsequently referred to as a scanning loop to differentiate between experiments where two temperature reversals are made as opposed to one (for curves). Again, this is analogous to Chapter 7. Figure 10.5 depicts examples of some of the different types of loops that have also been employed in this work. Figure 10.5 (a) depicts a loop that commences with a temperature reversal part way up the boundary melting curve at 270.6 K (shown as open squares), and includes another reversal in temperature at 268.2 K before all of the core void space has frozen (shown as open diamonds). This will be termed a freezing scanning loop. It is noted from Figure 10.5 (a) that the melting arm of the loop (open diamonds) begins to rise in intensity immediately following the second temperature reversal, while, in this same temperature range, the boundary melting curve (closed diamonds) remains horizontal. This suggests that melting occurs at lower temperatures in the loop than for the boundary curve. This finding is consistent with the occurrence of advanced melting, initiated from the pores that still contain molten liquid at the lower tip of the loop. Figure 10.5 (b) depicts a loop that commences with a temperature reversal part way down the boundary freezing curve at 267.9 K, and includes another reversal in temperature at 269.5 K. There is no observable hysteresis for the loop depicted in Figure 10.5 (b), which will be termed a melting scanning loop.

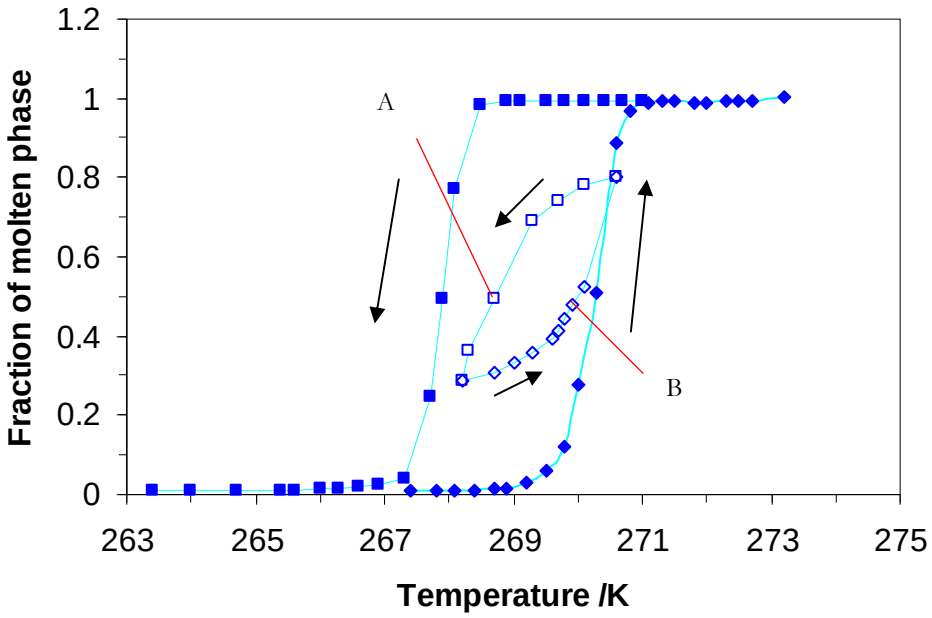

Figure 10.5 (a): A freezing scanning loop, where Points A and B are the studied positions referred to in the text. The arrows shown are to guide the eye

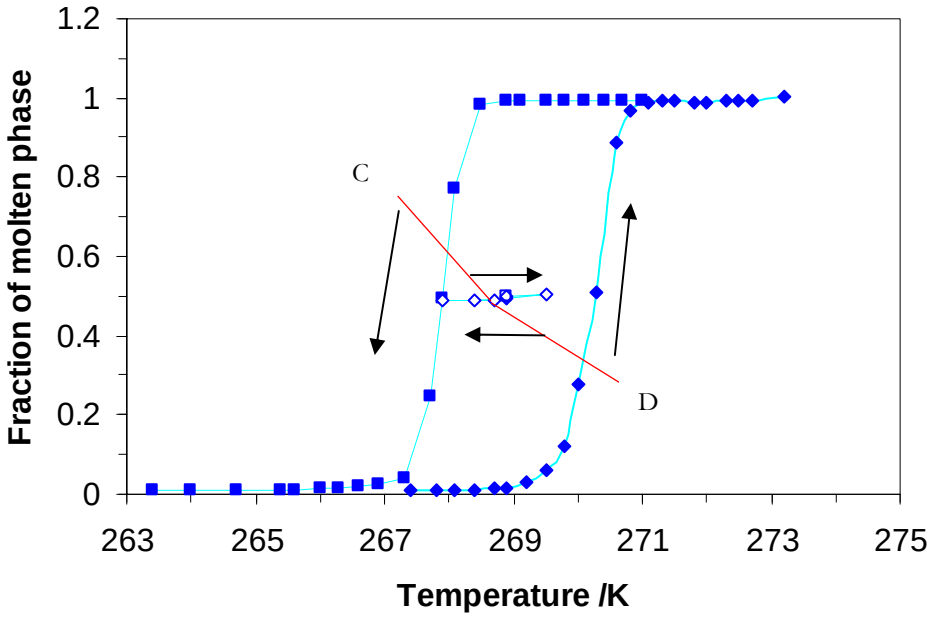

Figure 10.5 (b): A melting scanning loop, where regions C and D are the studied positions referred to in the text. The arrows shown are to guide the eye

The reversibility of the different types of loops has also been studied. For both the types of loops shown in Figure 10.5, initiated from either the boundary freezing or the boundary melting curves, the respective loops closed at the same points. While for the freezing scanning loop (Figure 10.5 (a)), hysteresis was observed, in contrast, the melting scanning

loop (Figure 10.5 (b)) appeared reversible at all temperatures studied. To facilitate probing of the underlying processes, it was ensured that the melting and freezing scanning loops intersected a point with the same total molten fraction and temperature. Since the loops followed different paths to/from this point, previous proposals from the literature (Kondrashova *et al.*, 2010) would suggest that each loop should possess different distributions of the molten fraction.

10.5.4 Scanning loops diffusion and relaxometry studies

To probe the distribution of molten phase, ^{1}H PFG-NMR experiments were performed, at the four labelled points (A, B, C and D) shown in Figure 10.5, during the scanning loops. As discussed above, the raw PFG-NMR data was fitted to Equation 10.1, the measured tortuosity, τ_p, was obtained using Equation 10.2, and the T_2 relaxometry data fitted to Equation 10.3; all resulting data are shown in Table 10.1. Examples of typical raw data sets are shown in Appendix A6. The diffusion experiments were studied progressively with increasing values of large delta (from 0.05 s to 0.20 s). To ensure the diffusion experiments were not heating the sample, thus, changing the ice-liquid interface and causing a systematic variation in the diffusivity values for successive diffusion experiments, the first diffusion experiment was repeated for Points A and C. These two experiments are shown in brackets in Table 10.1 and were within the experimental fit error of the first diffusion experiments. Therefore, the diffusion experiments were not significantly heating the sample to change to solid-molten fraction boundaries. Points A and B are in the freezing scanning loop, and are of the same molten fraction but different temperatures. Points C and D are in the melting scanning loop (but on the initial melting arm, and freezing arm, respectively), and are at the same molten fraction and temperature, which is also the same molten fraction and temperature as Point A. It is noted that the tortuosity values for the molten fractions for Points A and C are different. This suggests that the configuration and/or connectivity of the molten fraction is different for Points A and C. This provides direct evidence, not given in previous work (Kondrashova *et al.*, 2010), that the different thermal histories of the different pathways to reach the same point do result in different spatial dispositions of the molten phase, even though the pathways intersect at the same molten fraction and temperature. This means that the positions of the solid ice fronts are arranged differently in space in Regions A and C, and, therefore, will penetrate through S1 in separate ways.

Region	Temperature /K	Δ/s	$D\times10^{10}$ /(m^2s^{-1})	τ_p	RMS displacement /μm	T_2 Relaxation constant /ms
A	268.7	0.05	3.65 ± 0.02 (3.67 ± 0.03)	2.45	10.5	3.50 ± 0.05
		0.1	3.62 ± 0.04	2.47	14.7	
		0.15	3.54 ±0.03	2.52	17.8	
		0.2	3.50 ±0.04	2.55	20.5	
B	269.9	0.05	3.96 ± 0.04	2.36	10.9	3.56 ± 0.05
		0.1	3.84 ± 0.03	2.44	15.2	
		0.15	3.75 ± 0.02	2.50	18.4	
		0.2	3.74 ± 0.04	2.50	21.2	
C	268.7	0.05	4.39 ± 0.03 (4.38 ± 0.04)	2.03	11.5	8.68 ± 0.07
		0.1	4.31 ± 0.03	2.07	16.1	
		0.15	4.25 ± 0.03	2.10	19.6	
		0.2	4.23 ± 0.04	2.12	22.5	
D	268.7	0.05	4.39 ± 0.03	2.03	11.5	8.65 ±0.04
		0.1	4.30 ± 0.03	2.07	16.1	
		0.15	4.25 ± 0.04	2.10	19.6	
		0.2	4.21 ± 0.04	2.12	22.5	
E	270	0.05	4.81 ± 0.02	1.95	12.0	4.98 ± 0.05
		0.1	4.68 ± 0.03	2.00	16.8	
		0.15	4.59 ± 0.02	2.04	20.3	
		0.2	4.53 ± 0.04	2.06	23.3	
E′	270	0.05	4.78 ± 0.02	1.96	12.0	4.91 ± 0.04
		0.1	4.63 ± 0.02	2.02	16.7	
		0.15	4.57 ± 0.03	2.05	20.3	
		0.2	4.53 ± 0.03	2.07	23.3	

Table 10.1: Tortuosities and relaxation times measured at specified points in cryoporometry scanning loops as indicated in the relevant Figures. The errors quoted were found using the non-linear curve fit in Origin.

From Table 10.1 it is noted that the tortuosity for Points B and C increases with increasing diffusion time and then gives some indication of flattening out to become independent of diffusion time. This finding is consistent with the rms displacement of diffusing molecules increasing with diffusion time such that after a certain time they probe length-scales greater than a value (the correlation length) over which the structure becomes statistically uniform. The results suggest that the correlation lengths for Points B and C are ~15-18 μm, and ~16-19 μm, respectively. This value greatly exceeds the size of a pore in S1 (~15 nm) and suggests heterogeneity in the spatial distribution of molten phase up to these length-scales. The tortuosity data for Point A suggests an even longer correlation length than for Points B and C.

To probe the size(s) of pores associated with the molten fraction in Points A and C, T_2 relaxometry data were also obtained. Since the two points compared are at the same temperature, then no temperature correction for the T_2 data was required. From Table 10.1, it can be seen that, since it has a larger T_2, Point C is associated with larger pores relative to Point A. This difference can be understood in terms of the different thermal histories to achieve the same point. To reach Point A the system was completely frozen (~263 K) and the temperature was then increased incrementally, thereby melting progressively larger pores. On reversing the temperature at the start of the scanning freezing loop the larger pores of S1 still remained in the frozen state. For Point C to be reached all imbibed liquid within S1 was initially molten (~272 K) and when the temperature was lowered the narrow outer necks of S1 prevented the ice front from penetrating the network until the temperature at which the necks would freeze, via a hemispherical meniscus, was reached. On obtaining the necessary temperature to achieve Region C, there must still be void space regions guarded by further narrower necks otherwise the ice front would be able to penetrate throughout S1. Moreover, behind these additional narrow necks there must be larger pore bodies according to the relaxometry data.

In addition, it was of interest to know whether the hysteresis observed in the freezing scanning loop was due to the different freeze-thaw mechanism predicted for cryoporometry single pore hysteresis or whether structural differences were causing the effect. Points A and B, of the freezing scanning loop, were at the same molten fraction but Point A was studied when the system temperature was being lowered and Point B when the temperature had been reversed. The temperature corrected tortuosity values for both Points A and B were the same within experimental error, suggesting the connectivities of both regions were identical (Hollewand and Gladden 1992). From Figure 10.2 the variation in the T_2 relaxometry constants between 268.7 K (Point B) and 269.9 K (Point A) was less than the measurement error. Therefore, the temperature difference between Points A and B are so small no temperature correction was deemed necessary. Thus, there was, similarly, no variation in the relaxometry data for Points A and B, which probes shorter length scales, and these two results suggest no difference at all in the regions of void space occupied by molten fluid at Points A and B. However, it was noted that the freezing and melting point depressions corresponding to Points A and B, respectively, are not related by a factor of two, as was found for points with equivalent molten volume

fractions located on the boundary freezing and melting curves for fragmented samples (Perkins *et al.* 2008).

Further, the tortuosity and relaxometry data for Points C and D are the same within experimental error indicating the melting scanning loop is completely reversible. This means that as the temperature was increased and then reversed in moving from Point C to Point D, the increased temperature had not been enough to initiate melting of the frozen water and, therefore, the system was returned to Point C where the distribution of the molten fraction was unchanged.

10.5.5 Comparing whole and fragmented S1

Figure 10.6 shows a comparison of the melting curves for whole and fragmented samples from batch S1, where the two have been overlaid. From Figure 10.6, it can be seen that the step up in signal intensity on the melting curve for the whole pellet sample is more abrupt, and occurs over a narrower temperature range, than the corresponding curve for the fragmented sample. Additionally, T_2 relaxometry experiments were carried out at similar molten fractions on the boundary melting curves for both whole and fragmented samples. From Table 10.2 it is clear that the T_2 relaxation constant, at similar molten fractions, is greater for the whole sample.

Sample form	Temperature /K	Relative signal intensity	T_2 Relaxation time constant /ms
Whole	270.1	0.4	5.61 ± 0.03
Fragmented	270.8	0.46	3.70 ± 0.05

Table 10.2:. Comparison of relaxation times at similar temperatures and molten volume fractions for whole and fragmented samples from batch S1. As stated in the Preface, these experiments were carried out by Dr John Lowe.

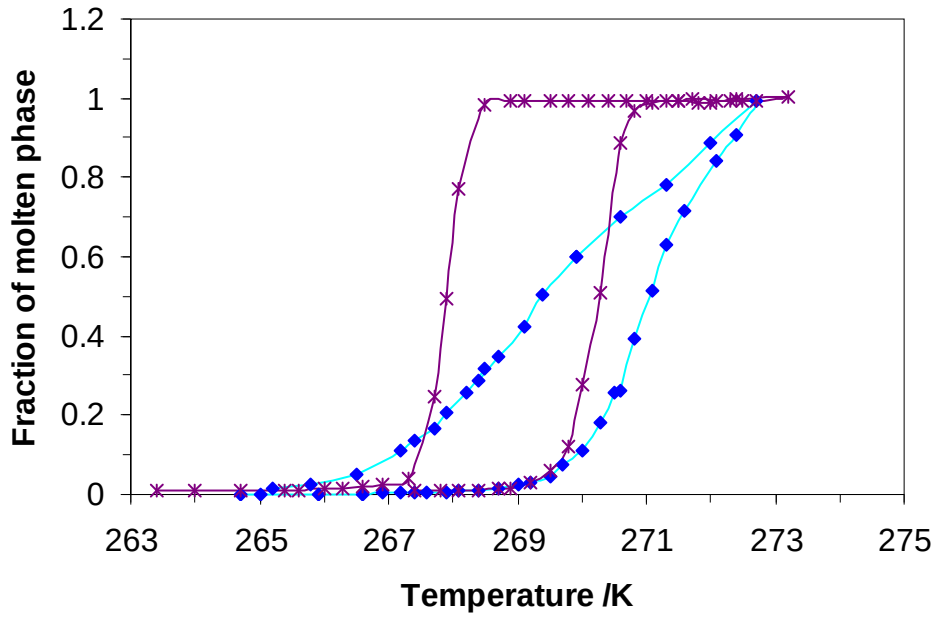

Figure 10.6: An overlay plot of typical data-sets, consisting of freezing and melting boundary curves, for whole (stars) and fragmented (diamonds) samples from batch S1

10.5.6 Spiral scanning loops

In a further experiment for the whole pellet sample, scanning loops were repeated over smaller temperature ranges, to form a 'scanning spiral', and the hysteresis loop progressively narrowed to the point where hysteresis became negligible (Figure 10.7 (a) and (b)). As with points A-D in Figure 10.5, the distribution of the molten phase was probed at two labelled points (E and E´) shown in Figure 10.7 (a). Points E and E´ are at the start and end of the sub-loop respectively (crosses), both at the same molten fraction and temperature. There was no difference in the tortuosity and relaxometry data for points E and E´, suggesting no difference at all in the regions of void space occupied by the molten fluid.

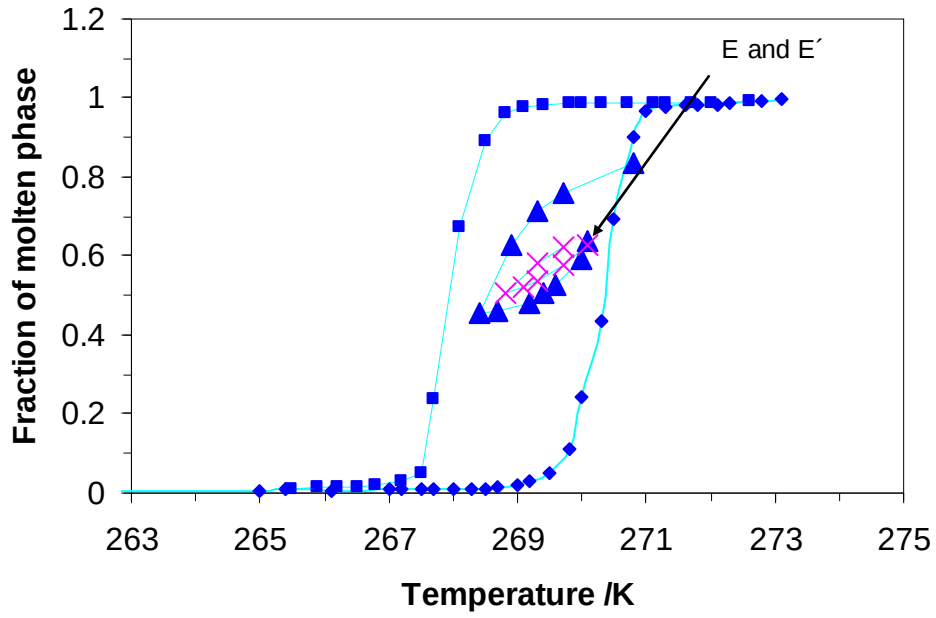

Figure 10.7 (a): A freezing/melting spiral, consisting of a freezing scanning loop (triangles) with an additional freezing loop (crosses) within, for a whole pellet sample from batch S1. Also shown are the boundary melting and freezing curves. The arrows shown are to guide the eye

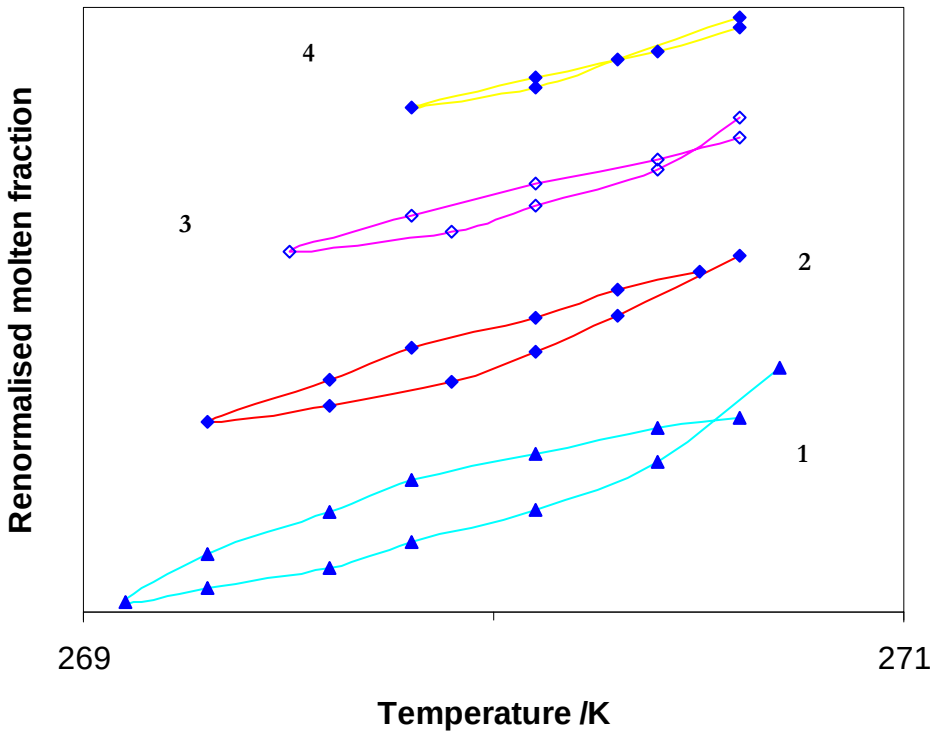

Figure 10.7 (b): Further detail of a freezing/melting spiral for a whole pellet sample from batch S1. For clarity, the boundary melting and freezing curves are now omitted, and each successive loop (diamonds, loops 2-4) of the spiral, following the first (triangles), has been vertically offset upwards in molten fraction, by an arbitrary amount, from its predecessor

10.6 Discussion

Previously, dead end pores have been proposed (Kondrashova *et al.* 2010) as a way to explain why melting scanning curves do not cross directly from the boundary freezing curve to the boundary melting curve, and the lack of a factor of two relationship between the freezing and melting point depressions within a freezing scanning loop. However, as will be seen below, a consideration of the direct characterisation data of the spatial configuration of the molten fraction rules out this explanation. Referring to the schematic representations depicted in Figures 10.8 (a) and (b) this can be explained as follows. In the scenario depicted in Figure 10.8 (a), the void space consists of a series of dead-end cylindrical pores of increasing sizes, and through cylindrical pore systems consisting of a large pore shielded, at both ends, by two layers of progressively smaller pores towards the exterior. At the upper tip of the loop, depicted in Figure 10.8 (a) as UT, the largest pores in the dead-end and through pore regions are considered to be still frozen. During the scanning freezing loop, when the temperature is being lowered, the ice front can advance via a hemispherical meniscus from either the bulk, or the large pores to the more narrow pores at least by the temperature at which they become below their freezing point (Figure 10.8 (a) point A). Hence, by the lower tip of the scanning loop (Figure 10.8 (a) LT), all of the pore regions are then frozen. On reversing the temperature, through pores adjoined only by frozen pores can melt only starting from the outer liquid-like layer between the ice core and the pore wall (cylindrical sleeve-type meniscus). However, dead-end pores can melt by the liquid layer at the closed pore end (hemispherical meniscus). The mechanism by which dead-end pores melt occurs at a lower temperature to that for through pores melting from a cylindrical sleeve meniscus. Hence, raising the temperature to reach point B (Figure 10.8 (a)) from the lower tip of the loop may mean that for pores of identical diameter, the dead-end pores may have melted but the through pore adjoined by ice-filled pores will not. Therefore, the regions of void space occupied by the same molten fraction would differ between Point B and Point A. Thus, if there were dead end pores and no advanced melting, then this difference would be expected to manifest itself in the tortuosity and relaxation data. As seen above, experimentally, this is not observed. Moreover, for a system with only cryoporometry single pore hysteresis, where freezing progresses by a hemispherical meniscus and melting by a sleeve type meniscus, one would expect Points A and B to have the same distribution of the molten fraction, and, therefore, the tortuosity and relaxometry data to be identical; experimentally this is observed. However, for cylindrical pores, as found in S1, if only the cryoporometry single pore hysteresis

mechanism is operating, it would be expected that the freezing and melting point depressions would differ by a factor of 2, and this is not what is experimentally observed.

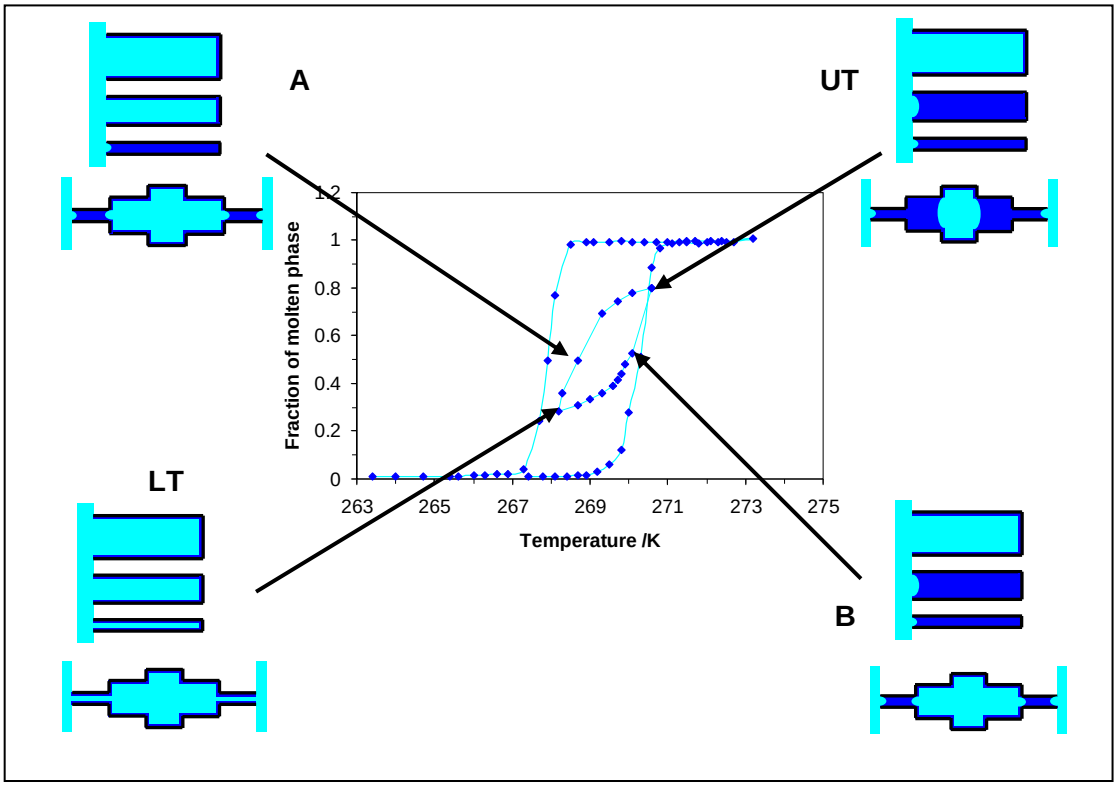

Figure 10.8 (a): A schematic representation of both cryoporometry single pore hysteresis and dead-end type pores. Freezing for both pore systems is by a hemispherical meniscus, while melting occurs by a sleeve-type meniscus, and a hemispherical meniscus, for open, and dead-end pores, respectively. Dark shading represents molten phase, and lighter shading represents frozen phase

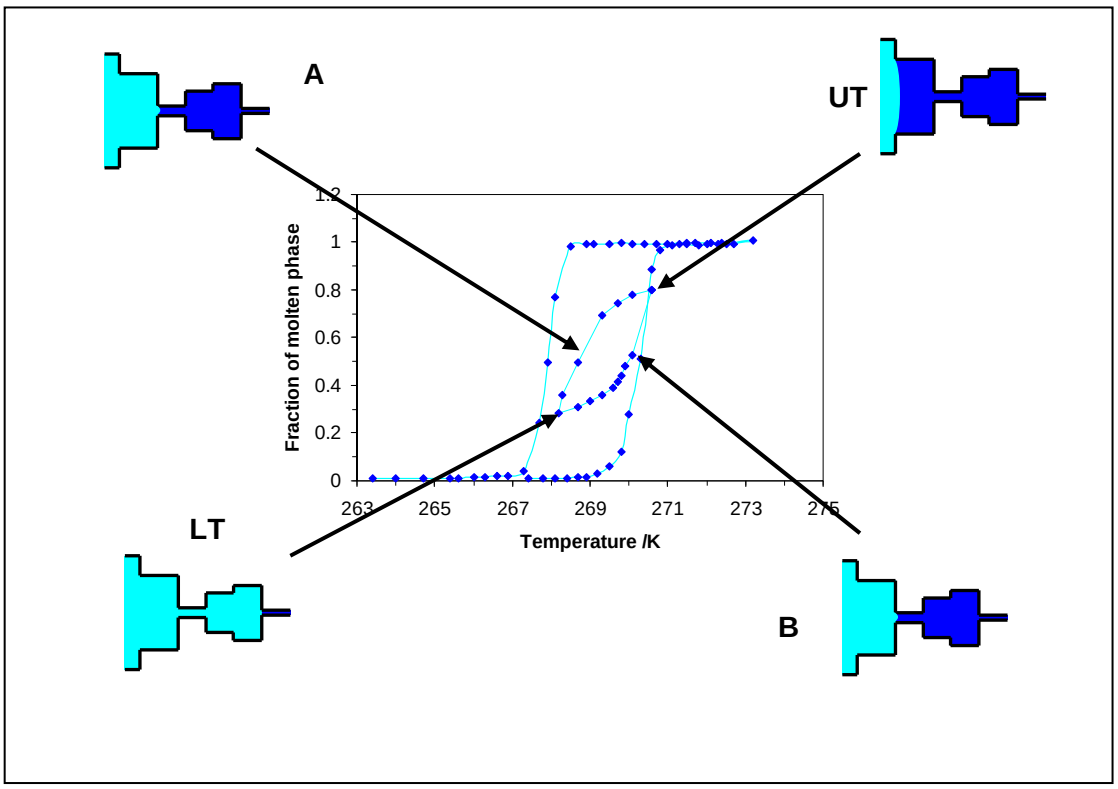

Figure 10.8 (b): A schematic representation of freezing and melting, occurring by hemispherical menisci, at various points around a freezing scanning loop performed on a shielded pore network. Freezing and melting are delayed through structural effects. Dark shading represents molten phase, and lighter shading represents frozen phase

An alternative explanation, and the one propounded here, is that the freezing loop is based upon a hemispherical meniscus entering and leaving S1 through different size constrictions (depicted in Figure 10.8 (b)) and the mechanism includes advanced melting. Initially, as the temperature is decreased from the upper tip of the loop (UT), the meniscus can freeze a large pore, but more extensive freezing is then delayed by a narrow constriction (Point A). On lowering the temperature further, the hemispherical meniscus can then penetrate through the narrow constriction and progress through shielded pores of greater radius, located beyond the constriction, immediately, as the system is then below the freezing point for these pores. For the freezing to be capable of being stopped at different intermediate points, during the freezing part of the scanning loop, or the boundary freezing curve, is suggestive of the existence of even narrower constrictions than initially halting ice ingress. After freezing is halted at the lower tip of the loop (LT), melting can then be initiated through a pseudo-dead end type pore, where a frozen pore is connected to a molten pore and the molten end acts as a melting nucleation seed with a hemispherical meniscus. Melting will then start once the temperature is high enough for a hemispherical meniscus to advance, and any subsequent narrower neighbouring pores will also melt automatically (Point B). As can be seen from Figure 10.8 (b) the presence of advanced melting together with pore shielding in the freezing process naturally leads to identical

configurations of molten phase at Points A and B on the scanning loop, as determined experimentally by diffusometry and relaxometry. The idea of advanced melting was discussed by Kondrashova *et al.* (2010), although they failed to demonstrate, or suggest, an experimental method to directly test for the mechanism.

It was noted above that the range of temperatures over which melting occurred on the boundary curves for whole pellet samples was much narrower than for fragmented samples. If an advanced melting mechanism was occurring, it would be expected that the melting of the whole sample would occur at lower temperatures, when compared with the fragmented sample, because neighbouring molten pores could initiate melting of adjoining frozen pores before the temperature required for melting according to a sleeve type meniscus. Since, as shown by MRI data (Hollewand and Gladden 1995b), there is a macroscopic correlation in the spatial distribution of pore sizes for pellets of S1, then fragmentation should lead to a severing of the connections between regions of smaller and larger pores. Hence, in the fragmented sample, the potential for advanced melting of larger pores by ingress of hemispherical menisci from neighbouring, molten smaller pores would be curtailed. This is clear in Figure 10.6 and gives further support to the melting and freezing mechanism proposed to explain the shape of the scanning freezing loop. Furthermore, the distribution of the molten phase amongst the various pores of different sizes, at the same molten volume fraction for both the whole and fragmented sample, was probed using T_2 relaxation studies. If an advanced melting mechanism was occurring for whole pellet samples but not for fragmented samples, then it would be expected that larger pores in the whole pellet sample would have melted in advance of the corresponding same sized pores in the fragmented sample and, therefore, a higher T_2 relaxation constant should arise for the whole sample compared to the fragmented sample, at an equivalent molten volume fraction. This is exactly what has been observed experimentally, as shown in Table 10.2.

The progressive disappearance of the freeze-thaw hysteresis shown in Figure 10.7 is also consistent with the freezing and melting mechanism proposed above (Figure 10.8 (b)) as follows. When the freezing loop spans only a small temperature range, only a small number of pores, accessible by the advancing hemispherical meniscus, will freeze. On reversing the temperature, these pores can melt immediately, initiated by a hemispherical meniscus originating from the pseudo-dead end type pores created by adjoining molten pores. The system is thus reversible, which is supported by the identical tortuosity and relaxometry data for points E and E´, and explains why the hysteresis is removed. This is

analogous to the removal of pore shielding effects by the mini-loop approach in mercury porosimetry (Portsmouth and Gladden 1991), though single pore hysteresis is retained in mercury porosimetry because it arises from contact angle variation between retreating and advancing menisci. When the freezing loop is over a larger temperature range the hysteresis then includes additional structural effects on the advancing and retreating hemispherical meniscus, as already discussed.

The advanced melting mechanism proposed above is analogous to the advanced condensation/adsorption phenomenon in gas adsorption. Advanced adsorption has been observed for pellets from batch S1 using the integrated gas sorption and mercury porosimetry technique (Rigby and Chigada 2009) and also from the work presented in Chapter 7. Chapter 7 studied desorption scanning curves that started immediately upon the pressure reversal, which suggested that there are some pores that fill and empty by a hemispherical meniscus. Furthermore, hysteresis could be purged using gas sorption scanning loops, which is explained by an advancing (advanced adsorption) and retreating hemispherical meniscus. Together the findings reported here from cryoporometry, the gas sorption work in Chapter 7 and those reported earlier (Rigby and Chigada 2009) for gas adsorption, suggest that pore size distributions obtained from cryoporometry melting curves and gas adsorption isotherms for whole pellet samples are both subject to errors due to previously undetected advanced melting/adsorption effects.

10.7 Conclusions

In order to interpret scanning loop experiments in NMR cryoporometry properly, it is necessary to also use PFG NMR and relaxometry data to probe the configuration of the molten phase to eliminate ambiguities. It has been shown how different scenarios for the form of the pore network and the freezing/melting mechanisms can be tested using these techniques. In particular, these data demonstrate the need to incorporate advanced melting effects to interpret scanning loop data properly, without invoking unproven dead-end pores. It has also been shown that the freeze-thaw hysteresis in cryoporometry can be purged from scanning loops to give a reversible process, as expected if advanced melting was occurring.

Chapter 11

Determining the location of platinum in a bifunctional zeolite catalyst

11.1 Introduction

Ethylbenzene is an important intermediate in the formation of styrene. Degnan *et al.* (2001) estimated that in 2001 worldwide ethylbenzene production was 23 million tonnes, which was expected to grow by ~4 % each year. Ethylbenzene is synthesised by the alkylation of benzene with ethene. However, this method is not favourable because ethene is a product of a highly energy intensive processes such as dehydrogenation of ethane (Chua 2010). A recent method to form ethylbenzene has used a bifunctional Pt-ZSM-5 zeolite catalyst that has an operating reaction temperature of 370 °C (Lukyanov and Vazhnova 2008). The chemical reaction for this process can be expressed by:

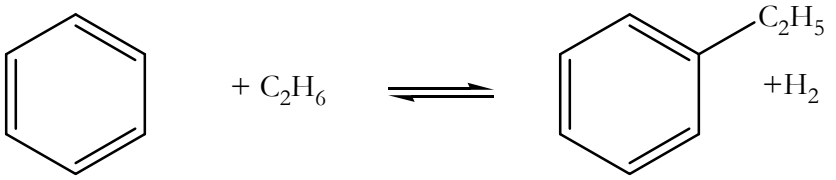

11.1

Due to the high operating temperatures and the hydrocarbon reactant stream the catalyst becomes deactivated by the formation of coke (Chua 2010). Coke is a mixture of carbonaceous compounds that form as a by-product of the reaction and can deactivate catalysts in the following ways (Sotelo *et al.* 1994; de Lucas *et al.* 1997): coke deposits can be large such that they block pores and prevent reactants accessing the active sites in the catalyst; alternatively, the coke may form at and cover active sites, which can then inhibit the chemical reaction.

An understanding of where coke forms in a catalyst is important because it is known to influence the selectivity of a catalyst. For example, ZSM-5 catalysts have been used in the formation of particular dialkylbenzene products as they selectively favour the *para* isomer (Sotelo *et al.* 1994; Chen *et al.* 2002). This is because the *para* isomer product has dimensions compatible with the micropores so it can diffuse faster (through the zeolite) than the *ortho* or *meta* products (Atkins and de Paula 2002). However, as the catalysts deactivate, the selectivity to *para* products is seen to vary depending on the location of coke

on the catalyst. As an example, Sotelo *et al.* (1994) found when toluene was alkylated using methanol that the *para* selectivity of the dimethylbenzene product decreased as coke formed in the micropores.

The amount of coke deposited on a catalyst may be calculated by comparing the adsorption capacity of the coked and fresh catalysts (Bibby *et al.* 1986; Guisnet and Magnoux 1989; de Lucas *et al.* 1997). However, this does not give clear information on where the coke forms in the catalyst and can be wrong if the coke isolates free void space. Recently, Chua *et al.* (2010) have determined the spatial location of the coke in two Pt-ZSM-5 catalysts by nitrogen gas sorption and this is explained as follows using Figures 11.1 and 11.2. Figure 11.1 shows a schematic of the Pt-ZSM-5 catalyst used during a nitrogen gas sorption experiment and it shows the micropores and mesopores. The mesopores were generated by pressing the zeolite crystallites together, with the gaps formed between the particles being the mesopores. Figure 11.1 depicts the adsorbed nitrogen as shading, which will adsorb into the micropores before it adsorbs onto the surface of the mesopores/outer surface of the zeolite crystallites. In addition, the black circles indicate regions where coke has been formed.

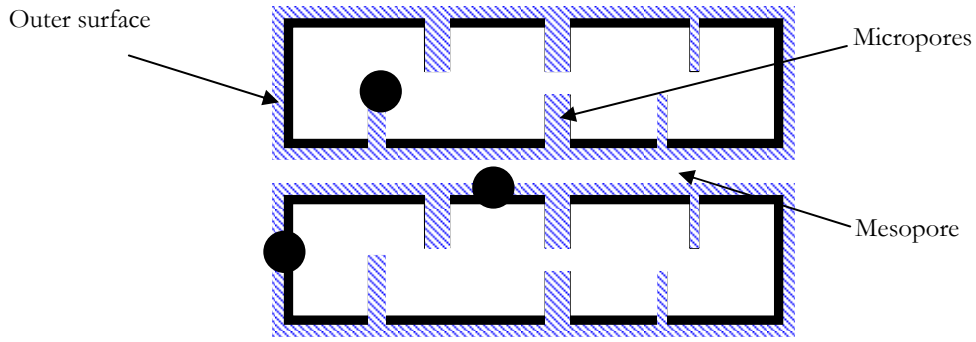

Figure 11.1: Schematic of the Pt-ZSM-5 catalyst with coke (black circles). The shading shows an adsorbed gas phase in the micropores and on the surface of the crystallites

Chua *et al.* (2010) modelled the nitrogen adsorption in the micropores using the Langmuir model, and the adsorption in the mesopores using the BET model, which was discussed in Chapter 2. By comparing the gas adsorption isotherm on the fresh and coked catalyst they determined whether the coke was formed in the micropores or the mesopores/outer surface. If the coke had formed in the micropores the Langmuir component to the model changed but the BET component did not. If the coke had formed in the mesopores/outer

surface, the BET component of the model changed but not the Langmuir component. This explanation is made clearer in Figure 11.2.

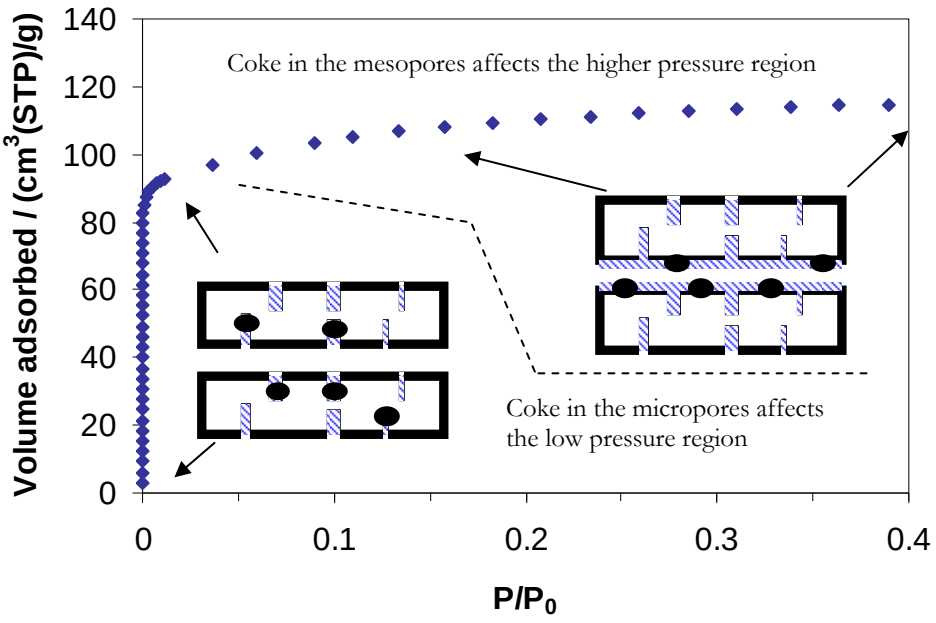

Figure 11.2: Schematic of a gas sorption isotherm between relative pressures 0-0.4. A modified version of Figure 11.1 is shown with the coke in the micropores or the mesopores and arrows showing which region of the isotherm the coke will affect. A dashed line has been added to separate the schematics

Another method to gauge the catalysts efficiency is to determine the location of the platinum; whether it is in the micropores or on the outside of the zeolite crystallites (Rivallan *et al.* 2010a). If the platinum is located in the micropores it can catalyse the shape selective reactions as discussed above. Figure 11.3 shows a schematic of the Pt-ZSM-5 materials used by Chua *et al.* (2010), which is analogous to Figure 11.1. It is shown that the platinum can either be located in the micropores, the mesopores or on the outer surface.

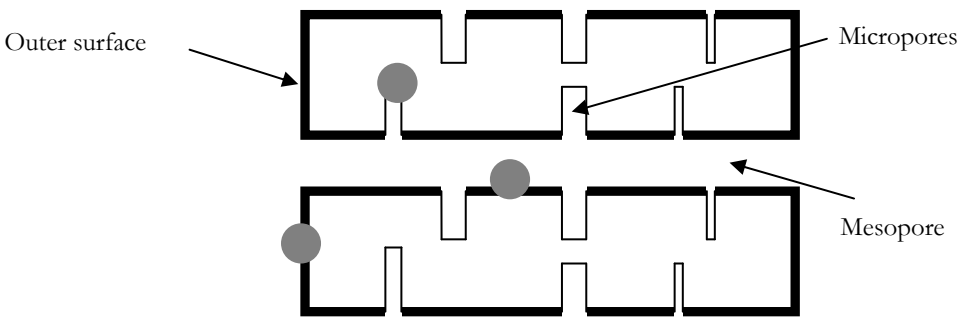

Figure 11.3: Schematic of the Pt-ZSM-5 catalyst. The platinum is shown as silver circles

To determine the location of the platinum in a ZSM-5 sample, Rivallan *et al.* (2010a) have used a 2-dimensional pressure jump infra-red spectroscopy technique (Chenevarin and Thibault-Starzyk 2004). They first introduced carbon monoxide into a cell that contained Pt-ZSM-5 allowing adsorption onto the platinum surface. They then applied a sudden change in pressure to excite the adsorbed carbon monoxide molecules and monitored the relaxation process by time resolved infra-red spectroscopy. The carbon monoxide that adsorbed to platinum located in the micropores/mesopores relaxed at a higher frequency to the carbon monoxide adsorbed to platinum located on the external surface. This is because the mean free path of the carbon monoxide molecules located in the micropores/mesopores was shorter compared to the carbon monoxide molecules located outside the pores. This technique can only determine whether platinum is located in the pores (micropores and mesopores) or on the external surface. As discussed above, it is of interest to know whether the platinum is located in the micropores only and this technique is not able to distinguish between platinum located in the micropores or the mesopores.

The study in this Chapter will combine a chemisorption experiment with a nonane pre-adsorption experiment (Gregg and Langford 1969) to determine whether platinum in two Pt-ZSM-5 catalysts, is located in the micropores or outside the micropores. Catalysts from the same batch were used to study the alkylation reaction in equation 11.1 (Chua *et al.* 2010). As discussed above, Chua *et al.* determined the location of coke during the reaction in equation 11.1. This Chapter, therefore, compares the location of the coke (previous studies by Chua *et al.*) with the location of the platinum.

The chemisorption and nonane pre-adsorption experiments will now be introduced to the reader before the experimental results are presented.

11.2 Background and theory

11.2.1 Chemisorption experiments

Unlike the physisorption experiments, which were discussed at the start of this thesis (Chapters 2, 4-7), chemisorption is based on the formation of a strong chemical bond between the adsorbate and the adsorbent. The chemisorption technique has been used to determine the surface area of metals on porous supports (Raddi de Araujo and Schmal 2000). The chemisorption experiment will now be explained in detail.

The amount of chemisorbed gas to a metal can be determined using a static method similar to the physisorption experiments studied in the previous Chapters. A sample is prepared for chemisorption by first heat treating under vacuum to remove any physisorbed gases from the surface of the material. Following this, the metal must then be reduced, which is usually done using hydrogen gas. This is because if the metal has an already formed oxide (or carbonate) layer no adsorbate will be able to chemisorb onto its surface. A suitable adsorbate is then chosen, which chemisorbs only to the metal surface and not the support material. By progressively increasing the pressure, the gas adsorbs onto the metal surface and an isotherm can be generated by plotting the pressure against the volume adsorbed. The isotherm is typically of a Langmuir form (Lowell *et al.* 2004) and the volume of the chemisorbed monolayer (V_m) can be found by extrapolating the linear region of the isotherm to zero pressure. This procedure only works provided the adsorbate does not interact strongly with the porous support. It is possible that the adsorbate weakly chemisorbs onto the support material. This means the calculated monolayer volume will be a combination of the chemisorption process to the metal and the weak chemisorption process to the support. To determine the amount of weak chemisorption a second isotherm can be studied. After the first isotherm the system is evacuated to remove the weakly chemisorbed gas. Due to the strong chemisorption interaction with the metal, this adsorbed phase remains bound to the metal surface. The following isotherm will then measure only the weak chemisorption process as the metal already has a chemisorbed monolayer of gas. To calculate the chemisorption volume adsorbed to the metal the second isotherm should be subtracted from the first isotherm. An example of this process is shown in Figure 11.4 (a) and (b). Figure 11.4 (a) shows the first isotherm as closed diamonds and the second isotherm as a fixed line. Figure 11.4 (b) shows the second isotherm subtracted from the first isotherm and the linear region is extrapolated back to zero pressure to calculate the chemisorption monolayer volume.

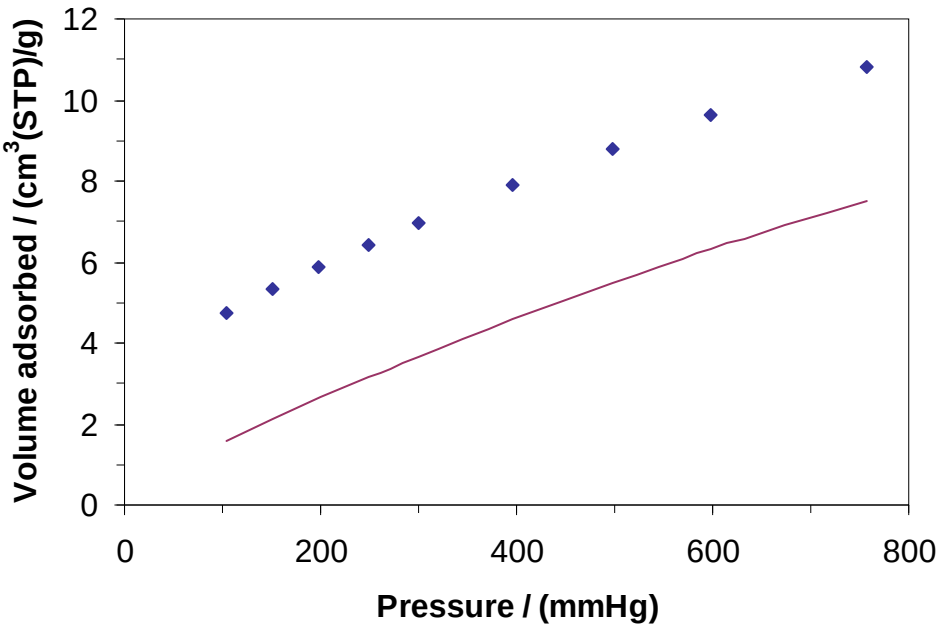

Figure 11.4 (a): The first isotherm (closed diamonds) is a contribution from strong and weak chemisorption. The second isotherm (fixed line) is due to weak chemisorption only

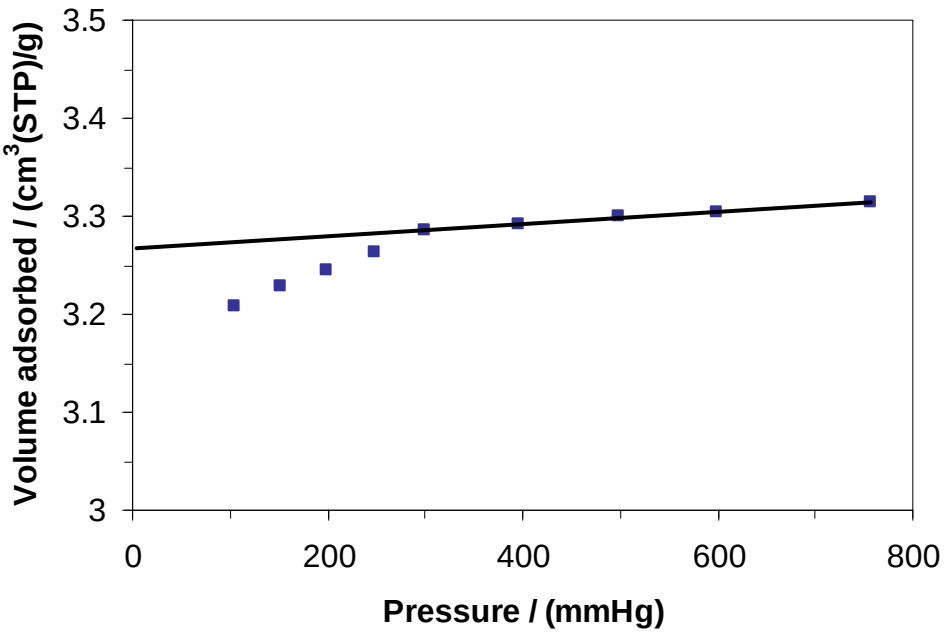

Figure 11.4 (b): The fixed line isotherm in Figure 11.4 (a) has been subtracted from the closed diamond isotherm. The resultant isotherm (closed squares) is the strong chemisorption isotherm only. A solid line has been drawn through the linear region of the isotherm and extrapolated back to zero pressure

After determining the chemisorption monolayer, the stoichiometry between the gas and the metal needs to be known before a metal surface area can be calculated. The stoichiometry is the average number of adsorbed gas molecules per metal atom. For example, a stoichiometry of one means there is one gas molecule adsorbed per metal atom. Hydrogen

is recognised as having a stoichiometry of two when it chemisorbs onto platinum because it dissociatively adsorbs (Lowell *et al.* 2004). In this study, carbon monoxide is to be used as the adsorbate and its stoichiometry can vary between one and two (Gregg and Sing 1967). This is because carbon monoxide can either bind with one metal atom or it can bridge between two metal atoms. To determine the stoichiometry of carbon monoxide on a metal infra-red spectroscopy can be used. The absorption energy is different for bridging and non bridging carbon monoxide molecules allowing a distinction to be made between the sites (Rivallan *et al.* 2010a). When the carbon monoxide bridges between two metal centres there are two metal atoms that back bond into the carbon monoxide π* orbital, which weakens the carbon-oxygen bond. If the carbon monoxide is coordinated to only one metal atom it means only one atom will back bond into the π* orbital. As only one metal atom back bonds, the carbon-oxygen bond is not weakened as much and infra-red spectroscopy can be used to detect this difference.

Once the monolayer volume and stoichiometry have been determined, the metal surface area (m^2) per gram of catalyst, A, can be calculated by (Lowell *et al.* 2004):

$$A = \frac{V_m}{22414} \cdot N_A \cdot s \cdot \sigma_m \qquad 11.2$$

where V_m is the monolayer volume in cm^3 (STP)g^{-1}, N_A is the Avogadro number, s the stoichiometry factor, σ_m the atomic metal cross sectional area in m^2. The cross sectional area of a platinum atom is reported to be 0.08 nm^2 (Anderson and Pratt 1985). A stoichiometry factor of one will be used in this thesis and is explained as follows. The ratio between bridging and linear coordinated carbon monoxide molecules on a platinum zeolite has been studied by Mojet *et al.* (1999). They changed the acidity of the zeolite support by exchanging protons with potassium ions using potassium nitrate. It was found that when the alkalinity increased (more potassium in the support) there were more bridging carbon monoxide groups. This is because the higher alkalinity of the support meant the electron density on the platinum clusters increased. Therefore, it is possible to have more back bonding, which means the carbon monoxide molecules bridge two platinum atoms. In addition, Thomas *et al.* (2011) used infra-red spectroscopy to determine whether carbon monoxide formed linear or bridging bonds to platinum in a Pt-ZSM-5 catalyst. They found that the carbon monoxide formed linear bonds to the platinum. The Si/Al ratio for their zeolite was 50, while the Si/Al ratio for the zeolites that are to be studied in this Chapter (see below) is 40 and 15. The supports in this study therefore have more acidic sites than the one used by Thomas *et al.* (2011). This means it is reasonable to assume that

the stoichiometry factor for carbon monoxide on platinum, in this study, will also be 1. Other studies have also used a stoichiometry factor of 1 when studying carbon monoxide chemisorption on a Pt-ZSM-5 catalyst (Canizares *et al.* 1997; Stakheev *et al.* 1997; Raddi de Araujo and Schmal 2000; Rivallan *et al.* 2010b).

Lepage *et al.* (2008) have shown, using infra-red spectroscopy, that the pore curvature has little effect on the stoichiometry factor for carbon monoxide on platinum. They studied a microporous, mesoporous and macroporous silica with a 1 % platinum loading and found the ratio between the bridging and linear bonded carbon monoxide molecules to be approximately the same. Therefore, it will be assumed in this study that the stoichiometry factor, for carbon monoxide chemisorbing onto platinum in the micropores, the mesopores and the outer surface is the same.

11.2.2 Background to the nonane pre-adsorption experiment

Nonane pre-adsorption is a method introduced by Gregg and Langford (1969) to evaluate the microporosity of a sample. The aim of the method is to fill the micropores of a porous material with *n*-nonane leaving the larger pores empty. This means that if a (nitrogen) gas sorption experiment is studied before and after the nonane pre-adsorption step, the difference between the isotherms must be due to the nonane in the micropores. Nonane was chosen because of its high physisorption energy, which means it can only be removed from the micropores at high temperatures and vacuum (Lowell *et al.* 2004).

The following experimental procedure for the nonane pre-adsorption experiment was used by Gregg and Langford. They out gassed the sample and then cooled the sample, using liquid nitrogen, in the presence of nonane vapour saturated at 25 °C. The difference in temperature ensured the rapid transfer of the nonane to the sample (Ali and McEnaney 1985). After charging the sample with nonane for 30 minutes the system was out gassed at room temperature for 6 hours. This removed the nonane adsorbed in the large pores (mesopores and macropores), but not from the micropores as nonane has a high physisorption energy. Following this, a nitrogen sorption isotherm was determined at 77 K. The sample was then out gassed at increasing temperatures and a nitrogen sorption isotherm was determined after each out-gassing temperature. It was found that to remove the nonane completely from the sample the system had to be out gassed at 400 °C. Early investigations studied microporous carbon materials using the nonane pre-adsorption technique (Gregg and Langford 1969; Rodriguez-Reinoso *et al.* 1984; Ali and McEnaney

1985; Carrott *et al.* 1988). Subsequent research has investigated micropores in zeolite materials (Grillet *et al.* 1993) and most recently SBA-15 has been studied (Silvestre-Albero *et al.* 2009).

This study used the nonane pre-adsorption method to determine the location of platinum in Pt-ZSM-5 catalysts. Before nonane pre-adsorption, the metal surface area was determined using carbon monoxide chemisorption. The carbon monoxide was able to access the platinum in the micropores, the mesopores and the outer surface. Following this, the nonane pre-adsorption experiment was used with the aim to fill only the micropores of the Pt-ZSM-5 catalysts. A second carbon monoxide chemisorption experiment was then studied but the carbon monoxide was no longer able to access the platinum in the micropores. This is because the sizes of pores in ZSM-5 are 5.5 x 5.6 Å (Atlas of Zeolite Framework Types). Rouquerol *et al.* (1999) report that the width of a *n*-nonane molecule is 4 Å and Roszak and Balasubramanian (1993) report the bond length of a platinum-carbon and a carbon-oxygen bond is 1.88 Å and 1.14 Å respectively. This means that when nonane is situated in the micropores of a Pt-ZSM-5 zeolite, the carbon monoxide molecules is not be able to enter them and chemisorb to the platinum surface. This is schematically shown in Figure 11.5. Therefore, the calculated metal surface area following nonane pre-adsorption will be for the platinum in the mesopores and the outer surface only. This means the total amount of metal in the micropores and the mesopores/outer surface can be calculated using the above method.

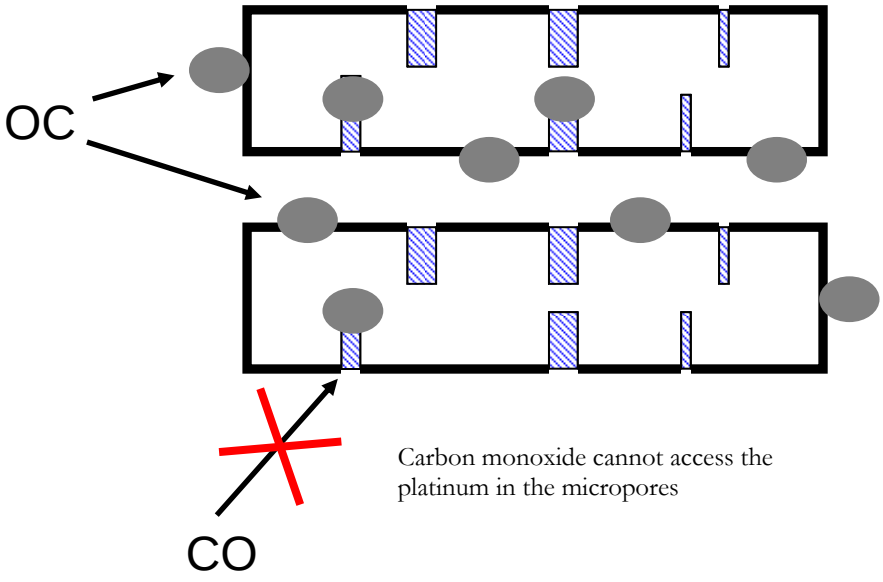

Figure 11.5: Schematic of a chemisorption process using CO as the adsorbate. The CO can bind to the platinum (grey) in the mesopores/on the outer surface. The CO cannot bind to the platinum in the micropores as nonane (shading) has been pre-adsorbed

11.3 Experimental

11.3.1 Samples studied

The catalysts used in this Chapter were prepared as described by Chua *et al.* (2010). The materials are Pt-ZSM-5 with Si/Al ratios of 15 and 40. The two catalysts will be referred to as Pt-ZSM-5(15) and Pt-ZSM-5(40). As stated in the Preface, the Pt-ZSM-5 catalysts were supplied by Dr Li Min Chua and were not synthesised for the thesis. They both had 1% wt. of platinum.

11.3.2 Nitrogen adsorption experiment before nonane pre-adsorption

The nitrogen sorption experimental procedure was identical to Chapter 3 but the sample was prepared by heating it to 250 °C for 4 hours. The isotherm was studied with an equilibration time of 45 s, as was used by Chua (2010).

11.3.3 Nonane pre-adsorption (physisorption experiment)

Following the gas sorption experiment the sample and sample tube were transferred to a desiccant chamber with a beaker of liquid nonane. The sample was left for one week to adsorb the nonane vapours.

11.3.4 Nitrogen adsorption experiment following nonane pre-adsorption

After the nonane pre-adsorption step the sample and sample tube were transferred back to the ASAP 2020 apparatus. The sample was prepared by heating it to 70 °C for 12 hours to remove the nonane from the mesopores but leave the nonane in the micropores. The sample was then analysed by nitrogen sorption at 77 K again.

11.3.5 Metal surface area analysis before nonane pre-adsorption

Platinum metal surface area experiments were performed at 35 °C using carbon monoxide by use of a Micromeretics 2010 Chemisorption Analyzer. The sample was inserted into a preweighed Micromeretics chemisorption analysis tube. The sample was initially evacuated at 250 °C for 4 hours (Chua 2010) to remove any physisorbed gases from the surface of the catalyst. The sample was backfilled with dry nitrogen gas and removed from the Chemisorption Analyzer. A bung was placed at the top of the tube to ensure the sample remained under the nitrogen atmosphere and the dry mass was calculated. The sample tube was then reinserted into the Chemisorption Analyzer and the platinum was reduced using a flow of H_2 (20 ml min^{-1}) at 70 °C for 12 hours. The flow of hydrogen across the catalyst ensured that the water by-product was removed. The system was then evacuated at 70 °C for a further 12 hours to remove any adsorbed hydrogen. The sample was then prepared for the chemisorption experiment by cooling the system to 35 °C. The first chemisorption experiment was studied using carbon monoxide in the pressure range 100-760 mmHg. Following this experiment the system was evacuated at 35 °C for 30 minutes to remove the carbon monoxide that was weakly bound to the zeolite surface. Once this period of time was over the second chemisorption experiment was studied at 35 °C, and the amount of chemisorbed carbon monoxide was calculated (see Figures 11.4 (a) and (b)).

11.3.6 Nonane pre-adsorption (chemisorption experiment)

After the second isotherm the sample was back filled with nitrogen gas and the sample and sample tube were transferred to a desiccant chamber with a beaker of liquid nonane. The sample was left for one week to adsorb nonane vapours.

11.3.7 Metal surface area analysis following nonane pre-adsorption

Following nonane pre-adsorption, the sample was transferred back to the chemisorption apparatus and evacuated at 70 °C for 12 hours. This process removed the nonane from the mesopores only leaving the nonane in the micropores. The procedure to reduce the

catalyst with hydrogen gas and measure the adsorption isotherms with carbon monoxide was identical to the description given above.

11.4 Results and discussions

11.4.1 Nitrogen sorption studies before and after nonane pre-adsorption

Figure 11.6 shows the nitrogen sorption isotherm for ZSM-5. It is a combination of a Type I and Type IV isotherm (see Chapter 2). At low relative pressures the Type I behaviour is clearly visible, and in this region of the isotherm the micropores fill. At higher relative pressures (>~0.4) there is hysteresis which is indicative of the sample having mesopores. As the pressure approaches relative pressure 1, the increase in the amount adsorbed corresponds to capillary condensation into large mesopores (Lowell *et al.* 2004).

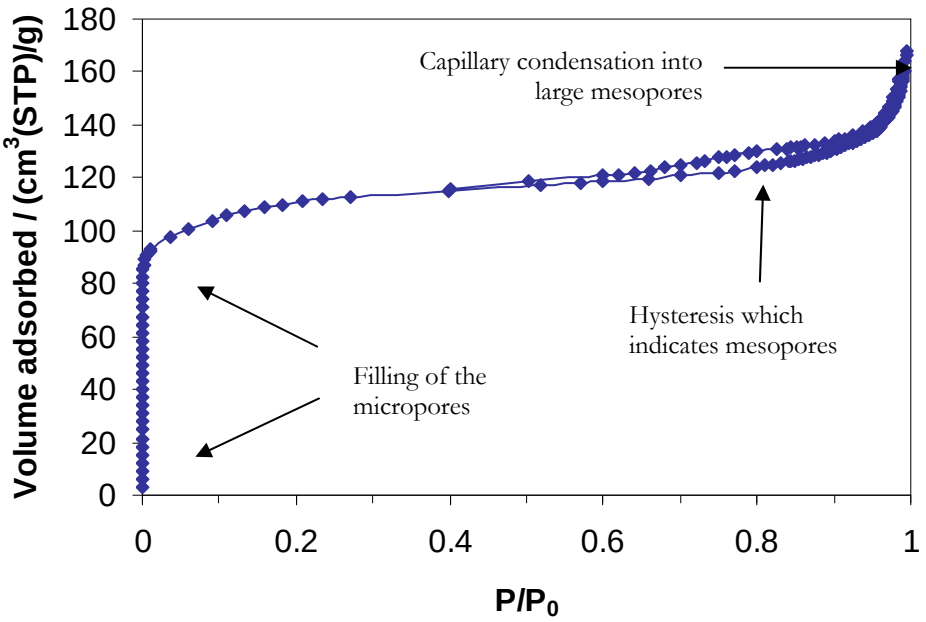

Figure 11.6: Nitrogen gas sorption isotherm at 77 K for ZSM-5

Figure 11.7 (a) shows the nitrogen sorption isotherm at 77 K before (fixed line) and after (crosses) the nonane pre-adsorption experimental procedure. It is clear that the amount of nitrogen adsorbed following the nonane pre-adsorption experiment is less than the analogous experiment before the nonane pre-adsorption experiment. This is because nonane has become entrapped in some of the pores, which means the total amount of nitrogen adsorbed is less. Figure 11.7 (b) shows the same isotherms overlaid, but where the volume adsorbed for all data points, in the isotherm following the nonane pre-adsorption experiment, have been adjusted upwards by 80 $cm^3(STP)g^{-1}$. When the

isotherm is adjusted upwards by 80 $cm^3(STP)g^{-1}$ the hysteresis regions approximately overlay. This suggests that the nonane has been removed from the mesopores and is entrapped only in the micropores. Therefore, when analysing the chemisorption studies, following the nonane pre-adsorption experiment, it will be assumed that carbon monoxide can access the platinum situated in the mesopores/outer surface but not the platinum inside the micropores.

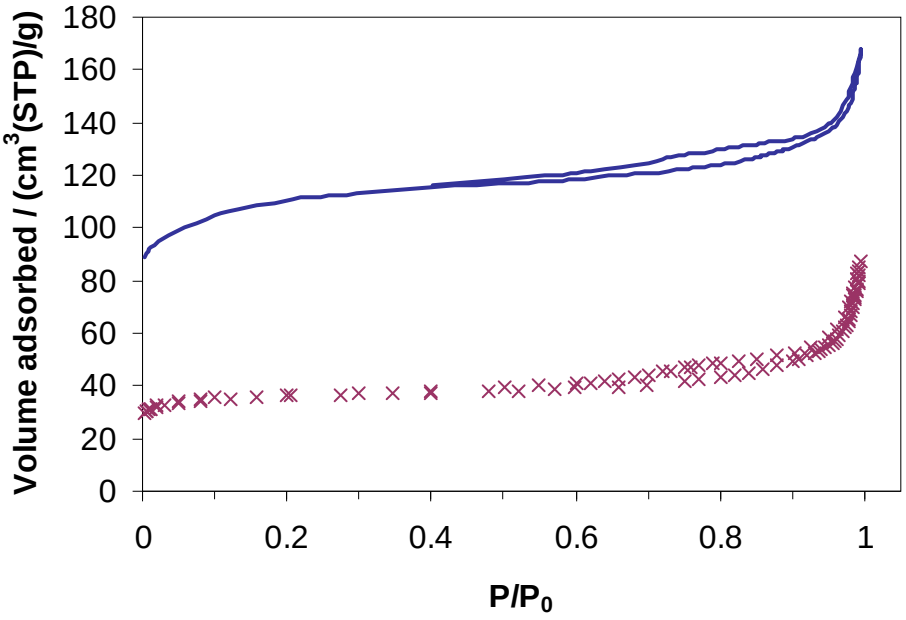

Figure 11.7 (a): Nitrogen sorption experiment on ZSM-5 before (fixed line) and after (crosses) nonane pre-adsorption

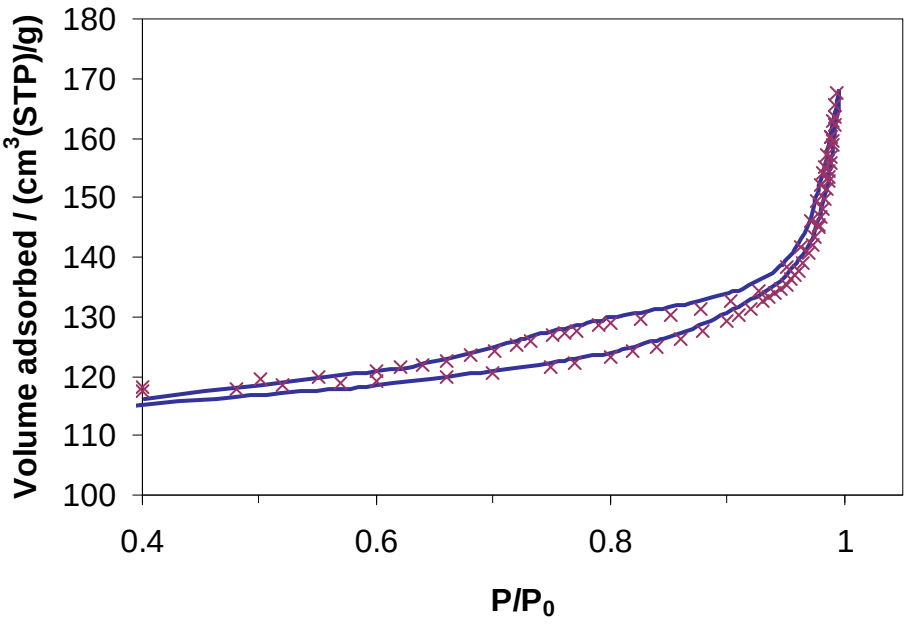

Figure 11.7 (b): An enlarged area of Figure 11.7 (a). All data points following nonane pre-adsorption have been adjusted upwards by 80 $cm^3(STP)g^{-1}$

11.4.2 Carbon monoxide chemisorption studies before and after nonane pre-adsorption for Pt-ZSM-5

Table 11.1 shows the chemisorption monolayer capacity and the calculated metal surface areas, using equation 11.2, before and after nonane pre-adsorption for the Pt-ZSM-5(15) catalyst. It can be seen that after nonane pre-adsorption the chemisorption monolayer decreases. This is because the nonane is situated in the micropores so the carbon monoxide can no longer chemisorb with the platinum in the micropores. Therefore, the chemisorption monolayer after nonane pre-adsorption represents carbon monoxide chemisorbing onto the platinum in the mesopores/out surfaces only. The metal surface area has been calculated using equation 11.2 and assuming the stoichiometry factor for carbon monoxide on platinum to be one, which is discussed above. It was found that there is 0.111 m^2g^{-1} of platinum in the micropores, which means ~30 % of the metal surface area is in the micropores. ZSM-5 zeolites are used as shape selective catalysts and metals, such as platinum, are added to increase their ability to catalyse reactions. If only ~30 % of the platinum is in the micropores this means that there is ~70 % of the platinum outside the micropores. If the platinum is outside the micropores, the reaction it catalyses will not be shape selective.

	Chemisorption monolayer / (cm^3(STP)g^{-1})	Metal surface area/ (m^2g^{-1})
Before nonane pre-adsorption	0.170	0.365
After nonane pre-adsorption	0.118	0.254
The amount of metal in the micropores	0.111 m^2g^{-1}	

Table 11.1: The chemisorption monolayer volumes and metal surface areas before and after nonane pre-adsorption for Pt-ZSM-5(15)

Analogous studies were carried out on the Pt-ZSM-5(40) catalyst and the results are presented in Table 11.2. Similar to the Pt-ZSM-5(15) catalyst, approximately 30% of the metal surface area is in the micropores. However, the total metal surface area for the Pt-ZSM-5(40) catalyst is lower than the Pt-ZSM-5(15) catalyst. As each catalyst has 1% wt. of platinum, this indicates that the size of the platinum particles on the Pt-ZSM-5(40) catalyst are greater than the size of the platinum particles on the Pt-ZSM-5(15) catalyst.

	Chemisorption monolayer / (cm^3(STP)g^{-1})	Metal surface area/ (m^2g^{-1})
Before nonane pre-adsorption	0.091	0.196
After nonane pre-adsorption	0.058	0.125
The amount of metal in the micropores	0.071 m^2g^{-1}	

Table 11.2: The chemisorption monolayer volumes and the metal surface areas before and after nonane pre-adsorption for Pt-ZSM-5(40)

The following section will relate the metal surface area measurements with previous studies that determined the location of coke in the catalysts following the reaction in equation 11.1.

11.4.3 Comparing the metal surface area measurements with previous studies

Using the method discussed above (see Figure 11.2), Chua *et al.* (2010) found that a higher amount of coke formed in the micropores of the Pt-ZSM-5(15) catalyst compared to the Pt-ZSM-5(40) catalyst, following the reaction in equation 11.1. Previous studies have suggested (Guisnet and Magnoux 2001) that coke occurs by a bifunctional mechanism using both acid sites and metal sites. Therefore, this would indicate that more coke should form when there is more platinum. The nonane pre-adsorption studies presented here suggest that there is more metal surface area in the micropores of the Pt-ZSM-5(15)

catalyst compared to the Pt-ZSM-5(40) catalyst. Presumably, since in the micropores of the Pt-ZSM-5(15) catalyst there is higher platinum surface area compared to the Pt-ZSM-5(40) catalyst, this explains why more coke occurs in the micropores of the Pt-ZSM-5(15) catalyst.

11.5 Conclusions

This Chapter has shown a novel method for determining the amount of active metal that is incorporated into the micropores of a ZSM-5 zeolite. By conducting a chemisorption experiment before and after a nonane pre-adsorption experiment, the amount of metal incorporated in the micropores (rather than mesopores/outer surface) of a Pt-ZSM-5 has been calculated. Previous studies have only been able to distinguish between platinum located in the micropores/mesopores and the outer surface. As stated above, determining the location of the platinum is important as it affects the catalysts activity and selectivity.

Additionally, the studies in this Chapter have been related to previous findings by Chua *et al.* (2010) who studied the location of coke formation following the reaction shown in equation 11.1. They found that for the Pt-ZSM-5(15) catalyst there was a higher amount of coke in the micropores compared to the Pt-ZSM-5(40) catalyst. Guisnet and Magnoux (2001) have discussed that coke occurs due to a bifunctional mechanism using metal and acid sites. This agrees with the findings in this Chapter that found the Pt-ZSM-5(15) catalyst has a higher surface area of platinum in the micropores compared to the Pt-ZSM-5(40) catalyst.

This Chapter has studied platinum in a ZSM-5 zeolite, but it is anticipated that similar methods can be used to investigate any other metals that can chemisorb suitable adsorbate molecules such as carbon monoxide and hydrogen.

Chapter 12

Conclusions and proposed future work

12.1 Conclusions

The studies in this thesis have been carried out to improve the accuracy and precision of the void space descriptors that can be obtained from the gas sorption technique, by improving the fundamental understanding of the underlying physics. New techniques, such as cryoporometry, and the integrated gas-mercury-gas and the chemisorption-nonane-chemisorption experiments, have also been developed to provide information not previously obtainable for porous solids. The following sub sections will now summarise the main findings of the work in this thesis.

12.1.1 Detecting advanced adsorption using MRI relaxometry

The IUPAC (Rouquerol *et al.* 1994) have suggested that the gas adsorption isotherm should be used to calculate a pore size distribution. However, the conversion of gas adsorption isotherms into pore size distributions generally relies on the assumption of thermodynamically independent pores. If the phenomenon known as advanced adsorption occurs and is not accounted for, the derived pore size distribution from the adsorption isotherm will be significantly skewed to smaller pores sizes. For example, the Kelvin equation predicts that there is a potential error of a 100% between actual and derived pore sizes if advanced adsorption occurs and is neglected when the adsorption data is analysed. It is important therefore to determine whether advanced adsorption occurs. This work has shown directly that advanced adsorption happens by use of spatially resolved NMR T_2 relaxometry data. Transverse relaxation time (T_2) images were obtained at different relative pressures during adsorption of water onto G2 (a sol gel silica sphere). It was shown that some of the largest pores in G2 became capillary filled before other smaller pores. Moreover, any large pore that became capillary filled was always connected to a filled neighbouring pore of smaller size, which is the advanced adsorption mechanism. Previous studies have only invoked the advanced adsorption phenomenon to explain the shape of hysteresis loops, but have not directly shown the effect. Additionally, the NMR relaxometry data showed that advanced adsorption can occur when there is a factor of five between a pore neck and a pore body. This is different to the factor of two predicted by the Kelvin equation. An implication of this is the possibility that there is potentially a 500% error in a derived pore size distribution, instead of the 100% error predicted by the

Kelvin equation, if the advanced adsorption phenomenon is neglected when analysing gas adsorption data. Pore size distributions are commonly quoted for heterogeneous catalysts, and are used as an indirect measurement to gauge likely catalyst activity. These findings suggest that great care must be taken when interpreting differences in pore size distributions obtained from gas adsorption data for a series of catalyst supports.

12.1.2 Validating the DFT method to calculate pore size distributions

In this investigation, it has been the aim to assess previous studies of Neimark and Ravikovitch (2001). They have argued that for pore sizes less than 20 nm the pore size distribution should be calculated using DFT rather than the Kelvin-Cohan equations. This is because the Kelvin-Cohan equations are based on macroscopic properties, but DFT provides a microscopic model of the gas sorption process taking into account gas-gas, gas-liquid, gas-solid and liquid-solid interactions. To verify the DFT calculations, Neimark and Ravikovitch have compared them to experimental gas sorption studies using templated mesoporous materials, such as MCM-41 and SBA-15 which had pore sizes less than ~10 nm. However, they did not experimentally calibrate the DFT approach for pore sizes greater than ~10 nm. This investigation used the integrated gas-mercury-gas experiment and determined the adsorption and desorption processes in the cylindrical pores of S1 (a sol gel silica sphere) which entrapped mercury. The cylindrical pores which entrapped mercury capillary filled and emptied like independent pores. DFT predicted (Neimark and Ravikovitch) that the adsorption and desorption relatives pressure for independent open cylindrical pores of size ~15-20 nm should be related by a power of 1.8. In this study, it was shown experimentally that the adsorption and desorption relative pressures were instead related by a power of 1.5. This result has indicated that the DFT calculations used by Neimark and Ravikovitch do not correctly predict the capillary condensation and evaporation processes in pores which are ~15-20 nm in size. Therefore, the above findings have indicated that DFT should not be used to derive a pore size distribution for porous materials that have pore sizes in this range.

12.1.3 Determining the meniscus geometry in the Kelvin equation

Before deriving a pore size distribution from gas adsorption data using the Kelvin equation an assumption of the meniscus geometry must be assumed; it can either be hemispherical or cylindrical in shape. As discussed above, a potential discrepancy of a factor of two, between estimated and actual pore sizes, would be anticipated from employing the wrong meniscus geometry in the Kelvin equation. At the start of this study, deciding the

meniscus geometry for disordered amorphous mesoporous materials was an arbitrary choice. A method, however, has been developed to determine whether a hemispherical or cylindrical meniscus geometry should be used when analysing adsorption data. The developed method used the integrated gas-mercury-gas experiment and is summarised as follows. The pore sizes at the onset of mercury entrapment were determined from mercury porosimetry data analysed by the Kloubek equations. The Kloubek equations have been calibrated by electron microscopy so an actual pore size can be obtained. The onset of mercury entrapment was also determined by use of the 'change in incremental amount adsorbed plots' proposed by Rigby *et al.* (2008). A pore size was then calculated using the Kelvin equation by assuming either a hemispherical or cylindrical shaped meniscus. By comparing this to the analysed mercury porosimetry data, it was found that the pores at the onset of mercury entrapment filled by cylindrical menisci for S1 and hemispherical menisci for EA1. As stated above, pore size distributions are commonly quoted for heterogeneous catalysts, and are used as an indirect measurement to gauge likely catalyst activity. The method developed means that choosing the meniscus geometry, for the pores which entrap mercury, is not arbitrary and, thus, derived pore size distributions will not have a potential 100% error.

12.1.4 Gas sorption scanning loop experiments and scanning curve experiments before and after mercury porosimetry

Gas sorption scanning curve and loop experiments were used to study advanced adsorption and pore blocking effects in S1 (a sol gel silica sphere) and the main findings are as follows. Scanning loop experiments were studied over progressively smaller pressure ranges and it was found that hysteresis was purged. No hysteresis meant that the capillary condensation and evaporation processes were reversible. To explain this, it was proposed that capillary condensation and capillary evaporation occurred by advancing and retreating hemispherical menisci respectively. This was further evidence that adsorption does not have to occur by cylindrical type menisci in amorphous mesoporous materials. As mentioned above, if the incorrect meniscus geometry is assumed when analysing gas sorption data there is a potential 100% error in the derived pore size distribution and the actual pore size distribution. When the scanning loops were studied over larger pressure ranges, the width of hysteresis progressively increased. It was discussed that the hysteresis width in the loops was narrower than would be anticipated for single pore hysteresis. Therefore, it was suggested that hysteresis was because of delayed advancing and retreating hemispherical menisci, due to irregular cross sections in the pores; this is explained as follows. At a specific pressure in a gas adsorption experiment, capillary condensation can

occur in an open cylindrical pore, thus creating pseudo dead end pores at its pore ends. The menisci at the ends of the pore can ingress into neighbouring pores until a critical (large) pore size is reached. At this point the menisci cannot enter the pores (delayed) until the pressure is increased. An analogous scenario occurs for the retreating hemispherical menisci. However, the retreating menisci are delayed when they reach a critical (narrow) pore size instead. For desorption to continue, the pressure needs to be lowered further. These finding indicate that a pore size distribution obtained from either the adsorption or desorption isotherms is subject to errors. This is because cooperative effects between pores occur during both the adsorption and desorption processes.

Scanning curve experiments before and after mercury porosimetry were additionally studied. The gas sorption data for the pores which entrapped mercury were deconvolved from that for all other pores, and the scanning curves for these pores were then determined. It was found that the scanning curves crossed directly between the boundary curves, and this is anticipated for thermodynamically independent pores (Everett 1967). However, it was proposed that the crossing scanning curves were not due to thermodynamically independent pores. This was because mercury became entrapped in these pores because of structural effects (Rigby *et al.* 2008), which meant that these pores could not be thermodynamically independent. To explain why the pores which entrapped mercury capillary filled and emptied like independent pores a through ink bottle pore model was used. It was proposed that mercury became entrapped in the body of the ink bottle pore. The ratio between the pore body and outer necks was such that capillary condensation in the necks and body happened at the same time due to advanced adsorption, and capillary evaporation happened also at the same time due to the pore blocking mechanism. This meant that gas sorption could not distinguish between the pore necks and the pore body. Mercury porosimetry, however, was able to distinguish between the same neck to body ratio, as mercury became entrapped in the pore body following porosimetry. This finding suggests that mercury porosimetry is more sensitive to changes in pore size compared to the gas sorption technique and, therefore, the two techniques must probe different pore size distributions. Since mercury porosimetry can distinguish between smaller neck to body ratios, it is recommended that the mercury porosimetry technique should be used over the gas sorption technique to determine pore size distributions.

12.1.5 Cryoporometry: the advanced melting mechanism

Since there are problems deriving a pore size distribution from gas adsorption data, due to the advanced adsorption phenomenon, the cryoporometry technique was investigated. Analogous to gas sorption studies, hysteresis between the melting and freezing processes, of an imbibed material, is observed in cryoporometry. Therefore, an understanding of the freeze-thaw mechanism is necessary before pore size distributions are derived from the experimental data. At the start of this study it was believed that the melting curve should be used to calculate a pore size because the liquid like layer between the frozen imbibed material and the pore wall can act as a seed to initiate melting (Petrov and Furó 2006). Moreover, as each pore has a liquid like layer, it was thought that each pore could melt independently. Kondrashova *et al.* (2010), however, suggested that if the imbibed material in one pore melts, the molten phase could then act as a nucleation seed to melt the imbibed material in a neighbouring pore by a hemispherical meniscus. Melting by hemispherical menisci occurs at lower temperatures, and if the wrong melting mechanism is assumed when analysing the cryoporometry data, there is a potential discrepancy of a factor of two between estimated and actual pore sizes (Petrov and Furó 2006). Kondrashova *et al.* predicted this alternative melting mechanism, but they failed to demonstrate experimentally that it happens. This study, however, has shown that the alternative melting mechanism does occur and has termed it advanced melting. Scanning loops were studied, and PFG NMR and relaxometry data were used to probe the configuration of the molten phase to eliminate ambiguities when interpreting the scanning loops. Kondrashova *et al.* failed to do this and suggested unproven dead end pores to interpret scanning loop data. Analogous to the gas sorption scanning loops, hysteresis was purged when the cryoporometry scanning loops were studied over small temperature ranges. This meant that the melting and freezing mechanisms were reversible, which suggested that the melting and freezing processes occurred by advancing and retreating hemispherical menisci respectively. To demonstrate the advanced melting mechanism, the melting curves for whole and fragmented S1 were compared. By fragmenting S1, the macroscopic 'necks' and 'bodies' were separated, which meant that the advanced melting mechanism was curtailed. Therefore, the fragmented sample melted at higher temperatures compared to the whole sample, proving the advanced melting mechanism. These findings suggest that pore size distributions obtained from cryoporometry melting curves for whole pellet samples are subject to errors due to previously undetected advanced melting.

12.1.6 Comparing gas sorption, and cryoporometry, scanning curve and loop experiments

Analogous scanning curve and scanning loop experiments for the gas sorption and cryoporometry techniques were studied. This sub section will now compare these experiments for the two different techniques. The scanning loops for both techniques had very similar elliptical shapes. Moreover, when the scanning loops were studied over a smaller control variable range, hysteresis could be purged for both techniques. This suggested that the adsorption and desorption mechanisms were similar to the melting and freezing mechanisms. This is because of the advanced adsorption and advanced melting mechanisms, which have been discussed in the above sections. However, the scanning curves for the two techniques differed. Gas sorption and cryoporometry scanning curve experiments were started when the pore system was ~50% saturated with condensate and ~50% molten, respectively. This ensured that the scanning curves for the two techniques approximately studied the same pore size range. The gas adsorption and desorption scanning curves crossed between the boundary curves while the cryoporometry melting and freezing scanning curves converged to the upper and lower closure points of hysteresis respectively. It must mean that the advancing and retreating hemispherical menisci, for the cryoporometry technique, percolated through the pore structure over a narrower range of the control variable compared to the gas sorption technique. This is schematically shown in Figure 12.1, which shows equivalent adsorption (Points A, B and C) and melting (Points 1, 2 and 3) scanning curves. At Point A or 1 the pore model has no condensed gas or the imbibed material is frozen, respectively. As the control variable is increased gas condenses in the smallest pore by a cylindrical meniscus and the neighbouring larger pore fills by the advanced adsorption phenomenon (Point B). For the analogous melting scanning curve, the smallest pore melts by the liquid like layer propagating toward the pore centre, but now two neighbouring larger pores melt by the advanced melting phenomenon (Point 2). As the control variable is increased further, adsorption and melting in larger pores happens and Points C and 3 are reached respectively. Therefore, it is hypothesised that cryoporometry scanning curves are less sensitive to changes in the pore size compared to the gas sorption curves. This means if both advanced melting and advanced adsorption occur and are not accounted for, the derived pore size distribution from the melting curve will be skewed more to smaller pore sizes compared to the pore size distribution obtained from the adsorption isotherm. This indicates that the cryoporometry (melting) technique is perhaps not a better alternative to the gas adsorption technique to derive a pore size distribution. The proposed future work section below provides an experimental test that

may compare the gas sorption and cryoporometry techniques more directly than what has been done in this thesis.

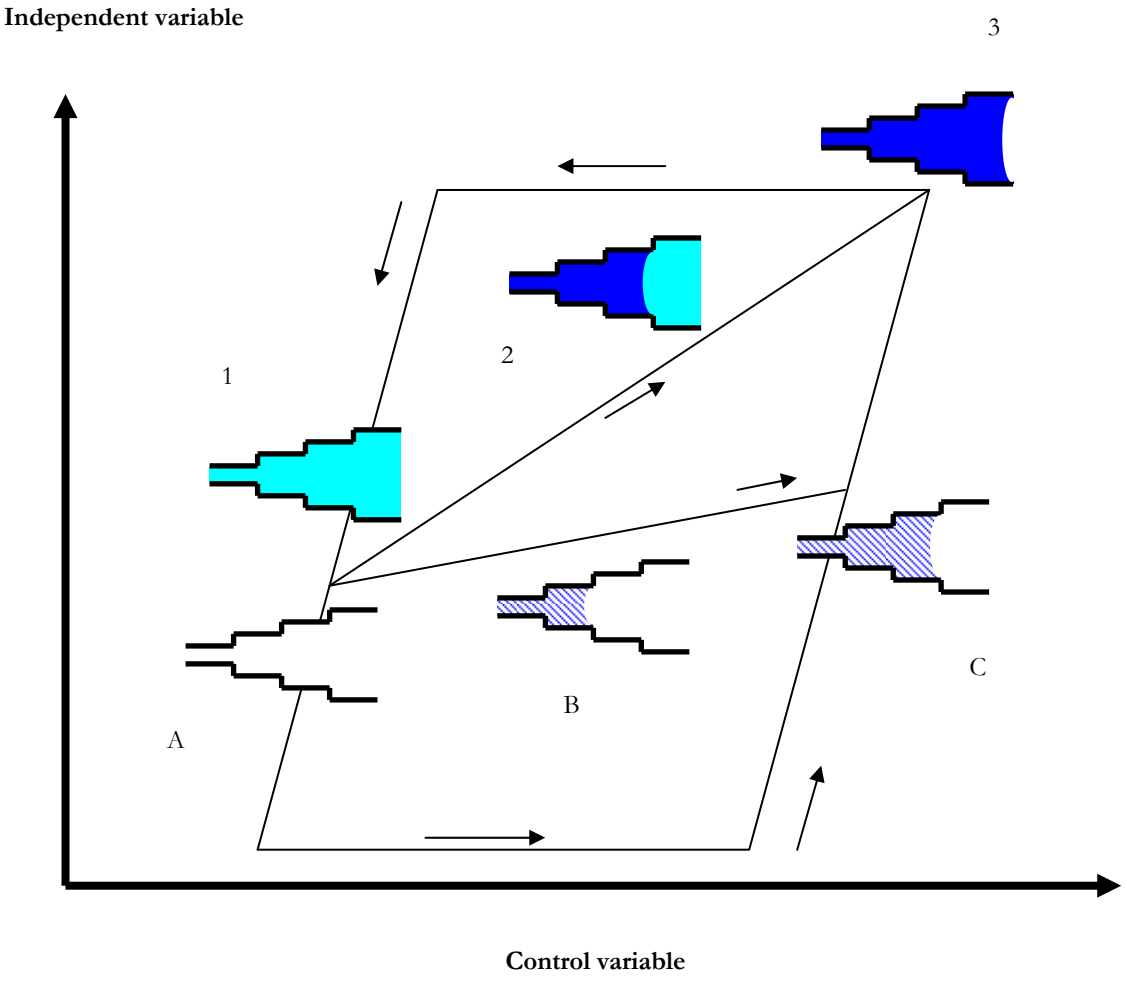

Figure 12.1: Schematic of an adsorption scanning curve (Points A, B and C) and a melting scanning curve (Points 1, 2 and 3) as the control variable is increased. Points 1-3: The light shading is the frozen fraction and the dark shading the molten fraction. Points A-C: The shading is the capillary condensed phase. The arrows show the direction of the change in the control variable

12.1.7 Nonane pre-adsorption

The location of platinum particles in a ZSM-5 zeolite support can determine the efficiency of the catalyst as it may influence the accessibility of the platinum to the reactant gases (Rivallan *et al.* 2010a). A technique was developed that was based on the nonane pre-adsorption experiment, to find whether platinum was located in the micropores of two ZSM-5 supports. By studying a chemisorption experiment before and after a nonane pre-adsorption experiment, the amount of platinum located in the micropores was determined. The Pt-ZSM-5(15) catalyst had a higher amount of metal surface area in the micropores compared to the Pt-ZSM-5(40) catalyst. Previous studies (Chua *et al.* 2010)

indicated that more coke formed in the micropores of the Pt-ZSM-5(15) catalyst compared to the Pt-ZSM-5(40) catalyst. This must be because there is a higher platinum surface area in the micropores of the Pt-ZSM-5(15) catalyst. Previous studies have only managed to determine whether platinum is either located in the pores (micropores and mesopores) or on the outer surface of the ZSM-5 crystallites (Rivallan *et al.* 2010a). This study, however, developed a method that can determine how much platinum is located in the micropores of a Pt-ZSM-5 catalyst.

12.2 Proposed future work

This section will now describe possible future experiments.

12.2.1 Combining gas sorption and cryoporometry experiments

This thesis has demonstrated that the freezing and melting mechanisms in a cryoporometry experiment, for S1, are similar to the adsorption and desorption mechanisms in the gas sorption experiment. The current study has only examined the cryoporometry and gas sorption experiments separately. To test and compare the mechanisms more directly, a gas sorption experiment can be combined with a cryoporometry experiment. For example, a water gas sorption experiment can be studied by suspending S1 above different salt concentrations to achieve different equilibrium saturation levels. This procedure is identical to the one used in Chapter 4 to study the water sorption process in G2. A cryoporometry melting experiment can then be studied at each equilibrium saturation level. This will enable a more direct comparison between the two experimental techniques.

An initial investigation has been made where melting cryoporometry experiments have been studied on saturated and partially saturated samples of S1. Partial saturation of S1 was achieved by a kinetic drying experiment. A saturated pellet was placed on a bench top for approximately 10 minutes, which allowed the water to evaporate. Figure 12.2 shows the results of these experiments. It can be seen that the melting curve for the partially saturated sample (closed diamonds) overlays the melting curve for the saturated sample (closed squares) at temperatures lower than 269.5 K. Above this temperature the melting curves diverge and they both plateau at ~ 271 K. This would perhaps indicate that the largest pores in the sample are still filled after the sample has been partially dried. An alternate explanation, however, can be made using the advanced melting mechanism. To explain this, Figure 12.3 shows a schematic of a partially filled and saturated system.

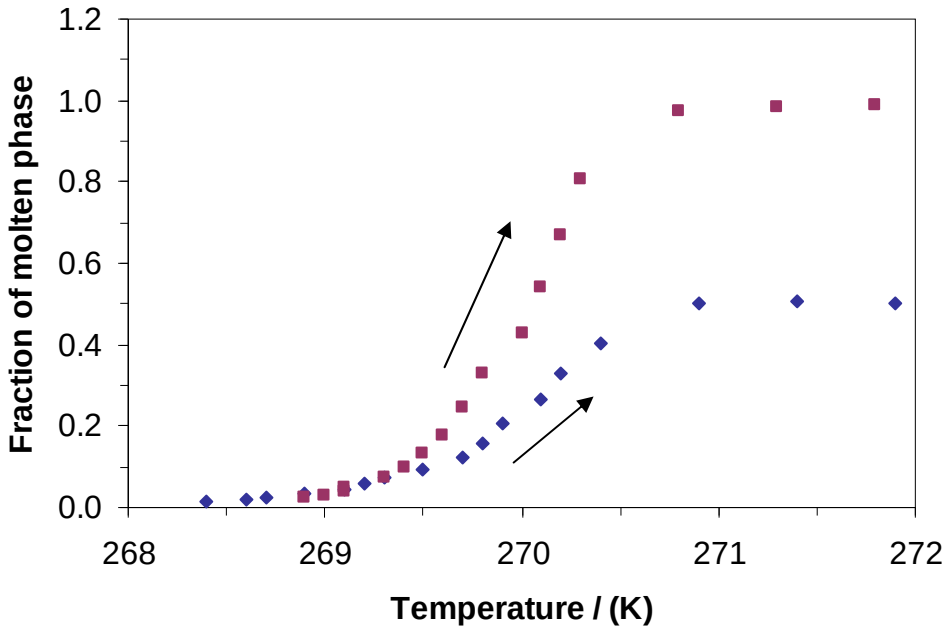

Figure 12.2: Melting curves for a partially saturated (closed diamonds) and saturated (closed squares) sample of S1. The molten fraction has been normalised to the saturated pellet. Arrows have been added to indicate the direction of the change in temperature

Starting when the system is frozen (light shading): The saturated system has all pores filled but the partially saturated system has only the smallest and medium sized pores filled. As the temperature is increased the smallest pore melts first at the same temperature for both systems. As soon as the small pore melts the neighbouring larger pores melt by the advanced melting mechanism. The medium and largest pore in the saturated system melt, but only the medium sized pore in the partially saturated system can melt. All of this would happen at the melting point of the smallest pore. From the cryoporometry melting curves, you may conclude that the saturated and partially saturated system had the same sized pores occupied as melting would occur at the same temperature. The only difference would be that more imbibed material melts for the saturated system. However, this conclusion is incorrect because the partially saturated system has only the smallest and medium sized pores occupied by the imbibed material. The incorrect conclusion is a result of the advanced melting mechanism. Early inspection of Figure 12.2 would suggest that below 269.5 K there is no advanced melting. Above this temperature, the melting curves diverge indicating the advanced melting mechanism.

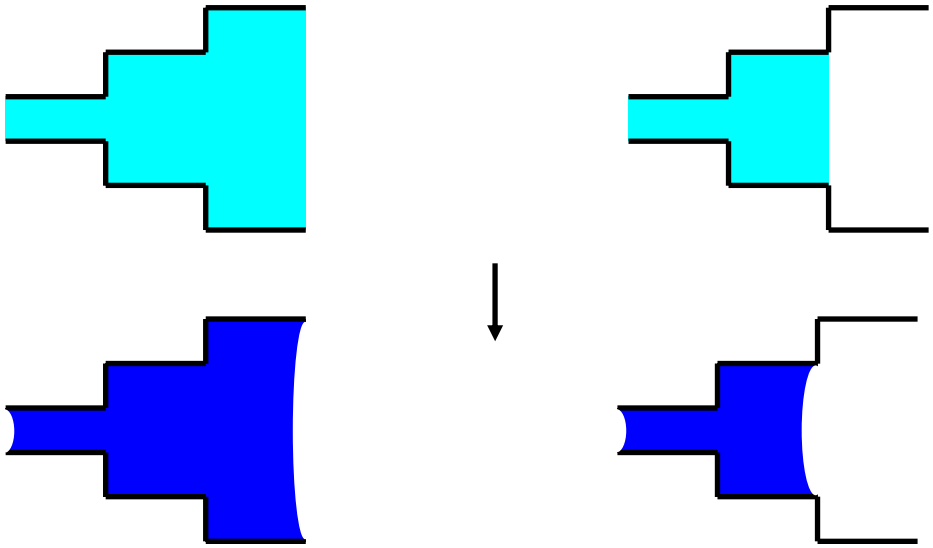

Figure 12.3: A saturated and partially saturated system. When the system is frozen the imbibed material is shown as light shading. When the system is molten the imbibed material is shown as dark shading

It is proposed for future work, that the melting curves, at different equilibrium saturation levels, should be combined with PFG NMR diffusion and T_2 relaxation studies. This may indicate the length scales over which advanced melting/advanced adsorption occurs (PFG NMR) and the size of pores that are occupied by the imbibed material (T_2). The configuration of the water in the partially saturated system shown in Figure 12.2 may give rise to a different spatial configuration than would be achieved by equilibrium adsorption. The experiment proposed above can be used to compare the gas adsorption and cryoporometry melting experiments more directly than was done is this thesis.

12.2.2 The integrated gas-mercury-gas experiments

The introduction to this thesis discussed the strategy to design ideal catalysts; it is desirable for all of the catalyst pellets to be used in a reaction. Catalysts are typically designed with macropores to increase the mass transfer of reactants from the outside of the catalyst into the mesopores and the products from the mesopores to the outside of the catalyst (Wijngaarden *et al.* 1998) to increase the effectiveness factor of the catalyst. However, the macropores make the catalyst weak, which means that the catalyst is susceptible to fracturing in reaction beds, so there is an optimisation of volume of macroporosity necessary. An experiment is proposed below that can test the usefulness of the macropores.

The integrated gas-mercury-gas experiments in this thesis studied the equilibrium sorption processes before and after mercury porosimetry. A kinetic experiment can potentially be

studied to compare the rate of adsorption of a gas before and after mercury porosimetry. This would provide a test to determine how useful the macropores in a catalyst are. A schematic of this experiment is shown in Figure 12.4. Initially a gas adsorption experiment is studied and the rate of adsorption of the gas is calculated. Following this, a mercury porosimetry experiment is then studied and the mercury will become entrapped in a set of pores following the experiment. The rate of adsorption of the gas can be measured again, after the mercury porosimetry experiment. The difference between the rates of adsorption will indicate how useful the pores, which entrap mercury, are at aiding diffusion into the mesopores. For example, if the rate of adsorption decreases it would suggest that pores which entrap mercury are useful to help reactants to diffuse into the catalyst and products to diffuse out.

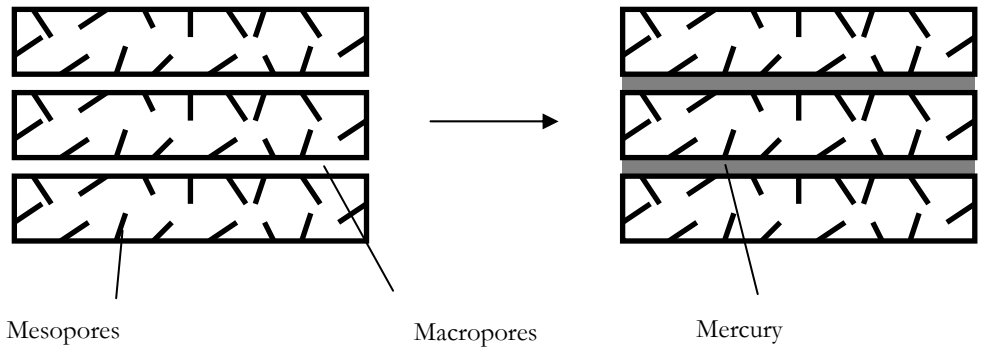

Figure 12.4: A porous material before and after a mercury porosimetry experiment. A rate of adsorption experiment is studied before and after the mercury porosimetry experiment

References

Ali, S. and McEnaney, B., 1985. *Journal of Colloid and Interface Science*, **107**, 355.

Anderson, J. R. and Pratt, K. C., 1985. *Introduction to Characterisation and Testing Catalysts*. Sydney: Academic Press.

Androutsopoulos, G. P. and Salmas, C. E., 2000. *Industrial and Engineering Chemistry Research*, **39**, 3474.

Atkins, P. and de Paula, J., 2002. *Atkin's Physical Chemistry*. 7th ed., New York: Oxford University Press Inc.

Baba, M., Nedelec, J-M., Lacoste, J., Gardette, J-L. and Morel, M., 2003. *Polymer Degradation and Stability*, **80**, 305.

Ball, P. C. and Evans, R., 1989. *Langmuir*, **5**, 714.

Barrett, E. P., Joyner, L. G. and Halenda, P. P., 1951. *Journal of the American Chemical Society*, **73**, 373.

Beck, J. S., Vartuli, J. C., Roth, W. J., Leonowicw, M. C., Kresge, C. T., Schmitt, K. D., Chu, C. T. W., Olson, D. H., Sheppard, E. W., McCullen, S. B., Higgins, J. B. and Schlenker, J. L., 1992. *Journal of the American Chemical Society*, **114**, 10834.

Beyea, S. D., Caprihan, A., Glass, S. J. and DiGiovanni, A., 2003. *Journal of Applied Physics*, **94**, 935.

Bibby, D. M., Milestone, N. B., Patterson, J. E. and Aldridge, L. P., 1986. *Journal of Catalysis*, **97**, 493.

Booth, H. F. and Strange, J. H., 1998. *Molecular Physics*, **93**, 263.

Broekhoff, J. C. P. and de Boer, J. H., 1968. *Journal of Catalysis*, **10**, 368.

Brownstein, K. R. and Tarr, C. E., 1977. *Journal of Magnetic Resonance*, **26**, 17.

Brunauer, S., 1945. *The Adsorption of Gases and Vapours*, London: Oxford University Press Inc.

Brunauer, S., Emmett, P. H. and Teller, E., 1938. *Journal of the American Chemical Society*, **60**, 309.

Bruschi, L., Mistura, G., Liu, L., Lee, W., Gösele, U. and Coasne, B., 2010. *Langmuir*, **26**, 11894.

Buchmeiser, M. R., 2003. *Polymeric Materials in Organic Synthesis Catalysis*, Germany: Wiley-VCH.

Carr, H. Y. and Purcell, E. M., 1954. *Physical Review*, **94**, 630.

Carrot, P. J. M., Drummond, F. C., Roberts, R. A. and Sing, K. S. W, 1988. *Chemistry and Industry*, 371.

Canizares, P., de Lucas, A., Valverde, J. L. and Darado, F., 1997. *Industrial and Engineering Chemistry Research*, **36**, 4797.

Casanova, F., Chiang, C. E., Li, C-P. and Schuller, I. K, 2007. *Applied Physical Letters*, 243103.

Casanova, F., Chiang, C. E., Li, C-P., Roshschin, I. V., Ruminski, A. M., Sailor, M. J. and Schuller, I. K., 2008. *Nanotechnology*, **19**, 315709.

Chen, W. H., Tsai, T. C., Jong, S. J., Zhao, Q., Tsai, C. T., Wang, I., Lee, H. K. and Liu, S. B., 2002. *Journal Of Molecular Catalysis A:Chemical*, **181**, 41.

Chenevarin, S. and Thibault-Starzyk, F., 2004. *Angewandte Chemie International Edition*, **43**, 1155.

Chua, L-M., 2010. *Deactivation of PtH-ZSM-5 Bifunctional Catalysts by Coke Formation during Benzene Alkylation with Ethane*. Thesis (Ph.D). The University of Bath.

Chua, L-M., Vazhnova, T., Mays, T. J., Lukyanov, D. B. and Rigby, S. P., 2010. *Journal of Catalysis*, **271**, 401.

Coasne, B., Grosman, A., Dupont-Pavlovsky, N., Ortega, C. and Simon, M., 2001. *Physical Chemistry Chemical Physics*, **3**, 1196.

Coasne, B., Gubbins, K. E. and Pellenq, R. J. M., 2005. *Physical Review B*, **72**, 0243404.

Coasne, B., Hung, F. R., Pellenq, R. J. M., Siperstein, F. R. and Gubbins, K. E., 2006. *Langmuir*, **22**, 194.

Cohan, L. H., 1938. *Journal of the American Chemical Society*, **60**, 433.

Crank, J., 1975. *The Mathematics of Diffusion*, Oxford: Clarendon Press

D'Orazio, F. D., Bhattacharja, S., Halperin, W. P., Eguchi, K. and Mizusaki, T., 1990. *Physical Review B*, **42**, 42.

de Araujo, L. R. R. and Schmal, M., 2002. *Applied Catalysis A: General*, **235**, 139.

de Boer, J. H., 1958. *In*: Everett, D. H. and Stone, F. S. *The Structure and Properties of Porous Materials*. London: Butterworths, 68.

de Lucas, A., Canizares, P., Durfin, A. and Carrero, A., 1997. *Applied Catalysis A: General*, **156**, 299.

Degnan, T. F., Smith, C. M. and Venkat, C. R., 2001. *Applied Catalysis A: General*, **221**, 283.

Denoyel, R., Llewellyn, P., Beurroies, I., Rouquerol, J., Rouquerol, F. and Luciani, L., 2004. *Particle and Particle Systems Characterization*, **21**, 128.

Detcheverrey, F., Kierlik, E., Rosinberg, M. L. and Tarjus, G., 2004. *Langmuir* **2004**, *20*, 8006.

Detcheverrey, F., Kierlik, E., Rosinberg, M. L. and Tarjus, G., 2003. *Physical Review E*, **68**, 061504.

Dore, C., Webber, J. B. W. and Strange, J. H., 2004. *Colloids and Surfaces A-Physicochemical and Engineering Aspects*, **241**, 191.

Dosseh, G., Xia, Y. D. and Alba-Simionesco, C., 2003. *Journal of Physical Chemistry B*, **107**, 6445.

Esparza, J. M., Ojeda, M. L., Campero, A., Dominguez, A., Kornhauser, I., Rojas, F., Vidales, A. M., Lopez, R. H. and Zgrablich, G., 2004. *Colloids and Surfaces A-Physicochemical and Engineering Aspects*, **241**, 35.

Evans, R. and Marconi, U. M. B., 1986. *Chemical Physics Letters*, **114**, 415.

Evans, R., 1990. *Journal of Physics Condensed Matter*, **46**, 8989.

Everett, D. H. and Smith, F. W., 1954. *Transactions of the Faraday Society*, **50**, 187.

Everett, D. H. and Whitton, W. I., 1952. *Transactions of the Faraday Society*, **48**, 749.

Everett, D. H., 1954. *Transactions of the Faraday Society*, **50**, 1077.

Everett, D. H., 1955. *Transactions of the Faraday Society*, **51**, 1551.

Everett, D. H., 1967. *In*: Flood, E. A., The Solid Gas Interface. New York: Marcel Dekker Inc., 1055.

Everett, D. H., 1979. *In*: Gregg, S. J., Sing, K. S. W. and Stoeckli, H. F. *Characterisation of Porous Solids*. London: Society of Chemical Industry, 229.

Farrher, G., Ardelean, I. and Kimmich, R., 2007. *Magnetic Resonance Imaging*, **25**, 453.

Figueroa-Gerstenmaier, S., Avalos, J. B., Gelb, L. D., Gubbins, K. E. and Vega, L. F., 2003. *Langmuir*, **19**, 8592.

Findenegg, G. H., Gross, S. and Michalski. Th., 1993. *In*: Suzuki, M. *Fundamentals of Adsorption*. Tokyo: Kondanska, 161.

Findenegg, G. H., Gross, S. and Michalski. Th., 1994. *In*: Rouquerol, J., Rodriguez-Reinso, F., Sing, K. S. W. and Unger, K. K. *Characterisation of Porous Solids III*. Amsterdam: Elsevier Science BV, 71.

Foster, A. G., 1932. *Transactions of the Faraday Society*, **28**, 645.

Gane, P. A. C., Ridgway, C. J., Lehtinen, E., Valiullin, R., Furó, I., Schoelkopf, J., Paulapuro, H. and Daicic, J., 2004. *Industrial and Engineering Chemistry Research*, **43**, 7920.

Gelb, L. D. and Gubbins, K. E., 1998. *Langmuir*, **14**, 2097.

Gelb, L. D. and Gubbins, K. E., 1999. *Langmuir*, **15**, 305.

Giesche, H., A project student report. Dissertation (Masters). Alfred University.

Gregg, S. J. and Langford, J. F., 1969. *Transactions of the Faraday Society*, **65**, 1394.

Gregg, S. J. and Sing, K. S. W., 1967. Adsorption, *Surface Area and Porosity*. London: Academic Press.

Gregg, S. J. and Sing, K. S. W., 1982. Adsorption, *Surface Area and Porosity*. 2nd ed., London: Academic Press.

Grillet, Y., Llewellyn, P. L., Kenny, M. B., Rouquerol, F. and Rouquerol, J., 1993. *Pure and Applied Chemistry*, **65**, 2157.

Grosman, A. and Ortega, C., 2005. *Langmuir*, **21***,* 10515.

Grosman, A. and Ortega, C., 2005, *Langmuir*, **24***,* 3397.

Grünberg, B., Emmler, T., Gedat, E., Shenderovich, I., Findenegg, G. H., Limbach, H. H. and Buntkowsky, G., 2004. *Chemistry European Journal*, **10**, 5689.

Guisnet, M. and Magnoux, P., 1989. *Applied Catalysis*, **54**, 1.

Haller, W., 1965. *Nature*, **206**, 693.

Hann, E. L., 1950. *Physical Review*, **80**, 580.

Hansen, E. W, Gran, H. C. and Sellevold, E. J., 1997. *Journal of Physical Chemistry B*, **101**, 7027.

Hansen, E. W., Fonnum, G. and Weng, E., 2005. *Journal of Physical Chemistry B*, **109**, 24295.

Hansen, E. W., Schmidt, R. and Stocker, M., 1996. *Journal of Physical Chemistry*, **100**, 11396.

Haukka, S., 1993. *Characterisation of Surface Species Generated in Atomic Layer Epitaxy on Silica*. Thesis (Ph.D). The University of Helsinki.

Hollewand, M. P. and Gladden, L. F., 1992. *Chemical Engineering Science*, **47**, 1761.

Hollewand, M. P. and Gladden, L. F., 1993. *Journal of Catalysis*, **144**, 254.

Hollewand, M. P. and Gladden, L. F., 1995a. *Chemical Engineering Science*, **50**, 309.

Hollewand, M. P. and Gladden, L. F., 1995b. *Chemical Engineering Science* **50**, 327.

Hore, P. J., 1995. *Nuclear Magnetic Resonance*. New York: Oxford University Press.

Hunter, M. J., Hyde, J. F., Warrick, E. L. and Fletcher, H. J., 1946. *Journal of the American Chemical Society*, **68**, 667.

Iza, M., Woerly, S., Danumah, C., Kaliaguine, S. and Bousmina, M., 2000. *Polymer*, **41**, 5885.

Jackson, C. L. and McKenna, G. B., 1990. *Journal of Chemical Physics*, **93**, 9002.

Jackson, C. L. and McKenna, G. B., 1996. *Chemistry of Materials*, **8**, 2128.

Janssen, A. H., Talsma, H., van Steenbergen, M. J. and de Jong, K. P., 2004. *Langmuir*, **20**, 41.

Jones, R. A. Y., 1969. *Annual Review of NMR Spectroscopy*, **1**, 3.

Khokhlov, A., Valiullin, R., Karger, J., Steinbach, F. and Feldhoff, A., 2007. *New Journal of Physics*, **9**, 272.

Kierlik, E., Monson, P. A., Rosinberg, M. L., Sarkisov, L. and Tarjus, G., 2001. *Physical Review Letters*, **87**, 055701.

Kleitz, F., Bérubé, F., Guillet-Nicholas, R., Yang, C-M. and Thommes, M., 2010. *Journal of Physical Chemistry C*, **114**, 9344.

Kloubek, J., 1981. *Powder Technology*, **29**, 63.

Kondrashova, D., Reichenbach, C. and Valiullin, R., 2010. *Langmuir*, **26**, 6380.

Koptyug, I. V., Khitrina, L. Y., Aristov, Y. I., Tokarev, M. M., Iskakov, K. T., Parmon, V. N. and Sagdeev, R. Z., 2000. *Journal of Physical Chemistry B*, **104**, 1695.

Kruk, M. and Jaroniec, M., 2000. *Chemistry of Materials*, **12**, 222.

Kruk, M., Jaroniec, M., Ko, C-H. and Ryoo, R., 2000. *Chemistry of Materials*, **12**, 1961.

Lapkin, A., Bozkaya, B., Mays, T., Borello, L., Edler, K. J. and Crittenden, B., 2003. *Catalysis Today*, **81**, 611.

Lepage, M., Visser, T., van der Eerden, A. M. J., Soulimani, F. and Weckhuysen, B. M., 2008. *Vibrational Spectroscopy*, **48**, 92.

Li, C. L., Navaro, O., Munoz, E., Boldu, J. L., Boxhimi, X., Wang, J. A., Lopez, T. and Gomez, R., 2000. *Applied Catalysis A: General*, **199**, 210.

Liabastre, A. A. and Orr, C., 1978. *Journal of Colloid Interface Science*, **64**, 1.

Libby, B. and Monson, P. A., 2004. *Langmuir*, **20**, 4289.

Lippens, B. C., Linsen, B. G. and de Boer, J. H., 1964. *Journal of Catalysis*, **3**(1), 32.

Lowell, S. and Shields, J. E., 1984. *Powder Surface Area and Porosity*, 2nd ed., New York: Chapman and Hall.

Lowell, S., Shields, J. E., Thomas, M. A. and Thommes, M., 2004. *Characterisation of Porous Solids and Powders: Surface Area, Pore Size and Density*. Dordrecht: Spinger.

Lu, G. Q. and Zhao, X. S., 2004. *In.* Lu, G. Q. and Zhao, X. S. *Nanoporous Materials Science and Engineering*. Online version: World Scientific. 1.

Lukyanov, D. B. and Vazhnova, T., 2008. *Journal Of Catalysis*, **257**, 382.

Mahnke, M. and Mögel, H. J., 2003. *Colloids and Surfaces A*, ***216***, 215.

Mason, G., 1988. *Proceedings of the Royal Society of London. Series A, Mathematical and Physical*, **415**, 453.

McBain, J. W., 1935. *Journal of the American Chemical Society*, **57**, 699.

Mitchell, J., Webber, J. B. W., Strange, J., 2008. *Physics Reports*, **461**, 1.

Mojet, B. L., Miller, J. T. and Koningsberger, D. C., 1999. *Journal of Physical Chemistry B*, **103**, 2724.

Morishige, K. and Nakamura, Y., 2004. *Langmuir*, **20**, 4503.

Morishige, K., 2009. *Langmuir*, **25**, 6221.

Naumov, S., Valiullin, R., Monson, P. A. and Kärger, J., 2008. *Langmuir*, **24**, 6429.

Neimark, V. and Ravikovitch, P. I., 2001. *Microporous and Mesoporous Materials*, **44**, 697.

Overloop, K. and van Gerven, L., 1993. *Journal of Magnetic Resonance Series*. **101**, 179.

Open University, 2004. *Applications of Probability M343*.

Pellenq, R. J. M., Rousseau, B. and Levitz, P. E., 2001. *Physical Chemistry Chemical Physics*, **3**, 1207.

Perkins, E. L., 2009. *Nuclear Magnetic Resonance Studies of Drug Release Devices*. Thesis (Ph.D). The University of Bath.

Perkins, E. L., Lowe, J. P, Edler, K. J., Tanko, N. and Rigby, S. P., 2008. *Chemical Engineering Science*, **63**, 1929.

Perry, R. H. and Green, D. W., 1997. *Perry's Chemical Engineers' Handbook*, 7th ed., New York: McGraw-Hill

Petrov, O. and Furo, I., 2006. *Physical Review E*, **73**, 7.

Petrov, O. V. and Furo, I., 2009. *Progress in Nuclear Magnetic Resonance Spectroscopy*, **54**, 97.

Porion, P., Levitz, P., Van Damme, H., Raoof, A., Guilbaud, J. P. and Chevoir, F., 1998. *Magnetic Resonane Imaging*, **16**, 679.

Portsmouth, R. L. Gladden, L. F., 1991. *Chemical Engineering Science*, **46**, 3023.

Prado, P. J., Balcom, B. J. and Jama, M., 1999. *Journal of Magnetic Resonance*, **137**, 59.

Puibasset, J., 2009. *Langmuir*, **25**, 903.

Quinson, J. F. and Brun, M., 1988. *Characterization of Porous Solids*, 307.

Ravikovitch, P. I. and Neimark, A. V., 2001. *Journal of Physical Chemistry B*, **105**, 6817.

Ravikovitch, P. I. and Neimark, A. V., 2002. *Langmuir*, **18**, 9830.

Ravikovitch, P. I., O'Domhnaill, S. C., Neimark, A. V., Schuth, F. and Unger, K. K., 1995. *Langmuir*, **11**, 4765.

Rigby, S. P., Chigada, P. I., Perkins, E. L., Watt-Smith, M. J., Lowe, J. P. and Edler, K. J., 2008. *Adsorption*, **14**, 289.

Rigby, S. P., Fletcher, R. S. and Riley, S. N., 2004a. *Chemical Engineering Science*, **59**, 41.

Rigby, S. P., 2002. *In*. Hubbard, A. *Encyclopaedia of Surface and Colloid Science*. New York: Marcel Dekker Inc. 4825.

Rigby, S. P. and Chigada, P., 2009. *Adsorption*, **15**, 31.

Rigby, S. P. and Edler, K. J., 2002. *Journal of Colloid Interface Science*, **250**, 175.

Rigby, S. P. and Fletcher, R. S., 2004. *Journal of Physical Chemistry B*, **108**, 4690.

Rigby, S. P., 2000. In Proceedings of 5th International Symposium on the Characterisation of Porous Solids (COPS V), Heidelberg, *Studies in Surface Science and Catalysis*, **128**, 111.

Rigby, S. P., 2000. *Journal of Colloid Interface Science*, **224**, 382.

Rigby, S. P., Barwick, D., Fletcher, R. S. and Riley, S. N., 2003. *Applied Catalysis A*, **238**, 303.

Rigby, S. P., Watt-Smith, M. J. and Fletcher, R. S., 2004b. *Journal of Catalysis*, **227**, 68.

Rigby, S. P., Watt-Smith, M. J., Chigada, P., Chudek, J. A., Fletcher, R. S., Wood, T., Bakalis, S. and Miri, T., 2006. *Chemical Engineering Science*, **61**, 7579.

Rivallan, M., Seguin, E., Thomas, S., Lepage, M., Takagi, N., Hirata, H. and Thibault-Starzyk, F., 2010a. *Angewandte Chemie International Edition*, **49**, 785.

Rivallan, M., Thomas, S., Lepage, M., Takagi, N., Hirata, H. and Thibault-Starzyk, F., 2010. *ChemCatChem*, **2**, 1599.

Rodriguez-Reinoso, F., Martin Martinez, J. M., Molina-Sabio, M., Torregrosa, R. and Garrido-Segovia, J., 1985. *Journal of Colloid Interface Science*, **106**, 315.

Rojas, F., Kornhauser, I., Felipe, C., Esparza, J. M., Cordero, S., Dominguez, A. and Riccardo, J. L., 2002. *Physical Chemistry Chemical Physics*, **4**, 2346.

Rosinberg, M. L., Kierlik, E. and Tarjus, G., 2003. *Europhysics Letters*, **62**, 377.

Roszak, S. and Balasubramanian, K., 1993. *Chemical Physics Letters*, **212**, 150.

Rouquerol, F., Rouquerol, J. and Sing, K. S. W., 1999. *Adsorption by Powders and Porous Solids*. London: Academic Press.

Rouquerol, F., Rouquerol, J. and Grillet, Y., 1989. *Pure and Applied Chemistry*, **61,** 1933.

Rouquerol, J., Anvir, D., Fairbridge, C. W., Everett, D. H., Haynes, J. M., Pernicone, N., Ramsay, J. D. F., Sing, K. S. W. and Unger, K. K., 1994. *Pure and Applied Chemistry*, **66**, 1739.

Ryoo, R., Ko, C-H., Kruk, M., Antochshuk, V. and Jaroneic, M., 2000. *Journal of Physical Chemistry B*, **104**, 11465.

Ryu, S-Y., Kim, D. S., Joen, J-D. and Kwak, S. Y., 2010. *Journal of Physical Chemistry C*, **114**, 17440.

Saam, W. F. and Cole, M. W., 1975. *Physical Review B*, **11**, 1086.

Sarkisov, L. and Monson, P. A., 2001. *Langmuir*, **17**, 7600.

Scherer, G. W., 1999. *Cement and Concrete Research*, **29**, 1347.

Schmidt, R., Hansen, E. W., Stocker, M., Akporiaye, D. and Ellestad, O. H., 1995. *Journal of the American Chemical Society*, **117**, 4049.

Schreiber, A., Ketelsen, I. and Findenegg, G. H., 2001. *Physical Chemistry Chemical Physics*, 2001, **3**, 1185.

Silvestre-Albero, A., Jardim, E. O., Bruijn, E., Meynen, V., Cool, P., Sepulveda-Escribano, A., Silvestre-Albero, J. and Rodriguez-Reinoso, F., 2009. *Langmuir*, **25**, 939.

Sing, K. S. W., Everett, D. H., Haul, R. A. W., Moscou, L., Pierotti, R. A., Rouquerol, J. and Siemieniewska, T., 1985. *Pure and Applied Chemistry*, **57**(4), 603.

Sing, K. S. W. and Schüth, F., 2002. *In*: Schüth, F., Sing, K. S. W. and Weitkamp, J., *Handbook of Porous Solids*. Germany: Wiley-VCH, 25.

Sonwane, C. G., Bhatia, S. K. and Calos, N. J., 1999. *Langmuir*, **15**, 4603.

Sotelo, J. L., Uguina, M. A., Valverde, J. L. and Serrano, D. P., 1994. *Applied Catalysis A: General*, **114**, 273.

Stakheev, A. Y., Shipro, E. S., Tkachenko, O. P., Jaeger, N. I. and Schulz-Ekloff, G., 1997. *Journal of Catalysis*, **116**, 382.

Stejskal, E. O. and Tanner, J. E., 1965. *Journal of Chemical Physics*, **42**, 288.

Strange, J. H, Rahman, M. and Smith, E. G., 1993. *Physical Review Letters*, **71**, 3589.

Strange, J. H., Mitchell, J. and Webber, J. B. W., 2003. *Magnetic Resonance Imaging*, **21**, 221.

Thomas, S., Rivallan, M., Lepage, M., Takagi, N., Hirata, H. and Thibault-Starzyk, F., 2011. *Microporous and Mesoporous Materials*, **140**, 140.

Thommes, M., 2010. *Chemie Ingenieur Technik*, **82**, 1059.

Thommes, M., Smarsly, B., Groenewolt, M., Ravikovitch, P. I. and Neimark, A. V., 2006. *Langmuir*, **22**, 756.

Thomy, A., Regnier, J. and Duval, X., 1972. *In*: *Thermochimie*. Paris: CNRS, 511.

Tompsett, G. A., Krogh, L., Griffin, D. W. and Conner, W. C., 2005. *Langmuir*, **21**, 8214.

Valiullin, R. R., Skirda, V. D., Stapf, S. and Kimmich, R., 1997. *Physical Review E*, **55**, 2664.

Van Damme, H., 2000. *In*:Papirer, E. *Adsorption on Silica Surfaces*. New York: Marcek Dekker Inc. 119.

Vansant, E. V., Van der Voort, P. and Vrancken, K. C., 1995. *Characterisation of Chemiscal Modification of the Silica Surface*. Netherlands: Elsevier Science B. V.

Vargas-Florencia, D., Petrov, O. V. and Furo, I., 2007. *Journal of Colloid and Interface Science*, **305**, 280.

Vishnyakov, A. and Neimark, A. V., 2003. *Journal of Chemical Physics*. **119**, 9755.

Vyalikh, A., Emmler, T., Grünberg, B., Xu, Y., Shenderovich, I., Findenegg, G. H., Limbach, H. H. and Buntkowsky, G., 2007. *International Journal of Research in Physical Chemistry and Chemical Physics*, **221**, 155.

Washburn, E. W., 1921. *Physical Review*, **17**, 273.

Watt-Smith, M. J., 2006. *The Characterisation of Porous Catalysts using Magnetic Resonance Imaging and Other Experimental Techniques*. Thesis (Ph.D). The University of Bath.

Webber, J. B. W., 2010. *Progress in Nuclear Magnetic Resonance Spectroscopy*, **56**, 78.

Webber, J. B. W., Strange, J. H. and Dore, J. C., 2003. *Magnetic Resonance Imaging*, **19**, 395.

Wink, W. A., 1946. *Industrial and Engineering Chemistry-Analytical Edition*, **18**, 251.

Woo, H. J., Porcheron, F. and Monson, P. A., 2004. *Langmuir*, **20**, 4743.

Woo, H. J., Sarkisov, L. and Monson, P. A., 2001. *Langmuir*, **17**, 7472.

Wu, D., Chen, A. and Johnson, Jr. C. S., 1995. *Journal of Magnetic Resonance A*, **115**, 260.

Wulff, M., 2004. *Thermochimica Acta*, **419**, 291.

Zhao, D. Y., Feng, J. L., Huo, Q. S., Melosh, N., Fredrickson, G. H., Chemelka, B. A. and Stucky, G. D., 1998. *Science*, **279**, 548.

Appendix A1

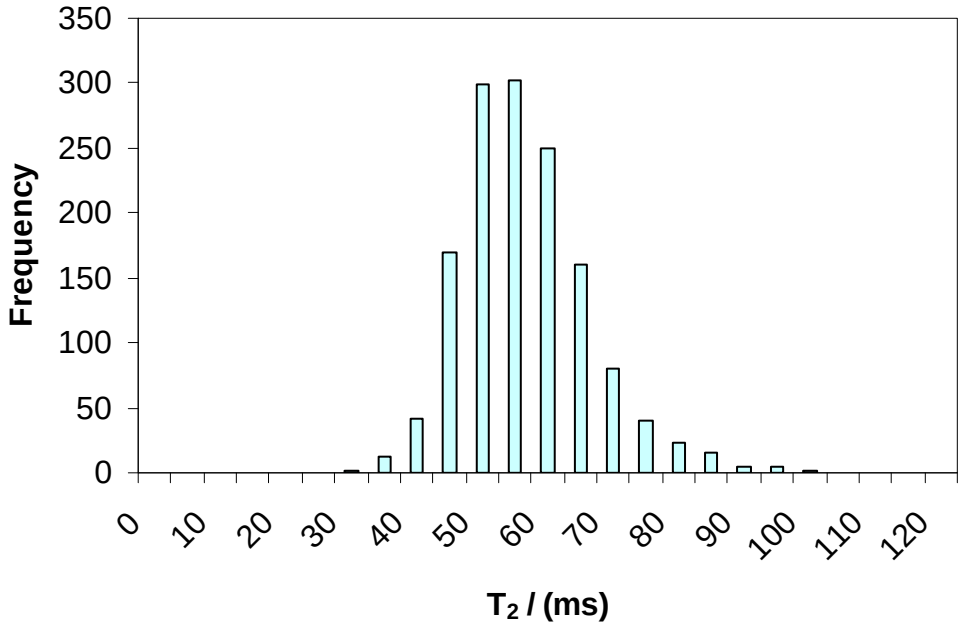

Figure A1.1: Frequency histogram for voxels from the transverse relaxation time (T_2/ms) image using the even echoes. The image was an arbitrary slice through a pellet from batch G2 exposed to a relative pressure of water vapour of 0.980

Appendix A2

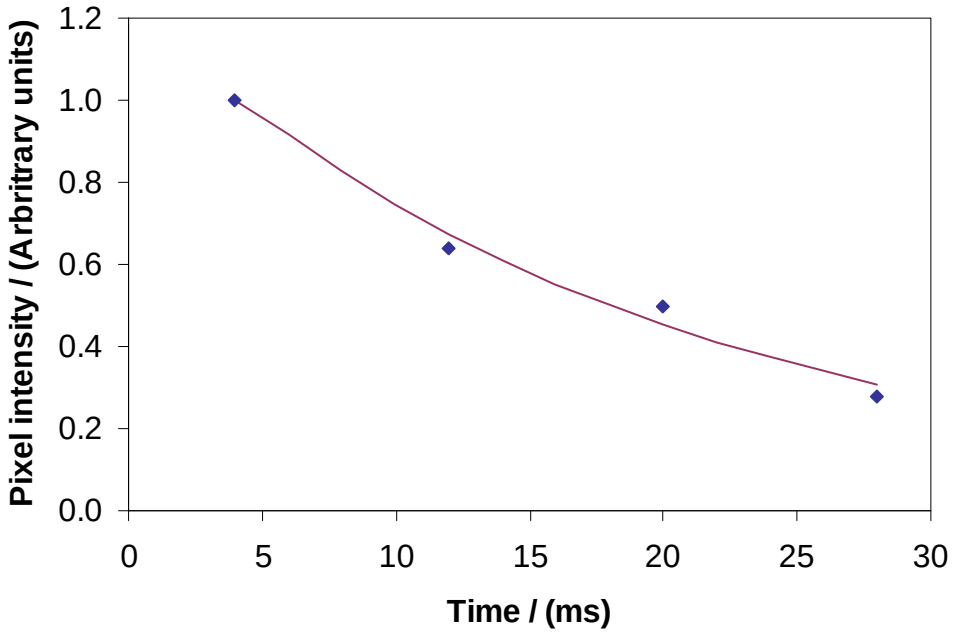

Figure A2.1: Relaxometry data (closed diamonds) acquired for a pellet at relative pressure 0.965 in Chapter 4. The fixed line shown is a fit to Equation 4.3

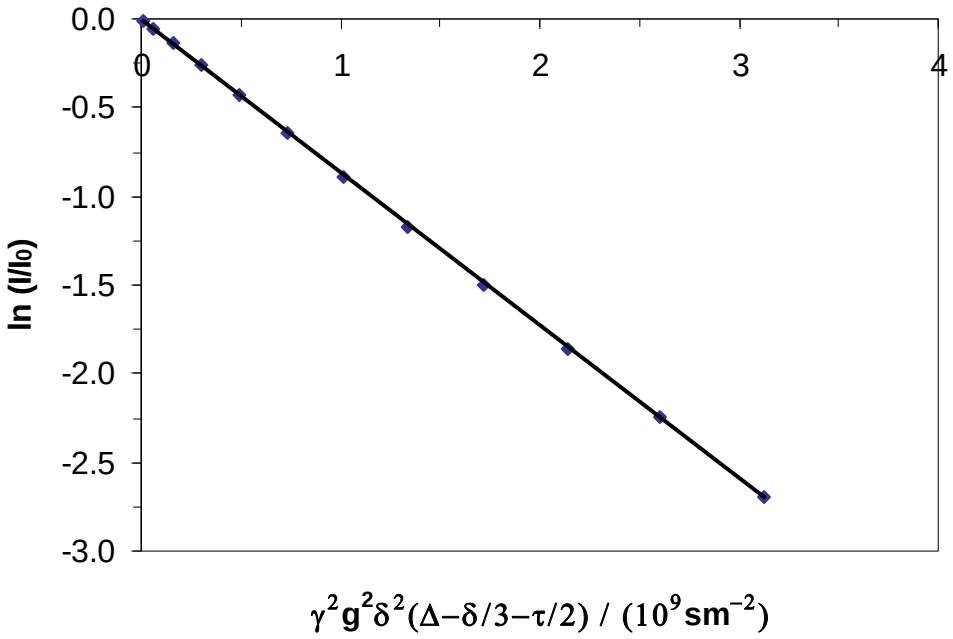

Figure A2.2: Log-attenuation plot of data from a PFG NMR experiment conducted on a pellet at relative pressure 0.965 in Chapter 4. The solid line shown is a fit of the data to Equation 4.1

Appendix A3

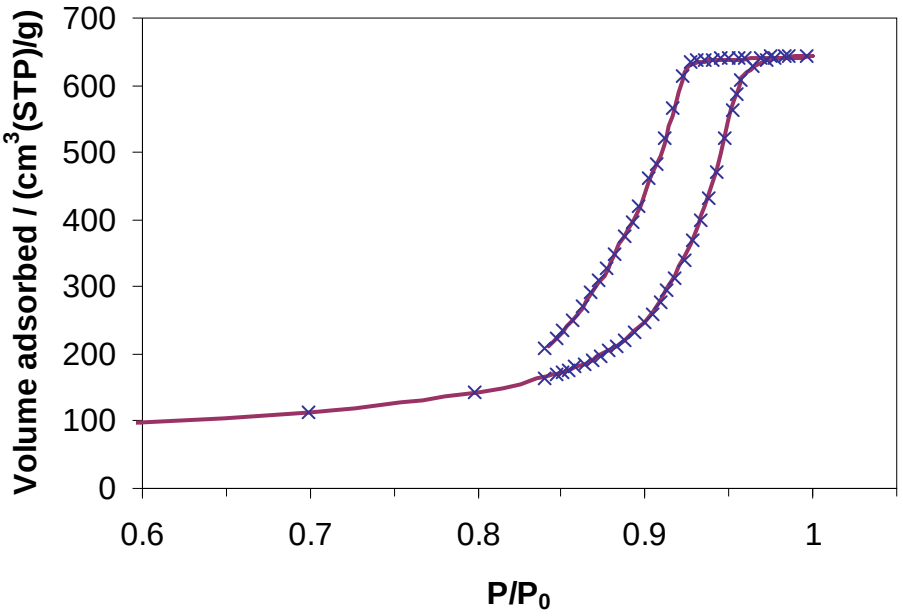

Figure A3.1: Gas sorption scanning curve isotherm for S1 using a 50 second equilibration time (fixed line) and 25 second equilibration time (crosses)

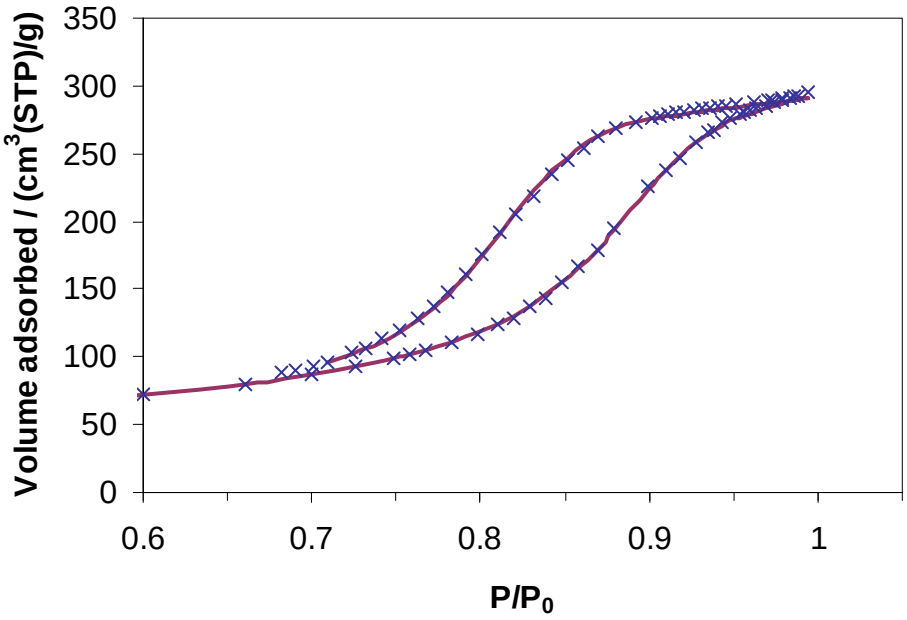

Figure A3.2: Gas sorption scanning curve isotherm for EA1 using a 50 second equilibration time (fixed line) and 25 second equilibration time (crosses)

Appendix A4

Error calculations

Diffusion coefficient and T_2 relaxometry errors were determined using the non-linear curve fitting function in Origin.

In Chapter 4, the % mass uptake from the MR spin density image data was determined to be 23.6 ± (1.0) % (at relative pressure 0.960) and 25.7 ± (1.1) % (at relative pressure 0.965). An example calculation will now be shown to calculate the error: The value of 23.6 % mass uptake (Z) was determined by dividing the average voidage fraction image at relative pressure 0.960 (A) by the average voidage fraction image at relative pressure 0.980 (B). The error in Z was calculated using equation A4.1.

$$\left(\frac{\Delta Z}{Z}\right)^2 = \left(\frac{\Delta A}{A}\right)^2 + \left(\frac{\Delta B}{B}\right)^2 \qquad \text{A4.1}$$

As stated in the text, the quoted error was assumed to be because of the uncertainty in the void fraction, which was 2.9 %. This means:

$$\left(\frac{\Delta Z}{23.6}\right)^2 = (0.029)^2 + (0.029)^2 \qquad \text{A4.2}$$

Therefore, ΔZ is 1.0 % mass uptake. An analogous calculation can be done to show 25.7 ± (1.1) % mass uptake.

Chapter 5 calculates the error in the total pore volume (from gas adsorption) and the error in the amount of mercury entrapment following porosimetry. The quoted errors were found by considering how the ASAP 2020 and Auto-pore IV 9450 apparatus work. For example, the ASAP 2020, as described in Chapter 5, doses an amount of gas and when the system is at equilibrium it automatically calculates the amount of gas that is adsorbed. Following this, another amount of gas is then dosed and the process continues. The error in the amount adsorbed for each collected data point is ~±0.30 cm^3g^{-1}. For all data points, the combination of errors can be calculated using equation A4.3.

$$(\Delta Z)^2 = (\Delta A)^2 + (\Delta B)^2 \qquad \text{A4.3}$$

where Z is a function of two variables A and B.

Appendix A5

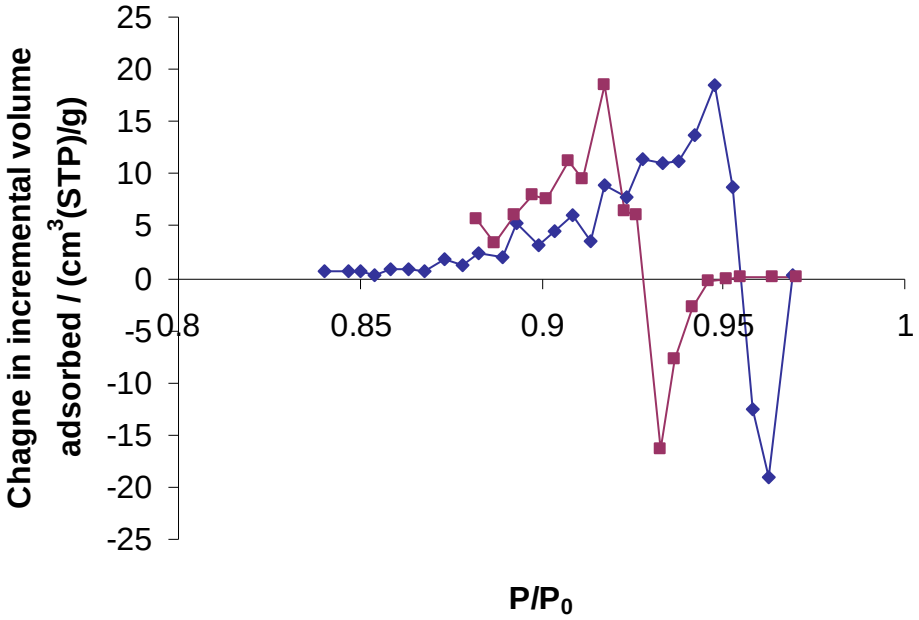

Figure A5.1: Adsorption (closed diamonds) and desorption (closed squares) change in incremental amount adsorbed plots for Ar at 87 K. Lines have been added to guide the eye

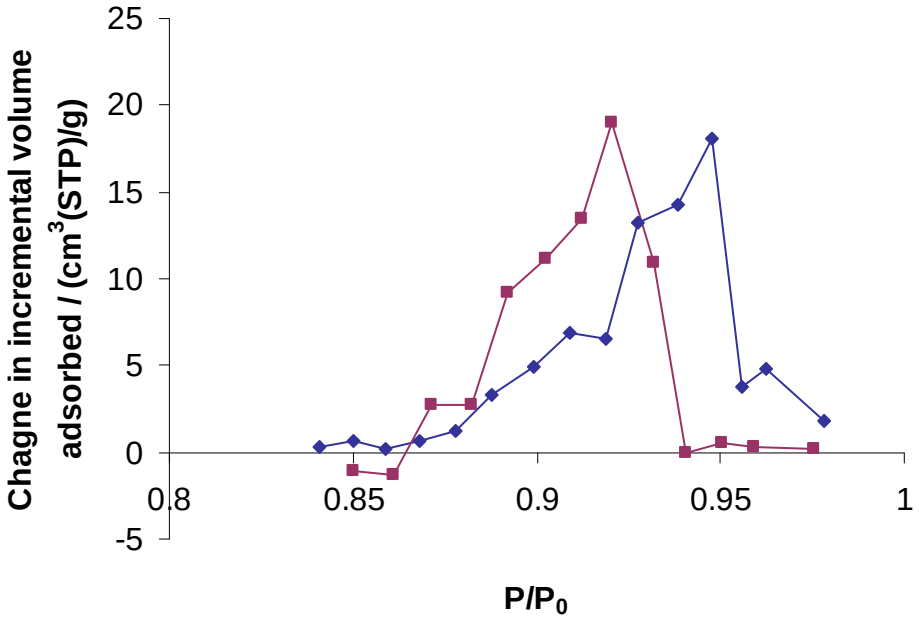

Figure A5.2: Adsorption (closed diamonds) and desorption (closed squares) change in incremental amount adsorbed plots for N_2 at 77 K. Lines have been added to guide the eye

Appendix A6

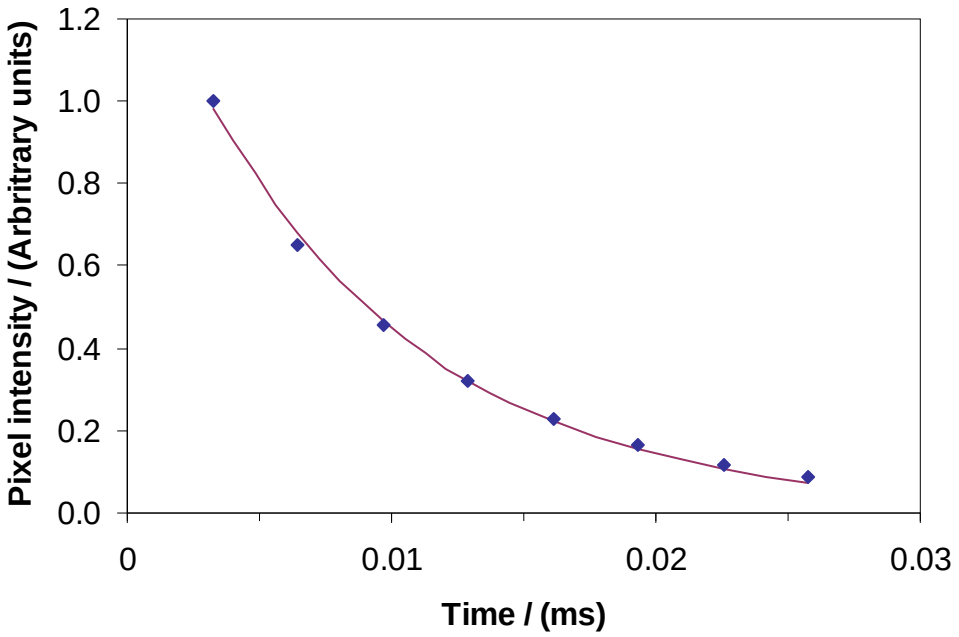

Figure A6.1: Relaxometry data acquired for point C in Chapter 10, corresponding to a temperature of 268.7 K, and a molten volume fraction of 0.49. The fixed line shown is a fit to Equation 10.3

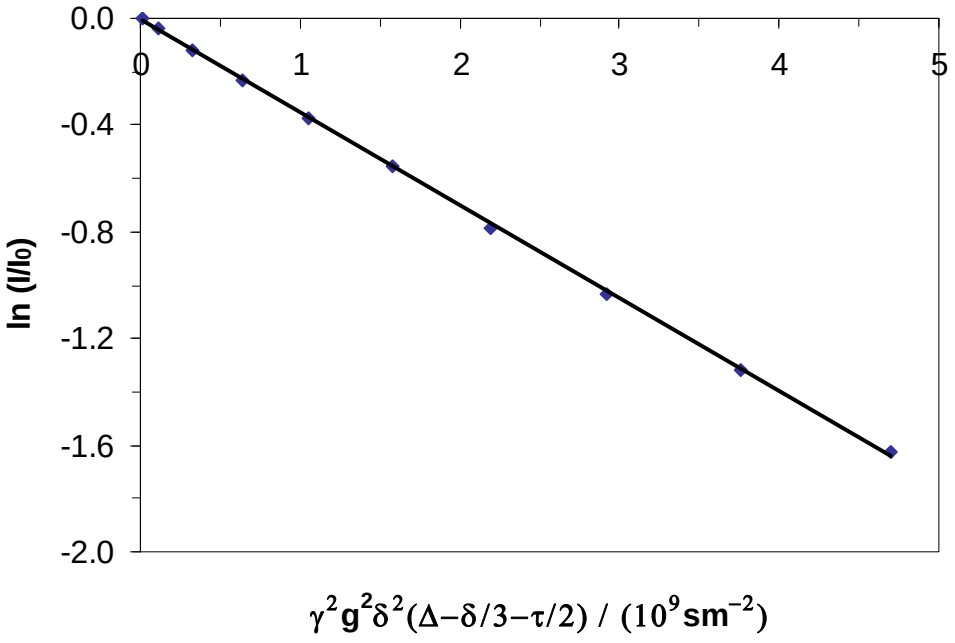

Figure A6.2: Log-attenuation plot of data from a PFG NMR experiment in Chapter 10, conducted on the molten fraction at point A, corresponding to a temperature of 268.7 K and a molten volume fraction of 0.49. The diffusion time was 0.15 s. The solid line shown is a fit of the data to Equation 10.1